The Dissertation Committee for Avik Roy
certifies that this is the approved version of the following dissertation:

Search for Singly Produced Top Partners in Trilepton Final State Using Data Collected by the ATLAS Detector from pp Collisions at $\sqrt{s} = 13$ TeV

Committee:

Timothy R Andeen Jr, Supervisor

Peter Onyisi

Can Kilic

Karol Lang

Michael Boylan-Kolchin

CERN-THESIS-2021-185
/ /2021

Search for Singly Produced Top Partners in Trilepton Final State Using Data Collected by the ATLAS Detector from pp Collisions at $\sqrt{s} = 13$ TeV

by

Avik Roy

DISSERTATION

Presented to the Faculty of the Graduate School of

The University of Texas at Austin

in Partial Fulfillment

of the Requirements

for the Degree of

DOCTOR OF PHILOSOPHY

THE UNIVERSITY OF TEXAS AT AUSTIN

August 2021

Dedicated to my parents and my late uncle

বাবা, মা, এই গবেষণার সার্থকতা তোমাদের মুখে হাসি ফোটাতে পারায় ।
জেঠু, তোমাকে বড় অসময়ে হারালাম । তোমার অনুপ্রেরণা ছাড়া এটা সম্ভব ছিল না ।

Acknowledgments

Coming from the orient, I have grown up with utmost respect for the relationship between a *guru* and a mentee. A Sanskrit prayer hymn reminds me- a mentor transcends the role of friends, parents, and even God when it comes to learning. My experience as Tim's student probably cannot be summarized better. I consider myself extremely lucky to have him as my supervisor. His passion and resourcefulness as a physicist have been a precise compass in navigating the alleys of experimental high-energy physics. And he yet manages to overcome the highly superior standards he sets for himself as a physicist with his genuine kindness and cheerfulness. He is a true do-gooder, a genuine joy-bringer. He has often gone way beyond what one would expect from an academic supervisor to support his students in their difficult times. Kudos, boss!

UT ATLAS is a neat group of people. I have always found Peter, our co-PI, to be an inexhaustible source of enthusiasm. He never turns down an invitation to discuss physics despite being on a plane with terrible internet or enjoying a lazy afternoon beer at the CERN cafeteria. I have also come to believe that there is no unsolvable problem for the vigorous and tireless Nikiforos. Physics always seemed merrier when Rohin was around. Moreover, it was a real treat to share the sixth-floor cubicles with the most charismatic group of peers. The experience of working with Harish, Aaron, Chuck, Mesut, Dev, Mark has paved my way of growing as a physicist, understanding and adapting to the culture of a foreign land.

The physics I have learned at UT Austin is valuable, but the human experience I have accumulated here is priceless.

My parents and my siblings have always been there to guide me and to encourage me with their wisdom and optimism event at the most difficult times. I never miss their warmth and love for a moment despite being away halfway across the world. My in-laws have always treated me with incredible adoration. I would also like to thank my friends, fellow Bangladeshi graduate students, Mohammed Ally *vai*, and Duke uncle for their support.

Finally, I probably cannot find any proper way of thanking enough my wonderful wife, Senjuti. Life as a graduate student was not easy. Plus, having the bonds of our marriage and families split across three timezones and five cities made it no easier. Over the past six years, she has turned mountains upside down but never conceded an inch of margin of our relationship. Her strength has made it possible for me to navigate the emotional battles that otherwise would have engulfed my sanity to the point of beyond recovery. As an uncompromising partner, she always plays the just role- a mentor, a critic, or a motivator, to bring the best out of me, sometimes beyond what I think is possible. Thank you, sweetheart– for believing in me, for being there with me at every turn of life, for driving 2200 miles in Florida, for putting up with my insomnia and amaxophobia. You made this journey possible.

Search for Singly Produced Top Partners in Trilepton Final State Using Data Collected by the ATLAS Detector from pp Collisions at $\sqrt{s} = 13$ TeV

Avik Roy, Ph.D.
The University of Texas at Austin, 2021

Supervisor: Timothy R Andeen Jr

This thesis presents the search for a heavy, up-type vector-like quark (VLQ), or Top Partner, with charge +2/3. Top Partners are predicted in well motivated models of new physics beyond the Standard Model. Having collected data with the ATLAS detector during 2015-2018 run of the LHC at a center-of-mass energy of 13 TeV, I describe in this dissertation an analysis searching for Top Partners produced by the fusion of a W boson and a bottom quark and decaying into a Z boson and a top quark with a kinematic signature of three leptons. Since the search performed by analyzing the data collected in 2015-16 does not provide sufficient evidence in favor of VLQ discovery, we set limits on Top Partner mass as a function of its coupling constants. In order to extend this search for the entire dataset collected by ATLAS in Run 2 and facilitate a general interpretation and combination of all single VLQ searches in ATLAS, a generalized, semi-analytical framework for model-independent interpretation of the results of a generic search for the single production of VLQs in terms of the free parameters in the VLQ Lagrangian is presented. Additional studies are performed to facilitate computationally manageable signal generation for a fine grid of VLQ mass and couplings, probe interference between VLQ and standard model processes, and quantify contribution of sub-dominant diagrams. Finally, an updated analysis strategy to expand the previously mentioned search for the entire Run 2 dataset is described with initial results for kinematic distributions as well as expected limits on cross-sections, Top Partner masses, and couplings.

Table of Contents

Acknowledgments **iv**

Abstract **vi**

List of Tables **x**

List of Figures **xi**

Chapter 1. The Standard Model of Particle Physics and Beyond **1**

1.1 The Standard Model: A Brief Review 1

1.1.1 The Gauge Bosons 2

1.1.2 The Fermions 2

1.1.3 The Higgs Boson 5

1.2 Limitations of the Standard Model 6

1.2.1 Gravity 7

1.2.2 Matter-Antimatter Asymmetry 7

1.2.3 Dark Energy and Dark Matter 7

1.2.4 The Strong CP Problem 8

1.2.5 Neutrino Masses 8

1.3 The Naturalness of the Higgs Mass 9

1.4 Vector-like Quarks (VLQs) to Solve the Naturalness Problem 10

1.5 Phenomenology and Search of VLQs at the LHC 11

1.6 Outline of the Thesis 15

Chapter 2. The LHC and the ATLAS Detector **17**

2.1 The Large Hadron Collider (LHC) 17

2.1.1 Accelerating the Protons 18

2.1.2 Luminosity 19

2.2 The ATLAS Detector 22

2.2.1 The Inner Detector 24

2.2.1.1 The Pixel Detector 25

2.2.1.2 The Semi-conductor Tracker 26

2.2.1.3 The Transition Radiation Tracker 26

2.2.2 The Calorimeters 27

2.2.2.1 Electromagnetic Calorimeter 28

2.2.2.2 Hadronic Calorimeter 30
2.2.2.3 Forward Calorimeter 31
2.2.3 The Muon Spectrometer 31
2.2.4 Trigger and Data Acquisition (TDAQ) 32

Chapter 3. A Search for Top Partners Using 36.1 fb^{-1}Data Collected by the ATLAS Detector in 2015-16 35
3.1 Signal and Background Modeling with Monte Carlo (MC) 36
3.1.1 Background Processes 37
3.1.2 Single-T Signal 39
3.2 Object Reconstruction 40
3.2.1 Electron Reconstruction 41
3.2.2 Muon Reconstruction 42
3.2.3 Jet Reconstruction 42
3.3 Event Selection 43
3.3.1 Primary Selection 43
3.3.2 Reduction of Contamination from Pair Production Signals 44
3.3.3 Optimization of the Signal Region 44
3.3.4 Background Modeling: Control Regions 45
3.4 Systematic Uncertainties 48
3.4.1 Detector-related uncertainties 53
3.4.2 Other uncertainties 54
3.5 Statistical Fitting 56
3.5.1 Limits and Combination 63

Chapter 4. Generalized Interpretation of single-VLQ Searches 69
4.1 The Philosophy of Interpretation of VLQ Searches 69
4.2 Framework for Interpretation of Singly Produced VLQs 72
4.3 Evaluation of P_{NWA} 76
4.4 Reinterpretation of Limits from Existing Analyses 81

Chapter 5. Single-VLQ Signal Modeling for Comprehensive Search and Interpretation 88
5.1 Modified MadGraph Reweighting for Signal Generation 88
5.2 Interfernce between Signal and SM Processes 100
5.3 Contribution of subleading Diagrams 105

Chapter 6. Extending the Search for Top Partners with 139 fb^{-1}data collected by the ATLAS Detector in Run 2 113

6.1 Updated Background and Signal Modeling 113
6.2 Optimization of Event Categorization 115
6.2.1 Modified Signal, Control, and Validation Region Definitions 115
6.2.2 Improving Background Modeling by Kinematic Reweighting 118
6.3 Results of Statistical Fitting 122
6.4 Limits and Interpretation 131

Chapter 7. Summary of a Phase Transition 139

Appendix A. Studies on Reduction of Pair Produced VLQ Signal 143

Appendix B. MadGraph Process Syntax for Different Processes 148

Appendix C. Expected Limits on $WTZt$ Process Cross-section for Different Choices of Discriminating Variables Full Run 2 data 151

Appendix D. Expected and Observed Limits on $WTZt$ Process Cross-section for Different Choices of κ from the Full Run 2 data 152

Bibliography 155

List of Tables

1.1 Properties of all SM particles 6

3.1 Summary of background MC samples 41
3.2 Definition of control and signal regions 47
3.3 Pre-fit data-MC comparison in control and signal regions 49
3.4 Post-fit data-MC comparison in control and signal regions 49
3.5 Cross-section uncertainties for the main background processes 54

4.1 The choice of couplings for event generation and cross-section calculation in MadGraph 77
4.2 The best fit values for the parametric representation of $\mathrm{P_{NWA}}$ in equation (4.19) for different values of M_T. 80
4.3 The best fit values for the parametric representation of $\mathrm{P_{NWA}}$ in equation (4.19) for different values of M_B. 80
4.4 The best fit values for the parametric representation of $\mathrm{P_{NWA}}$ in equation (4.20) for different values of $M_{T/B}$. $\mathrm{P}_{\mathrm{NWA},ZTHt} \approx 1.0$ for all $\frac{\Gamma}{M}$ at $M_T = 1.0$ TeV 81
4.5 Comparison of reduced cross-section values calculated from equation (4.24) with the values reported in Ref. [74] 86

5.1 Interference cross-section for singly produced Top partners decaying to a Z boson and a top quark for different choices of VLQ mass and coupling 102

6.1 Summary of CR, VR and SR definition 118
6.2 Prefit data-MC comparison in control, validation, and signal regions 122
6.3 Postfit data-MC comparison in control, validation, and signal regions 122
6.4 Different types of uncertainties and number of NPs associated with them . . 128

A.1 Pair and signal production yields in signal region before and after applying the $n(jets) \times H_T(jets) < 6$ TeV cut 146
A.2 Yields from pair production events and standard model backgrounds in control regions before and after applying the $n(\mathrm{jets}) \times H_{\mathrm{T}}(\mathrm{jets}) < 6$ TeV cut 146
A.3 Exclusion limits on $\sigma(pp \to T\bar{b}q) \times BR(T \to Zt)$ [pb] at 95% confidence level before and after the pair production contamination suppression 147

List of Figures

1.1 First order loop diagram for the Higgs propagator involving top quark loop. 9
1.2 First order loop diagrams for the Higgs propagator involving VLQs 11
1.3 Branching ratio of Top Partners as a function of mass for singlet T and doublet (X, T) representations 13
1.4 Dominant contributing diagrams for (a) pair production and (b) single production of VLQs 14
1.5 Cross-section of VLQ pair and single production processes from pp collisions as a function of VLQ mass for a (a) $\sqrt{s} = 8$ TeV and (a) $\sqrt{s} = 13$ TeV [51]. . 15

2.1 The CERN accelerator complex 19
2.2 Integrated luminosity of ATLAS Run-2 data 21
2.3 Pileup distribution of ATLAS Run-2 data 21
2.4 A cutaway view of the ATLAS detector 23
2.5 A cutaway view of the Inner Detector and its radial coverage 25
2.6 A cutaway view of the ATLAS calorimeters 28
2.7 Granularity of readout channels at different layers of the LAr calorimeter . . 29
2.8 A cutaway view of the Muon Spectrometer 32
2.9 Schematic representation of the Trigger and Data Acquisition System of ATLAS 33

3.1 Signal topology and event selection of the proposed analysis 45
3.2 b-tagged jet and forward jet distributions after primary selection 46
3.3 Signal/background lineshape comparison for kinematic variables at primary selection 47
3.4 Signal efficiency in control and signal regions for different Top Partner masses 48
3.5 Pre-fit and Post-fit distributions in VV CR 50
3.6 Pre-fit and Post-fit distributions in $t\bar{t} + X$ CR 51
3.7 Pre-fit and Post-fit distributions in the signal region 52
3.8 Pull plot for signal-plus-background Asimov fit 58
3.9 Relative variation of VV background lineshapes due to $\pm 1\sigma$ variation of the `VV_HF` NP 59
3.10 Relative variation of VV background lineshapes due to $\pm 1\sigma$ variation of the `VV_PDFSCALE` NP 59
3.11 Correlation matrix for signal-plus-background Asimov fit 60
3.12 Pull plot for background-only fit with observed data 61
3.13 Correlation matrix for background-only fit with observed data 62
3.14 Ordered list of the 10 NPs with the highest impact on the signal strength with the highest impact NP on top. 62

3.15 (a) Expected and observed upper limits in $\sigma \times BR$ as a function of the mass of T at 95% C.L. for a benchmark coupling of $\kappa = 0.5$ and singlet representation. (b) Ratio of expected cross-section limits from stat-only fit setup and stat-plus-syst fit setup 64

3.16 Expected and observed upper limits in $\sigma \times BR$ as a function of the mass of T at 95% C.L. after combining the dilepton and trilepton channels for a benchmark coupling of $\kappa = 0.5$ for the singlet representation 65

3.17 Comparison of the T mass distribution from kinematic reweighting with original simulation for a target coupling of (a) $\kappa = 0.1$ and (a) $\kappa = 1$ 66

3.18 Cross-section limits interpreted in terms of (a) coupling between a T and the W boson as a function of the VLT mass for BR($T \to Zt$) ≈ 0.25 in fixed branching ratio model and (b) mixing angle between the T and a top quark in a singlet model as a function of the VLT mass 67

3.19 (a) Expected and (b) observed cross-section limits interpreted in terms of upper limits on excluded T mass as a function of TWb and TZt vertex couplings (c_W and c_Z) requiring equal branching ratios in the H and Z channels 68

4.1 Distribution of (a) Top Partner invariant mass and (b) transverse momentum of the top quark from its decay in association with a Z boson for coupling values set to $c_{L,W} = 0.5$ (red) and $c_{L,W} = 0.8$ (green) in singlet representation 72

4.2 Estimated values of $P_{\rm NWA}$ plotted as a function of $\frac{\Gamma}{M}$ for different values of M_T for the $WTZt$ process. The red line shows the best fitted polynomial estimate for the correction factor. 78

4.3 Estimated values of $P_{\rm NWA}$ plotted as a function of $\frac{\Gamma}{M}$ for different values of M_T for the $WTHt$ process. The red line shows the best fitted estimate of an exponential function for the correction factor. 79

4.4 Distribution of differential cross-section in $E(T)$ of singly produced Top partner (T) of mass $M_T = 1.6$ TeV at narrow-width and finite-width for the $WTZt$ process with $\tilde{c}_W$ is set 0.05, 0.20, and 0.40 respectively in (a), (b), and (c) while requiring $\tilde{c}_W = \tilde{c}_Z = \tilde{c}_H$ 79

4.5 Distribution of differential cross-section in $E(T)$ of singly produced Top partner (T) of mass $M_T = 1.6$ TeV at narrow-width and finite-width for the $WTHt$ process with $\tilde{c}_W$ is set 0.05, 0.20, and 0.40 respectively in (a), (b), and (c) while requiring $\tilde{c}_W = \tilde{c}_Z = \tilde{c}_H$ 81

4.6 Representation of the exclusion limits on VLQ mass in the $\frac{\Gamma_T}{M_T}$ −BR($T \to Wb$) plane requiring $\tilde{c}_Z = \tilde{c}_H$ (a) in the CMS analysis in Ref. [74] and (a) in the ATLAS analysis in Ref. [71] 83

4.7 Reinterpretation of observed limits on top partner mass from Ref. [71], plotted as a function of $\tilde{c}_W$ and $\tilde{c}_Z$ for (a) $f = 0$ and (b) $f = \sqrt{2}$ 85

4.8 Representation of limits from the CMS (ATLAS) analysis in the $\tilde{c}_W$–$\tilde{c}_Z$–M_T ($\frac{\Gamma_T}{M_T}$–M_T–$\sigma_{\rm lim}$) hyperplane 87

5.1 Comparison between nominally simulated and reweighted distributions of Top Partner Invariant Mass (without LHE modifications) 90

5.2 Feynman Diagrams corresponding to (a) `PROC-PARTDECAY` and (b) `PROC-PARTDECAY` processes 91

5.3 Comparison of transverse momenta of electrons, muons, and jets when vector boson decays are performed in MadGraph and Pythia 92
5.4 (a) Distribution of parton momentum adjustment in the `LHE Refurbishing` Algorithm and (b) Comparison between nominally simulated distribution of Top Partner mass and the one obtained by reweighting after LHE Refurbishing for $M_T = 1100$ GeV at $\kappa = 0.3$ 95
5.5 Comparison between nominally simulated and reweighted distributions of electron and muon p_T for $M_T = 1100$ GeV at $\kappa = 0.3$ (with LHE modifications) . 96
5.6 Comparison between nominally simulated and reweighted azimuthal distributions of electrons and muons for $M_T = 1100$ GeV at $\kappa = 0.3$ (with LHE modifications) 97
5.7 Comparison between nominally simulated and reweighted pseudorapidity distributions of electrons and muons for $M_T = 1100$ GeV at $\kappa = 0.3$ (with LHE modifications) 98
5.8 Comparison between nominally simulated and reweighted distributions of partonic jet p_T, η, and ϕ for $M_T = 1100$ GeV at $\kappa = 0.3$ (with LHE modifications) 99
5.9 Comparison of the sum of `PROC-BKGONLY` and `PROC-SIGONLY` distributions with the inclusive process distributions for $M_T = 1100$ GeV and $\kappa = 0.3$ . . . 103
5.10 Comparison of the sum of `PROC-BKGONLY` and `PROC-SIGONLY` distributions with the inclusive process distributions for $M_T = 1100$ GeV and $\kappa = 1.0$ . . . 103
5.11 Comparison of the sum of `PROC-BKGONLY` and `PROC-SIGONLY` distributions with the inclusive process distributions for $M_T = 2000$ GeV and $\kappa = 0.3$ . . . 104
5.12 Comparison of the sum of `PROC-BKGONLY` and `PROC-SIGONLY` distributions with the inclusive process distributions for $M_T = 2000$ GeV and $\kappa = 1.0$ . . . 104
5.13 Feynman Diagrams corresponding to subleading contribution to single production of T with a Z boson and a top quark in the final state 105
5.14 Comparison of $WTZt$ process cross-sections when both s and t channel diagrams are included with cross-section from s-channel only diagrams 106
5.15 Comparison of the $m(Zt)$ distribution for $WTZt$ process with $M_T = 1200$ GeV when both s and t channel diagrams are included with s-channel only . . . 107
5.16 Comparison of the $m(Zt)$ distribution for $WTZt$ process $M_T = 2000$ GeV when both s and t channel diagrams are included with s-channel only . . . 108
5.17 Comparison of $ZTZt$ process cross-sections when both s and t channel diagrams are included with s-channel only 110
5.18 Comparison of the $m(Zt)$ distribution for $ZTZt$ process with $M_T = 1200$ GeV when both s and t channel diagrams are included with s-channel only . . . 111
5.19 Comparison of the $m(Zt)$ distribution for $ZTZt$ process $M_T = 2000$ GeV when both s and t channel diagrams are included with s-channel only . . . 112

6.1 MC predicted distributions of b-tagged jet multiplicity, p_T of the Z boson candidate, $\Delta\phi$ between the Z candidate and the third lepton, and $\Delta\phi$ between the Z candidate and the leading b-tagged jet for major background processes and the signal benchmark at primary selection. 116
6.2 The process topology and the signal region event selection for the analysis aiming 139 fb^{-1} data collected by the ATLAS detector in Run 2. 117

6.3 Comparison of MC predicted pre-fit distributions with data for the Z candidate p_T in (a) VV CR, (b) Mixed CR, and (c) $t\bar{t} + X$ CR. The overlaid black line represents the signal contribution for a Top partner with a mass of 1500 GeV and a coupling of $\kappa = 0.5$. 119
6.4 Comparison of MC predicted pre-fit distributions with data for the central jet multiplicity at primary selection for events with (a) 0 b-tagged jets and (b) ≥ 1 b-tagged jets. Only statistical uncertainties are considered. The overlaid black line represents the signal contribution for a Top partner with a mass of 1500 GeV and a coupling of $\kappa = 0.5$. 120
6.5 Kinematic reweighting factor for VV and $t\bar{t} + X$ processes as a function of the number of central jets. 120
6.6 Comparison between kinematically reweighted pre-fit background distributions and data for the central jet multiplicity at primary selection for events with (a) 0 b-tagged jets and (b) ≥ 1 b-tagged jets. Only statistical uncertainties are considered. The overlaid black line represents the signal contribution for a Top partner with a mass of 1500 GeV and a coupling of $\kappa = 0.5$. 121
6.7 Post-fit distribution (right) compared with the pre-fit distributions (left) for the Z candidate p_T (top) and H_T(jets + leptons) (bottom) distributions in the VV CR. The overlaid black line represents the signal contribution for a Top Partner with a mass of 1500 GeV and a coupling of $\kappa = 0.5$. 123
6.8 Post-fit distribution (right) compared with the pre-fit distributions (left) for the Z candidate p_T (top) and H_T(jets + leptons) (bottom) distributions in the mixed (1 b-jet) CR. The overlaid black line represents the relative shape of the signal contribution for a Top Partner with a mass of 1500 GeV and a coupling of $\kappa = 0.5$. 124
6.9 Post-fit distribution (right) compared with the pre-fit distributions (left) for the Z candidate p_T (top) and H_T(jets + leptons) (bottom) distributions in the $t\bar{t}$+X CR. The overlaid black line represents the relative shape of the signal contribution for a Top Partner with a mass of 1500 GeV and a coupling of $\kappa = 0.5$. 125
6.10 Post-fit distribution (right) compared with the pre-fit distributions (left) for the Z candidate p_T (top) and H_T(jets + leptons) (bottom) distributions in the Validation Region. The overlaid black line represents the relative shape of the signal contribution for a Top Partner with a mass of 1500 GeV and a coupling of $\kappa = 0.5$. 126
6.11 Post-fit distribution (right) compared with the pre-fit distributions (left) for the Z candidate p_T (top) and H_T(jets + leptons) (bottom) distributions in the SR. The overlaid black line represents the relative shape of the signal contribution for a Top Partner with a mass of 1500 GeV and a coupling of $\kappa = 0.5$. 127
6.12 Pull plot of the post-fit nuisance parameters for a background-only fit with ASIMOV dataset in control regions. 130
6.13 Relative variation of Z+jets background lineshapes due to $\pm 1\sigma$ variation of the `Zjets_Generator` NP 131
6.14 Pull plot of the post-fit nuisance parameters for background-only fit with observed data in control regions. 132
6.15 Correlation matrix of the post-fit nuisance parameters in the trilepton single-production channel for the background-only fit in control regions. 133

6.16 Ranking plot for the highest impact post-fit nuisance parameters in the trilepton single-production channel for the signal-plus-background fit in control and signal regions. Data is blinded in the signal region and ASIMOV dataset is used instead. 136
6.17 (b) Expected and observed upper limits on the $WTZt$ process cross-section for $\kappa = 0.5$ 136
6.18 (a) Cross-section limits interpreted in terms of coupling between a T and the W boson as a function of the VLT mass while the branching ratio is set to $\mathrm{BR}(T \to Zt) \approx 0.25$ in fixed branching ratio model. (b) The same limits are recast in terms of mixing angle between the T and a top quark in a singlet model as a function of the VLT mass where the region enclosed by the two branches are excluded. 137
6.19 (a) Expected and (b) Observed cross-section limits interpreted in terms of upper limits on excluded T mass as a function couplings c_W and c_Z. The grey regions in the low coupling corners represent parametric subspaces beyond the sensitivity of the analysis. In (c) and (d) respectively, the same limits are recast in terms of upper limits on excluded T mass as a function couplings $\mathrm{BR}(T \to Wb)$ and relative decay width $\frac{\Gamma}{M}$ (%). The coupling to the Higgs channel is set by requiring equal branching ratios in the H and Z channels. . 138

A.1 Jet Multiplicity distribution of single and pair production events in unconstrained signal region for 900 GeV (a), 1200 GeV (b), and 1400 GeV (c) mass points. 143
A.2 H_{T}(jets) distribution of single and pair production events in unconstrained signal region for 900 GeV (a), 1200 GeV (b), and 1400 GeV (c) mass points. 144
A.3 n(jets) $\times$ H_{T}(jets) distribution of single and pair production events in unconstrained signal region for 900 GeV (a), 1200 GeV (b) and 1400 GeV (c) mass points. 144
A.4 Efficiency, as a function of VLT mass, of the n(jets),H_{T}(jets) and n(jets) $\times$ H_{T}(jets) cuts in selecting the single production events (solid lines) and in selecting the pair production events (dashed lines) 145
A.5 H_{T}(jets + leptons) distribution in signal region before and after applying the n(jets) $\times$ H_{T}(jets) $<$ 6 TeV cut for 900 GeV (a), 1200 GeV (b), and 1400 GeV (c) mass points. 146

C.1 Excluded cross-section limit at 95% CL for $\kappa = 0.5$ when the discriminating variable is chosen as (a) scalar sum of jet and lepton p_T, H_T(jets + leptons), (b) scalar sum of lepton p_T, H_T(leptons), (c) invariant mass of the three leptons, $m_T(l_1 l_2 l_3)$, (d) p_T of Z boson candidate, $p_T(Z)$, (e) invariant mass of the Z boson candidate and the leading b-jet, $m_T(Zb_{\mathrm{lead}})$, and (f) invariant mass of the three leptons and the leading b-jet, $m_T(l_1 l_2 l_3 b_{\mathrm{lead}})$. Only statistical uncertainties are considered. The Z-boson candidate gives the strongest limit and has the strongest sensitivity for this analysis 151

D.1 Excluded cross-section limit at 95% CL for κ values of 0.15, 0.2, 0.25 (top row, left to right), 0.3, 0.35, 0.4 (middle row, left to right) and 0.45, 0.5, 0.6 (bottom row, left to right) respectively 153
D.2 Excluded cross-section limit at 95% CL for κ values of 0.7, 0.8, 0.9 (top row, left to right), 1.0, 1.1, 1.2 (middle row, left to right) and 1.3, 1.4, 1.5 (bottom row, left to right) respectively 154

Chapter 1

The Standard Model of Particle Physics and Beyond

In the twenty-first century, our understanding of the fundamental construct of the universe has become finer, more detailed, and exceedingly more structured. This unknotting of the deepest secrets of the universe did not come from an euphoric eureka, but rather has been an arduous, patient odyssey led by brilliant experimental design as well as insightful theoretical excursions across the time span of more than a century. Starting with the discovery of electron by Thomson in 1897, our journey of understanding the basic building blocks of this world reached a major milestone in 2012 with the discovery of the Higgs boson, giving us a theory that successfully describes three out of four fundamental forces of nature. This theory, the Standard Model (SM) of particle physics, is often boasted of as the most successful theory of nature. However, SM is far from being complete – and demystifying the riddles that constrain the SM is and will remain the primary challenge for today's and tomorrow's particle physicists.

1.1 The Standard Model: A Brief Review

SM is a field theoretic description of the fundamental particles of the universe and their interactions via electromagnetism, the weak force, and the strong force. It should be noted that gravitational interactions between the SM particles are generally ignored as they are much weaker than the other fundamental forces at the energy and length scales at which we currently investigate the properties of these particles. A comprehensive summary of the the Standard Model is available in Refs. [1, 2]. The following is a brief highlight of the basic constituents of the Standard Model. The content of the Standard Model can be broadly summarized into three categories:

1.1.1 The Gauge Bosons

The force carriers are responsible for mediating the interactions among particles. In the Standard Model, the fundamental forces are represented by spin-1 gauge fields invariant under transformations within local symmetry groups. The electroweak force manifests itself as a unified field theory for electromagnetism and the weak force [3–5], represented by a $SU(2) \times U(1)$ gauge group. The gauge bosons associated with this symmetry group are identified as the weak force mediating vector bosons $W^{\pm}, Z$ and the electromagnetic force carrier photon (γ). On the other hand, the strong force is modeled as invariance of the quark fields under local $SU(3)$ transformations. The corresponding force carriers are collectively called gluons [6]. While gluons and photons are massless, as required by symmetry preserving gauge theories, the vector bosons are massive. The masses of the vector bosons is the result of the electroweak symmetry group spontaneous breaking down to a $U(1)$ symmetry. The boson corresponding to the unbroken $U(1)$ symmetry is the massless photon, while the other three bosons representing the broken symmetry are massive.

1.1.2 The Fermions

There are three generations of spin-$\frac{1}{2}$ matter particles with a mass hierarchy in the SM. Each generation consists of two quarks and two leptons. Associated with each particle in the Standard Model, there is an anti-particle that has the same mass but opposite additive quantum numbers (like electric charge or color charge). In fact, all charged particles in the SM have a distinct anti-particle while the neutral photon and Z boson are their own anti-particles. For most part of this dissertation, denominations used to identify particles represent both the particle and the anti-particle inclusively, unless mentioned otherwise.

Other than charge and spin, the representation of the fermions is also associated with *chirality*. Although chirality is a Lorentz-invariant abstract property of a particle, it can be partly understood in terms of a related concept called helicity. A particle is called left (right) helical if the orientation of its spin vector is opposite to (same as) the direction of its motion. Evidently, while helicity is Lorentz-invariant for massless particles, it can vary with the choice of frame of reference in case of a massive particle. Chirality and helicity are identical for massless particles, but chirality is also Lorentz-invariant for massive particles. The left chiral fermions have a different electroweak representation compared to the right chiral fermions, causing the charged weak current to only couple with left chiral particles and right chiral anti-particles.

Ordinary matter in today's universe is composed of fermions belonging to the lightest of the three fermionic generations. The $+\frac{2}{3}e$ charged up quark and $-\frac{1}{3}e$ charged down quark compose protons and neutrons that constitute the nucleus of an atom. The negatively charged first generation lepton is the electron with a charge of $-e$, the lightest of all charged fermions. The heavier cousins of electron from the second and third generations are respectively called muon and tau. These particles behave the same way as electrons. However, owing to their larger masses, they can only be generated in high energy particle interactions (e.g. muons are created by cosmic rays interacting with atomic nuclei in the upper atmosphere). The lepton family of each generation also includes an electrically neutral particle called neutrino. For each generation, the neutrinos are named after their charged counterpart. Neutrinos are very light and interact only via the weak force. As a result, they can pass through most matter without interacting. Whether the neutrinos are their own anti-particles remains an unresolved mystery of modern particle physics.

Both muons and taus are unstable particles and decay into other particles within a short period of time. The decay of unstable, heavy fermions (leptons and quarks alike) to lighter, stable fermions, often described as a flavor changing current, is exclusively supported by the charged weak interaction via an exchange of the W boson. However, because the muon is much lighter than the quarks, it can exclusively decay to electrons. The mean lifetime of a muon is significantly larger than that of tau which, unlike muons, can decay to both lighter leptons and quarks. High energy muons can travel between tens to thousands of meter, depending on the matter they are traveling across, before decaying.

The second and third generation up-type quarks are called charm and top quarks, while the down-type quarks are called strange and bottom quarks. Similar to their charged leptonic cousins, these heavier quarks also appear in high energy interactions and quickly decay into lighter, more stable particles. The top quark, the heaviest charged fermion, decays almost immediately after being produced at very high energy interactions and decays exclusively to a bottom quark and a W bososn. The other heavy quarks can either directly decay to lighter particles or form relatively more stable bound states called hadrons before decaying to other stable particles. However, even the lightest of the quarks don't appear as free particles at typical energy scales. The strong force causes the quarks to be confined as part of composite hadrons, and only at high energies and correspondingly small length scales, the strong force is subdued to a scale that allows free quarks to be produced.

Each particle is identified with a quantum number identifying its representation under the symmetry groups. The triplet representation of the $SU(3)$ group allows the quarks to assume one of the three possible quantum numbers representing their strong eigenstate. The corresponding quantum number is identified as the color charge and the three eigenstates are called the red, blue, and green states. The left-handed quarks and leptons form doublet representation under the $SU(2)$ group of electroweak interaction. The corresponding quantum number is identified as the weak isospin (T_3), and the eigenstates of the doublet representation with $T_3 = +\frac{1}{2}$ are identified with the up type quarks and neutrinos while the down type quarks as well as the charged leptons have $T_3 = -\frac{1}{2}$. Each fermion is also associated with a weak hypercharge (Y) for coupling with the $U(1)$ subgroup of the electroweak theory. The electric charge (Q) represents a specific combination of the weak isospin and the hypercharge, $Q = T_3 + Y$ [1], and represents the coupling constant of the corresponding fermionic field under the unbroken $U(1)$ symmetry group representing the electromagnetic interaction.

[1] In some formulations, the electric charge is identified as $Q = T_3 + \frac{1}{2}Y$

1.1.3 The Higgs Boson

The residual representative of the Higgs field is a central piece of the Standard Model. A gauge theory for electroweak interactions is in tension with two important observations–

- The extremely short length scale for weak interaction is a definitive signature of the vector bosons W and Z being massive. However, preserving gauge symmetries prevents these bosons from acquiring masses. Having massive vector bosons requires the $SU(2)$ symmetry to be broken.

- The charged weak current interacts only with left-handed particles (and right-handed anti-particles), which indicates that the electroweak theory needs to be a chiral theory, with different representations for left and right-handed particles. This prevents the fermions from having explicit mass term in the Standard Model Lagrangian. Fermionic mass terms explicitly mix the left and right chiral particles and therefore, these terms won't be invariant under the local $SU(2)$ transformations that transform the left and right chiral fermions differently.

The Higgs mechanism [7] addresses these questions in a theoretically consistent manner. Under the unbroken $SU(2)$ transformation group, the Higgs field is a doublet augmented with a scalar potential that reaches a local minima for a non-zero expectation value of the field. In other words, the potential of the Higgs field has a non-zero Vacuum Expectation Value (VEV) – even in the absence of any interactions, the Higgs field takes a non-zero value and any excitation of the field is obtained as fluctuation around that value. The Higgs VEV remains invariant only up to a scalar rotation under an unbroken $U(1)$ transformation combining the local rotations under the original $U(1)$ and T_3 (the so-called third component of the weak $SU(2)$ group) transformations.

Spontaneously breaking the $SU(2) \times U(1)$ symmetry to a $U(1)$ causes the lost degrees of freedom to be eventually absorbed by the broken generators of the $SU(2)$ group, making them massive. The remaining degree of freedom represents an uncharged, massive, scalar

Type	Generation	Particle	Mass	Spin	Color	T_3	Y	Q
Leptons	1	Electron neutrino (ν_e)	< 1.1 eV	1/2	–	+1/2	-1/2	0
		Electron (e^-)	511 keV	1/2	–	-1/2	-1/2	-1
	2	Muon neutrino (ν_μ)	< 1.1 eV	1/2	–	+1/2	-1/2	0
		Muon (μ^-)	105.7 MeV	1/2	–	-1/2	-1/2	-1
	3	Tau neutrino (ν_τ)	< 1.1 eV	1/2	–	+1/2	-1/2	0
		Tau (τ^-)	1.78 GeV	1/2	–	-1/2	-1/2	-1
Quarks	1	Up quark (u)	2.16 MeV	1/2	Triplet	+1/2	+1/6	+2/3
		Down quark (d)	4.67 MeV	1/2	Triplet	–1/2	+1/6	-1/3
	2	Charm quark (c)	1.27 GeV	1/2	Triplet	+1/2	+1/6	+2/3
		Strange quark (s)	93 MeV	1/2	Triplet	–1/2	+1/6	-1/3
	3	Top quark (t)	172.76 GeV	1/2	Triplet	+1/2	+1/6	+2/3
		Bottom quark (b)	4.18 GeV	1/2	Triplet	–1/2	+1/6	-1/3
Bosons		Photon (γ)	0	1	–	0	0	0
		Gluon (g)	0	1	Octet	0	0	0
		$W^\pm$ boson	80.38 GeV	1	–	± 1	0	± 1
		Z boson	91.19 GeV	1	–	0	0	0
		Higgs boson (H)	125.10 GeV	0	–	-1/2	+1/2	0

Table 1.1: Properties of all Standard Model particles. Particle masses are extracted from Ref. [1]. The hypercharge (Y) and weak isospin (T_3) listed here are for the left handed $SU(2)$ doublet quarks and leptons. Their right handed counterparts are $SU(2)$ singlets with $T_3 = 0$ and $Y = Q$.

boson, known as the Higgs boson. The Higgs field, originally being a $SU(2)$ doublet, allows mixing the left and right chiral quarks via Yukawa couplings. The VEV converts these mixing terms into mass terms for the fermions.

The important properties of the SM particles are summarized in Table 1.1.

1.2 Limitations of the Standard Model

While the Standard Model remains the uncontested theory of fundamental particles and their interactions, it is far from being a complete theory of nature. In attempts to explain the existing limitations of the SM, a wide range of extensions of the SM have been explored by theorists. Search for signatures of such beyond the Standard Model (BSM) theories constitutes a major effort in today's high energy collider experiments. The following subsections briefly summarize some of the major limitations of the Standard Model as perceived by many contemporary physicists.

1.2.1 Gravity

The SM has survived extreme experimental scrutiny in modern physics for up to TeV energy scales. The effects of gravity can be safely ignored for these energies. The energy scale at which the gravitational effects become equally as important as the electroweak or strong forces is called the Planck scale, which is associated with energies of $\mathcal{O}\left(10^{19}\right)$ GeV [8]. Incorporating gravity into the SM is a major challenge for the physics of the future. While contesting theories of quantum gravity have been formulated and are being perfected by theorists [9, 10], absence of clear experimental evidence and humanly verifiable predictions makes it difficult to establish their concrete connections with the Standard Model.

1.2.2 Matter-Antimatter Asymmetry

Our observable universe is predominantly composed of matter and observably devoid of antimatter. There is no adequate explanation of this asymmetry between matter and antimatter within the SM. The direct source of such asymmetry within the SM comes from CP[2] violating complex phase in the quark mixing matrix of weak interactions. However, the electroweak CP violating phase does not account for the observed magnitude of matter-antimatter asymmetry in our universe [11,12]. A number of theories beyond the scope of the SM have been put forward to explain the physics of this asymmetry [13,14] but no conclusive experimental signature of such theories have been observed.

1.2.3 Dark Energy and Dark Matter

A large fraction of the universe's energy content, approximately 95%, is potentially accounted for by dark energy and dark matter [15]. The SM does not account for dark matter or dark energy, neither does it explain how these exotic forms of matter interact with the ordinary fermionic matter of the visible universe. Search for direct and indirect signatures of potential dark matter candidates inspired by BSM theories has resulted in no

[2]Charge-Parity Symmetry – identified as the invariance of physical interactions when a particle is replaced by its anti-particle with opposite chirality

significant excess over the predictions from the SM, resulting in constraints on the dark matter models [16, 17].

1.2.4 The Strong CP Problem

While the strong force appears to conserve the CP symmetry, there is no obvious explanation of such conservation within the SM. Absence of CP violation in strong interactions remains an unresolved aspect of the Standard Model [18]. It has been suggested that additional symmetries might be responsible for CP conservation in strong interactions. Such additional symmetries often require the existence of additional particles like axions [19]. Search for axions is a major effort at current collider experiments as well as dedicated experiments.

1.2.5 Neutrino Masses

Neutrinos are massless particles in the SM, which makes it impossible to obtain neutrino flavor mixing within the framework of the SM. However, modern neutrino experiments have discovered neutrino mixing and obtained strong limits on neutrino mass splitting parameters [1,20,21]. Although neutrinos are much lighter compared to the other SM particles, having massive neutrinos requires important modification to the theoretical structure of the SM that can influence its symmetry structure and renormalizability [3]. Also, the prospect of CP violation in the mixing of lepton families can add additional clues in understanding matter-antimatter asymmetry of the universe [22, 23].

While we have addressed some of the most commonly addressed limitations of the SM, the aforementioned subsections is far from being comprehensive. There is no theoretically motivated reason of having three generation of matter particles, neither is there any explanation of the trans-generational mass hierarchy. In the following section, we will elaborate on the naturalness problem of the Higgs boson's mass, which has been the primary

[3] Renormalization is the process of controlling theoretical divergences that allows observable quantities to have definite and finite magnitude

motivation for the work summarized in this dissertation.

1.3 The Naturalness of the Higgs Mass

The Higgs boson was discovered by the ATLAS and CMS collaborations at the Large Hadron Collider (LHC) in 2012 [24–26]. The mass of the Higgs boson has been found to be 125.1 ± 0.14 GeV [1], in the same energy scale of $\mathcal{O}(10^2)$ GeV as that of the electroweak physics. The physical mass of the Higgs boson (m_H), as observed and measured by the LHC experiments, is a combination of the bare mass term ($m_{H,b}$) from the SM Lagrangian and additional contribution from quantum fluctuations–

$$m_H^2 = m_{H,b}^2 + \delta m_H^2 \tag{1.1}$$

where the corrective term δm_H^2 receives it primary contribution from one-loop diagrams involving top quark (Figure 1.1). The corrective contribution from the top quark loop diverges quadratically,

$$\delta m_H^2 \sim \int_0^{\Lambda_c} \frac{d^4p}{p^2} \propto \Lambda_c^2 \tag{1.2}$$

where Λ_c represents the cut-off scale for SM physics. A typical choice for Λ_c is the Planck scale, that renders $\delta m_H^2 \sim (10^{19}\text{GeV})^2$. With the quantum corrections for the Higgs mass being larger than its physical mass, the bare Higgs mass, a free parameter of the SM, needs to be so finely tuned that these large corrections are precisely compensated to yield the physically observed mass of the Higgs boson.

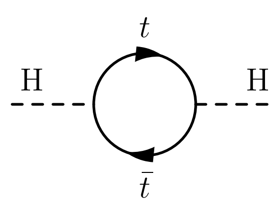

Figure 1.1: First order loop diagram for the Higgs propagator involving top quark loop.

This unnatural requirement of fine-tuning the bare Higgs mass in the SM has been commonly dubbed as the *naturalness problem*. Naturalness arguments have been a primary driving force not only towards discovery but also in better understanding the connections between the mathematical theories and the physical world [27, 28]. The requirement of fine tuning for SM physics strongly suggests that avoiding this problem would require intervention from new physics at a much lower cut-off scale. Placing an upper limit on fine tuning scale at $\mathcal{O}(1-10)$, the cut-off scale for new physics is set in the TeV scale [29, 30], right up the alley of LHC physics.

The naturalness problem of the Higgs boson's mass has inspired a number of BSM theories. Most notable among such theories is supersymmetry (SUSY) [31, 32]. SUSY extensions of the Standard Model offer landscapes to solve a number of problems within the SM, including promising dark matter candidates and additional corrections to Higgs mass from loops involving bosonic superpartners of the top quark that cancel out the corrections from top quark loop and constrains the need for fine tuning. Another class of BSM theories predict the Higgs boson as a pseudo Nambu-Goldstone boson (pNGB) that emerges from spontaneous breaking of a larger, more fundamental symmetry group. The essential Standard Model physics is captured by the unbroken subgroup of the larger symmetry group. Additional bosonic and fermionic states emerge in the process, and interaction among these particles and the pNGB Higgs boson can regularize the divergences. Ref. [33] has a detailed review of the state of the art theory models, usually identified as composite Higgs model, that explain the pNGB kinematics of the Higgs boson.

1.4 Vector-like Quarks (VLQs) to Solve the Naturalness Problem

Vector-like Quarks (VLQs) appear in a number of BSM theories including the composite Higgs models [34–43]. VLQs are $SU(3)$ color-triplets with the same strong coupling as the Standard Model quarks but maintain identical electroweak representation for both chiralities. VLQs can have their own gauge-invariant mass terms in the Lagrangian without relying on the Higgs mechanism. The spectrum of the VLQ species consists of four particles, denoted as $X_{+\frac{5}{3}}, T_{+\frac{2}{3}}, B_{-\frac{1}{3}}$ and $Y_{-\frac{4}{3}}$ where the subscript indicates the electric charge of the corresponding particle in units of the charge of an electron. They can exist as (T) or (B) singlets, (X, T), (T, B), or (B, Y) doublets and (X, T, B) or (T, B, Y) triplets under the electroweak $SU(2)$ group representation. In most representations, they couple to the Standard Model quarks via exchange of charged (W^{+}, W^{-}) or neutral (Z, H) bosons.

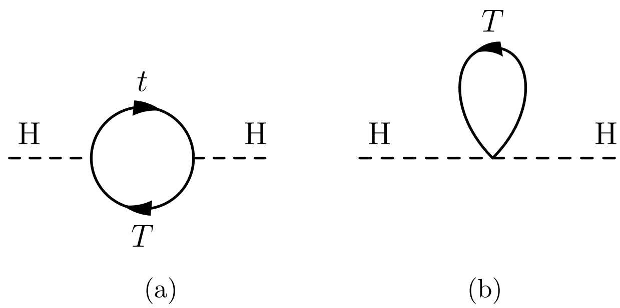

Figure 1.2: First order loop diagrams for the Higgs propagator involving VLQs

Interaction between the Higgs boson and VLQs contribute additional diagrams to the calculation of physical Higgs mass (Figure 1.2). Corrections from these diagrams can reverse the effect of the SM top quark loop and hence provide a concrete solution to the naturalness problem of the Higgs boson mass. Setting upper limits on the fine tuning sets scale for VLQ masses near the TeV range, slightly above the electroweak energy scale. Additionally, precision measurement of Higgs production cross-section at the LHC sets strong constraints on the possibility of extending the SM via a fourth chirally asymmetric generation [44, 45]. Therefore, VLQs are excellent search candidates for physics beyond the SM in the post-Higgs era at the LHC.

1.5 Phenomenology and Search of VLQs at the LHC

A standard experimental search for VLQs benefits from a relatively *model-independent* parameterization of these particles. Such a representation utilizes a collection of arbitrary parameters- the VLQ masses (M_Q) and their couplings $\vec{c} = \{c^{Qq}_{L/R,V/H}\}$ to the Standard Model quarks via exchange of the gauge bosons, $V \in \{W^{\pm}, Z\}$ and the Higgs boson, H. These couplings are dimensionless parameters and each coupling $c^{Qq}_{L/R,V/H}$ represents the interaction vertex of a left or right chiral (L/R) VLQ of type Q with an SM quark q while exchanging a gauge boson (V) or a Higgs boson (H). An experimental search evaluates the statistically excluded cross-section, $\sigma_{\text{lim}}(M_Q, \vec{c})$, for a grid of points of the parametric hyperspace. These limits can be interpreted in the context of a certain theoretical model as long as the model does not dramatically deviate from the assumptions of the model-independent representation. This approach has been dubbed the "Bridge Model" by Matsedonsky et. al [46]. In the same paper, the authors describe the following simplified Lagrangian for VLQs in terms of these generalized couplings,

$$\mathcal{L} = \sum_{\zeta,q,Q} \left[\frac{g_w}{2} \sum_V c^{Qq}_{\zeta,V} \bar{Q}_\zeta \not{V} q_\zeta + c^{Qq}_{\zeta,H} H \bar{Q}_{\zeta'} q_\zeta \right] + \text{h.c.} \tag{1.3}$$

where Q represents the usual VLQs $\{X_{+\frac{5}{3}}, T_{+\frac{2}{3}}, B_{-\frac{1}{3}}, Y_{-\frac{4}{3}}\}$, ζ and ζ' represent alternate chiralities and q represents a SM quark of up or down type. Some of these couplings may be constrained by the conservation of certain quantum numbers. For example, the $+\frac{5}{3}$ charged partner X can only couple with SM up-type quarks by the exchange of a W boson. The parametric hyperspace of this model-independent representation can be mapped to those of similar formulations in [47–51] by a one-to-one correspondence among the tree-level couplings. Owing to the mass hierarchy of the SM generations, VLQs are often expected to couple predominantly with the third generation of SM quarks. Hence, the $+\frac{2}{3}$ positively charged T and $-\frac{1}{3}$ negatively charged B are recognized as Top and Bottom Partners respectively.

For the benchmark representations like a singlet T or a (X, T) doublet, the branching ratios of top partners in the three decay channels become asymptotically independent of the mass of T. As can be seen in Figure 1.3, the branching ratio of a singlet T can be well approximated as $\text{BR}(T \to Wb) \approx 2 \times \text{BR}(T \to Zt) \approx 2 \times \text{BR}(T \to Ht) = 0.5$ for $M_T > 600$ GeV. On the other hand, the branching ratio for $T \to Wb$ is almost identically zero for a T in (X, T) doublet while the other two branching ratios tend to become equal as the VLQ mass gets larger. Hence, BR($T \to Zt$) $\approx$ BR($T \to Ht$) $= 0.5$ is a good approximation for doublet representations at higher masses for T. [4]

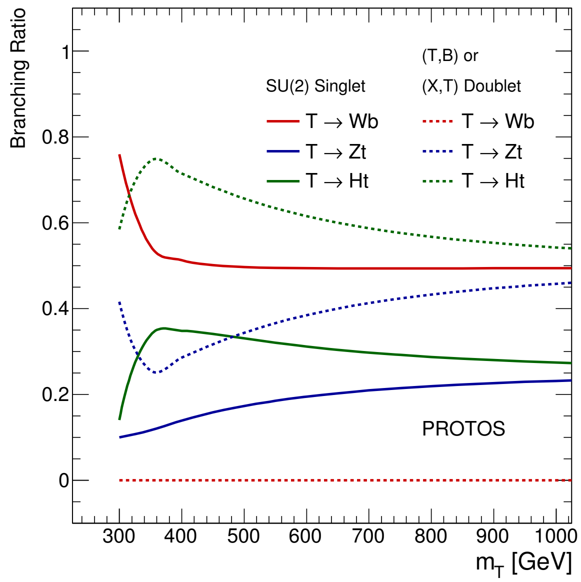

Figure 1.3: Branching ratio of Top Partners as a function of mass for singlet T and doublet (X, T) representations. This figure has been taken from Ref. [52]

The search efforts for VLQs in collider experiments such as ATLAS and CMS can be broadly categorized into two classes: (a) searches for VLQ pairs and (b) searches for singly produced VLQs. In general, each analysis targets a generic final state that is dominantly sensitive to one, or occasionally more than one, decay modes of the VLQs. Searches for pair production of VLQs have been traditionally more popular compared to searches for singly produced VLQs. This is primarily because, in many theoretical models, pair production of VLQs is dominated by a model-independent, strong-force-mediated process (Figure 1.4a). The standard QCD representation of VLQs is identical to that of the SM quarks– VLQs also form $SU(3)$ color triplets under the same gauge group as the one for the SM quarks. The strong coupling at the $gQ\bar{Q}$ vertex is the same as the one for SM quarks, hence the production cross-section of pair produced VLQs is only a function of the VLQ mass (Figure 1.5). This,

[4]Constant VLQ branching ratios is a very good approximation for small values of the $c^{Qq}_{\zeta,V}$ couplings. At relatively larger values of the couplings branching ratios can depend on the choice of couplings.

along with the fact that VLQ BRs are almost fixed for heavy VLQs, generated a lot of interest in search for pair production of VLQs. It should be noted that alternate production modes of pair produced VLQs, e.g. via heavy gluons [53, 54], and interpretation of VLQ search results in context of such models [55] have also been explored, although such explorations remain beyond the context of this dissertation. Using the data collected at 8 TeV center of mass energy during Run 1 at the LHC between 2009 and 2013, a number of analyses concentrated on pair production of VLQs [52, 56–60]. Although no significant excess was seen in data, each analysis independently set exclusion limits on a VLQ mass in the range of approximately 600–1000 GeV that has served as the benchmark for the complementary Run 2 searches. Similar limits were obtained from the searches that focused on single production of VLQs in Run 1 [52, 61].

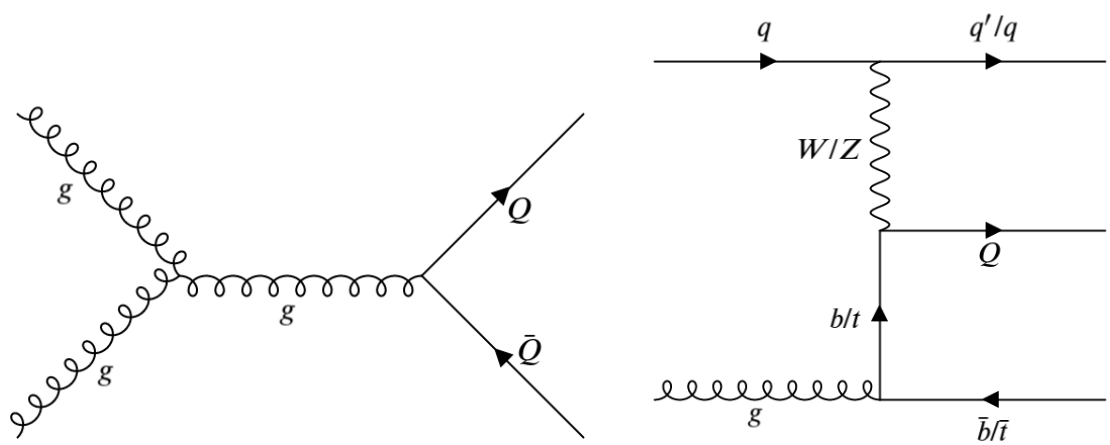

(a) (b)

Figure 1.4: Dominant contributing diagrams for (a) pair production and (b) single production of VLQs

At a center of mass energy of 13 TeV in Run 2, the ATLAS collaboration has not only performed a number of searches looking for the pair production of VLQs [62–66] but also combined the results of these analyses to set the strongest current limits on the VLQ masses [67]. Complementary pair production analyses from CMS [68–70] have also set limits in the range of $\mathcal{O}$(1 TeV) for up- and down-type VLQs.

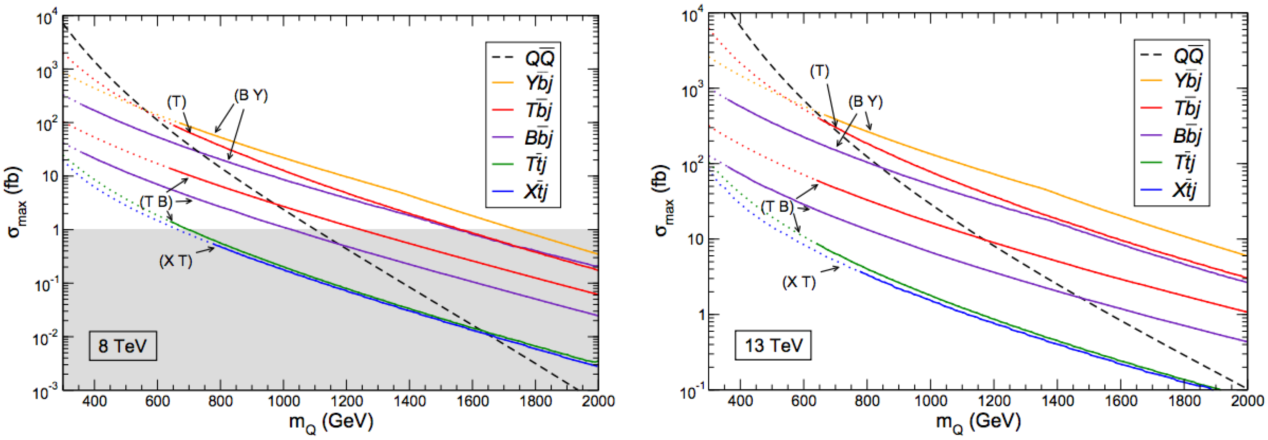

(a) (b)

Figure 1.5: Cross-section of VLQ pair and single production processes from pp collisions as a function of VLQ mass for a (a) $\sqrt{s} = 8$ TeV and (a) $\sqrt{s} = 13$ TeV [51].

During Run 2, there has been a significant increase in the number of searches of singly produced VLQs [71–77]. This is partly because, depending on how strongly VLQs couple with SM bosons and quarks, single production processes can have a larger cross-section at the range of masses that Run 2 searches have been focusing on (Figure 1.5). However, unlike pair production, the production of single VLQs is dominated by electroweak processes (Figure 1.4b) and they decay via exchange of electroweak gauge bosons and the Higgs boson. Hence, production and decay of single VLQs depend on the electroweak representation of these heavy fermions.

1.6 Outline of the Thesis

In Chapter 2 we review the basic construction of the LHC and the ATLAS detector. Chapter 3 elaborates a search for singly produced Top Partners in trilepton final states performed using the partial Run 2 dataset from 2015–2016. Chapters 4 and 5 dive into greater details of modeling the physics signatures of VLQs. Chapter 4 explains how the results from a generic single VLQ search can be interpreted in a model-independent way to make them useful in the context of a wide range of VLQ theories. In Chapter 5 we elaborate issues related with better understanding of VLQ physics– what is the impact of interference between VLQ and SM physics and how the different production topologies contribute to the process of single production of VLQs. In the same chapter we propose a new algorithm that allows computationally efficient Monte Carlo simulation of VLQ physics. Chapter 6 extends the analysis presented in Chapter 3 for the entire Run 2 dataset. The final chapter summarizes the prospect of the work presented in this dissertation in the context of the present and the future of high energy collider physics.

Chapter 2

The LHC and the ATLAS Detector

The discovery of the Higgs boson or search for new particles like VLQs require replicating high energy environments such as those that existed shortly after the big bang. In order to produce and observe particle interactions at such high energies, scientists have designed the largest machine on Earth, the Large Hadron Collider (LHC) and multiple multi-purpose particle detectors.

2.1 The Large Hadron Collider (LHC)

The LHC [78] is designed to create high energy particle collisions at the TeV energy scale. This 27 km long circular particle accelerator, placed about 100 m underground at the border of France and Switzerland, is operated by the European Organization for Nuclear Research (CERN). The LHC is designed to perform proton-proton, proton-ion, and ion-ion collisions. These collisions take place a four different locations along the LHC ring. Each of these locations houses a major particle detectors. The ATLAS [79] and CMS [80] are general purpose detectors that probe a wide range of physical processes. On the other hand, ALICE [81] and LHCb [82] are specialized detectors designed to investigate heavy ion physics and B-hadron physics, respectively. The work presented in this dissertation is done by analyzing proton-proton collision data obtained by the ATLAS detector between 2015 and 2018.

The LHC is designed to operate at a maximum center-of-mass (c.o.m.) energy of $\sqrt{s} = 14$ TeV for proton-proton (pp) collisions. Two opposing bunches of accelerated protons, focused within a radial spread of a few micrometers collide at the designated interaction point of the desired detector. The LHC officially started its physics program in 2009 and first TeV-scale collisions were observed in November that year. In 2010 and 2011, *pp* collisions operated at $\sqrt{s} = 7$ TeV. Later in 2012, the c.o.m energy was elevated to 8 TeV which continued until the early months of 2013 before LHC operations were stopped for planned upgrades to reach higher energy. The entire physics program of the LHC between 2009 and 2013 is called Run 1.

LHC resumed *pp* collisions at a higher c.o.m energy of 13 TeV in 2015. It continued data taking till the end of 2018 before going into another planned shutdown in order to commission a number of upgrade projects for the accelerator and the detectors. LHC's physics program between 2015 and 2018 is known as Run 2.

2.1.1 Accelerating the Protons

The LHC proton beams are obtained from ionized hydrogen atoms. They pass through a series of accelerator systems that incrementally increase the energy of the protons. The LHC accelerator system along with relative positions of the major detectors are shown in Figure 2.1.

The first accelerator in this sequence is a linear accelerator called LINAC-2[1] [83]. Small quadruple magnets are used to ensure beam alignment and cylindrical conductors charged by Radio-Frequency (RF) cavities accelerate the protons to 50 MeV. These protons enter the Proton Synchotron Booster (PSB) [84], made of four superimposed synchotron rings, where protons receive energies up to 1.4 GeV.

The next two stops for the proton beams are Proton Synchotron (PS) [84] and Super Proton Synchotron (SPS) where the beam energies reach 25 GeV and 450 GeV respectively. The PS houses 277 room temperature electromagnets, including 100 dipoles to bend the beams. The SPS, formerly the highest energy accelerator [85], contributed to the discovery of the W and Z bosons from proton-antiproton collisions in 1983 [86]. Equipped with 1317

[1]The LINAC-2 accelerator has been permanently switched off in 2018 after *pp* data taking was completed for Run 2. For future operations, it has been replaced by a newer linear accelerator LINAC-4

room-temperature electromagnets including 744 beam bending dipoles, SPS is now the last stop for proton beams before entering the LHC ring.

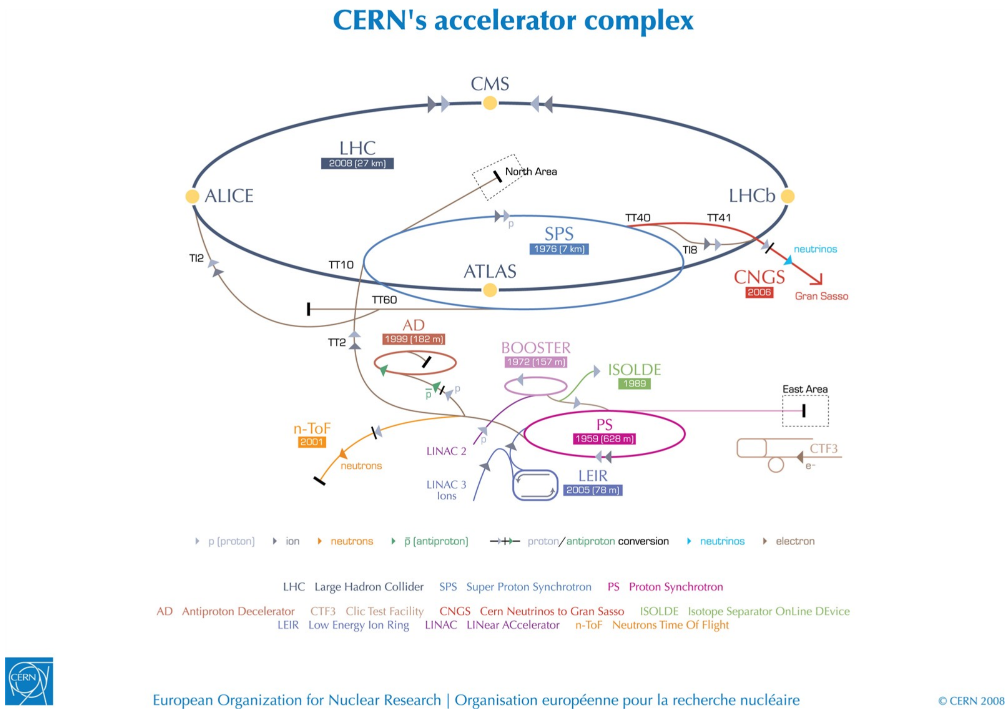

Figure 2.1: The chain of accelerators for LHC and location of major experiments on the LHC ring. This diagram has been taken from Ref. [87].

The LHC ring houses 16 superconducting RF cavities that can accelerate the protons up to 7 TeV per beam, giving a c.o.m. energy of 14 TeV. In Run 2, however, the operational c.o.m. energy was 13 TeV. The proton beams have to pass through these cavities more than 10 million times before they can reach the desired energy. A total of 1232 superconducting dipole magnets ensure that the beams maintain their circular trajectory. Additional quadruple magnets are placed near the insertion points of each major detector to tightly focus the beams to a few micrometers in order to maximize the probability of collisions.

2.1.2 Luminosity

The proton beams are organized in 2808 discrete bunches. Along the circumference of the LHC ring, these bunches are spaced 25 ns apart. Each bunch consists of approximately 1.15×10^{11} protons. Before the bunches approach the interaction point, the quadruple magnets reduce the lateral spread of the beams to a few microns.

The number of collisions that take place when the opposing bunches cross each other per unit area and unit time is called *instantaneous luminosity*, calculated as [88]

$$\mathcal{L} = \frac{N_b^2 n_b f_{\text{rev}}}{4\pi\sigma_x\sigma_y} F \tag{2.1}$$

where N_b is the number of protons per bunch, n_b is the number of bunches, f_{rev} is the bunch revolution frequency, $\sigma_{x/y}$ is the physical spread of the beam in x/y direction, and F is a geometric reduction factor associate with the non-zero crossing angle of the beams.

The design instantaneous luminosity for the LHC is $1 \times 10^{34}\text{cm}^{-2}\text{s}^{-1}$. However, in Run 2 the peak luminosity observed in 2018 surpassed the design limit by a factor of 2. Over the course of a ”Fill” that can last up to almost 48 hours, as more and more protons are used up from the proton bunches, the instantaneous luminosity decreases following the pattern of an exponential fall. Integrating instantaneous luminosity over the period of detector operation gives the integrated luminosity

$$L = \int \mathcal{L} dt \tag{2.2}$$

Integrated luminosity has a unit of inverse area and is typically expressed in terms of inverse barns[2] or its prefixed multiples. The LHC provided an integrated luminosity of 5.46 fb^{-1}at 7 TeV c.o.m energy and 22.8 fb^{-1}at 8 TeV in Run 1 out of which ATLAS used 4.9 $\text{fb}^{-1}$and 20 fb^{-1}, respectively, for physics analyses. As shown in Figure 2.2, the physics analyses of ATLAS are using an integrated luminosity of 139 fb^{-1}out of the 156 fb^{-1}delivered by the LHC during Run 2 [89].

Multiple *pp* collisions take place during each bunch crossing, and the detector receives signals from simultaneous collision products. The number of *pp* interactions during a single

[2] 1 barn (b) = 10^{-24}cm^2

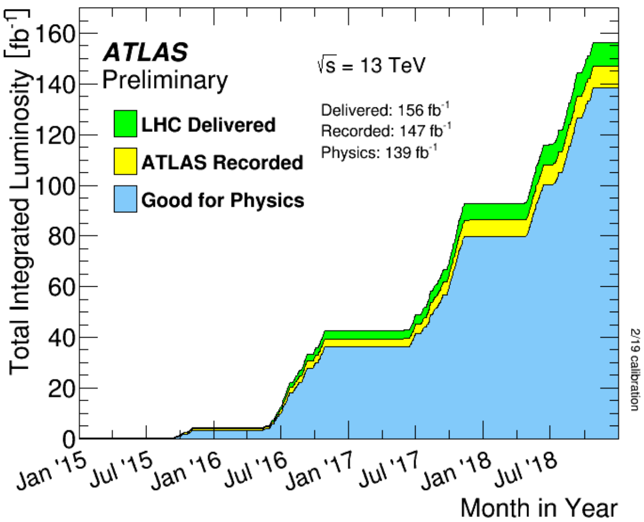

Figure 2.2: Integrated luminosity delivered by LHC, recorded by ATLAS, and identified as usable for physics analyses as a function of different data taking periods during Run 2. This figure has been taken from Ref. [89].

bunch crossing is called *pile-up*. The pile-up distributions for the ATLAS detector at different data taking periods in Run 2 are shown in Figure 2.3.

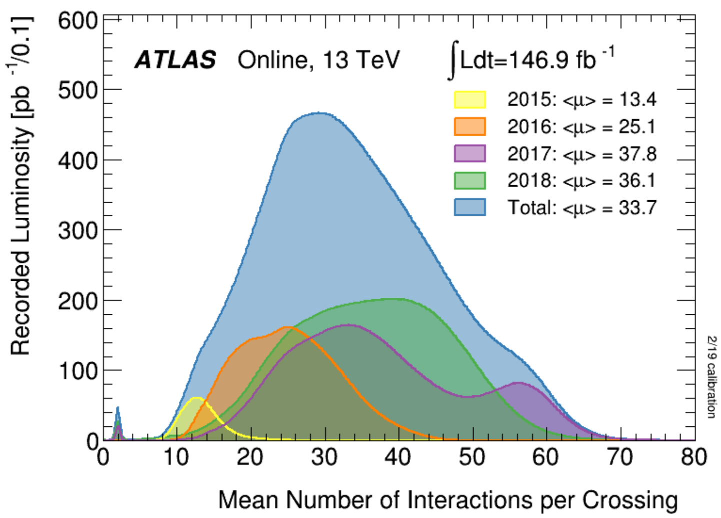

Figure 2.3: Luminosity-weighted distribution of the mean number of pp interactions per bunch crossing for different data-taking periods of Run-2 data

2.2 The ATLAS Detector

The ATLAS (A Toroidal LHC Apparatus) detector [79] is the largest volume general purpose particle detector ever built for a collider experiment. It is built as a stratified assembly of concentric cylindrical sub-detectors, each meticulously designed to serve a unique purpose in identifying the physical characteristics of a certain subset of the particles created in proton-proton collisions at the heart of the detector. Overall, the physical dimension of ATLAS spans a length of 46 m and a diameter of 25 m, weighing about 7000 tonnes and provides an almost 4π coverage in solid angles for detection of collision results.

A cylindrical coordinate system is a natural choice for identifying the geometry of the ATLAS detector. With a right handed coordinate system where the origin is set at the interaction point, the x axis is set towards the center of the LHC ring while the z axis is defined in accordance with setting the y axis upwards. The semi-cylinder in the positive (negative) z axis is identified as the **A (C)** side of the detector. The trajectory of each particle is identified with two angular coordinates. The azimuthal angle, ϕ, determines the angular separation between the positive x axis and the transverse projection of a particle trajectory. The longitudinal angle, however, is not directly measured by an angular coordinate. Rather, it is represented in terms of pseudorapidity (η), which is given as

$$\eta = -\ln\left(\tan\frac{\theta}{2}\right) \tag{2.3}$$

where θ is the longitudinal angle between the z axis and the particle's trajectory in the laboratory rest frame. $\eta = 0$ represents the transverse plane, while higher magnitudes in η represent regions progressively more along the beam axis. The η values in A and C sides are included with positive and negative signs respectively. The reason of choosing η instead of θ is because in ultra relativistic limits with $E \gg m$, pseudorapidity closely approximates the rapidity of a particle, defined as $y = \frac{1}{2}\ln\left(\frac{E+p_z}{E-p_z}\right)$. Rapidity difference is Lorentz invariant with respect to a boost in the z direction. Together ϕ and η creates a coordinate system that allows a Lorentz-invariant Euclidean metric for distances between particles, given as

$\Delta R = \sqrt{\Delta\phi^2 + \Delta\eta^2}$. As for the detector geometry, the region with $|\eta| < 2.5$ is often called the central region while the the forward region (closer to the beam pipe) is identified with $2.5 < |\eta| < 4.5$.

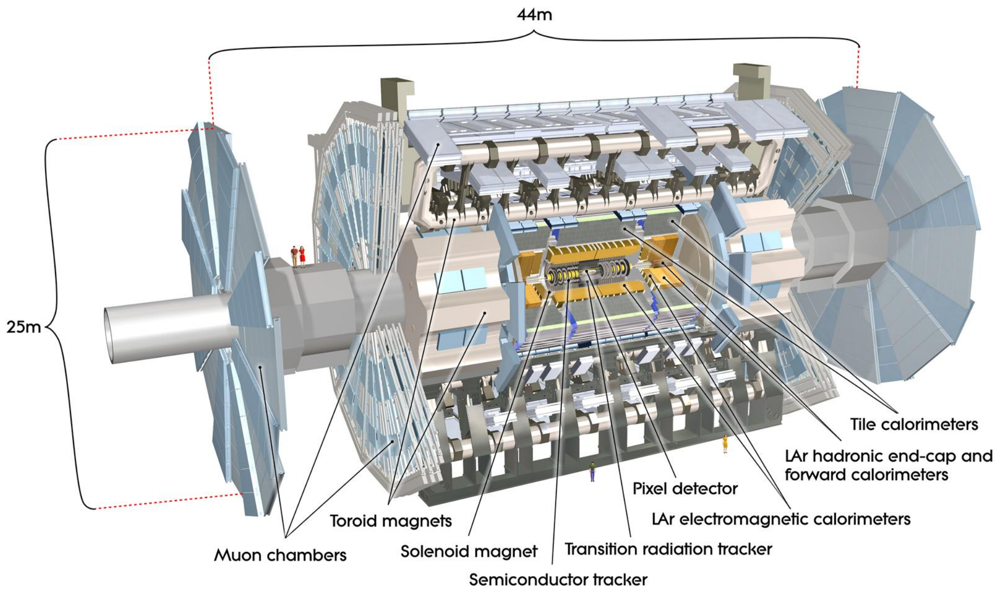

Figure 2.4: A cutaway view of the ATLAS detector with its major subsystems identified. This diagram is drawn to scale and has been taken from Ref. [79].

The major sub-detectors of ATLAS are (i) the Inner Detector, (ii) the Calorimeter System, and (iii) the Muon Spectrometer. The Inner Detector determines the track of charged particles and also calculates their transverse momenta. The calorimeter system is responsible for the energy measurement of electrons, photons, and hadroinc jets[3]. Finally, together with the measurements obtained from the Inner Detector, the Muon spectrometer calculated the trajectory and energy of muons. Neutrinos (and other potential invisible BSM physics signatures like long-lived dark matter candidates) do not interact with any part of the detector. However, crucial information about such particles can be obtained by calculating Missing Transverse Energy (MET).[4] Each sub-system has two components

[3]Quarks and gluons cannot stay as free particles. Soon after they are produced, they transform into hadrons. These hadrons create showers of energy in the calorimeter that are identified as jets

[4]MET is defined as the negative sum of transverse momenta of all particles originating from a single

distinguished by their geometric configuration and assembly. The *barrel* is a cylindrical construction that encompasses the interaction point and assembled in layers in a concentric fashion. On the other hand, *endcap* components are disc-shaped and placed side-by-side along the longitudinal axis on both sides of the detector.

The Inner Detector and the Muon Spectrometer utilize independent magnet systems. Respectively known as the solenoidal and toroidal magnets, they cause charged particles to bend and hence facilitate the determination of their charge and momenta. The major sub-systems of the ATLAS detector are illustrated in Figure 2.4. In addition to these sub-detectors and the magnet systems, the ATLAS detector is equipped with a large electronic computational network, the Trigger and Data Acquisition (TDAQ) system, that allows filtering, processing, and storage of proton-proton collision data.

2.2.1 The Inner Detector

The Inner Detector (ID) [90], as the name suggests, is the innermost part of the ATLAS detector. As the first subdetector that interacts with the shower of particles that emerge from *pp* collisions, this subdetector is responsible for identifying the tracks of these particles. Reconstruction of the tracks of charged particles allows identification of the collision vertex. Additionally, the ID determines the transverse momenta of the charged particles which, along with measurements from the calorimeters, reconstructs the energy-momentum four vector of these charged particles. The entire ID is placed inside a solenoidal magnetic field of 2 T. The underlying technology of the ID relies on tracking based on ionization in semiconductors and noble gases. The two innermost layers, the Pixel Detector and the Semiconductor Tracker, rely on semiconductor technology while the outermost layer, the Transition Radiation Tracker, utilizes tracking based on ionization in gas. Figure 2.5a shows the arrangement of ID subsystems and Figure 2.5b illustrates their radial coverage in the

collision, i.e. $E_{T,\text{miss}} = -\sum_i \vec{p}_{T,i}$ where the index i runs over all visible particles. By virtue of momentum conservation, MET represents the the vector sum of transverse momenta of all invisible particles in a single event. Since the initial energies of the interacting quarks and gluons in the longitudinal direction are unknown, momentum conservation can only be definitively applied in the transverse plane.

barrel region.

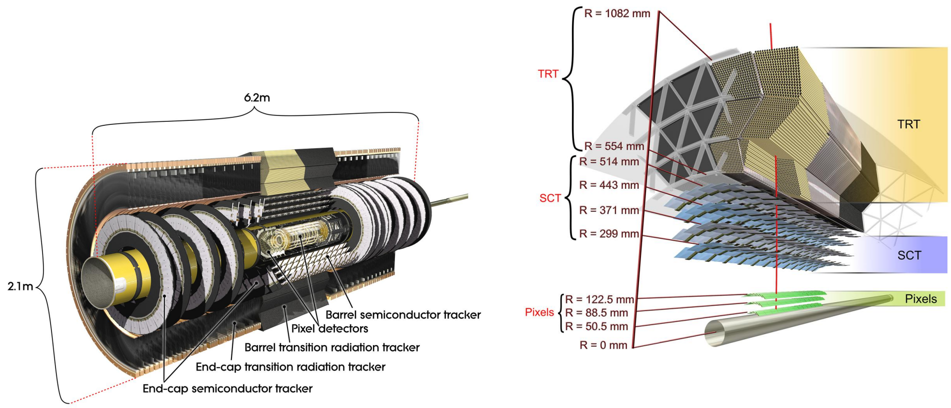

(a) (b)

Figure 2.5: (a) A cutaway view of ATLAS's Inner Detector with its major subsystems identified. This diagram is drawn to scale. (b) The radial coverage of these sub-systems in the barrel region. This diagram does not include the innermost layer of the Pixel detector, the Insertable B-Layer that is placed at a mean radius of 33.2 mm. These figures have been taken from Ref. [79]

2.2.1.1 The Pixel Detector

The innermost part of the inner detector is called the Pixel Detector [91]. It is made of four concentric cylindrical barrel layers with three endcap discs on each side of the barrel. It should be noted that the operational design during Run 1 had only the three outermost layers located at mean radii of 50.5, 88.5, and 122.5 mm. The three discs on each side at means longitudinal distances of 495, 580, and 650 mm respectively. The innermost layer, the Insertable B-layer (IBL) [92], was inserted before the start of Run 2. It sits at a mean radius of 33.2 mm. This additional layer has greatly improved the resolution of the pixel detector [93] and therefore, made it possible to identify jets originating from the shower of b quarks with higher accuracy [94].

The basic building block of the Pixel Detector is a module that comprises the necessary silicon sensors and additional circuitry to facilitate and control the electronic readout from these sensors. The entire pixel detector is made of periodic repetitions of these modules. A single module consists of about 46,000 pixels each spanning a physical dimension of $50 \times 250(400) \times 230(250)$ μm^3 in the IBL (other barrel/endcap layers). The IBL alone consists of 12 million readout channels, while the remaining barrel layers and endcap discs have 80 million pixels. The transverse and longitudinal spatial resolution of the IBL (the rest of the detector) are 8(10) μm and 40(115) μm respectively.

2.2.1.2 The Semi-conductor Tracker

The Semi-conductor Tracker (SCT) [95] operates in the same physical principle as the pixel detector. However, unlike the pixel detector that uses small 3D blocks of semiconductors, SCT uses a microstrip geometry, with each strip having a physical area of 80 μm$\times$12 cm embedded on 6×6 cm^2 silicon sensors with 300 μm thickness. Sitting right outside the pixel detector, it allows continued reconstruction of tracks based on particle interactions over a much larger volume than the Pixel Detector and with a much finer precision than what is offered by the Transition Radiation Tracker (TRT).

The SCT consists of four concentric barrel layers with nine endcap discs on each endcap region. The barrel layers are located at mean radii of 299, 371, 443, and 514 mm respectively. The endcap discs are placed between approximately 820 mm and 2700 mm from the interaction point along the beam line in both sides. Together they constitute 6.3 million readout channels that record particle hits with transverse and longitudinal resolutions of 17 μm and 580 μm respectively.

2.2.1.3 The Transition Radiation Tracker

Similar to Pixel and SCT, TRT [96, 97] is divided into barrel and endcap regions. In the barrel TRT is a transverse assembly of gas-filled straws, with each straw spanning the entire longitudinal physical dimension of the corresponding subsystem. As a result, they cannot provide any useful information on the longitudinal coordinate (radial coordinate in the endcaps as the straws are placed radially there) of the hits other than the side where these hits take place. Each straw is made of carbon-polyimide with an aluminium coating on the inner surface, has a diameter of 4 mm, and houses a 30 μm diameter gold-plated tungsten wire in the center that acts as an electrode. These straws are filled with 70% Xe, 27% CO_2, and 3% O_2. The 52544 straws in the barrel are 144 cm long, embedded in polypropylene radiator foils in which transition radiation is produced. The endcaps are composed of 160 planes of in total 122880 radially arranged straws of 37 cm length. The space between each pair of planes is filled with polypropylene radiator. As high energy charged particles pass through these TRT modules, they create a shower of photons (known as transition radiation) as they move into the gas straw from the radiator material. This transition radiation ionizes the gas inside the straws. The charged constituents of the ionized gas are collected by the electrodes and recorded as an electrical signal.

Besides recording the hits of particle trajectories, TRT is particularly useful in distinguishing heavier particles from lighter particles. The radiation intensity in the TRT tubes depends on $\gamma = \frac{E}{m}$. Hence, lighter particles like electrons will deposit a stronger signal compared to heavier particles like pions. The spatial resolution of TRT is about 130 μm. Although the TRT offers a lower resolution, it makes up by providing a large number of hits per track. A typical charged track leaves about 36 hits in the TRT.

2.2.2 The Calorimeters

The ATLAS calorimeters sit right outside the solenoid magnet and are responsible for energy measurement of electrons, photons, and jets. The inner part of the calorimeter system is the Electromagnetic (EM) calorimeter which measures the energy of particles that interact electromagnetically, i.e. electrons and photons. While charged hadronic jets also tend to deposit some energy in the EM calorimeter, they deposit most of their energy in the one that is dedicated for this very purpose- the Hadronic calorimeter. Both these calorimeters are sampling calorimeters, made of alternate layers of absorber and active material. The absorber is a high density material that, as the name suggests, absorbs a significant portion of the energy carried by the incoming particle. The active material collects the electrical signal generated by electrons and ions when ionizing radiation passes through them.

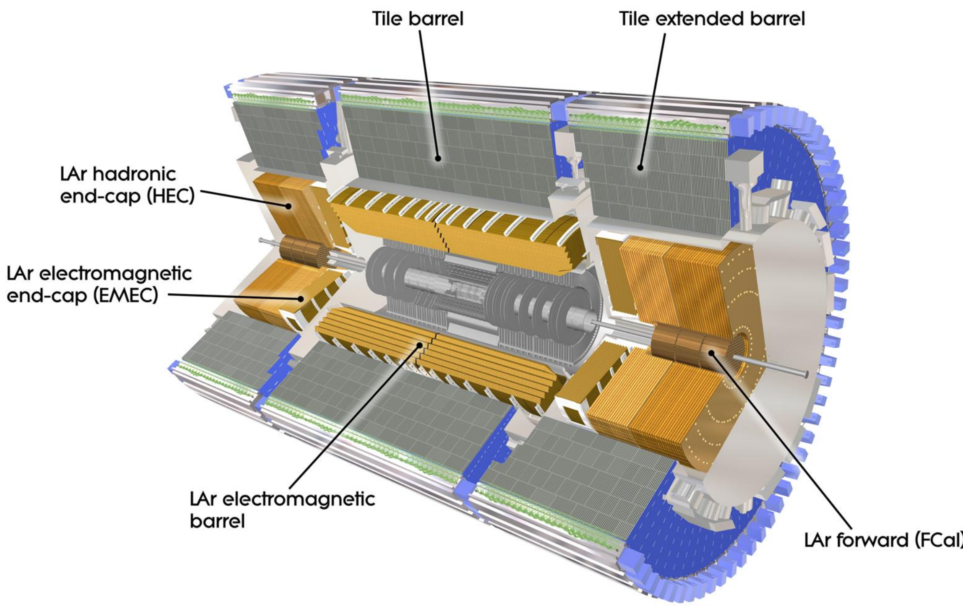

Figure 2.6: A cutaway view of the ATLAS's calorimeters with their major subsystems identified. This diagram is drawn to scale and has been taken from Ref. [79].

2.2.2.1 Electromagnetic Calorimeter

The active medium in ATLAS's EM calorimeter is Liquid Argon (LAr) and hence this calorimeter is also called the LAr calorimeter [98]. The LAr calorimeter is an accordion shaped cascade of alternating layers of LAr and Lead, the absorbing material, with high voltage copper electrodes submerged in LAr to collect the ionization signals. The accordion shape allows a continuous coverage in ϕ without any dead region. The barrel portion of the LAr calorimeter gives coverage in the region $|\eta| < 1.47$ while the endcap regions cover $1.4 < |\eta| < 3.2$.

The process of creating EM showers in the calorimeter is a combination of two primary effects- (i) e^+e^- pair production and (ii) Bremsstrahlung. In the strong electric field of the heavy nuclei, high energy incoming photons can create pairs of electrons and positrons. On the other hand, scattering of electrons and positrons by these nuclei reduce their energy and create bremsstrahlung photons in the process. The cascade of these effects create a shower of particles as a high energy electron or photon passes through the calorimeter and eventually stops only when the energy of individual photons becomes lower than a critical energy. These processes are primarily dominated by the properties of the material the electrons are passing through. Perhaps, the most important of the properties is the **Radiation Length** (X_0), defined as the length an electron needs to travel in a given material to lose $1-\frac{1}{e}$ fraction (i.e. about 62%) of its initial energy. For a material with atomic number Z and mass number A, X_0 varies according to $\frac{A}{Z^2}$. Another important parameter is the **Molière Radius**, the transverse radius of the electromagnetic shower initiated by a high energy photon or electron that contains 90% of the shower energy. A smaller value of the Molière Radius allows better resolution of the EM shower and also allows a compact design. Hence, choosing a material with high Z is typically desired for compact calorimeter designs.

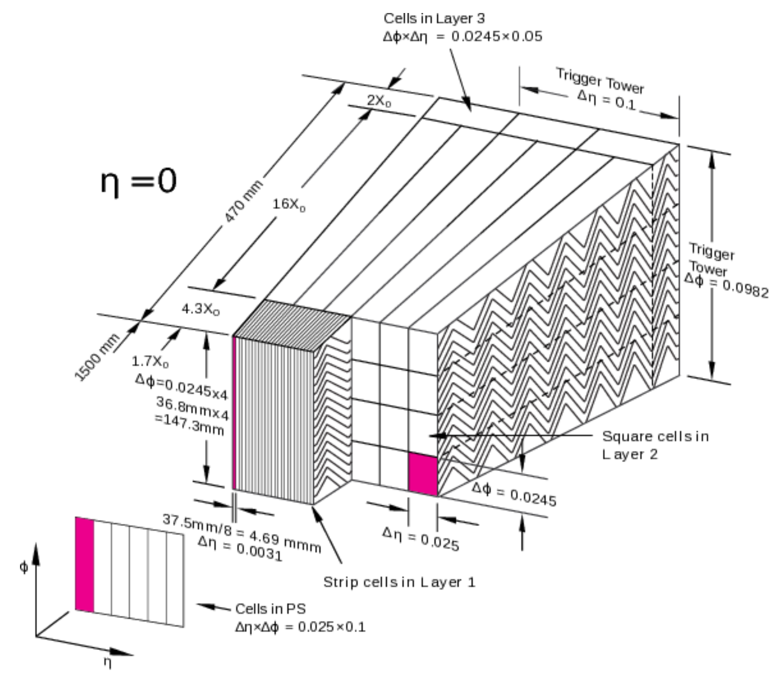

Figure 2.7: Granularity of readout channels at different layers of the LAr calorimeter. This figure has been taken from Ref. [98]

The physical dimensions of the calorimeter geometry varies according to granularity of readout channels in the three layers (Figure 2.7). The first layer provides a $4.3X_0$ coverage with readout channels separated with $\Delta\phi \times \Delta\eta = 0.1 \times 0.0031$. The fine segmentation in η enables distinguishing single photons from photon showers from neutral pion decay. The readout channels in the second layer are repeated with $\Delta\phi \times \Delta\eta = 0.025 \times 0.025$. This layer has a $16X_0$ coverage and most of the electromagnetic energy is deposited here. Finally, the third layer provides an additional coverage of $2X_0$ with a granularity of $\Delta\phi \times \Delta\eta = 0.025 \times 0.05$.

In addition to the three layers mentioned above, an additional thin layer of presampler readout channels are placed before the first layer in the region $|\eta| < 1.8$. These channels are responsible for estimating energy loss in the upstream material. These channels are made of a single active layer of LAr with $\Delta\phi \times \Delta\eta$ coverage of 0.1×0.025. Together with Hadronic Endcaps and Forward Calorimeter, which also use LAr as active medium and are usually considered as a part of the LAr calorimeter system in ATLAS, a total of almost 180,000 readout channels are operated.

2.2.2.2 Hadronic Calorimeter

Placed outside the EM calorimeter, the hadronic calorimeter measures energy of jets. The barrel portion of this calorimeter uses steel as absorber while the active medium is tiles of scintillating plastic, hence earning it the name Tile Calorimeter (TileCal) [99]. As shower of particles pass through these scintillating plastic tiles, they produce light which is collected by Photomultipliers (PMTs). On each side, the TileCal is divided into two sections- the Long Barrel (LB) covers the region $|\eta| < 0.8$ and the Extended Barrel (EB) covers the region $0.8 < |\eta| < 1.7$. The azimuthal coverage of TileCal is segmented into 64 modules. Each module is further segmented into three longitudinal layers (A, BC, D). Cells in the first two layers have a granularity of $\Delta\phi \times \Delta\eta = 0.1 \times 0.1$ while cells in the outermost layer has a $\Delta\eta$ span of 0.2. Each cell is redundantly readout by two PMTs and hence the approximately 5000 cells of TileCal are covered by 10000 readout channels.

The endcap section of the hadronic calorimeter, known as the Hadronic End-cap (HEC), consists of two independent wheels and covers the region $1.5 < |\eta| < 3.2$. It uses copper absorbers and LAr as active material.

2.2.2.3 Forward Calorimeter

The Forward Calorimeter (FCal) extends the coverage of EM and Hadronic calorimeters to even higher ranges in $|\eta|$, all the way to values as high as 4.9. In each side, the FCal consists of three longitudinally assembled layers. The layer closest to the interaction point is the EM layer. It uses copper absorbers. The other two layers are hadronic ones and they use tungsten absorbers. All FCal layers use LAr as active medium and together with HEC, FCal is generally considered a part of the LAr calorimeter system.

2.2.3 The Muon Spectrometer

Muon Spectrometer (MS) [100] is the farthest subsection from the interaction point of the ATLAS detector placed outside the hadronic calorimeter. Most muons do not leave a trail of energy in the calorimeters and travel tens of meters before reaching this subsystem where their tracks and energies can be measured. It is housed in a air-core toroidal magnetic field generated by eight coils in each section- the barrel and two endcaps.

The MS is designed to have an impressive resolution of $\frac{\delta p}{p} \sim 3\%$ at 100 GeV and around 10% at 1 TeV. This is achieved by assembling together multiple layers of densely packed Monitoring Drift Tubes (MDTs). These are cylindrical aluminum tubes with a diameter of 30 mm filled with a mixture of Ar and CO_2 gases. Each tube houses a tungsten-rhenium wire operated at 3000 V to collect the ionization signal created by a passing muon. As muons pass through these tubes, it leaves behind a trail of ionization signal in these tubes. Since the MDTs are stacked radially and oriented azimuthally, the MDT train reconstructs the track coordinates in the $r - z$ plane. In the barrel region, three layers of stacked MDTs are placed at mean radial distances of 5, 7.5, and 10 m. In the endcaps, four wheels of MDT chambers are respectively placed at 7.5, 10, 14, and 22 m along the beam line. However, in a small endcap region with $2.0 < |\eta| < 2.7$, MDTs are unsuitable at the very first layer because of high level activity, instead Cathode Strip Chambers (CSCs) are used.

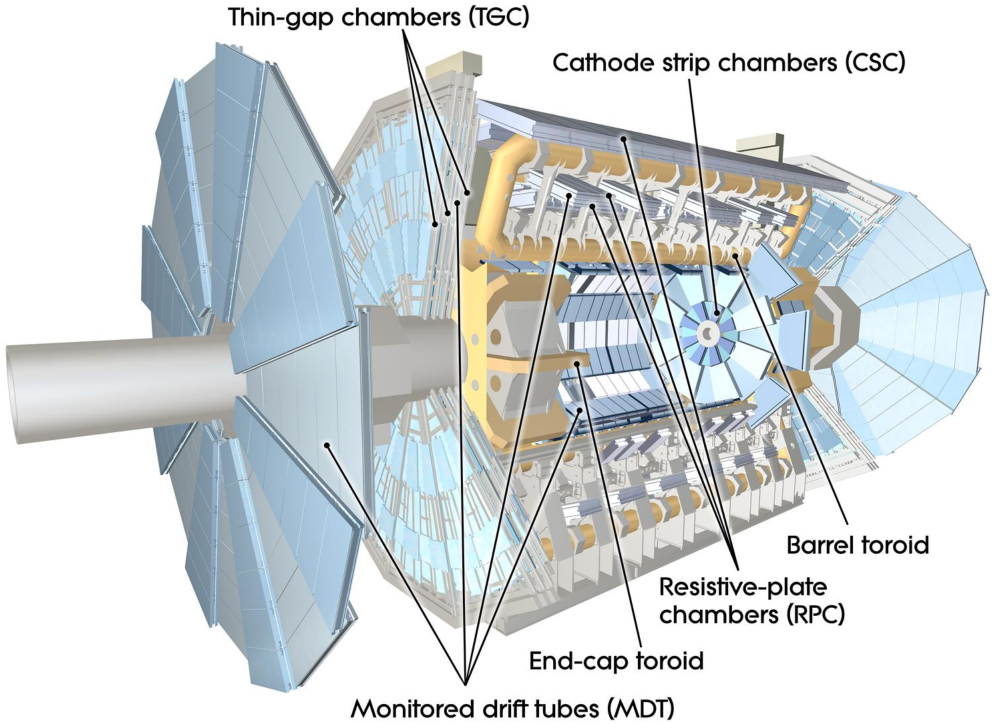

Figure 2.8: A cutaway view of the Muon Spectrometer with its major subsystems identified. This diagram is drawn to scale and has been taken from Ref. [79].

Measurements from the MDTs are accompanied by signals obtained by MS's trigger[5] hardware- the Resistive Plate Chambers (RPCs) in the barrel and Thin Gap Chambers (TGCs) in the endcap. Both of these detector systems use ionization in gaseous media to detect a passing muon. Besides providing trigger decisions, these detectors also measure the second coordinate of muon tracks in the $r - \phi$ plane.

2.2.4 Trigger and Data Acquisition (TDAQ)

In Run-2 ATLAS operated with a peak luminosity of $2 \times 10^{34}\text{cm}^{-2}\text{s}^{-1}$ with a bunch crossing rate of 40 MHz. More than a billion *pp* collisions take place every second and it is practically impossible and unnecessary to store the data from every collision. Events that contain interesting physics signature are kept. The entire process of filtering out uninteresting collision data and processing and storing the interesting ones are done by the TDAQ system.

[5]A trigger is an acceptance decision regarding a *pp* collision event.

A schematic representation of the TDAQ network is shown in Figure 2.9.

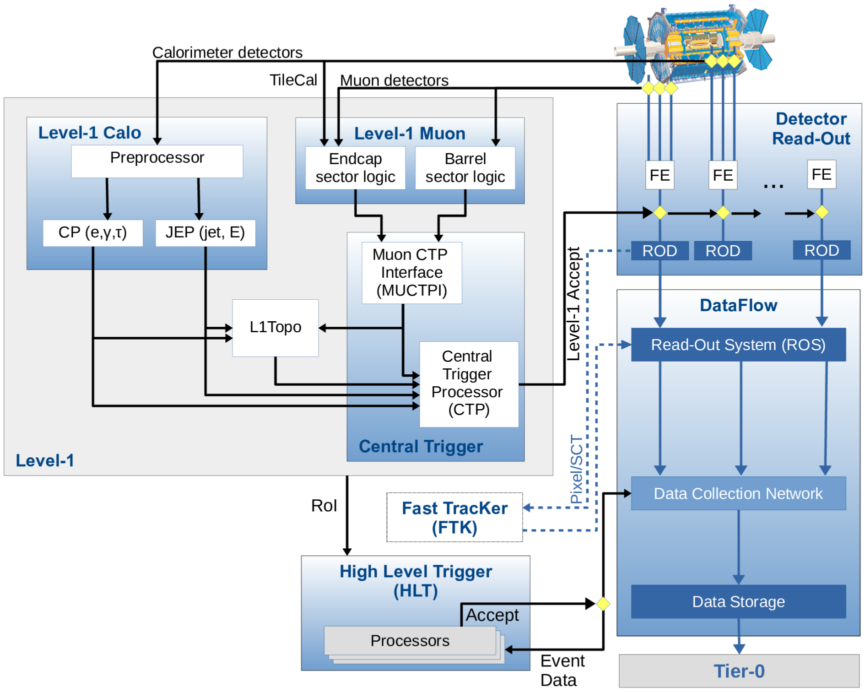

Figure 2.9: Schematic representation of the Trigger and Data Acquisition System of ATLAS. This figure has been taken from Ref. [101].

ATLAS performs the filtering of events in two stages. The first level of filtering, known as the **L1** triggers, is done at the hardware level. L1 signals are generated based on information collected from the calorimeters and the MS. L1 calorimeter (L1Calo) triggers come from coarse-grained sums of signals deposited in calorimeter cells sent to Cluster Processors (CPs) and Jet/Energy-sum Processors (JEPs). CPs identify plausible photon, electron, and tau candidates while JEPs are responsible for jets and MET. L1 muon (L1Muon) triggers come from RPCs and TPGs. L1Calo and L1Muon signals are sent to identify potential L1Topo triggers that look for interesting geometric or kinematic features like invariant mass of or angular separation between physics objects. The accepted events by L1 triggers are limited to maximum of rate of 100 kHz while these acceptance decisions are made every 2.5 μs. For each event that is accepted by the L1 trigger, regions of interests are identified in η and ϕ coordinates to be analyzed by the next stage of triggers.

Each event that generates at least one L1 acceptance is read out and processed by a chain of CPUs. The ReadOut System (ROS) holds that data in buffer and sends it for next level of filtering to the High Lever Trigger (HLT). HLT is software-based that utilizes a series of algorithms in increasing complexity to make decisions about the events that are fed to it. HLT reduces the event rate from 100 kHz to something close to 1 kHz. In Run 2, the average output rate of HLT was 1.2 kHz [101]. The content of a single event is $\mathcal{O}(1)$ MB, hence requiring the HLT-selected events to be written on permanent discs at a speed of around 1.2 GB/s

Chapter 3

A Search for Top Partners Using 36.1 fb^{-1}Data Collected by the ATLAS Detector in 2015-16

The Top Partner (T) can decay to SM quarks in association with the W, Z, or Higgs boson. Assuming the decays being limited to third generation quarks only, the branching ratios in these three channels add up to unity. This chapter[1] describes an analysis of the data collected by the ATLAS detector in 2015-16 in search of Top partners (T) that eventually decay to a Z boson and a top quark (t). This search looks for pp collision events where multiple reconstructed leptons (electrons or muons) are present in the final state. Selected events contain a high transverse momentum Z boson candidate reconstructed from a pair of oppositely charged same-flavor leptons. Additionally, a third lepton is required that emanates from the W boson from the $t \to Wb$ decay. While discarding the hadronic branching ratios for both W and Z bosons reduces the acceptance of signal, the trilepton selection also suppresses the background contribution from the Standard Model processes yielding a high degree of signal purity. In combination with an analysis that focused on hadronically decaying top quarks with a dilepton signature from the Z bososn decay, this analysis performs the search for a wide range of VLT masses and couplings, giving a generalized interpretation in context of most popular theory models for VLQs.

The search for any novel particle requires a comprehensive search strategy. In order to predict the kinematic distribution of pp collision events in the desired signature, we use Monte Carlo (MC) simulation of various physics processes. MC is also used to evaluate the contribution of Top Partner production events in the same kinematic phase space. These predictions are subject to a number of uncertainties. Statistical uncertainties arise from

[1]The work described in this chapter has been published in Ref. [71] as an official ATLAS publication

the finite size of the simulated MC sample. Detector performance and resolution as well as uncertainties associated with the theoretical model for these MC simulations, jointly known as systematic uncertainties, also play a role in correctly predicting the kinematic distribution of events. The predicted distribution with its associated distributions is statistically fitted against the data actually observed in the detector. The result of the statistical fitting allows us to determine the potential existence of Top Partners. The subsequent sections elaborate the different aspects of performing this analysis with greater details.

3.1 Signal and Background Modeling with Monte Carlo (MC)

The SM processes with a topology and kinematic signature similar to that of the *signal* process collectively constitute what we call *background* events. The background contribution is estimated from dedicated MC samples generated using established MC generator softwares. These MC samples are categorized according to the type of SM processes they represent, and for each type of process they are further split into subsets based on the combination of particles in final states and/or some selection applied on a kinematic variable. From the set of MC samples that are centrally generated and recommended for background modeling by the ATLAS collaboration, only the subset of samples that have a reasonable contribution in the phase space that best describes our signal are chosen for the analysis. The main backgrounds in this analysis are diboson ($VV = WZ, ZZ, WW$) processes and top quark pair production in association with vector bosons ($t\bar{t} + V$). Although the primary contribution in the $t\bar{t} + V$ category comes from $t\bar{t} + Z$ events, minor contributions from $t\bar{t} + W$, $t\bar{t} + WW$ and SM four top ($t\bar{t}t\bar{t}$) processes are included in this category and hence, the denomination $t\bar{t} + X$ is used to collectively represent them. The event selection also receives with small background contributions from production of Z bosons with associated jets (Z+jets), top quark pair production ($t\bar{t}$), single-top, and triboson (VVV) processes. In addition to the SM processes, dedicated MC samples are generated to simulate the potential signal signatures for a wide range of masses and couplings of the Top Partner.

3.1.1 Background Processes

- **Diboson** The contribution from diboson processes is evaluated using samples generated by SHERPA 2.2.1 [102–105]. The parton distribution functions (PDF)[2] are evaluated using the NNPDF3.0 [106] PDF set at next to next to leading order (NNLO). The VV samples are subdivided into samples according to the final state combinatorics of the number of leptons and neutrinos coming from the decay of W or Z bosons. Samples are normalized to the NLO cross-section calculation obtained with SHERPA. All samples with at least one lepton in the final state are considered in the analysis.

- **SM $t\bar{t}$ with associated vector bosons** $(t\bar{t}+V)$ The samples for the production of a top anti-top quark pair in association with vector bosons are generated by MADGRAPH5_aMC@NLO [107] (for $t\bar{t}+W$ and $t\bar{t}+Z$ process) and MADGRAPH [108, 109] (for $t\bar{t}+WW$ processes) interfaced with PYTHIA 8 [110] for hadronization using the NNPDF2.3 PDF set at LO [111] and the A14 [112] tune [3]. Processes such as $t\bar{t}+W$, $t\bar{t}+WW$ and $t\bar{t}+Z$ with Z decaying to $\nu\bar{\nu}$, $q\bar{q}$ and $\ell\ell$, where $\ell = (e,\mu,\tau)$, are considered. These samples are normalized with the NLO cross-section calculated by MADGRAPH5_aMC@NLO.

  As a generator uncertainty extra samples produced with SHERPA 2.1 with the NNPDF3.0 PDF set at NNLO for matrix element calculations. These samples are produced with fast detector simulation using the AF2 algorithm [113]. To evaluate the uncertainty associate with the choice of tuning parameters extra samples with fast detector simulation have been also used with the same generator and showering setup as the nominal samples while the A14 tuning parameters are varied by ± 1 standard deviation.

- **Z+jets** For the description of the Z boson production plus associated jets, the samples produced by SHERPA 2.2.1 using the NNPDF3.0 NNLO PDF set are used. In order

[2]Parton distribution functions give the probability to find quarks and gluons, collectively called partons, in the proton as a function of the fraction of the proton's momentum carried by the parton

[3]A tune determines a set of parameters associated with a particular MC generator software that control the QCD effects

to ensure enough statistics in the high p_{T} range, the samples are produced in slices of $\max(H_T, p_T(Z))$[4] and a combinatorial composition of presence of charm and bottom quarks.

Samples produced with MadGraph, using the NNPDF3.0 NLO PDF set and interfaced to Pythia 8 with the A14 NNPDF2.3 LO tune for showering are used to assign a generator uncertainty. These samples are sliced in H_{T}.

- **SM** $t\bar{t}$ The SM $t\bar{t}$ background samples are generated using the POWHEG method [114, 115] implemented in Powheg-Box v2 [116] using the NNPDF3.0 NNLO PDF set. Powheg-Box is interfaced with Pythia 8 with the A14 set of tuneable parameters for parton showering and hadronization. In this sample non all-hadronic final states are considered, since the main contribution for the multilepton topology of this analysis comes from the semi-leptonic decay of at least one of the two top quarks. This sample was normalized to the NNLO cross section from TOP++ [117–119].

  Extra samples have been used for the evaluation of systematic uncertainties. Showering uncertainties have been included using using samples with the same generator and PDF set as the nominal case but using Herwig 7 [120, 121] with the H7UE tune and MMHT2014 PDF set [122] for the showering. Uncertainties associated with the choice of MC generator are included using samples generated with aMC@NLO with the NNPDF3.0 NNLO set and the showering done by Pythia 8 with the A14 NNPDF2.3 LO tune. Extra samples are also used (produced with the same generator and showering as the nominal case but with fast detector simulation) to evaluate the renormalization and factorization scale variations, shower tuning and NLO radiation. The factorization and renormalization scales are scaled up and down by a factor of 2 and 0.5 respectively. For the shower tune uncertainty A14 tuning parameters are varied.

- **Singletop** The singletop background processes have been generated with Powheg-

[4] H_T represents the scalar sum of transverse momenta of jets in the final state

Box v1 and interfaced to Pythia 8 with the Perugia 2012 [123] set of tuneable parameters. These samples were normalized to NLO cross sections with additional corrections associated with low energy gluons [124–126].

- **SM 4 top quark production** The SM production of four top quarks is a small source of background which is integrated into the $t\bar{t}+X$ background category in the analysis. It has been generated with MadGraph 5 and Pythia 8 using the NNPDF2.3 LO PDF set and the A14 tune. For normalization, NLO cross-sections obtained from MadGraph5_aMC@NLO have been used.

- **Triboson processes** The production of triboson events including WWW, WWZ, WZZ and ZZZ processes have been generated by Sherpa 2.1 with the CT10 PDF set [127]. These samples are normalized to NLO cross-section from Sherpa.

3.1.2 Single-T Signal

With an electric charge of $+\frac{2}{3}e$, the single production of Top partner is mediated by the electroweak force (Figure 1.4b). At the production vertex, Ts can be generated either by the fusion of an off-shell $W(Z)$ boson with a $b(t)$ quark coming from gluon splitting. However, a $g \to t\bar{t}$ vertex is significantly more suppressed compared to a $g \to b\bar{b}$ vertex because of the significantly larger mass of the top quark. This results in the production cross-section of Z-mediated production single T to be about an order of magnitude smaller than that of the W-mediated production of single T [46]. For the purpose of this analysis, we only focus on the W mediated production of single T which can decay to third generation SM quarks via exchange of W, Z, or the H bosons. Dedicated MC samples were generated using MadGraph [108, 109] with NNPDF2.3 LO for W-mediated single-T decaying to a Z boson and a top quark for M_T in the range of $700 - 2000$ GeV. The simulation was based on the Universal FeynRules Output (UFO) model [128] implementation on the VLQ parameterization in Ref. [47]. The coupling constant was set to $\kappa = 0.5$ with branching ratios in the W, Z, and H channels set to 0.4, 0.3, and 0.3 respectively. The decay of the Z boson and the t quark in these samples remained inclusive, to allow these MC samples to be efficiently used by multiple analyses searching for single T in the $T \to Zt$ mode (e.g. the exclusive dilepton channel accompanying the trilepton analysis as well as the invisible Z channel [73]). These samples were interfaced with Pythia 8 with A14 tune settings for showering. In order to extend the analysis for choices of κ beyond the benchmark, an approximate reweighting method based on parton level distribution of the mass of T was used. These samples were normalized with cross-section obtained from Ref. [46] with additional corrections applied at larger couplings for the signal's deviation from Narrow Width Approximation (NWA).

For all background and signal processes, the detector response is simulated in GEANT4 [129] with a full model of the ATLAS detector [130], unless stated otherwise. The simulations include the contributions from additional pp collisions in the same or an adjacent bunch crossing (pileup). Each simulated event receives additional correction factors, determined as a multiplicative weight factor to adjust its relative contribution in the entire simulated dataset. These weights include corrections for efficiencies of ATLAS triggers, efficiencies associated with the algorithms that identify different physics objects like electrons, muons, and jets, and for efficiencies associated with identifying jets emerging from b quarks. Correction factors for energy and momentum scales and resolutions of the objects are applied to the simulated samples, based on the differences observed between data and MC samples in reference processes. The choice of MC generator and associated details for different processes are summarized in Table 3.1.

3.2 Object Reconstruction

Based on the electronic signals observed at the inner detector, the calorimeters, and the muon spectrometer, electron, muon, and jet candidates are reconstructed for each pp collision event that passes the trigger selections. The reconstruction algorithm not only identifies the type of an object, but also evaluates its energy-momentum four vector in the laboratory rest frame for each of the reconstructed. These reconstructed electrons, muons,

Background Type	Generator	Shower and Tune	PDF Set (ME)	Crosssection
Diboson (VV)	Sherpa 2.2.1	Sherpa 2.2.1	NNPDF3.0 NNLO	NNLO
$t\bar{t}+V(W/Z)$	MadGraph5_aMC@NLO	Pythia 8, A14	NNPDF3.0 NNLO	NLO
$t\bar{t}+WW$	MadGraph	Pythia 8, A14	NNPDF2.3 LO	NLO
$t\bar{t}t\bar{t}$ (4 tops)	MadGraph	Pythia 8, A14	NNPDF2.3 LO	NLO
Z+jets	Sherpa 2.2.1	Sherpa 2.2.1	NNPDF3.0 NNLO	NNLO
Single top	Powheg-Box v1	Pythia 8, Perugia 2012	CT10	NLO+NNLL
$t\bar{t}$	Powheg-Box v2	Pythia 8, A14	NNPDF3.0 NNLO	NNLO+NNLL
Triboson (VVV)	Sherpa 2.1	Sherpa 2.1	CT10	NLO

Table 3.1: List of background MC samples used, giving information about the matrix-element generator, the parton shower program to which it is interfaced and its set of tuned parameters ("tune", if applicable), the PDF sets used in the matrix element (ME), and the order of QCD in the cross-section calculation

and jets are the primary physics objects that eventually determine which subset of events are most interesting for the analysis being performed.

3.2.1 Electron Reconstruction

Electrons are reconstructed [131] from clusters in the electromagnetic calorimeter with inner-detector tracks matched to them, and they are required to fulfill the *tight likelihood* identification criteria [132]. Electrons are calibrated [133] and are required to have a transverse energy of at least 28 GeV and to be in the fiducial region $|\eta| < 2.47$, excluding the barrel-endcap transition regions ($1.37 < |\eta| < 1.52$). In order to suppress background from non-prompt electrons[5] and from hadrons being misidentified as electrons, electron candidates are required to meet certain isolation criteria- the scalar sum of the p_{T} of all tracks pointing to the primary vertex within a certain conical region around the electron candidate must be less than 6% of its transverse momentum. The size of this conical region, ΔR, is defined as $\min\left(\frac{10\mathrm{GeV}}{p_{\mathrm{T}}}, 0.2\right)$, with p_{T} being the transverse momentum of the object [134]. Furthermore, electron candidates must be likely to originate from the primary vertex. This is ensured by requiring the d_0 significance, defined as $\frac{d_0}{\sigma_{d_0}}$ to be smaller than 5 where d_0 represents the smallest distance between the beam axis and the reconstructed track in the transverse plane and σ_{d_0} is the uncertainty associated with it. Additionally, the electron track needs to satisfy

[5]a non-prompt electron does not originate from the scattering event from pp collision, but rather created by a secondary process like e^+e^- pair production from a high energy photon

$|z_0 \cdot \sin\theta| < 0.5\,\text{mm}$ where z_0 is the longitudinal distance between the reconstructed primary vertex and the track's closest point of approach that determines the value of d_0.

3.2.2 Muon Reconstruction

Muons are reconstructed [135] from combined tracks in the muon spectrometer and the inner detector, and they are required to fulfill *medium* identification criteria [135]. Muons are calibrated and are required to have a transverse momentum of at least 28 GeV and to be in the fiducial region $|\eta| < 2.5$. In order to suppress background from non-prompt muons, an isolation criteria similar to the one used for electrons is applied with the variable cone radius defined as $\Delta R = \min\left(\frac{10\text{GeV}}{p_{\text{T}}}, 0.3\right)$. Furthermore, muon candidates must be likely to originate from the primary vertex in the event by requiring the d_0 significance to be smaller than 3 and $|z_0 \cdot \sin\theta| < 0.5\,\text{mm}$.

3.2.3 Jet Reconstruction

Small-R jets are reconstructed with the anti-k_t algorithm [136] using FastJET [137] with a radius parameter of 0.4 from topological clusters in the calorimeter [138, 139]. Small-R jets are calibrated to the jet energy scale (JES) [140, 141] and are required to fulfill $p_{\text{T}} > 25$ GeV for $|\eta| < 2.5$ and $p_{\text{T}} > 35$ GeV for $2.5 < |\eta| < 4.5$, i.e. jets in the forward calorimeters are also considered. Small-R jets with $|\eta| < 2.4$ and $p_{\text{T}} < 60$ GeV are required to fulfill a value of the jet-vertex tagger (JVT) [142] of at least 0.59. A high value of the JVT corresponds to a high probability of the jet originating from the primary vertex, hence a requirement on JVT removes contamination from pile-up vertices. Whether a central jet is originating from a b quark is determined by a Boosted Decision Tree (BDT) based multivariate classifier called MV2c10 [143, 144]. This classifier is trained with MC events where $t\bar{t}$ events in association with b jets is considered as signal and events associated with c and light jets comprise the background of which 7% come from c-associated events and rest include lighter jets. This classifier is used at 77% efficiency with rejection rates[6] for c and light jets

[6] The rejection factor is defined as the inverse of the b-tagging efficiency for non-b jets.

being 6 and 130 respectively.

In order to avoid any double counting of tracks or calorimetric energy clusters, an overlap removal procedure among the reconstructed physics objects is applied sequentially. First any electron which shares a track in the ID with a muon is removed. Any jet within a $\Delta R < 0.2$ of an electron is removed. Electrons within $\Delta R < 0.4$ of the remaining non pile-up jets [7] are removed. Any jet with at most 2 tracks with $p_{\mathrm{T}} > 0.5$ GeV within a $\Delta R = 0.04 + 10\,\mathrm{GeV}/p_{\mathrm{T}}(\mu)$ of a muon is removed. Any muon within the same ΔR of any remaining jet with at least 3 tracks is removed. This overlap removal improves the sensitivity on final states with high energy particles.

3.3 Event Selection

Events with the presence of heavy Ts are expected to have high energy objects in the final state. Both the signal topology and kinematics play important roles in identifying the set of selection criteria that would lead to an effective discrimination between the signal and background events.

3.3.1 Primary Selection

Events are required to have fired the single lepton triggers and events with less than two leptons with $p_{\mathrm{T}} > 28$ GeV are rejected. Events are then required to have at least two leptons (electrons or muons) of the same flavor and with opposite-sign electric charge (OS-SF). For each event, the Z boson candidate is identified with the OS-SF lepton pair that has an invariant mass ($m_{\ell\ell}$) closest to the pole mass of the Z boson (m_Z). Events for which this Z-boson candidate has an invariant mass outside of a 10 GeV window of m_Z are discarded. The event selection also requires the presence of at least one more electron or muon with $p_{\mathrm{T}} > 28$ GeV. Events are required to have at least two central jets, requiring $|\eta| < 2.5$ with $p_{\mathrm{T}} > 25$ GeV while the p_{T} requirement for Jets in the forward calorimeter ($2.5 < |\eta| < 4.5$)

[7] Pile-up jets are those with $p_{\mathrm{T}} < 60$ GeV, $|\eta| < 2.4$ and JVT < 0.59

is set to a minimum of 35 GeV.

3.3.2 Reduction of Contamination from Pair Production Signals

In addition to these requirements a cut on $H_{\mathrm{T}}(\text{jets}) \times n(\text{jets}) < 6$ TeV is applied in all regions in order to reduce pair production contamination. This reduction is needed in order to be able to properly derive coupling-vs-mass limits, where the cross sections scales with the square of the coupling modulo a polynomial-approximated correction factor at large decay widths. The event yield and the corresponding statistical limits cannot be translated according to the single-VLQ model if a sizable contribution of pair production events is present in the single production analysis. After considering a number of variables for this purpose and the aforementioned cut is selected that gives the best performance in reducing the contamination from potential pair produced VLQ events while not sacrificing the signal efficiency of single production process for a wide range of VLQ mass. The details of the optimization of this cut is outlined in Appendix A.

3.3.3 Optimization of the Signal Region

The signal region is designed to be dominated by signal-like events, i.e. the events that are more likely to appear when a Top Partner is present in the topology. This region is additionally designed to have a stronger rejection of background events to provide a maximized sensitivity for potential discovery of VLQ physics. As dictated by the signal topology (Figure 3.1), the final state signature requires the presence of at least one b-tagged central jet which would set VLT events apart from the SM processes, diboson (WZ, ZZ) processes in particular. Also, the production process of heavy VLQs require exchange of a largely off-shell vector boson, which results in the presence of a forward jet in the final state.

Figure 3.2a and Figure 3.2b show the distribution of multiplicities of b-tagged jets and forward jets after the applying the cuts explained in Section 3.3.1. As suggested in both figures, the signal-over-background ratio improves by an order of magnitude even at primary selection for events with at least one b-tagged or forward jets.

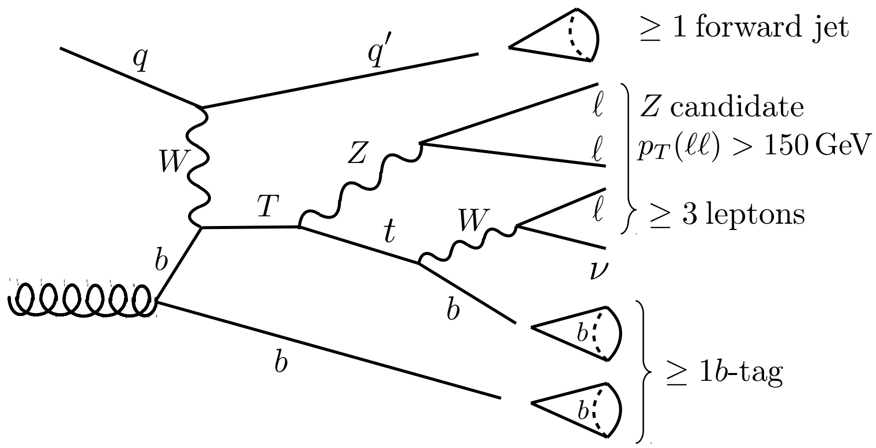

Figure 3.1: A sketch of the targeted process and the event selection applied in the proposed analysis. The event selection for the signal region requires the presence of at least one forward jet together with at least 3 leptons (2 from the Z boson and an extra lepton coming from the leptonic W decay). Extra b quarks are expected and at least one jet identified as coming from a b quark is required.

In the presence of b-tagged jets or forward jets, the Z candidate from the heavy VLQ shows a harder p_{T} spectra compared to the SM background processes (Figure 3.3a and Figure 3.3b respectively). Hence, in the signal enriched region, the Z candidate is required to have a minimum p_{T} of 150 GeV. Additional suppression of SM processes, $t\bar{t}+V$ processes in particular, is obtained by requiring a cut of 200 GeV on the transverse momentum of the leading lepton, defined as the lepton with the highest p_{T} (Figure 3.3c).

3.3.4 Background Modeling: Control Regions

While the signal region is designed to suppress background processes and maximize discovery potential for a singly produced T, it is important to ensure that the MC predicted background composition in that region is accurate. This can be obtained by designing the so-called *control* regions where cuts are chosen to suppress signal contribution in favor of keeping background events. Two control regions are defined to isolate, model, and validate

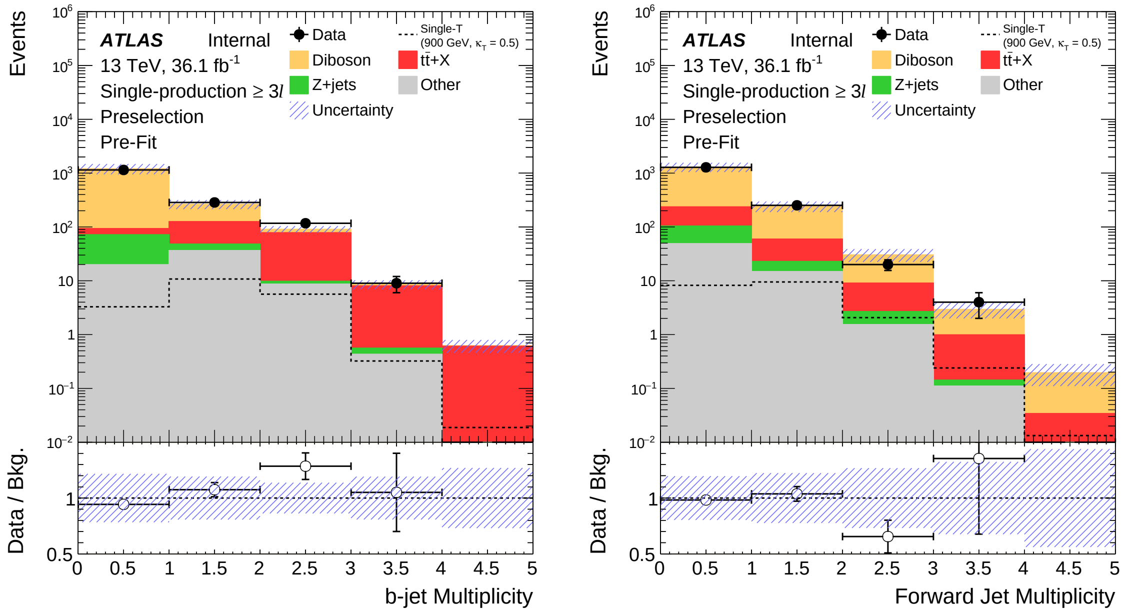

(a) (b)

Figure 3.2: Data/MC comparison for the (a) b-tagged jets multiplicity and (b) forward jets multiplicity distributions for events satisfying the primary selection. All MC samples are normalized to an integrated luminosity of $36.1 fb^{-1}$ and the bottom plot shows the ratio between observed data and background prediction. The overlaid black, dotted line is the prediction of signal events for a chosen benchmark signal of 900 GeV with a coupling of $\kappa = 0.5$ in the singlet representation. The last bin in both distributions is inclusive of a jet count of 4 or higher. The uncertainty bands include statistical and systematic uncertainties.

the main background sources in this analysis:

- **Diboson** (VV) **control region:** this region is defined rejecting events with any b-tagged jet. This allows the isolation of diboson production to remove contributions from processes with top quarks involved.

- $t\bar{t}$**+X control region:** this region is defined by selecting events with no forward jet and at least a b-tagged jet. Due to the low forward jet multiplicity found in background, it is a perfect candidate to isolate background from signal. Additionally, the cut on the leading lepton p_{T} is inverted to suppress signal selection in this control region.

All cuts described in the context of the control regions are applied on the events that pass the primary selection. By construction, the control regions are orthogonal to each other

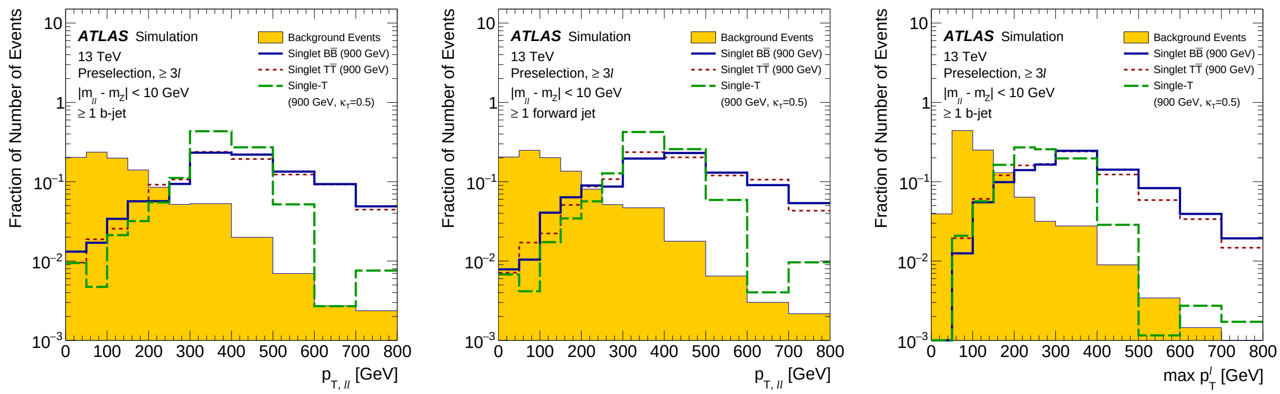

(a) (b) (c)

Figure 3.3: Signal/background lineshape comparison for the (a) transverse momenta of the Z candidate after applying the primary selection cuts on the subset of events with at least 1 b-tagged jet, (b) transverse momenta of the Z candidate after applying the primary selection cuts on the subset of event with at least 1 forward jet, (c) transverse momenta of the leading lepton after applying the primary selection cuts on the subset of event with at least 1 b-tagged jet. All lineshapes are normalized to have an integrated event count of unity.

as well as the signal region. Both control regions are designed to have a significantly lower signal efficiency compared to the signal region (Figure 3.4). The selection cuts for different regions are summarized in Table 3.2

Diboson CR	$t\bar{t}$+X CR	Signal Region
	≥ 3 leptons	
	≥ 1 pair of OS-SF leptons	
	$\lvert m_{\ell\ell} - m_Z \rvert < 10$ GeV	
	$H_{\mathrm{T}}(\text{jets}) \times n(\text{jets}) < 6$ TeV	
0 b-tagged jets	≥ 1 b-tagged jet	
	$\max p_{\mathrm{T}}(\ell) < 200$ GeV	$\max p_{\mathrm{T}}(\ell) > 200$ GeV
	0 fwd. jets	≥ 1 fwd. jet
		$p_{\mathrm{T}}(\ell\ell) > 150$ GeV

Table 3.2: Selection criteria for defining the control and signal regions

Table 3.3 shows the yields for background, signal and data in the control and signal regions before performing any statistical fitting. Diboson production is the dominant background in the diboson control region being $\approx 90\%$ pure in the diboson processes. The $t\bar{t}+X$ CR is $\approx 40\%$ pure in the $t\bar{t}+X$ processes with a significant contribution from diboson processes ($\approx 5\%$ higher than the $t\bar{t}$+V contribution). The modeling of diboson production, however, is already checked in the corresponding CR.

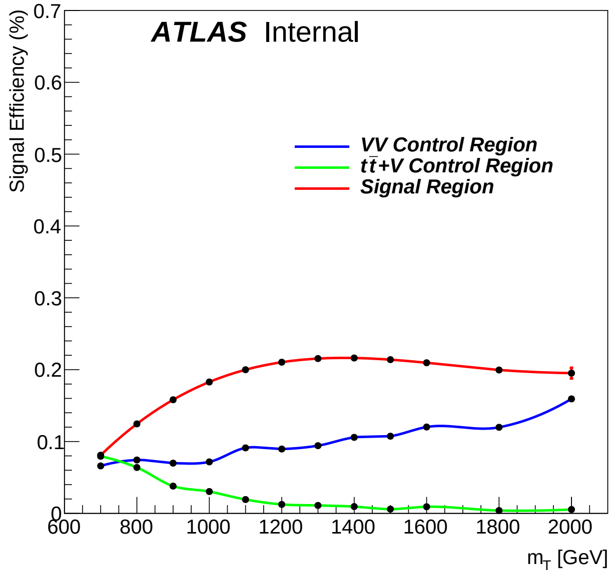

Figure 3.4: Signal selection efficiency in the control and signal regions. A VLT with a mass of 900 GeV and a coupling of $\kappa = 0.5$ in the singlet representation has been chosen as the benchmark.

The pre- and post-fit distributions for the main observables in this channel, the transverse momentum of the Z candidate ($p_{\mathrm{T}}(\ell\ell)$) and the scalar sum of transverse momenta of jets and leptons (S_{T}), are shown in Figures 3.5–3.7 for the different control and signal regions. The statistical fitting, as explained in section 3.5 is performed to validate the background MC distributions against data in the control regions. The S_{T} variable is used as the final discriminant to fit to data while the post-fit data-MC agreement in the $p_{\mathrm{T}}(\ell\ell)$ distribution serves as validation of quality and stability of the fit. The data and MC yields for different processes in the control and signal regions are given in Table 3.3 and Table 3.4 respectively.

3.4 Systematic Uncertainties

Accuracy of signal and background modeling via MC simulation is limited by two major source of uncertainties. The statistical uncertainties account for statistical fluctuation

	Diboson CR	$t\bar{t}+X$ CR	SR
Single-T (900 GeV, $\kappa_T = 0.5$)	3.3 ± 0.5	1.78 ± 0.22	7.9 ± 0.6
Z+jets	52 ± 29	9 ± 6	0.16 ± 0.10
$t\bar{t}$	7.1 ± 1.6	12.0 ± 2.7	0.000 ± 0.000
Single top	6.9 ± 0.9	18.9 ± 0.9	0.64 ± 0.11
$t\bar{t}+X$	22 ± 4	98 ± 15	5.6 ± 0.9
Diboson	1120 ± 260	110 ± 50	3.1 ± 1.4
Triboson	5.9 ± 0.4	0.46 ± 0.06	0.026 ± 0.007
Total Bkg.	1210 ± 260	250 ± 50	9.5 ± 2.0
Data	1145	279	14
Data/Bkg.	0.94 ± 0.20	1.13 ± 0.24	1.5 ± 0.6

Table 3.3: Observed number of events in data and pre-fit expected number of signal and background events in the control regions and the signal region, i.e. before the fit to data in the control regions and the signal region. For the signal, the expected number of events for the single-T benchmark process with M_T= 900 GeV and $\kappa = 0.5$ is shown. Statistical uncertainties from the limited size of Monte-Carlo samples and systematic uncertainties are added in quadrature. The uncertainty on the ratio of the observed and expected number of events additionally contains the statistical uncertainty on the prediction from Poisson fluctuations.

	Diboson CR	$t\bar{t}+X$ CR	SR
Z+jets	55 ± 27	11 ± 6	0.18 ± 0.11
$t\bar{t}$	7.3 ± 3.4	15 ± 6	0.000 ± 0.000
Single top	7.0 ± 3.3	20 ± 10	0.68 ± 0.34
$t\bar{t}+X$	22 ± 4	110 ± 14	6.2 ± 0.8
Diboson	1060 ± 50	116 ± 25	3.2 ± 0.7
Triboson	6.0 ± 2.5	0.50 ± 0.17	0.031 ± 0.014
Total Bkg.	1160 ± 40	280 ± 20	10.2 ± 1.0
Data	1145	279	14
Data/Bkg.	0.99 ± 0.04	1.01 ± 0.07	1.37 ± 0.14

Table 3.4: Observed number of events in data and post-fit expected number of background events in the control regions and the signal region, i.e. after the fit to the data S_T distributions in the control regions and the signal region in this channel under the background-only hypothesis. The uncertainty on the expected number of events is the full uncertainty from the fit, from which also the uncertainty on the ratio of the observed and expected number of events is calculated.

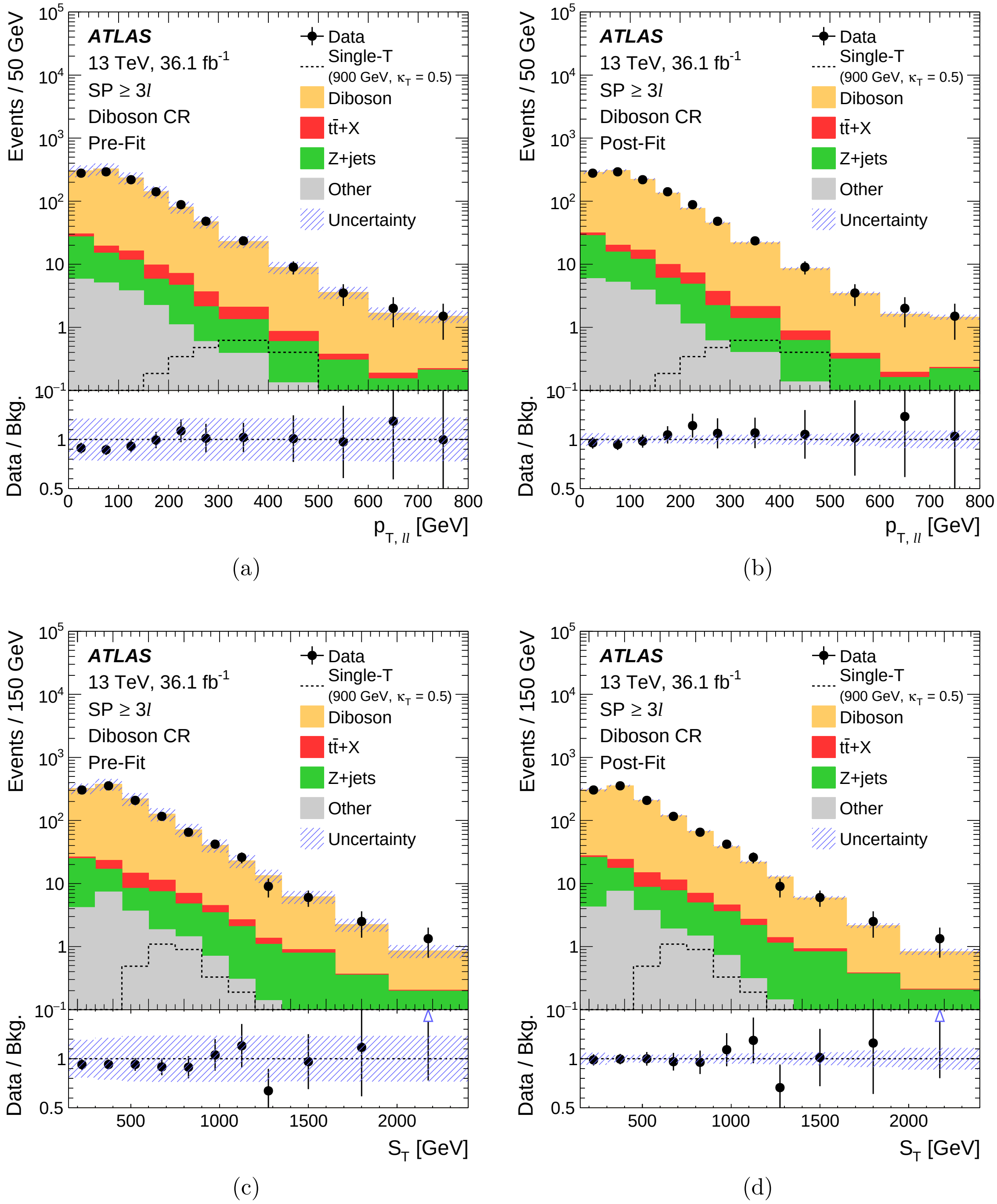

Figure 3.5: Post-fit distribution (right) compared with the pre-fit distributions (left) for the $p_{\mathrm{T}}(\ell\ell)$ (top) and S_{T} (bottom) distributions in the VV CR.

in the simulation process that emerges from the finite number of simulated events. Given the probabilistic nature of the pp interactions, statistical uncertainties are also inherent to data distributions. Additional uncertainties comes from a number of sources- resolution

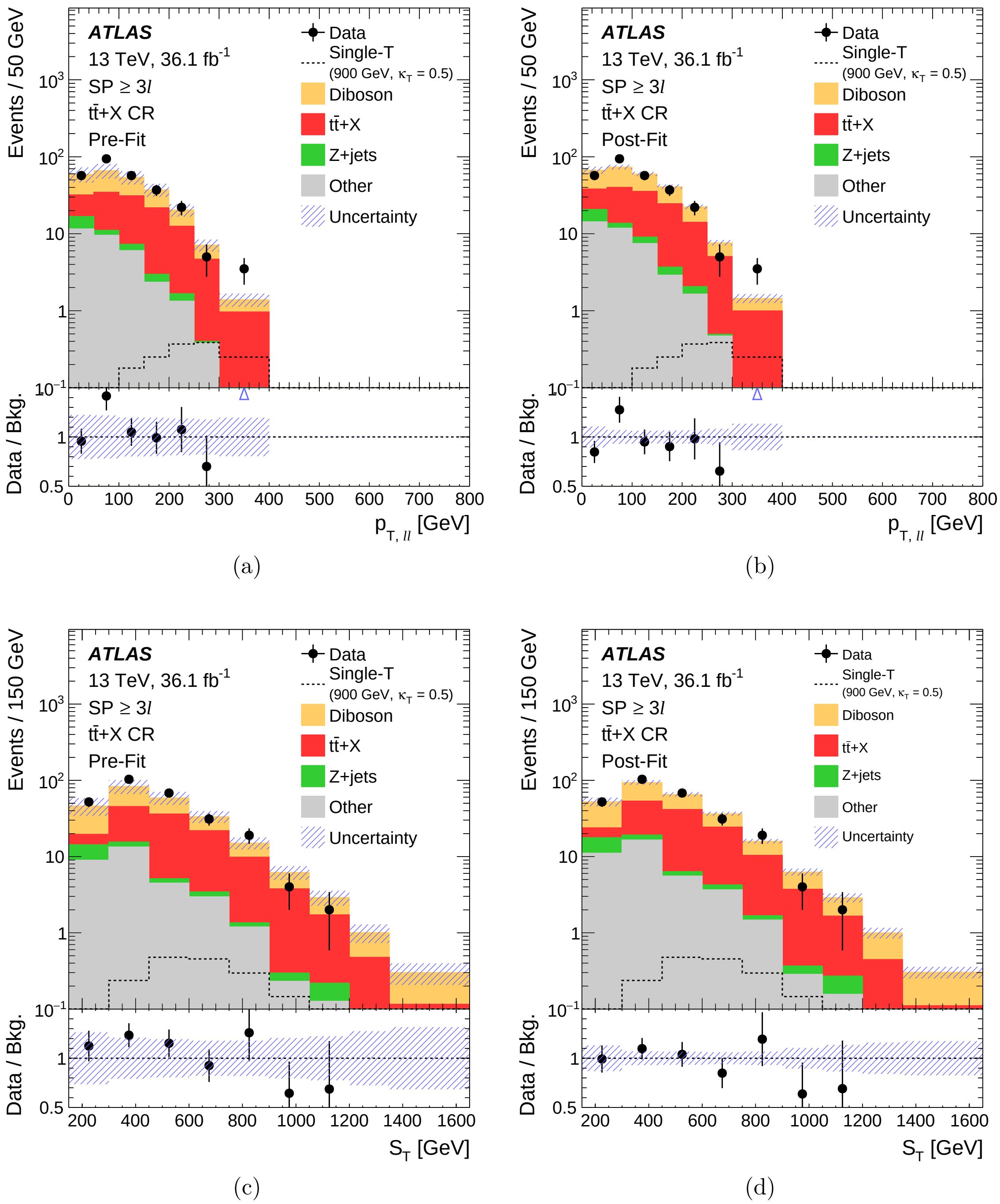

Figure 3.6: Post-fit distribution (right) compared with the pre-fit distributions (left) for the $p_{\mathrm{T}}(\ell\ell)$ (top) and S_{T} (bottom) distributions in the $t\bar{t} + X$ CR.

of the detector, uncertainties associated with object reconstruction and tagging, approximate or empirical nature of theoretical modeling, uncertainties from previous experimental measurements to name a few. These additional uncertainties, collectively known as *system-*

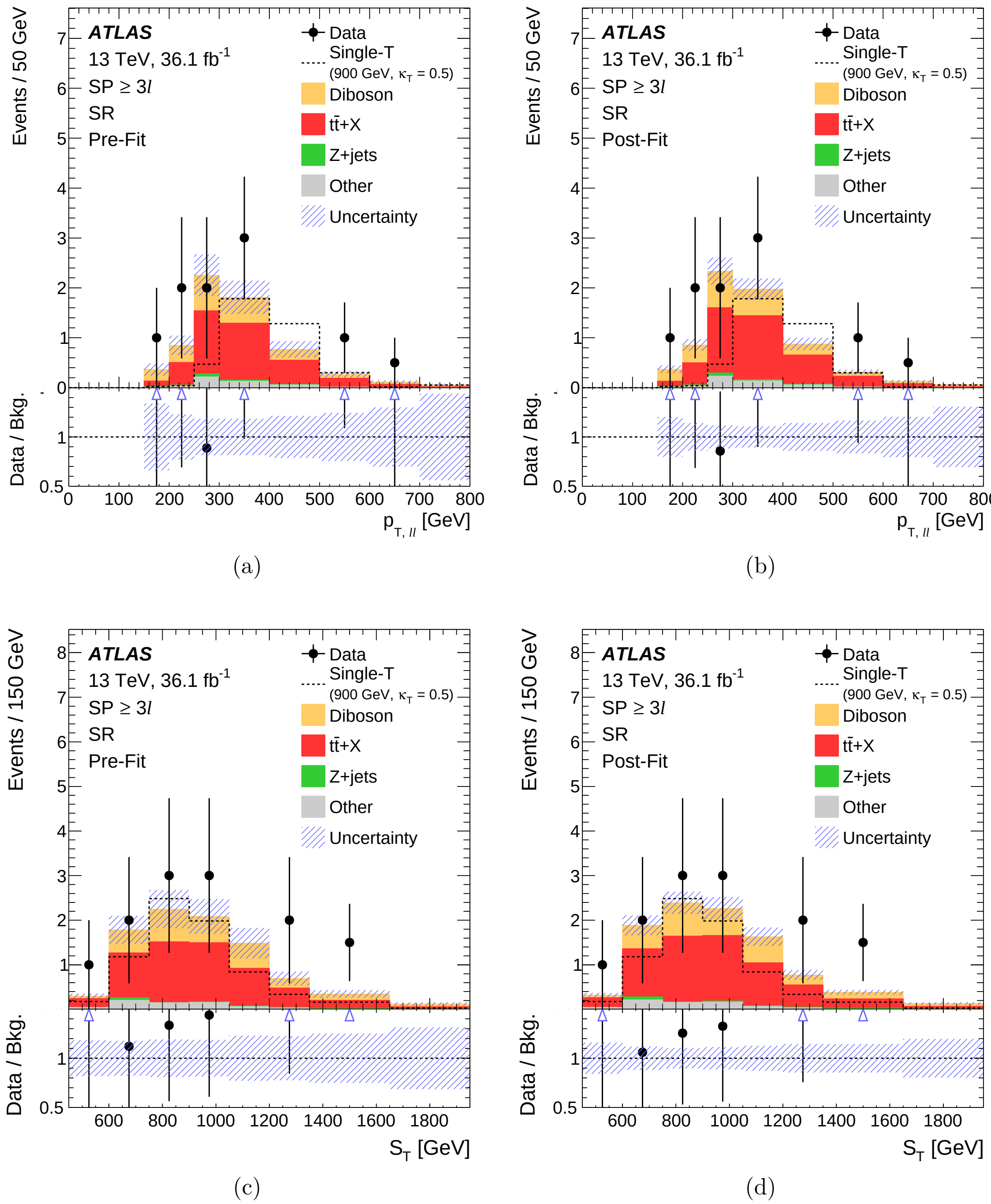

Figure 3.7: Post-fit distribution (right) compared with the pre-fit distributions (left) for the $p_{\mathrm{T}}(\ell\ell)$ (top) and S_{T} (bottom) distributions in the SR.

atic uncertainties play a significant role in limiting our ability to predict the physical data distributions from MC samples. This section describes the different sources of systematic uncertainties which are included in the analysis. These uncertainties can be broadly categorized in two categories corresponding to detector-related uncertainties and theory and modeling uncertainties.

3.4.1 Detector-related uncertainties

Uncertainties related with object reconstruction and detector performance are being included by reprocessing each MC sample with a different object reconstruction setup. The associated systematic uncertainties are:

- **Luminosity**: The preliminary uncertainty on the combined 2015+2016 integrated luminosity is 2.1%. It is derived, following a methodology similar to that detailed in Ref. [145] from a preliminary calibration of the luminosity scale using x-y beam-separation scans performed in August 2015 and May 2016.

- **Electron uncertainties**: The uncertainties on energy scale and resolution of the electromagnetic calorimeter impact the electron efficiencies in trigger, reconstruction, identification, and isolation algorithms. These efficiency variations are evaluated as function of (E_T, η) bins. These uncertainties are derived from tag-and-probe in $Z \to ee$ and $J/\psi \to ee$ events, where an isolated identified electron is used as the tag [146]. Uncertainties on electron energy reconstruction are evaluated using $Z \to ee$ events [147].

- **Muon uncertainties**: These uncertainties include variations in the p_{T} smearing in the ID, the MS as well as the choice p_{T} scale. Additionally, uncertainties associated to the scale factor variations due to the trigger, reconstruction, isolation and track-to-vertex-association (TTVA) efficiencies are evaluated to include two components, a statistical and a systematic uncertainty associated to the efficiencies derivations. The uncertainties are derived from tag-and-probe in $Z \to \mu\mu$ events [148].

- **Jets and flavor tagging**: Uncertainties on the jet energy scale is evaluated using MC samples validated against data for Z+jets, γ+jets, and multijet events [149]. The same subset of SM processes are used to evaluate uncertainties on the resolution of jets [141] and jet vertex tagger. Flavor tagging uncertainties are identified as deviations in b-tagging efficiency of light jets, c jets and b jets.

- **Pile-up**: All MC distributions are reweighted so that the distribution of the average number of interactions per bunch-crossing corresponds to the distribution in data. In order to assess the associated systematic uncertainty, the reweighting is varied within its uncertainty.

3.4.2 Other uncertainties

- **Cross-section Uncertainties**: These uncertainties are assigned to the different background processes as global variations on the cross-section calculation. They are usually obtained from theoretical arguments, precision measurements, or statistical limitation of MC generators. These global uncertainties associated to the different background processes are summarized in Table 3.5.

Process	Uncertainty (%)	Reference
Diboson	± 6	[150]
$t\bar{t}+V$	$+10.4/-11.9$	[151]
Z+jets	± 5	[150]
$t\bar{t}$	$+5.6/-6.1$	[152]

Table 3.5: Cross-section uncertainties for the main background processes

- **Z + jets Modeling Uncertainties**: Uncertainties are assigned to Z+jets by taking into account changes in the renormalization and factorization scales. Each event in the MC samples are reweighted for alternate choices of the renormalization (μ_R) and factorization (μ_F) scales. These additional weights are stored in the MC and used in order to study the impact of these variations testing 7 sets of variations of $(\mu_R, \mu_F) \in \{0.5, 1.0, 2.0\} \times \{0.5, 1.0, 2.0\}$ while the off-diagonal variations $(0.5, 2.0), (2.0, 0.5)$ are discarded. These variations are summarized by a bin-by-bin envelope extraction method- the largest positive and negative difference between nominal and the variations in each bin have been respectively taken as the $+1\sigma$ and -1σ variation in that bin while the variations across the bins are considered to be uncorrelated. An additional uncertainty due to the choice of PDF set is evaluated by comparing the nominal Sherpa sample using the NNPDF3.0 NLO PDF set with samples using the MMHT2014 NNLO [122] and CT14 NNLO PDF sets [153]. The same envelope extraction method has been used to estimate the $\pm 1\sigma$ variations due to choice of PDF sets. The MadGraph generated samples are compared with the nominal Sherpa 2.2.1 samples to assign a uncertainty associated with the choice of MC generator.

- $t\bar{t}$ **Modeling Uncertainties**: Extra MC samples described in Section 3.1.1 are used to assign generator and showering uncertainties respectively for $t\bar{t}$ samples. Samples simulated with fast simulation algorithm AF2 are also used for the factorization and renormalization scale variations. Since these samples are produced with AF2, fast simulation samples of the Powheg nominal samples are also processed and used to make a fair comparison. The AF2 variations samples are compared to the nominal AF2 ones and the relative difference is applied to the nominal samples produced with full simulation. This allows to disentangle possible differences found when comparing the variations samples produced with AFII and the nominal sample with full simulation. Additionally, internal weights provided by Powheg-Box v2 are used to evaluate the uncertainty associated to different PDF sets.

- $t\bar{t}+V$ **Modeling Uncertainties**: Extra samples using fast simulation and generated with Sherpa are used for the $t\bar{t}$+V process as a generator uncertainty. The nominal sample is also produced in AF2 and the relative difference between both of them is applied to the nominal full simulation sample as the uncertainty. Furthermore, showering uncertainties are evaluated using extra samples produced with AF2 with variations in the shower tuning.

- VV **Modeling Uncertainties**: For the diboson processes the internal weights of the Sherpa 2.2.1 are used to derive the renormalization and factorization scales variations in the same way as they have been used for the Z+jets samples. A similar prescription is used to evaluate uncertainties due to choice of PDF set. A 50% uncertainty in heavy flavor events is introduced since the diboson control region requires 0 b-tagged jets while the signal region requires at least one b-tagged jet. The heavy flavor events are identified using the truth flavor of the jets in the event and the uncertainty is applied when at least one heavy flavor jet (i.e. a jet that comes from charm or bottom quark) is found in the event.

- **Fakes**: Fakes are identified as events where at least one the three leptons that pass the selection criteria is actually a misidentified jet. The most common sources of fakes are Z+jets events where the Z bososn decays leptonically and a jet is misidentified as a lepton. A similar misidentification can take place in case of $t\bar{t}$ events, although $t\bar{t}$ contribution is generally quite low in all control and signal regions. The contribution of fakes, hence, is estimated by associating a global source of uncertainty on Z+jets and $t\bar{t}$ samples, uncorrelated across the regions. The $\pm 1\sigma$ variation due to this systematic is set to a conservative estimate of 25%, left as a free parameter to be pulled and constrained by the statistical fitting.

3.5 Statistical Fitting

The discriminant observable, S_{T}, is used to test the presence of signal by performing a binned likelihood fitting. The statistical analysis is based on a binned likelihood function $\mathcal{L}(\mu, \theta)$[8] as constructed in Equation 3.1 as a product of Poisson probability functions ($\mathrm{Pois}(n_i; \mu s_i + b_i)$) over all bins of the used distributions. The signal strength μ is a multiplicative factor for the signal production cross-section and is regarded as the Parameter of Interest (POI). For each bin, n_i denotes the observed data while s_i and b_i represent the predicted signal and background contribution from MC in the corresponding bin that depend on a set of nuisance parameters (NPs), θ, encoding the effect of systematic uncertainties

[8]At this point we have used the same symbol $\mathcal{L}$ to identify three different quantities, the Lagrangian density in Eqn. 1.3, instantaneous luminosity in Eqn. 2.1, and likelihood function in Eqn. 3.1. May be we should consider importing symbols from non-Greek and non-Roman alphabets

on the signal and background expectations and are implemented in the likelihood function as Gaussian or log-normal priors, collectively represented by the prior distribution function $P(\theta)$.

$$\mathcal{L}(\mu, \theta) = \Pi_{i=1}^{N_{\text{bins}}} \text{Pois}(n_i; \mu s_i + b_i) \times P(\theta) \tag{3.1}$$

Therefore, the total number of expected events in a given bin depends on μ and θ. The nuisance parameters θ allow variations of the expectations for signal and background according to the corresponding systematic uncertainties, and their fitted values correspond to the deviations from the nominal expectations that globally provide the best fit to the data. This procedure allows the potential for a reduction of the impact of systematic uncertainties on the search sensitivity by taking advantage of the highly populated background-dominated control regions included in the likelihood fit alongside with the signal regions.

In order to make the fitting procedure computationally more efficient, NPs are *pruned*, i.e. any NP with a relative impact of less than 1% in a given region is dropped from that region. Additionally, the $\pm 1\sigma$ variation for each NP is obtained by symmetrizing the positive and negative fluctuations around the nominal event count in each bin. The shape variation for each NP is also smoothed in every region to eliminate sources of instability in fitting due to large, local fluctuations.

The stability and convergence of the statistical fit in presence of a large number of NPs have been tested in different fit configurations. In the so-called *Asimov Fit*, the background and signal MC distributions are fitted against a representative dataset instead of the actual data. The representative dataset is created from the MC prediction with $\theta = 0$ while the value of signal strength is set to $\mu = 0(1)$ for a background-only (signal-plus-background) fit. The purpose of performing the Asimov fit is to validate the stability of the fit procedure by ensuring that the post-fit value of the pulls $\theta = 0$ is successfully retrieved (Figure 3.8). Additionally, the constraints on the NPs as seen in this pull plot identifies which NPs have the largest impact on the MC background modeling.

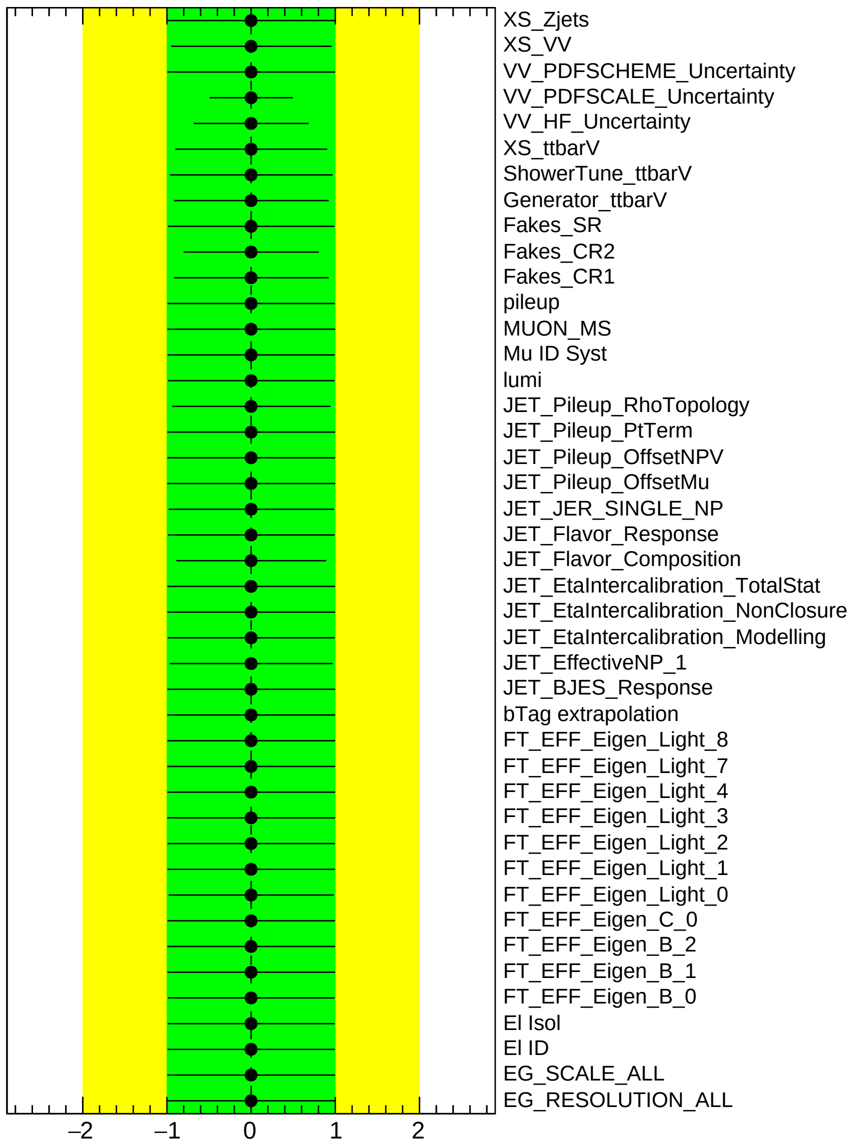

Figure 3.8: The pull plot is shown for a signal-plus-background Asimov fit in control and signal regions for the NPs which have not been removed by the pruning policy. All post-fit pulls are centered around $\theta = 0$, validating the convergence of the fit.

As seen from Figure 3.8, the largest constraints on the post-fit NPs are seen for the nuisance parameters associated with the uncertainties on heavy flavor fraction for diboson samples (`VV_HF`), diboson scale variation (`VV_PDFSCALE`), and fake contribution in $t\bar{t}+X$ CR (`Fakes_CR2`). As explained in section 3.5, the fake systematics apply a flat, conservative $\pm 25\%$ uncertainty on minor backgrounds, which leads this NP to be constrained. Constraints on the

VV_HF and VV_PDFSCALE variation stem from large relative variations, as shown in Figure 3.9 and Figure 3.10 respectively. The uncertainty from scale variation modeling has a maximum relative variation of $\mathcal{O}(20\%)$ in all regions. With significantly large statistics in the VV CR, this NP is expected to be constrained. The constraint on VV_HF is from very large uncertainties $\mathcal{O}(40-50\%)$ in the $t\bar{t}+X$ CR and the SR.

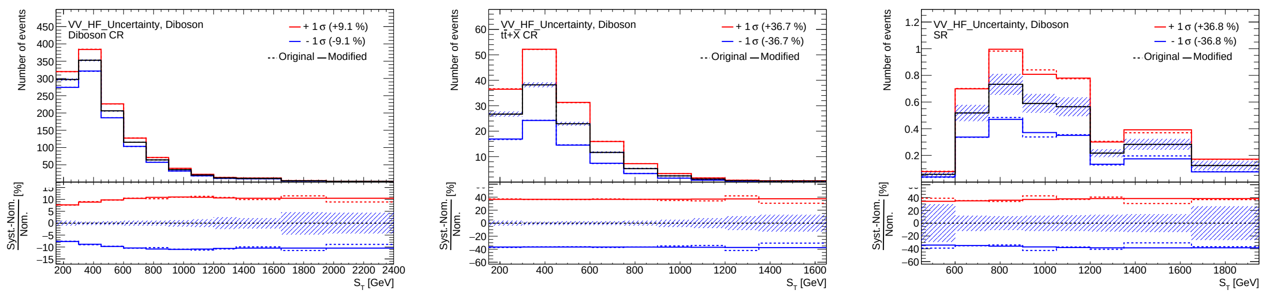

(a) (b) (c)

Figure 3.9: Relative variation of VV background lineshape in (a) VV CR, (b) $t\bar{t}+X$ CR, and (c) SR due to $\pm 1\sigma$ variation of the VV_HF NP.

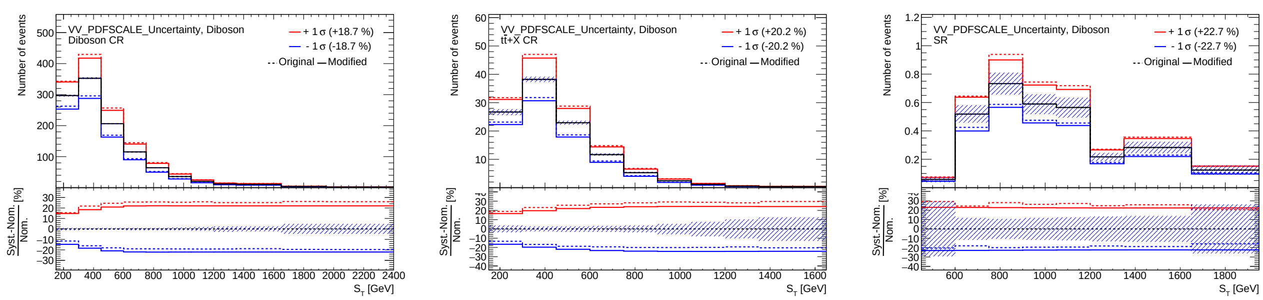

(a) (b) (c)

Figure 3.10: Relative variation of background lineshape in (a) VV CR, (b) $t\bar{t}+X$ CR, and (c) SR due to $\pm 1\sigma$ variation of the VV_PSDSCALE NP.

The Asimov fit also reveals important correlations among NPs, as shown in (Figure 3.11). There is a strong negative correlation between the fakes NP in $t\bar{t}+X$ CR and the VV_HF NP, which is expected since they both contribute in modeling the background normalization in the $t\bar{t}+X$ CR. Similar correlations exist between VV_HF and VV_PDFSCALE NPs. We also find strong negative correlations between two major contributors to VV yields normalization- VV_PDFSCALE and the NP XS_VV associated with the cross-section uncertainty of VV processes.

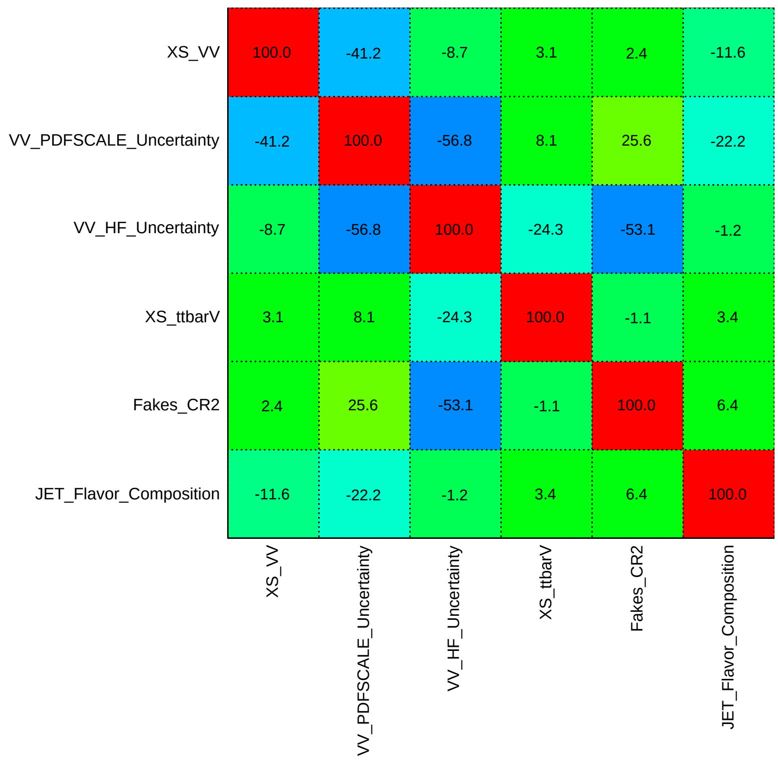

(a)

Figure 3.11: The correlation matrix for a signal-plus-background Asimov fit in control and signal regions for NPs with at last a correlation higher than 20% is shown.

A background-only fit with the actual data is used to obtain the post-fit values for the different NPs where the value of μ is set to zero and μ is removed from the fit. Figure 3.12 shows the pulls obtained for the NPs that survive the pruning in at least one of the regions. The constraints observed on the NPs are consistent with the constraints obtained in Asimov fit, as shown in Figure 3.8. Figure 3.13 shows the correlation matrix for a subset of the NPs.

To evaluate the impact of different NPs on the POI, a signal-plus-background fit was performed. In this setup, first the best fit value for each of the NPs as well as μ is evaluated. To quantify the impact of each of the NPs, the value of all NPs but the one in question is set to their best fit value while the NP in question is varied by $\pm 1\sigma$ and the shift in the best-fit value of μ is recorded. The ranking plot for the most impactful NPs is shown in Figure 3.14.

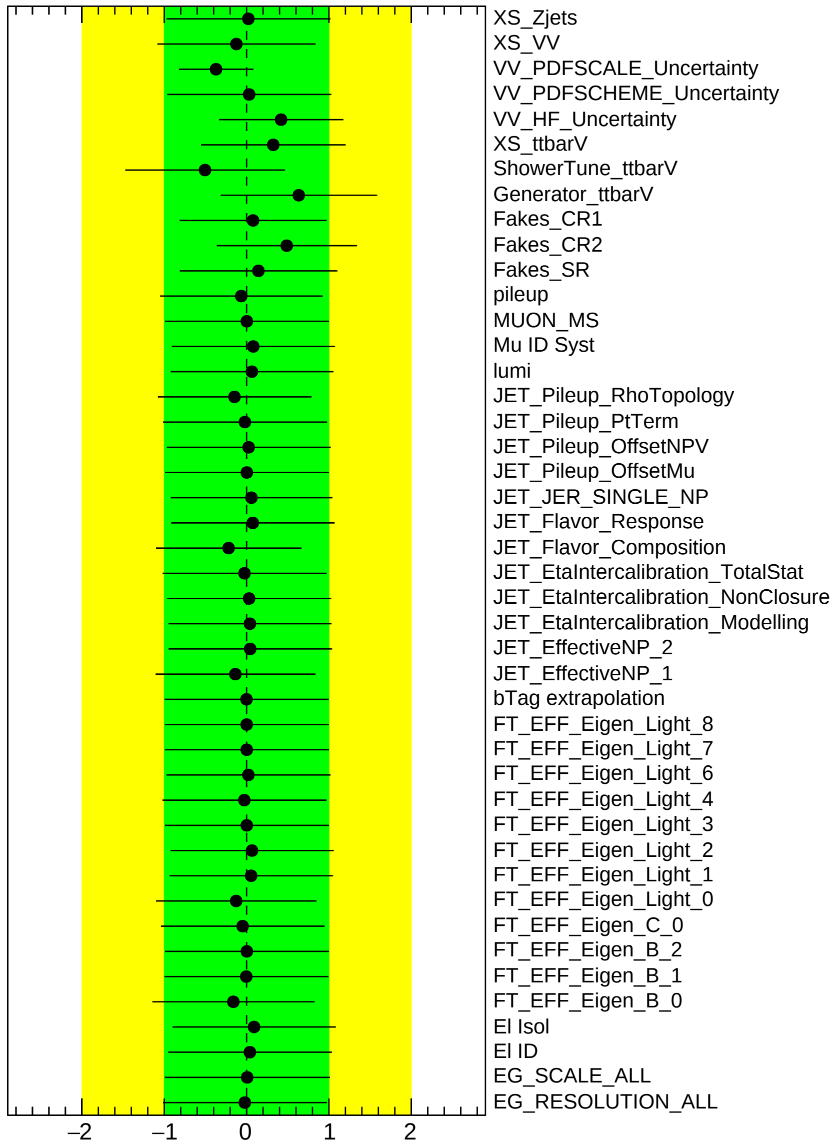

(a)

Figure 3.12: The pull plot is shown for the NPs which have not been removed by the pruning policy explained. As can be seen the NPs with bigger pulls are the ones concerning $t\bar{t}$+V, both the generator and the fakes uncertainty due to larger data/MC disagreement in that region. Only the diboson cross-section is being pulled for diboson which is due to the small normalisation difference between data and MC in the VV CR.

To test for discovery, a profile likelihood ratio test is performed against the null hypothesis of no signal presence in the data. The test statistic q_μ is defined as the profile

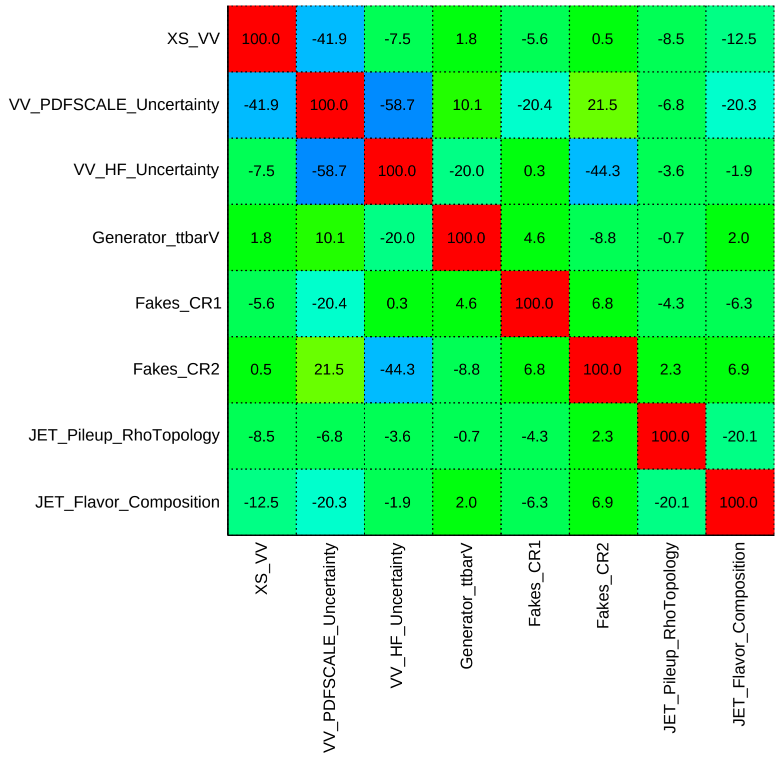

(a)

Figure 3.13: The correlation matrix for NPs with at last a correlation higher than 20% is shown.

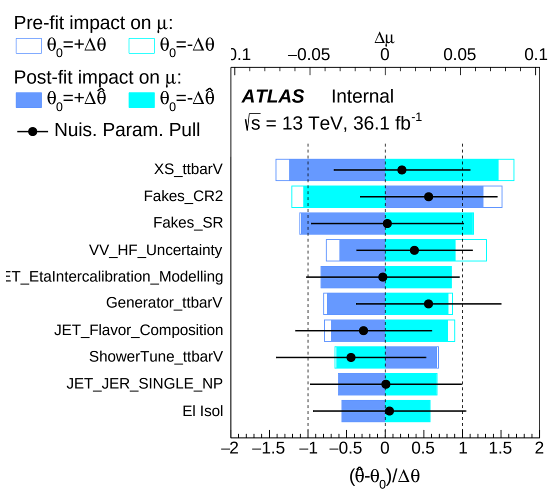

(a)

Figure 3.14: Ordered list of the 10 NPs with the highest impact on the signal strength with the highest impact NP on top.

likelihood ratio

$$q_\mu = -2\ln\left[\frac{\mathcal{L}\left(\mu, \hat{\hat{\theta}}_\mu\right)}{\mathcal{L}\left(\hat{\mu}, \hat{\theta}\right)}\right] \tag{3.2}$$

where $\hat{\mu}$ and $\hat{\theta}$ are the values of the parameters that maximize the likelihood function (with the constraint $0 \leq \hat{\mu} \leq \mu$), and $\hat{\hat{\theta}}_\mu$ are the values of the nuisance parameters that maximize the likelihood function for a given value of μ. The test statistic q_μ is implemented in the RooFit package [154] and is used to measure the compatibility of the observed data with the background-only hypothesis (i.e. the discovery test) setting $\mu = 0$ in the profile likelihood ratio. The actual statistical analysis package used is TRexFitter [155], which makes use of the RooFit and RooStats [156] packages. The p-value (referred to as p_0) representing the compatibility of the data with the background-only hypothesis (i.e. $\mu = 0$) is estimated by integrating the distribution of q_0 from background-only pseudo-experiments, approximated using the asymptotic formulae given in Refs. [157, 158], above the observed value of q_0. Some model dependence exists in the estimation of the p_0-value, as a given signal scenario needs to be assumed in the calculation of the denominator of q_μ, even if the overall signal normalization is left floating and fitted to data. Given the agreement between the data and MC predicted background prediction in the SR, as shown in Figure 3.7d, the value for $\hat{\mu}$ was found to be very close to zero for all choices of VLQ signal mass, implying the absence of sufficient evidence against the null hypothesis.

3.5.1 Limits and Combination

In the absence of any significant excess above the background expectation, upper limits on the signal production cross-section are derived by using q_μ in the CL_s method [159, 160]. Values of the production cross-section (parameterized by μ) yielding $\mathrm{CL}_s < 0.05$, where CL_s is computed using the asymptotic approximation [157, 158], are excluded at 95% confidence level. The limit on the product of VLT cross-section and the branching ratio $\sigma(pp \to T) \times \mathrm{BR}(T \to Zt)$ as a function of VLT mass is given in Figure 3.15a. Both statistical and systematic uncertainties have been accounted for while setting these limits, and a benchmark coupling of $\kappa = 0.5$ for the singlet representation has been chosen. However, the limits are primarily driven by the statistics and the systematic uncertainties have a marginal impact on them, as can be seen from Figure 3.15b.

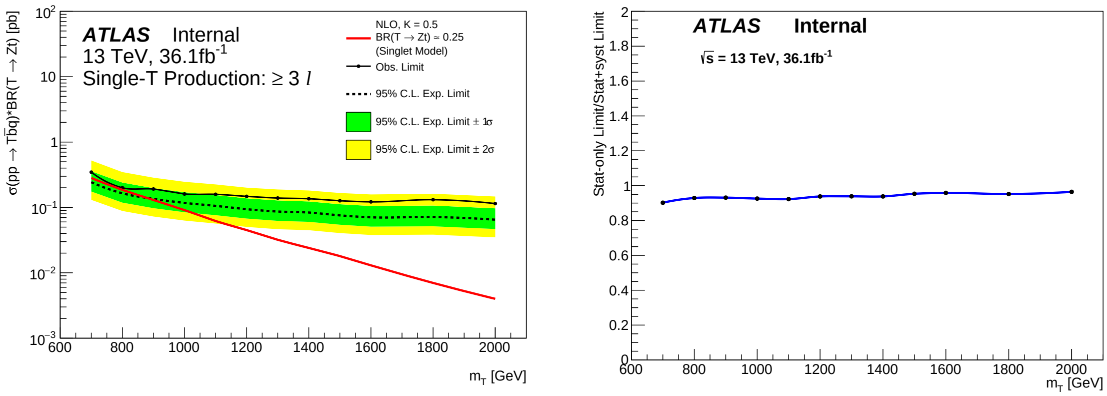

(a) (b)

Figure 3.15: (a) Expected and observed upper limits in $\sigma \times BR$ as a function of the mass of T at 95% C.L. for a benchmark coupling of $\kappa = 0.5$ and singlet representation. Both statistical and systematic uncertainties have been included. (b) Ratio of expected cross-section limits from stat-only fit setup and stat-plus-syst fit setup. The stat-plus-syst limits are found to be marginally weaker than the stat-only limits.

In order to maximize the sensitivity of the analysis, the results were combined with the complementary dilepton analysis, provided in the same paper [71] as result in this chapter. The dilepton channel looks for the same decay channel for the Top Partner where the leptonically decaying Z boson constitutes the two leptons for the signal selection. However, the accompanying top quark decays hadronically, and the signal selection particularly looks for boosted top quarks that instead of leaving behind a distinct jet signature for each decay component in the detector, appear as a single jet with larger radius and stronger energy signature. The signal selection allows the dilepton channel to retain more statistics and the primary source of background for that channel is Z+jets events. The dilepton analysis is orthogonal to the trilepton channel by construction and hence, only share correlated systematic uncertainties of common origin (e.g. detector related systematics) with the trilepton channel. The combined analysis provides stronger limits on the process cross-section, as shown in Figure 3.16.

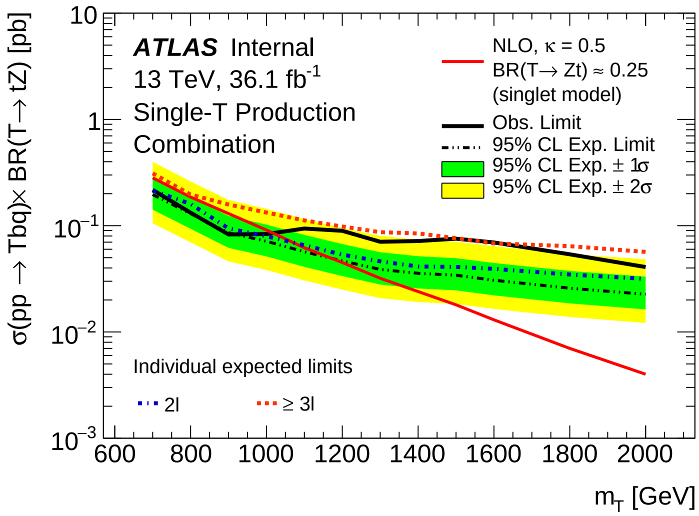

(a)

Figure 3.16: Expected (dashed line) and observed (solid line) upper limits in $\sigma \times BR$ as a function of the mass of T at 95% C.L. after combining the dilepton and trilepton channels for a benchmark coupling of $\kappa = 0.5$ for the singlet representation. Both statistical and systematic uncertainties have been included.

Since the cross-section of singly produced VLQs depend on the choice of couplings as well as their electroweak representations, the cross-section limits can be translated into limits on the VLQ couplings. However, changes in coupling also change the kinematic distributions of the VLQ masses. As a result, both the signal yield and distribution are functions of the VLQ couplings. To accommodate this variation in signal kinematics, additional corrections were used to reflect the changes in signal normalization and distribution at different values of the couplings:

- **Kinematic Reweighting**, a histogram based reweighting method to obtain an event-by-event corrective weight factor that projects the VLQ distributions for one choice of coupling to another. This method was devised by generating a large number of VLQ signals at truth level for different choices of masses and couplings. Such distributions were compared using a variable binning to ensure sufficient statistics in each bin and a correction factor for each event in the MC sample was obtained. Figure 3.17 compares the distribution of VLQ invariant mass at the initial selection level- after requiring the OS-SF criteria with an on-shell Z candidate, but without any constraint on the number of leptons. The reweighting method provides good closure among distributions at the truth level.

- **Correction for Narrow Width Approximation (NWA)** to calculate the deviation of the cross-section prediction for VLQs for larger decay widths. At narrow width, the VLQ cross section scales as the squared coupling at the production vertex, i.e. $\sigma_{\mathrm{NW}} \propto c_W^2$ [46]. However, as the VLQ decay width becomes large with increasing values of the couplings, this approximation ceases to hold. The deviation from the NWA approximation is approximated as a second order polynomial $P_{\mathrm{NWA}} = \frac{\sigma_{\mathrm{FW}}}{\sigma_{\mathrm{NW}}} = A_0 + A_1 c_W + A_2 c_W^2$ [72], where σ_{FW} is the finite width cross-section at the given choice of couplings.

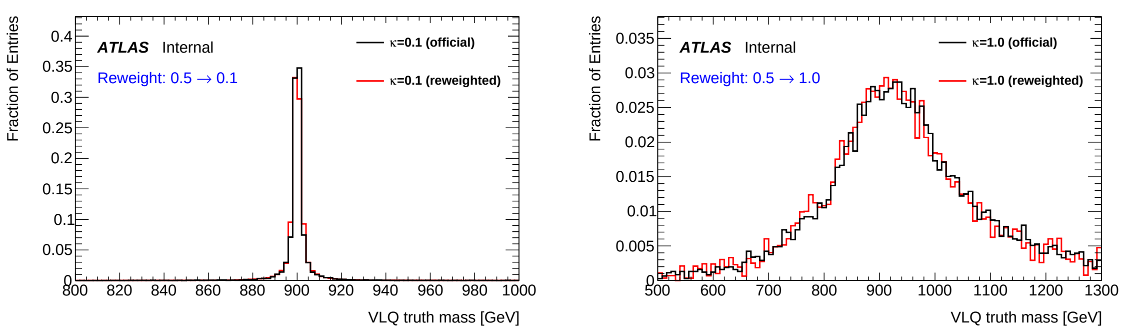

(a) (b)

Figure 3.17: Comparison of the T mass distribution obtained from reweighting with the distributions obtained from a set of events generated using the desired coupling for a target coupling of (a) $\kappa = 0.1$ and (a) $\kappa = 1$. All distributions are normalized to unity.

Upon including the aforementioned corrections, the cross-section limits were evaluated as a function of the mass of T and its coupling κ. These limits on cross-section were translated into limits on the free parameters of the VLQ Lagrangian to provide interpretive exclusion limits in model specific contexts. Figure 3.18a shows the limits on the coupling constant for the TWb vertex, c_W, while the branching ratio in the Z channel is set to a fixed value of 0.25.

As expected, the largest excluded coupling increases at larger VLQ masses to compensate for the decreasing interaction probability for heavier VLQs. The same limits are cast in terms of mixing angle between the T and the top quark in a singlet model. The two pronged structure of the limit bands emerge from the quadratic nature of couplings in the analytic expression for VLQ branching ratio. The area enclosed by the two branches are excluded at 95% confidence level.

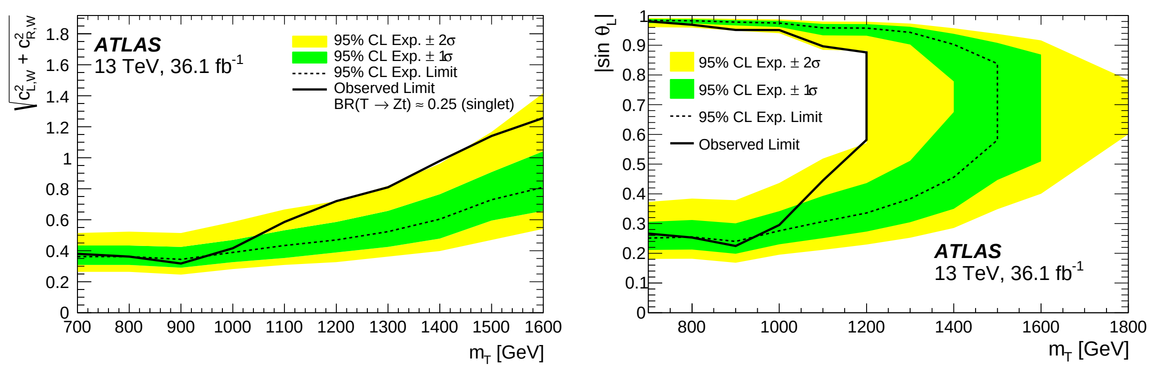

(a) (b)

Figure 3.18: Cross-section limits interpreted in terms of (a) coupling between a T and the W boson as a function of the VLT mass while the branching ratio is set to $\mathrm{BR}(T \to Zt) \approx 0.25$ in fixed branching ratio model. (b) The same limits are recast in terms of mixing angle between the T and a top quark in a singlet model as a function of the VLT mass where the region enclosed by the two branches are excluded.

A more generalized interpretation is provided in Figure 3.19 where the limits on expected (Figure 3.19a) and observed (Figure 3.19b) excluded VLQ mass are calculated as a function of c_W and c_Z couplings. The Higgs vertex coupling is set by requiring equal branching ratios in the Higgs and Z channels, as expected in most VLQ representations at larger VLQ masses [51].

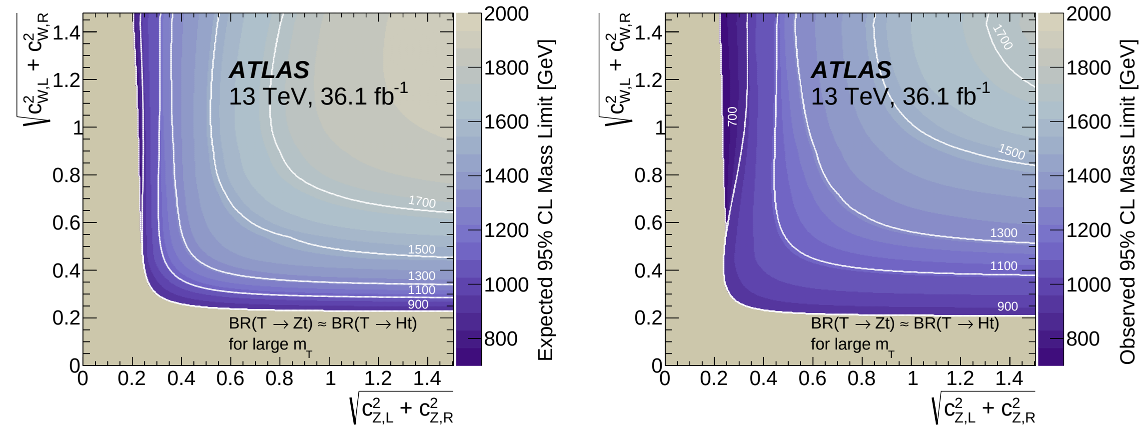

(a) (b)

Figure 3.19: (a) Expected and (b) observed cross-section limits interpreted in terms of upper limits on excluded T mass as a function of TWb and TZt vertex couplings (c_W and c_Z). The coupling to the Higgs channel is set by requiring equal branching ratios in the H and Z channels. The grey regions in the low coupling corners represent parametric subspaces beyond the sensitivity of the combined analysis.

Chapter 4

Generalized Interpretation of single-VLQ Searches

The model-dependent nature of single production of VLQs makes the interpretation of such search results significantly more involved than the pair produced VLQ searches. Different analyses have adapted different strategies, often inspired by model-specific assumptions. These diverging set of assumptions make it difficult to consistently compare or combine the results obtained by these analyses and hence, limiting the sensitivity of the collective VLQ search programs at the expensive collider physics experiments.

This chapter[1] lays out an experimentally-inspired, semi-analytical framework for a relatively model-independent interpretation of single VLQ production search results that can be adapted by most ongoing and future analyses. In section 4.1, we explain the details of and the challenges to a model-independent interpretation of single VLQ production searches and emphasize on why such a strategy is important. Section 4.2 introduces a minimal set of assumptions and presents the semi-analytical framework. In section 4.3, we introduce a novel parameterization for estimating the correction to the single VLQ production cross-section at finite widths. Finally, in section 4.4, we demonstrate how this framework can be used to compare, reinterpret and visualize existing search results from ATLAS and CMS.

4.1 The Philosophy of Interpretation of VLQ Searches

Pair production of VLQs has inspired an elegant interpretation strategy. The dominant, QCD-facilitated production mode for a pair of VLQs allows a model-independent estimate of the cross section for the pair production under a narrow width approximation

[1]Work summarized here is published in Ref. [161] where the other co-authors played a supervisory role in outlining the structure and physics goals

(NWA), i.e.:

$$\sigma(pp \to Q\bar{Q} \to V_1 q_1 V_2 \bar{q}_2; M_Q, \vec{c}) \xrightarrow{\text{NWA}} \sigma^{\text{NW}}_{\text{prod, } Q\bar{Q}}(M_Q) \times \text{BR}(Q \to V_1 q_1; \vec{c}) \times \text{BR}(Q \to V_2 q_2; \vec{c}) \tag{4.1}$$

Here, the value of the production cross-section $\sigma^{\text{NW}}_{\text{prod, } Q\bar{Q}}(M_Q)$ is independent of the electroweak group representation and the corresponding coupling parameters of the heavy fermions. This allows for a reformulation of the VLQ Lagrangian by treating the branching ratios themselves as free parameters while ignoring their complex dependence on the coupling parameters, $\vec{c}$. Moreover, most analyses looking for these heavy fermionic resonances also assume that these particles couple predominantly only with the third generation of standard model quarks, i.e.:

$$\text{BR}(Q \to Hq) + \text{BR}(Q \to Zq) + \text{BR}(Q \to Wq') = 1.0 \tag{4.2}$$

where $q, q' \in \{t, b\}$.

The assumption on the branching ratios in equation (4.2) allows, along with the NWA, for a simple interpretation for searches of pair production of VLQs, where the excluded region in the parametric hyperspace is evaluated by solving the following inequality:

$$\sigma^{\text{NW}}_{\text{prod, } Q\bar{Q}}(M_Q) \geq \sigma^{\text{NW}}_{\text{lim, } Q\bar{Q}}(M_Q, \text{BR}_W, \text{BR}_H) \tag{4.3}$$

where $\sigma^{\text{NW}}_{\text{lim, } Q\bar{Q}}$ is the statistically excluded cross section limit (usually computed at 95% confidence level) at narrow width, corresponding to the largest process cross-section compatible with the background only hypothesis given the observed distribution in data. The cross-section limit depends on the sensitivity of an analysis to different VLQ decay modes and hence, is a function of the choice of VLQ decay branching fractions. As a result, a parametrically model-independent interpretation of pair production searches can be done by solving equation (4.3) for some chosen grid of allowed values of $\text{BR}(Q \to Wq')$, $\text{BR}(Q \to Hq)$ to set a limit on the VLQ mass.

The importance of a universal, model-independent interpretation strategy is pivotal for a combination of multiple analyses. A consistent combination of multiple analyses requires a well defined correlation scheme among the various nuisance parameters as well as the parameter(s) of interest (POI), the latter usually being a function of signal cross-section. A generalized interpretation strategy, as given in equation (4.3), can be used to formulate a well-defined correlation scheme for the POIs of different analyses. Different analyses tend to be sensitive to different kinematic signatures and different regions of the phase space. A combination of such analyses guided by a well defined interpretation strategy can significantly boost the statistical power and hence, set stronger limits on the parametric hyperspace. The combination [67] performed by the ATLAS collaboration, excluded up (down)-type VLQ masess up to 1.31 (1.03) TeV for any combination of branching ratios respecting equation (4.2).

In light of the interpretation strategy for pair produced VLQs as given in equation (4.3), a framework of interpreting search results for singly produced VLQs can be laid out. The excluded region of parametric hyperspace can be evaluated by solving the inequality

$$\sigma_{VQAq}\left(M_Q, \vec{c}\right) \geq \sigma_{\text{lim},\, VQAq}\left(M_Q, \vec{c}\right) \tag{4.4}$$

where $VQAq$ is short-hand notation for the production of the VLQ Q being mediated by the vector boson V that subsequently decays to the boson A and SM quark q. The production and decay of single VLQs involve the relevant couplings at the corresponding vertices. The same couplings determine the partial decay widths and hence, the branching ratios of these VLQs in the associated decay channels. Moreover, the kinematic distributions of VLQ decay products also change with the change of VLQ decay widths and hence, with the choice of couplings (Figure 4.1). This changes the phase space sensitivity of the analyses and, as a result, the exclusion limit also becomes non-trivially dependent on the choice of not only the VLQ mass but also the couplings.

The non-trivial coupling dependence of the interpretation relation in equation (4.4) makes it somewhat challenging to formulate a generalized interpretation strategy. Previous ATLAS and CMS analyses incorporated simplified interpretation strategies by making model-dependent assumptions either about the branching ratios [61, 72] or about the rela-

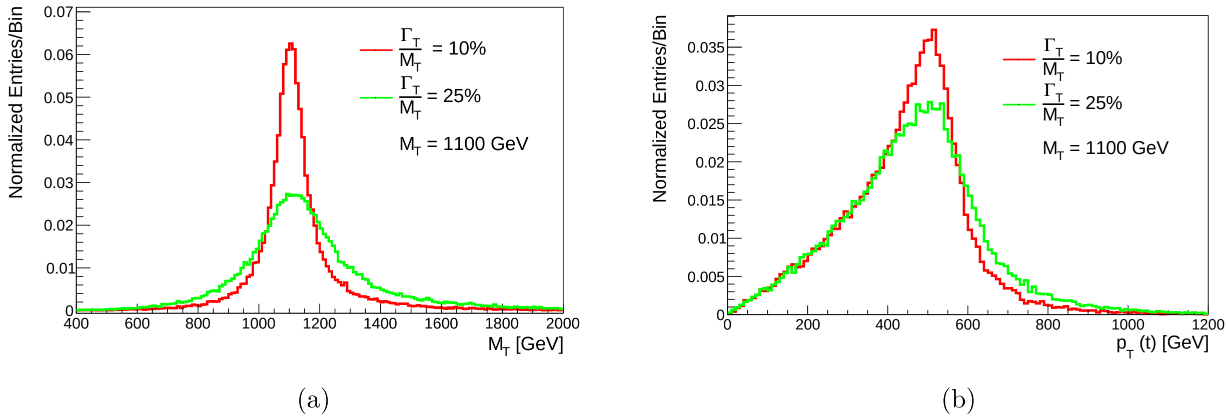

Figure 4.1: Distribution of (a) Top Partner invariant mass and (b) transverse momentum of the top quark from its decay in association with a Z boson. The coupling values are set to $c_{L,W} = 0.5$ (red) and $c_{L,W} = 0.8$ (green) in singlet representation to obtain the desired relative decay width. All histograms are normalized to unity.

tive decay widths [74, 75], or by interpreting the generic couplings in terms of the mixing angles between the heavy fermions and their SM counterparts [71–73]. Such diversity of interpretation strategies often makes it difficult to compare results from different analyses and formulate a consistent correlation scheme for a possible combination of such analyses.

In the following section, we present the formulation of a generalized interpretation strategy for singly produced VLQs. Following the footsteps of the interpretation strategy of searches for pair production of VLQs, we pursue a general idea of making a set of strategic assumptions to reduce the dimensions of the parametric hyperspace providing the avenue of translating the exclusion limits to excluded regions of the reduced hyperspace.

4.2 Framework for Interpretation of Singly Produced VLQs

The *first assumption* we make is to restrict VLQs to interact with third generation SM quarks exclusively. Additionally, we exclude models that incorporate single production of VLQs in association with heavy vector bosons [162, 163] or their decay via exotic scalars [164–169] although such models are often theoretically well-motivated. This results in the branching fractions to be constrained according to equation (4.2). In light of this assumption, we will drop the superscript indices Qq in the generalized couplings from this point forward– this association will be clear from the context of discussion.

Secondly, we assume that VLQs are much heavier than the SM fermions and bosons, i.e.:

$$M_Q \gg m_t \tag{4.5}$$

where m_t denotes the top quark mass of 172.5 GeV [1]. This assumption is inspired by the model-independent pair production search results from the ATLAS and CMS collaborations, which set a limit on VLQ masses in the range of $\mathcal{O}(1 \text{ TeV})$ independently of its electroweak representation. At the large M_Q limit, the interference term between left and right handed couplings in the analytic expressions of the partial decay widths become negligible. Therefore, the corresponding partial decay widths for $Q \to Vq$ and $Q \to Hq$ can be approximated as:

$$\Gamma(Q \to Vq) \approx \left(c_{L,V}^2 + c_{R,V}^2\right) \times \frac{g_w^2}{32\pi} \frac{p(M_Q, m_q, m_V)}{M_Q^2} \left(\frac{M_Q^2 + m_q^2}{2} + \frac{(M_Q^2 - m_q^2)^2}{2m_V^2} - m_V^2\right) \tag{4.6}$$

$$\Gamma(Q \to Hq) \approx \left(c_{L,H}^2 + c_{R,H}^2\right) \times \frac{1}{8\pi} \frac{p(M_Q, m_q, m_H)}{M_Q^2} \frac{M_Q^2 + m_q^2 - m_H^2}{2} \tag{4.7}$$

where g_w represents the electroweak coupling constant and,

$$p(X, y, z) = \frac{1}{2X}\sqrt{[X^2 - (y+z)^2][X^2 - (y-z)^2]}.$$

Since the decay width expressions only depend on the quadrature sum of the left and right handed couplings, we introduce a more convenient set of notations:

$$c_{W/Z/H}^2 = c_{L,W/Z/H}^2 + c_{R,W/Z/H}^2. \tag{4.8}$$

Defining $r_A = \frac{m_A}{M_Q}$, we introduce the following functions:

$$\begin{aligned}
\rho_W(Q) &= \sqrt{1 + r_W^4 + r_q^4 - 2r_W^2 - 2r_q^2 - 2r_W^2 r_q^2}(1 + r_W^2 - 2r_q^2 - 2r_W^4 + r_q^4 + r_W^2 r_q^2) \\
\rho_Z(Q) &= \sqrt{1 + r_Z^4 + r_q^4 - 2r_Z^2 - 2r_q^2 - 2r_Z^2 r_q^2}(1 + r_Z^2 - 2r_q^2 - 2r_Z^4 + r_q^4 + r_Z^2 r_q^2) \\
\rho_H(Q) &= \sqrt{1 + r_H^4 + r_q^4 - 2r_H^2 - 2r_q^2 - 2r_H^2 r_q^2}(1 + r_q^2 - r_H^2).
\end{aligned} \tag{4.9}$$

These functions evaluate to unity at leading order, i.e. $\rho_W \approx \rho_Z \approx \rho_H \approx 1.0$ because $r \ll 1$. They introduce some minor mass-dependent corrections that vanish for large values of M_Q. In order to simplify the expression of the branching ratios, we rescale the coupling parameters as follows:

$$\begin{aligned} c_W^2 &= c_{L,W}^2 + c_{R,W}^2 = \tilde{c}_W^2 \\ c_Z^2 &= c_{L,Z}^2 + c_{R,Z}^2 = \tilde{c}_Z^2 \frac{m_Z^2}{m_W^2} \\ c_H^2 &= c_{L,H}^2 + c_{R,H}^2 = \frac{g_w^2}{4} \tilde{c}_H^2 \frac{M_Q^2}{m_W^2}. \end{aligned} \tag{4.10}$$

Expressed in terms of the rescaled couplings and the $\rho_A(Q)$ functions, the decay widths become:

$$\Gamma(Q \to Aq) = \tilde{c}_A^2 \times \frac{g_w^2}{128\pi} \frac{M_Q^3}{m_W^2} \times \rho_A(Q). \tag{4.11}$$

Then, the equation for branching ratio reduces to:

$$\mathrm{BR}(Q \to Aq) = \frac{\tilde{c}_A^2 \rho_A(Q)}{\tilde{c}_W^2 \rho_W(Q) + \tilde{c}_Z^2 \rho_Z(Q) + \tilde{c}_H^2 \rho_H(Q)}. \tag{4.12}$$

Hence, the assumption in equation (4.5) allows the branching fractions to be independent of the chirality of the couplings. The same assumption makes the production cross-section of single VLQs independent of the choice of the chirality at leading order. For example, as argued by Matsedonsky et. al, [46] the production cross-section for Z and W boson mediated production modes under the narrow width approximation, are approximated as:

$$\begin{aligned} \sigma^{\mathrm{NW}}_{\mathrm{prod},\ VQ}(M_Q, \vec{c}) \approx & \left(c_V^2 + k \times c_{L,V} c_{R,V} \frac{m_q}{m_q + M_Q} \right) \\ & \times \sigma^{\mathrm{NW}}_{\mathrm{prod},\ VQ}(M_Q, c_V = 1) \end{aligned} \tag{4.13}$$

where k is a constant of $\mathcal{O}(1)$. Assuming $M_Q \gg m_q$ as in equation (4.5) suppresses the interfering term by $\mathcal{O}\left(\frac{m_q}{M_Q}\right)$. Furthermore, Aguilar-Saavedra et. al proved in [51] that independent of the representation, either of the chiral couplings is suppressed by an additional factor of $\mathcal{O}\left(\frac{m_q}{M_Q}\right)$ that emerges from the diagonalization of the mass matrix. As a result, the contribution of the interference term in equation (4.13) will be of subleading order and can be ignored. Based on similar arguments, it was also assumed in [47] that either of the chiralities dominates the model-independent representation of the VLQs. Many analsyes, in both ATLAS and CMS collaborations, have also reported that thier results are independent of the chiral structure of the couplings- the effect of different chiralities is indistinguishable within a coarse binning structure in the discriminant variables as well as the statistical and systematic uncertainties that dominate the limit setting. [71, 73, 74, 76, 77] Hence, we introduce our *third assumption*; an analysis is either insensitive to the relative structure of the chiral couplings or a single chirality dominates the signal kinematics. As a result, the statistical limits obtained from an analysis, σ_{lim}, now depends on M_Q and the chirality-ignorant rescaled couplings in equation (4.10), i.e. $\vec{c} = \{\tilde{c}_W, \tilde{c}_Z, \tilde{c}_H\}$.

The three assumptions made so far can be summarized as follows:

- *VLQs as Top- or Bottom-partners:* VLQs predominantly couple to the third generation SM quarks via exchange of W, Z and H bosons.
- *Heavy VLQs:* VLQs are much heavier than SM bosons and fermions.
- *Chirality-agnostic Analysis:* The search of single VLQ is either insensitive to relative chiral structure or dominated by a single chirality of the couplings.

Given the aforementioned set of assumptions, we can now derive the explicit expression for the inequality in (4.4). We can write the $VQAq$ process cross-section as a product of the production cross-section and the corresponding branching ratio for narrow widths:

$$\begin{aligned} \sigma_{VQAq}(M_Q, \vec{c}) \quad &\xrightarrow{\text{NWA}} \quad \sigma^{\text{NW}}_{\text{prod, }VQ}(M_Q, \vec{c}) \times \text{BR}(Q \to Aq) \\ &= \tilde{c}_V^2 \times \sigma^{\text{NW}}_{\text{prod, }VQ}(M_Q, \tilde{c}_V = 1) \times \text{BR}(Q \to Aq) \end{aligned} \tag{4.14}$$

where the branching ratio is given by equation (4.12). For larger widths, this estimate for the cross-section is corrected for the width dependence of the process cross-section. Following the recipe of [71, 72], we define the correction factor as:

$$\mathrm{P}_{\mathrm{NWA}}(M_Q, \vec{c}) = \frac{\sigma^{\mathrm{NW}}_{\mathrm{prod},\, VQ} \times \mathrm{BR}(Q \to Aq)}{\sigma_{VQAq}}. \tag{4.15}$$

Together with equations (4.14) and (4.15), the interpretation relation in equation (4.4) reduces to:

$$\frac{\tilde{c}_V^2 \times \sigma^{\mathrm{NW}}_{\mathrm{prod},\, VQ}\left(M_Q, \tilde{c}_V = 1\right) \times \mathrm{BR}(Q \to Aq)}{\mathrm{P}_{\mathrm{NWA}}(M_Q, \vec{c})} \geq \sigma_{\mathrm{lim},\, VQAq}\left(M_Q, \vec{c}\right). \tag{4.16}$$

4.3 Evaluation of $\mathbf{P_{NWA}}$

In the limit of narrow decay width, the Breit-Wigner distribution can be approximated as a delta function:

$$\frac{1}{(p^2 - M^2)^2 + \Gamma^2 M^2} \xrightarrow{\frac{\Gamma}{M} \to 0} \frac{\pi}{M\Gamma}\delta(p^2 - M^2). \tag{4.17}$$

For large widths, this approximation breaks down and the cross-section estimate accumulates corrections in higher order of $\frac{\Gamma}{M}$ [170, 171]. It is reasonable to assume that the correction factor for the cross-section will also depend only on the values of Γ_Q and M_Q and not on the individual choices for the couplings. As a result, the analytic expression for the correction factor takes the following form:

$$\mathrm{P}_{\mathrm{NWA}}(M_Q, \vec{c}) \equiv \mathrm{P}_{\mathrm{NWA}}\left(\frac{\Gamma_Q}{M_Q}\right) \approx 1 + \sum_n A_n \left(\frac{\Gamma_Q}{M_Q}\right)^n \tag{4.18}$$

where the values A_n will depend on the choice of the VLQ mass and the process of interest.

The traditional parameterization of the VLQ Lagrangian, as given in equation (1.3) and its equivalent formulations, allow signal event generation by fixing the coupling parameters while the partial decay widths can be calculated from equation (4.11). Therefore, using the VLQ Universal FeynRules Output (UFO) model [128] inspired by the parameterization

Process	Coupling Choice
$WTWb, WTZt, ZTWb,$ $WBWt, WBZb, ZBWt$	$\tilde{c}_W, \tilde{c}_Z \in C$ $\tilde{c}_H = 0$ or, $\tilde{c}_H = \tilde{c}_Z$
$WTHt,$ $WBHb$	$\tilde{c}_W, \tilde{c}_H \in C$ $\tilde{c}_Z = 0$ or, $\tilde{c}_Z = \tilde{c}_H$
$ZTZt, ZTHt,$ $ZBZb, ZBHb$	$\tilde{c}_Z, \tilde{c}_H \in C$ $\tilde{c}_W = 0$ or, $\tilde{c}_W = \tilde{c}_H$

Table 4.1: The choice of couplings for event generation and cross-section calculation in MadGraph

presented in Ref. [48], single production of top and bottom partners for both W and Z boson mediated single-T and single-B processes for M_Q in the range of 1000–2200 GeV in steps of 200 GeV was simulated in MadGraph. The actual choice of coupling values in relation to the representative set of couplings $C = \{0.05, 0.2, 0.4, 0.6, 0.8, 1.0\}$ is summarized in Table 4.1. We additionally required that $\frac{\Gamma_Q}{M_Q} < 0.5$ for any choice of couplings and disregard any coupling combination that violates this constraint. The $\kappa, \hat{\kappa}, \breve{\kappa}$ parameters introduced in [48] can be calculated from the rescaled couplings from a one-to-one correspondence with the tree-level couplings in equation (1.3).

We calculated the narrow-width and large-width cross section at leading order (LO) for all the processes mentioned in Table 4.1. Using equation (4.15), we evaluated the correction factor for each choice of coupling and mass.

Figures 4.2 and 4.3, respectively show the variation in P_{NWA} as a function of $\frac{\Gamma}{M}$ for the $WTZt$ and $WTHt$ processes. Confirming the initial assumption, there is no strong dependence on the choice of couplings. For example, as can be seen from Figure 4.2, for a given value of $\frac{\Gamma_Q}{M_Q}$, the correction factor calculated for $\tilde{c}_H = 0$ is almost identical to the one calculated for $\tilde{c}_H = \tilde{c}_Z$.

We also observe in Figure 4.2 that P_{NWA} monotonically rises from unity in the case of $WTZt$ processes. The differential cross-section distributions for $WTZt$ processes of a 1.6 TeV Top partner for different choices of the VLQ couplings are shown in Figure 4.4. Accounting for increased width causes a decrease in total cross-section because as the VLQ

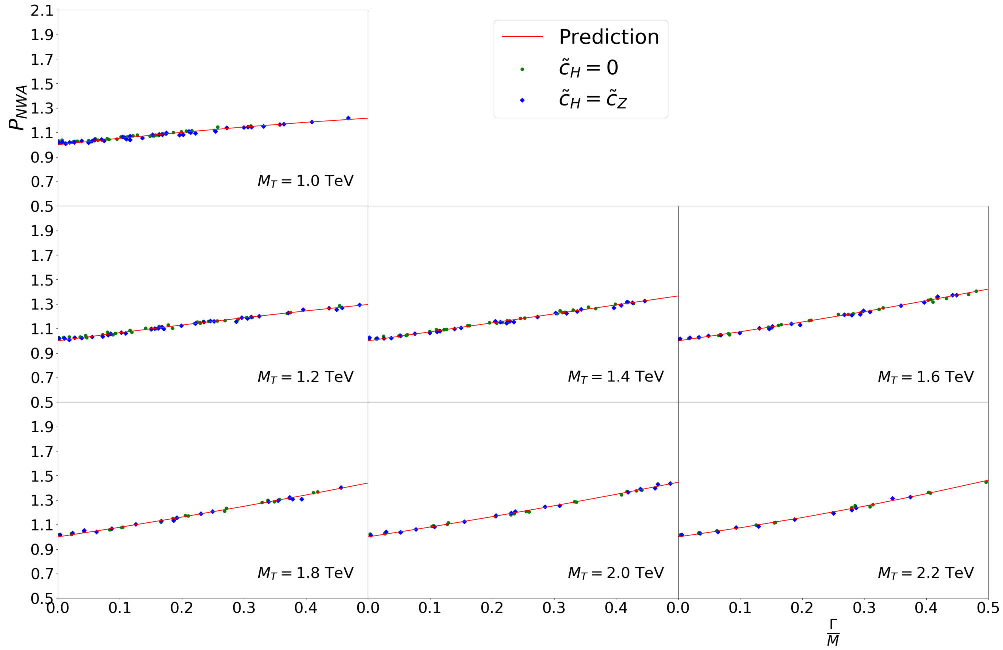

Figure 4.2: Estimated values of $\mathrm{P_{NWA}}$ plotted as a function of $\frac{\Gamma}{M}$ for different values of M_T for the $WTZt$ process. The red line shows the best fitted polynomial estimate for the correction factor.

kinematics reach a phase space away from the pole mass, the matrix element receives a compensating contribution from the VLQ propagator. The functional behavior of $\mathrm{P_{NWA}}$ is well approximated by a quadratic polynomial for processes that incorporate a decay to the vector bosons.

$$\mathrm{P}_{\mathrm{NWA},VQVq}\left(\frac{\Gamma_Q}{M_Q}\right) = 1 + A_1\frac{\Gamma_Q}{M_Q} + A_2\left(\frac{\Gamma_Q}{M_Q}\right)^2 \tag{4.19}$$

The A_1 and A_2 parameters in equation (4.19) for different processes with Top and Bottom partners decaying to vector bosons are evaluated by obtaining the least squared error fit to the observed values of the correction factor from simulation and are tabulated in Tables 4.2 and 4.3, respectively.

On the other hand, as can be seen in Figure 4.3, $\mathrm{P_{NWA}}$ becomes slightly higher than unity in the small but finite $\frac{\Gamma}{M}$ region before it starts to decrease. The differential cross-section distributions for $WTHt$ processes of a 1.6 TeV Top partner for different choices of the VLQ couplings are shown in Figure 4.5. At very low decay widths, the finite width

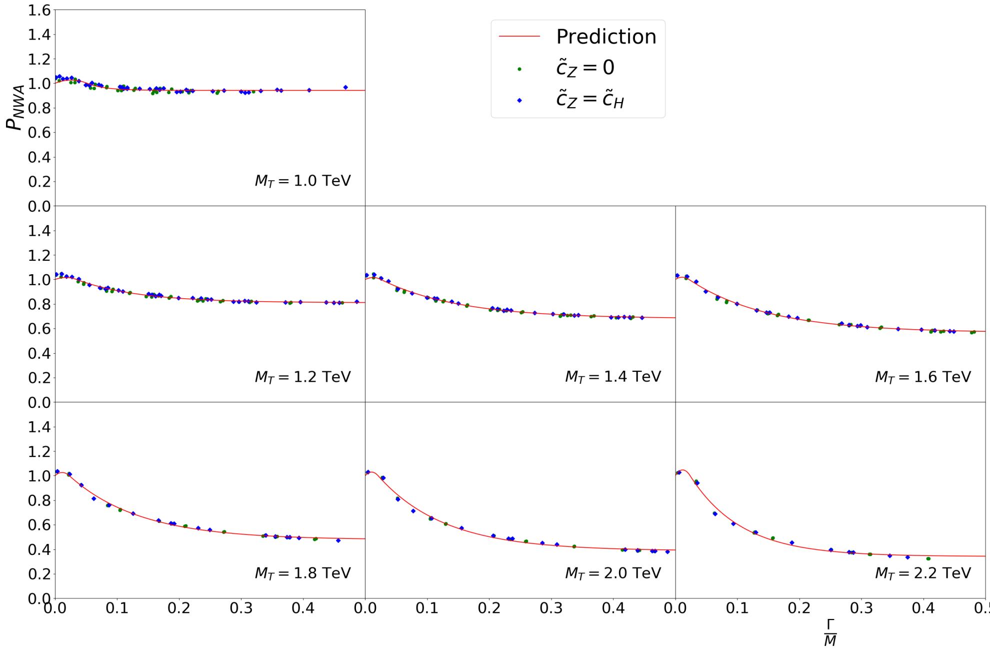

Figure 4.3: Estimated values of $\mathrm{P_{NWA}}$ plotted as a function of $\frac{\Gamma}{M}$ for different values of M_T for the $WTHt$ process. The red line shows the best fitted estimate of an exponential function for the correction factor.

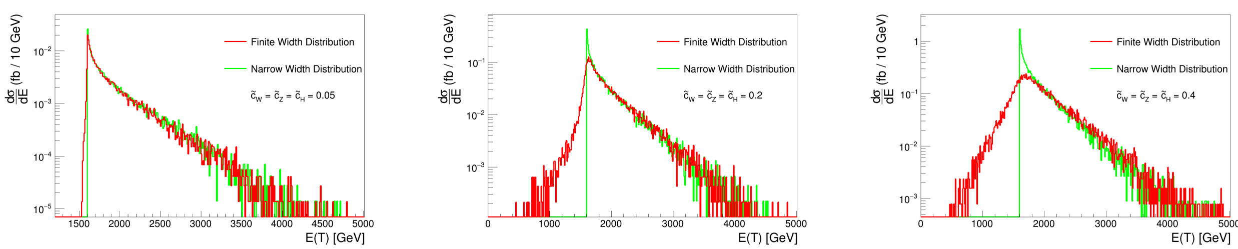

(a) (b) (c)

Figure 4.4: Distribution of differential cross-section in $E(T)$ of singly produced Top partner (T) of mass $M_T = 1.6$ TeV at narrow-width and finite-width for the $WTZt$ process. The coupling values $\tilde{c}_W$ is set 0.05, 0.20, and 0.40 respectively in (a), (b), and (c). All distributions assume $\tilde{c}_W = \tilde{c}_Z = \tilde{c}_H$.

cross-section of $WTHt$ processes is slightly smaller than what is predicted by NWA because of widening of the Breit-Wigner propagator, resulting in $\mathrm{P_{NWA}} > 1$. However, the VLQ energy distribution for a $WTHt$ process receives an enhancement at lower energies for larger decay widths. This can cause the finite width cross-section for $WTHt$ processes to be higher than what NWA predicts, resulting in $\mathrm{P_{NWA}} < 1$.

	$WTWb$		$WTZt$		$ZTWb$		$ZTZt$	
M_T (TeV)	A_1	A_2	A_1	A_2	A_1	A_2	A_1	A_2
1.0	0.526	-0.123	0.557	-0.247	0.507	-0.272	0.374	0.013
1.2	0.638	-0.048	0.681	-0.176	0.639	-0.126	0.550	0.035
1.4	0.708	0.054	0.733	-0.001	0.737	-0.046	0.664	0.087
1.6	0.697	0.171	0.715	0.257	0.757	0.141	0.730	0.166
1.8	0.784	0.153	0.759	0.240	0.807	0.160	0.746	0.312
2.0	0.764	0.235	0.777	0.227	0.820	0.195	0.786	0.275
2.2	0.720	0.346	0.696	0.456	0.754	0.356	0.709	0.477

Table 4.2: The best fit values for the parametric representation of $\mathrm{P}_{\mathrm{NWA}}$ in equation (4.19) for different values of M_T.

	$WBWt$		$WBZb$		$ZBWt$		$ZBZb$	
M_T (TeV)	A_1	A_2	A_1	A_2	A_1	A_2	A_1	A_2
1.0	0.506	-0.333	0.506	-0.280	0.548	-0.250	0.409	0.133
1.2	0.652	-0.178	0.646	-0.159	0.653	-0.111	0.542	0.105
1.4	0.741	-0.046	0.721	-0.015	0.727	-0.009	0.625	0.166
1.6	0.776	0.116	0.759	0.133	0.761	0.108	0.677	0.210
1.8	0.807	0.195	0.796	0.189	0.760	0.222	0.673	0.351
2.0	0.831	0.203	0.806	0.235	0.768	0.242	0.711	0.300
2.2	0.781	0.345	0.757	0.346	0.720	0.362	0.648	0.442

Table 4.3: The best fit values for the parametric representation of $\mathrm{P}_{\mathrm{NWA}}$ in equation (4.19) for different values of M_B.

The functional behavior of $\mathrm{P}_{\mathrm{NWA}}$ can be approximated by a piece-wise function of the form in equation (4.20).

$$\mathrm{P}_{\mathrm{NWA},VQHq}\left(\frac{\Gamma_Q}{M_Q}\right) = \begin{cases} 1 + AB\frac{\Gamma_Q}{M_Q} - \left(\frac{AB}{x_0}\right)\left(\frac{\Gamma_Q}{M_Q}\right)^2, & \frac{\Gamma_Q}{M_Q} < x_0 \\ 1 - A\left(1 - \exp\left(-B\left(\frac{\Gamma_Q}{M_Q} - x_0\right)\right)\right), & \frac{\Gamma_Q}{M_Q} \geq x_0 \end{cases}. \tag{4.20}$$

The two parts of the function are so chosen that $\mathrm{P}_{\mathrm{NWA}}(x_0) = 1$ and both functions and their derivatives are continuous at the joining point x_0. The values of A, B, and x_0 parameters for different processes with Top and Bottom partners decaying to the Higgs boson, subject to the constraints $B > 0$ and $0 < x_0 \leq 0.1$, are obtained by a least squared error fit to the observed values of the correction factor from simulation and and tabulated in Table 4.4.

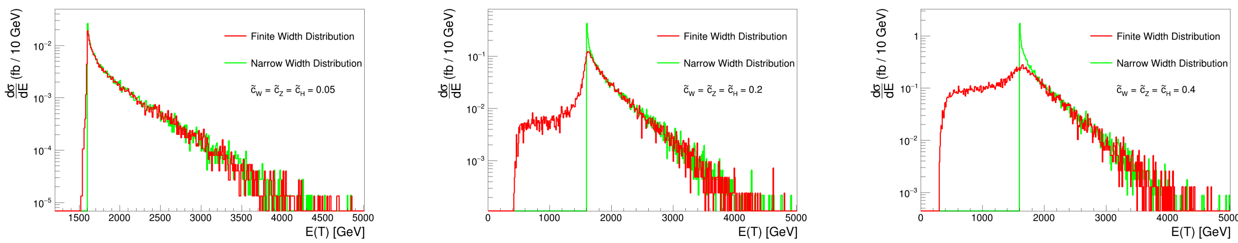

(a) (b) (c)

Figure 4.5: Distribution of differential cross-section in $E(T)$ of singly produced Top partner (T) of mass $M_T = 1.6$ TeV at narrow-width and finite-width for the $WTHt$ process. The coupling values $\tilde{c}_W$ is set 0.05, 0.20, and 0.40 respectively in (a), (b), and (c). All distributions assume $\tilde{c}_W = \tilde{c}_Z = \tilde{c}_H$.

	$WTHt$			$ZTHt$			$WBHb$			$ZBHb$		
M_T (TeV)	A	B	x_0	A	B	x_0	A	B	x_0	A	B	x_0
1.0	0.057	35.032	0.052	~ 0	~ 0	N/A	0.031	96.784	0.055	0.162	10.297	0.042
1.2	0.189	10.005	0.035	0.078	20.616	0.047	0.141	11.510	0.042	0.296	7.985	0.031
1.4	0.319	7.923	0.026	0.199	9.290	0.030	0.264	8.116	0.030	0.412	7.673	0.026
1.6	0.433	7.801	0.022	0.321	7.936	0.026	0.379	7.633	0.025	0.514	7.990	0.022
1.8	0.522	8.771	0.023	0.428	8.072	0.023	0.476	8.204	0.023	0.588	9.407	0.023
2.0	0.613	9.329	0.021	0.526	8.456	0.021	0.568	8.773	0.023	0.668	10.275	0.023
2.2	0.658	12.082	0.024	0.601	9.896	0.022	0.633	10.563	0.023	0.705	13.737	0.025

Table 4.4: The best fit values for the parametric representation of $\mathrm{P_{NWA}}$ in equation (4.20) for different values of $M_{T/B}$. $\mathrm{P}_{\mathrm{NWA},ZTHt} \approx 1.0$ for all $\frac{\Gamma}{M}$ at $M_T = 1.0$ TeV

4.4 Reinterpretation of Limits from Existing Analyses

The proposed interpretation strategy in equation (4.16) allows a more comprehensive representation of the search results that are currently ongoing in the ATLAS and CMS experiments. In order to illustrate the flexibility this interpretation strategy offers, we take the ATLAS analysis in Ref. [71] and the CMS analysis in Ref. [74] as examples. Both analyses target the search for singly produced top partners ($T_{+\frac{2}{3}}$) that eventually decay to a Z boson, decaying into a pair of electrons or muons, and a top quark. The ATLAS search focuses on two orthogonal analysis channels- the boosted dilepton channel and the trilepton channel described in Chapter 3. This analysis performs a statistical combination of the two channels and the ATLAS collaboration reports the exclusion limit on the $WTZt$ process cross-section for masses in the range of 0.7–2.0 TeV and coupling values, κ, between 0.1–1.6 following the parameterization prescribed in [47]. The aforementioned analysis has been stored as a entry in the HEPData [172] repository. The exclusion limits on the $WTZt$ process cross-section, as a function of M_T and κ are available in this HEPData entry [173]. On the other hand, the CMS analysis introduces a ten-category search strategy, based on the combination of lepton flavor from the Z boson decay and the resolution of the t quark decay products. In addition to calculating statistical limits on the $WTZt$ process cross-section under the NWA, assuming a coupling $c_W = 0.5$ and $\text{BR}(T \to Wb) = 0.5$, $\text{BR}(T \to Zt) = \text{BR}(T \to Ht) = 0.25$ for 0.7 TeV $\leq M_T \leq 1.7$ TeV, the CMS collaboration also report finite-width cross-section limits for $\frac{\Gamma_T}{M_T} = 10\%, 20\%,$ and 30% and 0.8 TeV $\leq M_T \leq 1.6$ TeV. However, instead of probing the variation of the analysis results in the coupling space, they report their exclusion limit, σ_{lim} as a function of relative decay width $\frac{\Gamma_T}{M_T}$ and the top partner mass, M_T.

Both of these analyses have reported their limits to be chirality-agnostic, only depending on the effective coupling strength of the VLQ couplings and not their chiral structure. The smallest VLQ mass considered in these analyses is 700 GeV, which is large enough that the approximations made in Section 4.2 can be applied. For instance, the relative contribution in decay width $\Gamma(T \to Zt)$ by the interference term between left and right chiral couplings is $6 \times \frac{\tilde{c}_{L,Z}\tilde{c}_{R,Z}}{\tilde{c}^2_{L,Z}+\tilde{c}^2_{R,Z}} \times \left(\frac{m_Z}{M_T}\right)^2 \frac{m_t}{M_T}$ [46], which evaluates to a maximum value of 0.013 at $M_T = 700$ GeV. This suggests that the assumptions made in Section 4.2 apply to both of the analyses reported in Refs. [71, 74] and we can apply the proposed semi-analytical framework to reinterpret their results.

Figure 4.6a gives a generalized representation of the limits reported in the CMS analysis [74]. To ensure a simplified visualization, we have set $\tilde{c}_H = \tilde{c}_Z$ which allows $\text{BR}(T \to Zt) \approx \text{BR}(T \to Ht)$ in the large mass limit. This assumption is well-motivated in light of the Goldstone Equivalence Theorem [174]; in the large-M_Q-limit, the longitudinal polarization dominates the Z-boson-mediated decay of the top partner which is related to the Higgs mode by a hypercharge rotation, independent of the $SU(2)$ representation of the VLQs [51, 175]. As a result, the Z and H boson decay vertices receive similar coupling strengths and the partial decay widths become similar, resulting in almost equal branching ratios independently of

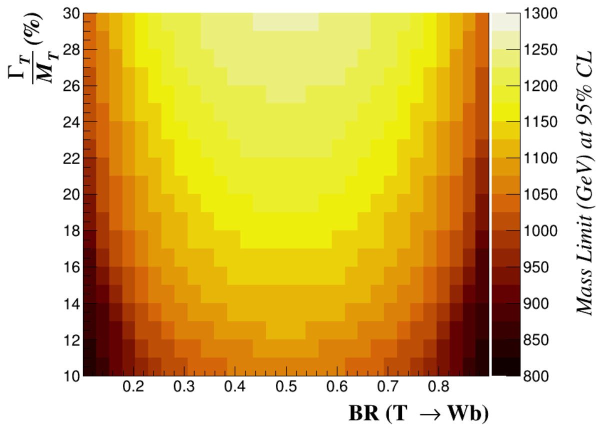

(a)

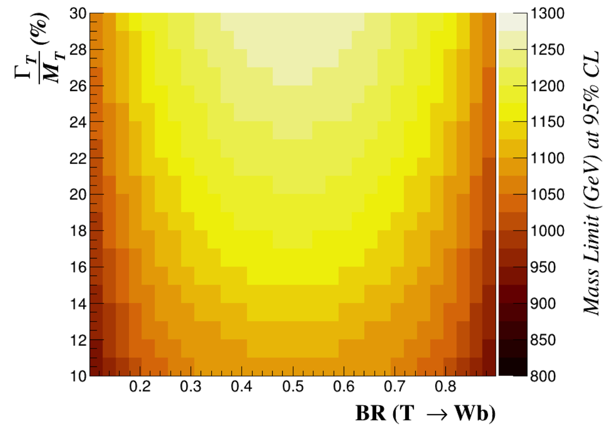

(b)

Figure 4.6: Representation of the exclusion limits on VLQ mass in the $\frac{\Gamma_T}{M_T} - \mathrm{BR}(T \to Wb)$ plane. This representation makes the assumption $\tilde{c}_Z = \tilde{c}_H$, deeming the branching ratios in the H and Z channels being equal in the large M_T limit. The limits reported in the CMS analysis [74] are shown in (a) and the limits obtained in the ATLAS analysis [71] are represented in (b).

the group representation. An equivalent representation of the limits reported by the ATLAS analysis [71] is given in Figure 4.6b.

However, it should be emphasized that the assumption of $\tilde{c}_H = \tilde{c}_Z$, albeit well motivated, is only necessary for the purpose of a convenient representation. We can perform a four-dimensional interpretation by allowing a generalized strategy of parametric reduction. We introduce the f parameter:

$$f = \frac{\tilde{c}_H}{\tilde{c}_Z} \tag{4.21}$$

which defines a plane of projection in the four-dimensional hyperspace of (4.16). This parameterization expresses the branching ratios as a function of $\frac{\tilde{c}_Z}{\tilde{c}_W}$ in the large-M_Q-limit.

$$\begin{aligned}
\mathrm{BR}(T \to Wb) &\approx \frac{1}{1+(1+f^2)\frac{\tilde{c}_Z^2}{\tilde{c}_W^2}} \\
\mathrm{BR}(T \to Zt) &\approx \frac{1-\mathrm{BR}(T \to Wb)}{1+f^2} \\
\mathrm{BR}(T \to Ht) &\approx f^2 \times \mathrm{BR}(T \to Zt)
\end{aligned} \tag{4.22}$$

For a given choice of f, the contours for constant branching ratios are represented by vertical straight lines in the $\frac{\Gamma_T}{M_T}$–BR($T \to Wb$) plane. At large M_Q limit, the branching ratios often become independent of the VLQ mass as well as the couplings for certain group representations [47, 51]. Hence, the f-factor-based reduction strategy makes it trivial to evaluate the sensitivity of an analysis in model-specific contexts.

Evidently, the representation of VLQ mass limits as a function of c_W and c_Z in the limit of $\mathrm{BR}(T \to Zt) \approx \mathrm{BR}(T \to Ht)$ proposed in [71] corresponds to the special case of $f = 1$. However, the proposed framework in equation (4.16) can accommodate other choices of f to probe the exclusion limits on alternate projections of the parametric hyperspace. We illustrate this in Figure 4.7 where we numerically re-interpret the limits reported by the ATLAS analysis [71] for alternate choices of f. In Figure 4.7a, we choose $f = 0$ which eventually implies that $\mathrm{BR}(T \to Ht) = 0$. On the other hand, $f = \sqrt{2} \Rightarrow \mathrm{BR}(T \to Ht) \approx 2 \times \mathrm{BR}(T \to Zt)$ is chosen for the re-interpretation in Figure 4.7b. For a given choice of f, the contours of constant branching fractions are given by straight lines passing through the origin in these plots. As expected, the analysis is sensitive to relatively lower top-partner masses for higher values of f.

We now demonstrate how the proposed interpretation strategy can be used to correlate the different strategies used by the aforementioned analyses and hence compare their results. The CMS analysis [74] adapted the interpretation proposed by Carvalho et. al [176]. If a particular analysis is mostly sensitive to a certain decay channel of the VLQ and relatively insensitive to other decay channels, the excluded cross-section, σ_{lim} in equation (4.16), becomes a function of the total VLQ decay width and not the individual choices of the

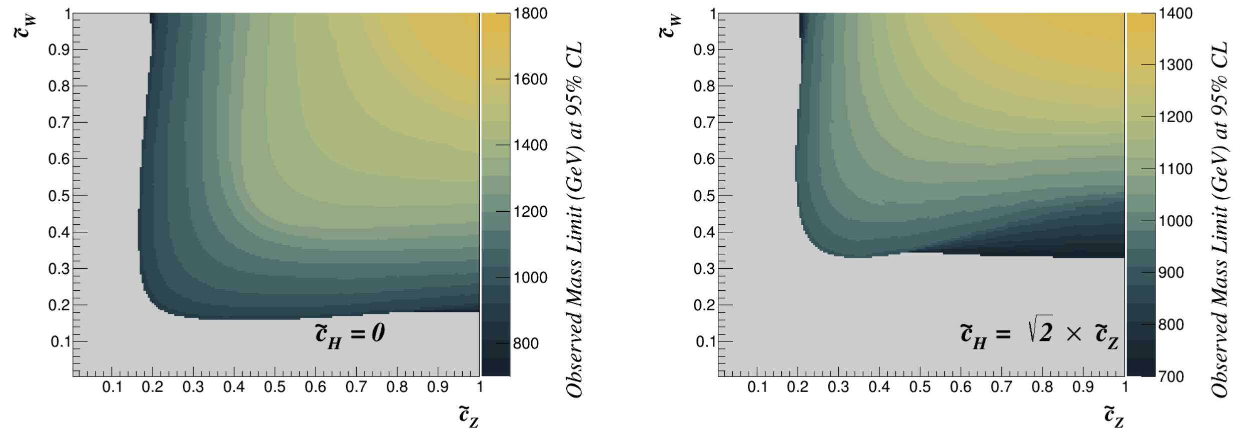

(a) (b)

Figure 4.7: Reinterpretation of observed limits on top partner mass from Ref. [71], plotted as a function of $\tilde{c}_W$ and $\tilde{c}_Z$ for (a) $f = 0$ and (b) $f = \sqrt{2}$. The grey regions enclose a parametric space not covered within the sensitivity of the analysis.

couplings. This is because the change in branching ratio for an alternate choice of couplings that produce the same decay width merely applies as a variation in normalization of the signal hypothesis and hence, is not reflected in the calculation of the exclusion limits for the process cross-section. Hence, the excluded cross-sections themselves can be represented as a function of M_Q and $\frac{\Gamma_Q}{M_Q}$. The exclusion region can be identified by comparing the exclusion limits with the process cross-section which, according to the authors in [176], can be expressed with factorized couplings as given by the following equation:

$$\sigma_{VQAq}(M_Q, \vec{c}) = C^2_{\text{prod}} C^2_{\text{dec}} \times \hat{\sigma}_{VQAq}(M_Q, \Gamma_Q) \tag{4.23}$$

where C_{prod} and C_{dec} are the couplings associated with the production and decay vertices of the singly-produced VLQs and $\hat{\sigma}$ represents a *reduced cross-section*, that only depends on the choice of VLQ mass and the total decay width. Using the parameterization proposed in sections 4.2 and 4.3, we can express the so-called reduced cross-section $\hat{\sigma}$ in terms of P_{NWA}

and $\sigma^{\text{NW}}_{\text{prod, }WT}$ for the $WTZt$ process considered in the analyses by the equation:

$$\hat{\sigma}_{WTZt}(M_T, \Gamma_T) \approx \frac{M_T^2 \rho_Z(T)}{8\pi g^2 m_Z^2} \times \frac{\sigma^{\text{NW}}_{\text{prod, }WT}(M_T, \tilde{c}_W = 1)}{\frac{\Gamma_T}{M_T} + A_1 \frac{\Gamma_T^2}{M_T^2} + A_2 \frac{\Gamma_T^3}{M_T^3}}. \tag{4.24}$$

M_T (TeV)	$\frac{\Gamma_T}{M_T}$ (%)	$\hat{\sigma}$ [pb] from (4.24)	$\hat{\sigma}$ [pb] from [74]
1.0	10	192	183
	20	92	87
	30	59	55
1.2	10	141	145
	20	67	68
	30	42	43
1.4	10	107	112
	20	50	52
	30	31	33
1.6	10	80	85
	20	37	39
	30	23	29

Table 4.5: Comparison of reduced cross-section values calculated from equation (4.24) with the values reported in Ref. [74]. The values show good agreement, the difference being at most of $\mathcal{O}(10\%)$ for most cases.

As shown in Table 4.5, equation (4.24) can faithfully predict the reduced cross-section that lies at the heart of the interpretation strategy proposed in [176]. This allows us to recast the limits reported in the CMS analysis [74] as exclusion limits on top-partner mass as a function of the rescaled couplings (Figure 4.8a).

As a final example of the flexibility the proposed interpretation strategy offers, we recast the limits from the ATLAS analysis [71] as a function of relative decay width, $\frac{\Gamma_T}{M_T}$, and the top partner mass M_T in figure (4.8b). In such representations, however, the excluded region in the parametric hyperspace depends on the choice of the branching ratios.

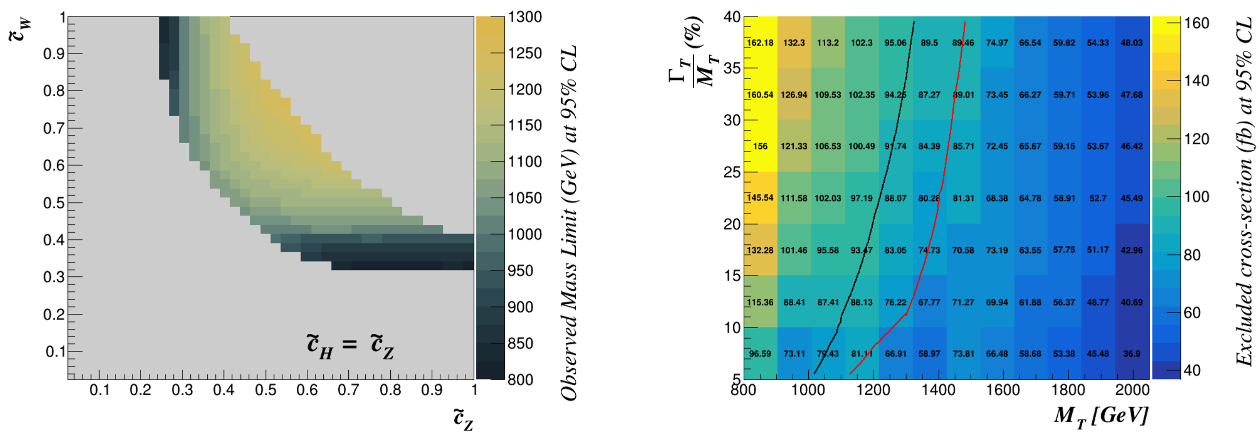

(a) (b)

Figure 4.8: (a) Representation of the exclusion limits on VLQ mass from the CMS analysis [74] in the $\tilde{c}_W$–$\tilde{c}_Z$ plane. This representation makes an assumption $f = 1$. The grey regions enclose a parametric space not covered within the sensitivity of the analysis. (b) Representation of exclusion limits from the ATLAS analysis [71] in the $\frac{\Gamma_T}{M_T}$–M_T plane. The overlaid black line represents the exclusion limit for the branching fractions to the W, Z, and H boson decay channels set to 0.5, 0.25, and 0.25, respectively. The overlaid red line corresponds to the exclusion limit for branching fractions set to 0.5, 0.5, and 0, respectively. In both cases, the region to the left of the exclusion line is excluded.

Chapter 5

Single-VLQ Signal Modeling for Comprehensive Search and Interpretation

As it has been pointed out in Chapter 4, both the kinematics and cross-section of singly produced VLQ processes depend on the choice of couplings, which in turn affects the sensitivity of an analysis and also the calculation of expected and observed limits. However, to address the impact of coupling variation on signal kinematics, we need signal samples with a comprehensive coverage in coupling grid. Generating such a fine grid of samples can be computationally very challenging. Additionally, given that the next round of single VLQ searches will utilize the entire 139fb^{-1}of ATLAS Run 2 dataset, subdominant diagrams that were previously ignored can make important contribution in certain corners of the parametric hyperspace. In this chapter, I look into the deeper issues about single-VLQ signal modeling in general (with particular examples from $WTZt$ and $ZTZt$ processes) and explore potential solutions to these issues that would be consequential in the broad spectrum of VLQ analyses within ATLAS.

5.1 Modified MadGraph Reweighting for Signal Generation

There are two non-trivial effects that determine the sensitivity of the single VLQ analyses as the coupling value is changed for a given mass. First, the process cross-section becomes a function of the decay width of the top partner since narrow width approximation starts to break down at higher couplings. Second, the change in decay width alters the phase space sensitivity of an analysis by modifying the shape of the final discriminant as the couplings are changed. Hence, the procedure of statistical fitting as well as the corresponding exclusion limits depends on the choice of couplings (and of course, the VLQ mass). This requires utilizing a signal grid that has a large coverage of VLQ masses and couplings. Generation and simulation of such a large number of MC signal points is computationally very expensive. Additional challenges arise in competitive memory requirements in the effort to store, manage, and analyze these MC datasets. In order to accommodate the full spectrum of mass-coupling variation of the parameter space of the Top Partner while circumventing issues related to computational and memory costs, our MC samples for the signal have made use of MadGraph-provided Reweighting module [177]. At Leading Order (LO), as in the case of our signal MC, the reweighting procedure re-evaluates the square matrix elements of the process of interest for an alternate set of values of the model parameters and introduces a multiplicliative weight factor for each event.

$$w^{\text{new}} = \frac{|\mathcal{M}^{\text{new}}|^2}{|\mathcal{M}^{\text{old}}|^2} w^{\text{old}} \tag{5.1}$$

Being analytically exact at LO, this procedure allows us to correctly replicate the shape distributions of the process for alternate mass and coupling hypotheses.

There are a number of important considerations while applying the reweighting procedure to obtain kinematic distributions for a modified set of parameters. Sufficiently large number of events needs to be generated for the original set of parameters. Also, the target phase space needs to be covered well by the original set of events. However, due to the choice of top partner mass and couplings, the original set of events may be sensitive to a significantly different phase space. For these reasons, it is always preferred to take a distribution with a larger width (i.e. higher coupling value or higher mass) as the benchmark coupling. Figures 5.1a, 5.1b, and 5.1c compare nominally simulated distributions for $M_T = 1100$ GeV and $\kappa = 0.5$ with distributions for the same parameters reweighted from event simulation obtained at $M_T = 1100$GeV for $\kappa = 0.3$, $\kappa = 0.7$, and $\kappa = 1.0$ respectively. It shows that how well matrix-element reweighting can reproduce kinematic distributions for different choices of benchmark couplings. Comparison of distributions reweighted from the three choices of κ shows that the tails are better modeled with smaller statistical fluctuations when distribu-

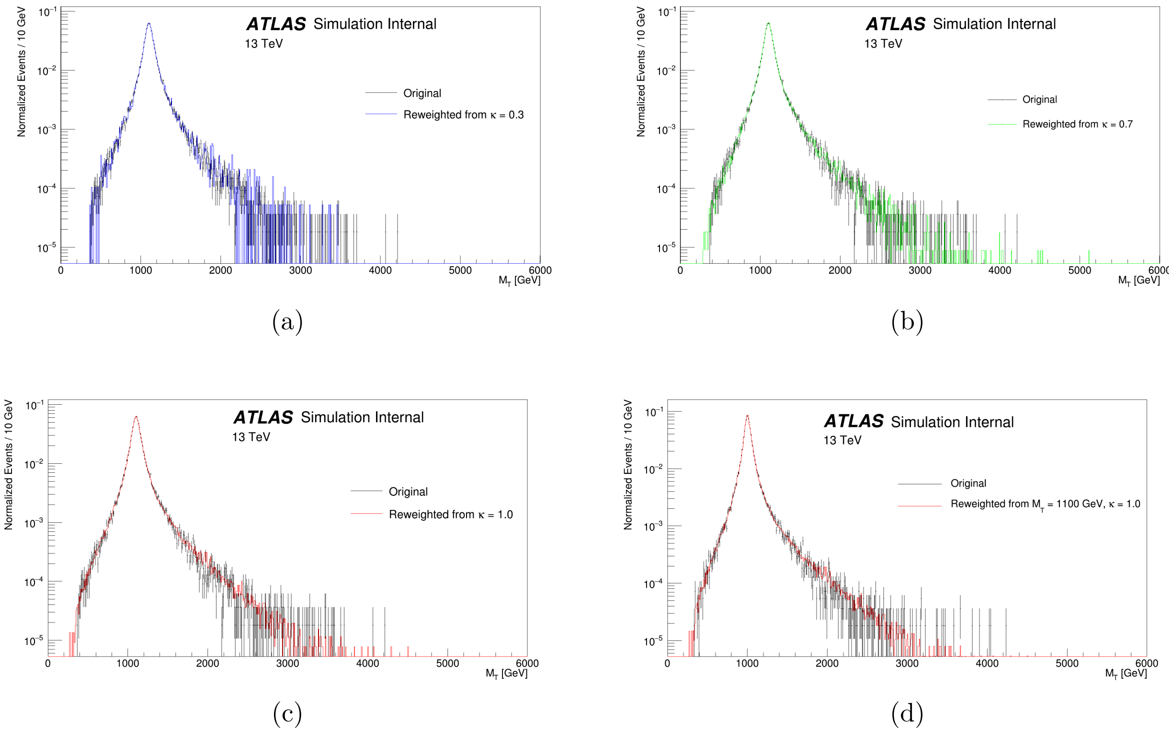

Figure 5.1: Comparison between original and reweighted distribution of Top Partner invariant mass for $M_T = 1100$ GeV (for (a), (b), (c)) and $M_T = 1000$ GeV (for (d)) for coupling of $\kappa = 0.5$. The reweighted distributions for $M_T = 1100$ GeV are obtained by reweighting events generated with the same Top Partner mass for couplings (a) $\kappa = 0.3$, (b) $\kappa = 0.7$, and (c) $\kappa = 1.0$. The reweighted distributions for $M_T = 1000$ GeV in (d) is obtained by reweighting events generated with Top Partner mass of $M_T = 1100$ GeV with a coupling of $\kappa = 1.0$

tions are reweighted from larger coupling thanks to a larger set of events that populate the tails to begin with.

The reweighting procedure can also be extended to reweighting in VLQ mass as well. Given that reweighting procedure performs better when the initial distribution is wider, it is preferred to reweight down in mass instead of going up since $\Gamma_T \propto \kappa^2 M_T^3$. Figure 5.1d shows the performance of reweighting simultaneously in mass and coupling by comparing the nominally simulated distributions for $M_T = 1000$GeV and $\kappa = 0.5$ with distributions for the same parameters reweighted from event simulation obtained at $M_T = 1100$GeV for $\kappa_T = 1.0$. Comparing the reweighted distributions with the original distributions, obtained from events actually generated with the relevant VLQ mass and couplings, it can be concluded that the reweighted events can faithfully reproduce the truth level distributions for a different choice of the mass and/or coupling parameters.

However, there's a major hurdle to implement the reweighting- the currently available reweighting module does not work in presence of the full decay chain of the top partner. This means, we can successfully implement reweighting for the process where the Top Partner is decayed to a Z boson and a t quark, but the Z and t are left undecayed in MadGraph syntax. The corresponding Feynman diagram for this process, which will be called `PROC-PARTDECAY` is given in Figure 5.2a.

On the other hand, when the decay chains of the Z boson and the top quark are added to the process description, which will be referred to as `PROC-FULLDECAY`, MadGraph reweighting does not directly work because of technical limitations in its implementation. The Feynan diagram in Figure 5.2b shows the extension of the diagram in Figure 5.2a where the decay chain of the Z boson and the t quark are included.

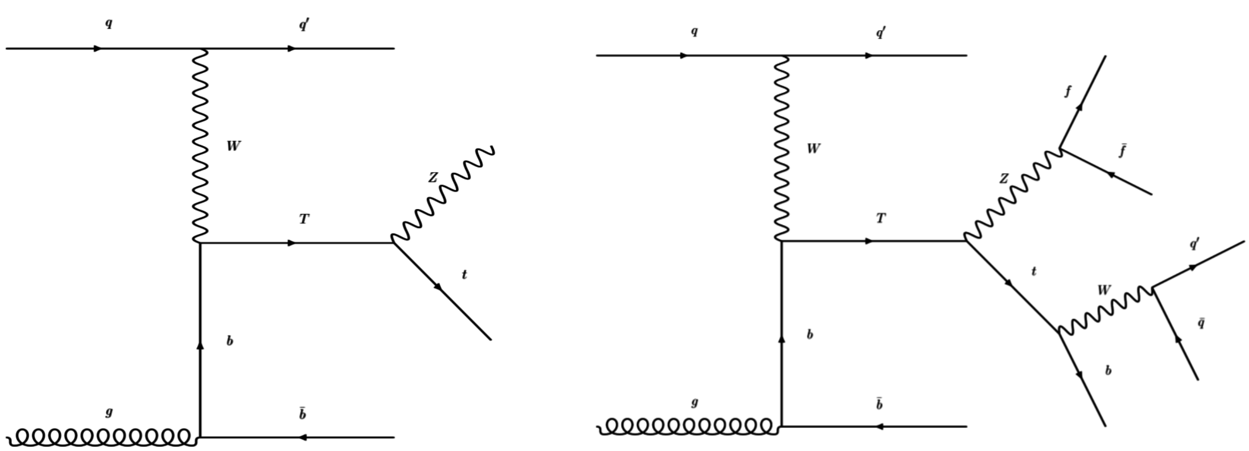

(a) (b)

Figure 5.2: Feynman diagrams corresponding to $WTZt$ process when the decay of the Z boson and top quark are (a) excluded from the process description (`PROC-PARTDECAY`), (b) included in the process description (`PROC-PARTDECAY`)

Between these two processes, `PROC-FULLDECAY` is the preferred way of generating events in MadGraph, since it preserves the complete spin correlations between the final state particles. If the heavy particles are left undecayed in MadGraph, the showering program Pythia incorporates their decays prior to showering. But this causes the spin correlations to be lost. Losing the spin correlations can significantly alter the momentum spectrum of final state particles, especially leptons. Figure 5.3 compares the kinematic distribution of electrons, muons, and partonic jets as obtained from decay of W and Z bosons in MadGraph against decays performed in Pythia. The stark disagreement between the kinematic distributions obtained from Pythia and MadGraph suggests that distributions obtained from decaying heavy bosons in Pythia can be unreliable.

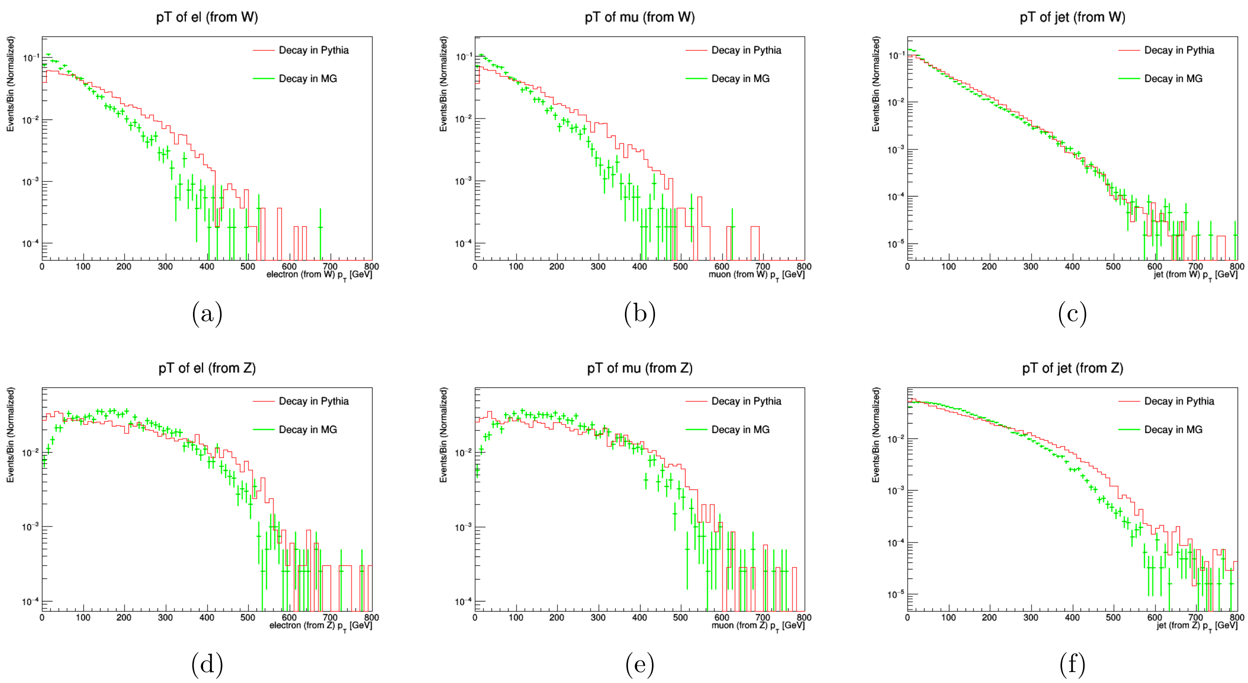

(a) (b) (c)

(d) (e) (f)

Figure 5.3: Comparison between transverse momenta of electrons (left), muons (middle), and jets (right) obtained from decay products of W (top) and Z (bottom) bosons when the heavy bosons are decayed in Pythia against decays performed in MadGraph.

In order to circumvent this issue, an alternate strategy has been developed. It can be noted that the parameters responsible for calculating the reweighting factor in Eqn. 5.1 enter the first part of `PROC-FULLDECAY` where T is decayed to a Z boson and a top quark. The decays of Z boson and t quark are SM processes with no dependence on the parameters of the VLQ Lagrangian. Additionally, both Z boson and top quarks are narrow resonances with $\frac{\Gamma}{M} = 2.73\%$ and 0.77% respectively [1]. Under narrow width approximation, the matrix element for `PROC-FULLDECAY` can be factorized as

$$\mathcal{M}_{\texttt{PROC-FULLDECAY}} \xrightarrow{\text{NWA}} \mathcal{M}_{pp\to T\to Zt} \times \mathcal{M}_{Z\to f\bar{f}} \times \mathcal{M}_{t\to f'\bar{f}b}$$
$$= \mathcal{M}_{\texttt{PROC-PARTDECAY}} \times \mathcal{M}_{Z\to f\bar{f}} \times \mathcal{M}_{t\to f'\bar{f}b} \tag{5.2}$$

Using the approximation from Eq. 5.2, the new event weight from Eq. 5.1 can be calculated as

$$w^{\text{new}}_{\texttt{PROC-FULLDECAY}} \approx \frac{|\mathcal{M}^{\text{new}}_{\texttt{PROC-PARTDECAY}}|^2}{|\mathcal{M}^{\text{old}}_{\texttt{PROC-PARTDECAY}}|^2} w^{\text{old}}_{\texttt{PROC-FULLDECAY}} \tag{5.3}$$

Hence, the event weight for the target set of parameters for `PROC-FULLDECAY` can be obtained from applying reweighting on the corresponding `PROC-PARTDECAY` event description. Since the MadGraph software allows event-by-event reweighting for event descriptions recorded in an LHE file [178], the so-called **LHE Refurbishing** algorithm was designed to create a `PROC-PARTDECAY` event record from the originally simulated `PROC-FULLDECAY` events. This algorithm implements the following steps–

- The fermions originating from the decay of the Z boson and the t quark are omitted from the event description
- The Z-boson and t-quark energies are modified to project these particles on-shell
- This modification in energy is propagated all the way back to the initial partons so that energy-momentum conservation is assured at every vertex
- The reweighting procedure is applied on the modified event description
- The reweighting factors obtained henceforth are propagated back to the event description with full decay chain

Since the Z and the t quark are both projected to be on-shell, conservation of energy-momentum at each vertex propagates the residual energy all the back to the initial partons.

However, since both these particles are narrow resonances, the overall adjustment made to the parton momenta is usually very small as seen from Figure 5.4a. This distribution is obtained from applying the LHE Refurbishing algorithm on 10000 $WTZt$ events recording the relative momentum adjustment of the incoming partons. The partonic momentum adjustment is less than 1% in about 90% of the cases, and less than 5% for more than 95% partons. The impact of this modification in the parton energy distribution is therefore minimal and has a negligible effect on the reweight factors as long as we maintain that $\Gamma(T) \gtrsim \Gamma(Z) + \Gamma(t) \approx 4$ GeV. Figure 5.4b shows the comparison of nominally simulated Top Partner mass distribution at $M_T = 1100$ GeV and $\kappa = 0.3$ with the distribution obtained by reweighting a refurbished sample generated with $\kappa = 1.0$ at the same mass.

Finally, the recalculated reweight factors were applied to the original event description to obtain other relevant kinematic distributions at the target mass-coupling combination. Figures (5.5), and (5.6), (5.7) respectively compare the distributions of transverse momenta (p_T), azimuthal angle (ϕ), and pseudorapidity (η) of electrons and muons originating from leptonic decays of Z and W bosons. Figure 5.8 compares the modified-reweighted distributions of p_T, ϕ, and η of partonic jets originating from hadronic decay of W bosons. All these comparisons show a very good agreement between the distributions obtained from an actual set of events at the desired mass and coupling generated according to the `PROC-FULLDECAY` process and corresponding modified-reweighted distributions obtained by applying the LHE Refurbishing algorithm.

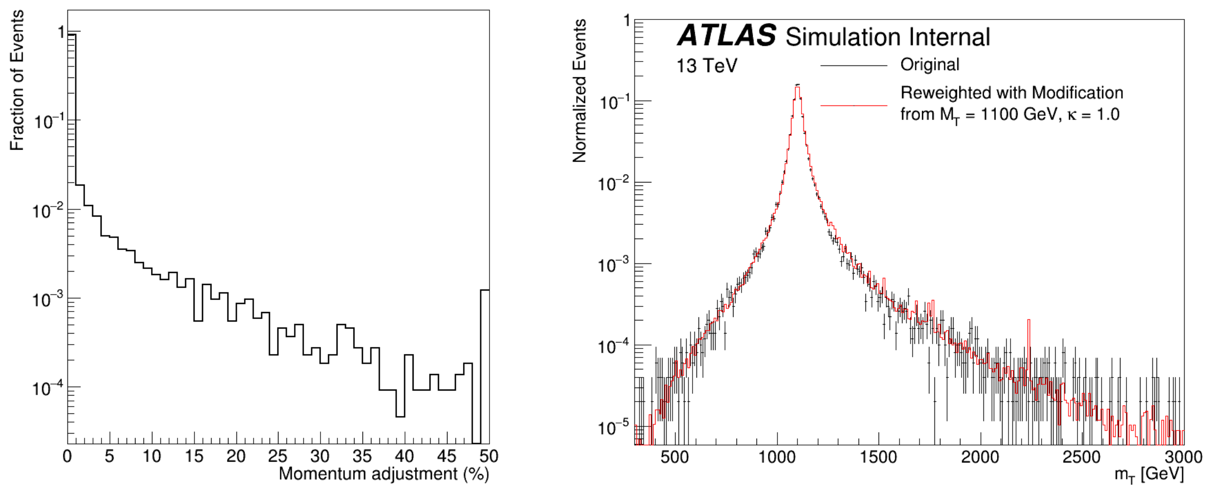

(a) (b)

Figure 5.4: (a) Distribution of parton momentum adjustment in the `LHE Refurbishing` Algorithm and (b) Comparison between original and modified-reweighted distribution of Top Partner invariant mass for $M_T = 1100$ GeV at a coupling of $\kappa = 0.3$. The reweighted distributions are obtained by reweighting events generated for a Top Partner mass of $M_T = 1100$ GeV with coupling $\kappa = 1.0$

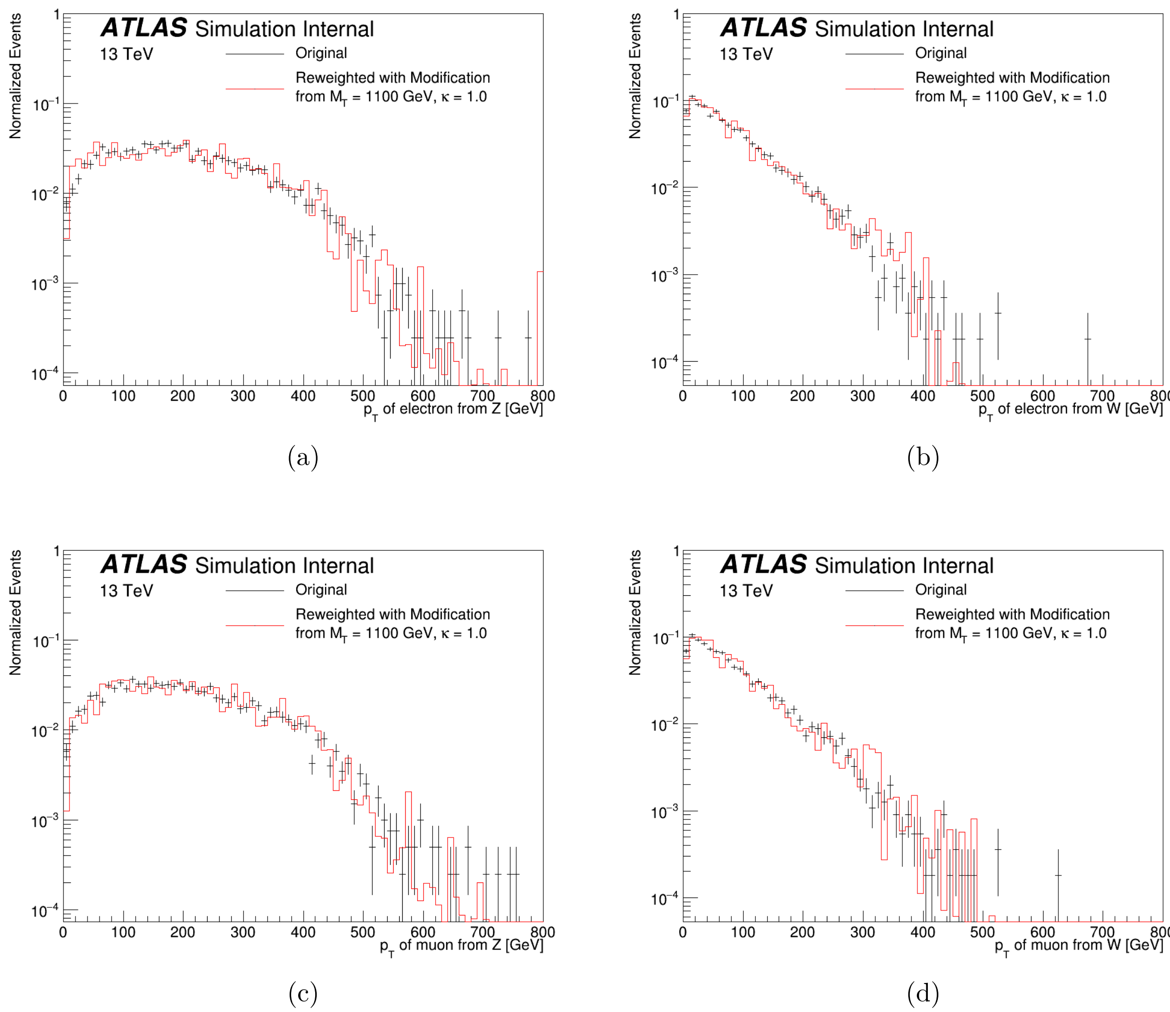

Figure 5.5: Comparison between original and modified-reweighted distributions of transverse momentum of electrons (top) and muons (bottom), where the lepton is obtained from the decay of the Z boson (left) and W boson (right) respectively, for $M_T = 1100$ GeV at a coupling of $\kappa = 0.3$. The reweighted distributions are obtained by reweighting events generated for a Top Partner mass of $M_T = 1100$ GeV with coupling $\kappa = 1.0$.

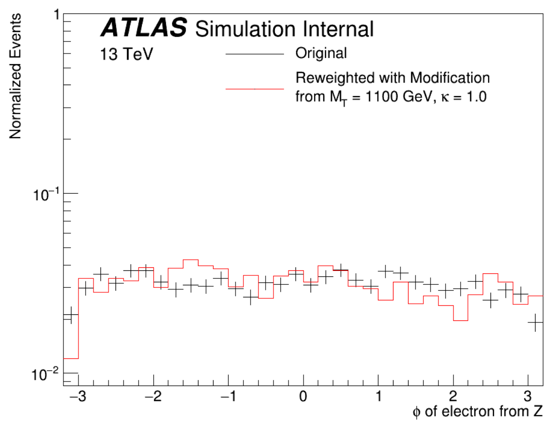

(a)

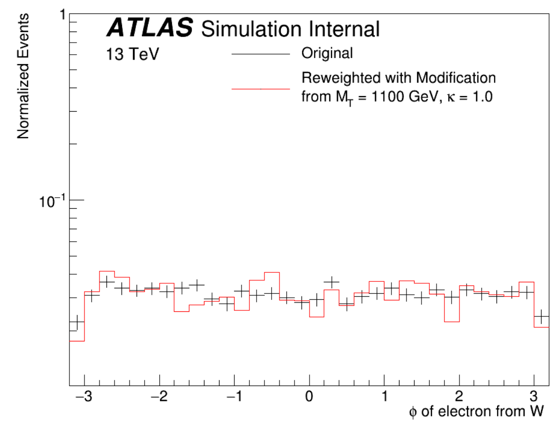

(b)

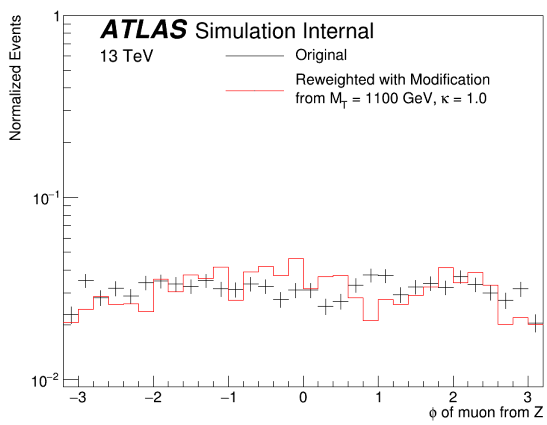

(c)

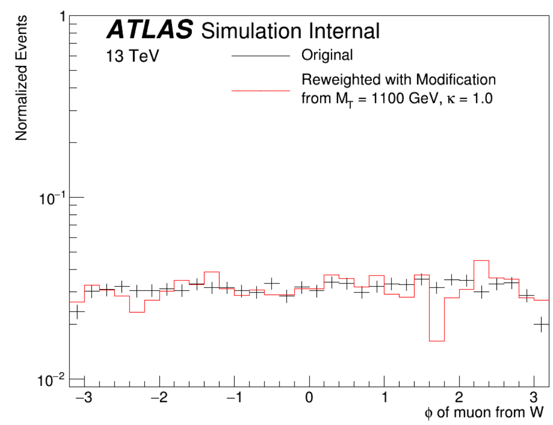

(d)

Figure 5.6: Comparison between original and modified-reweighted distributions of azimuthal angle of electrons (top) and muons (bottom), where the lepton is obtained from the decay of the Z boson (left) and W boson (right) respectively, for $M_T = 1100$ GeV at a coupling of $\kappa = 0.3$. The reweighted distributions are obtained by reweighting events generated for a Top Partner mass of $M_T = 1100$ GeV with coupling $\kappa = 1.0$.

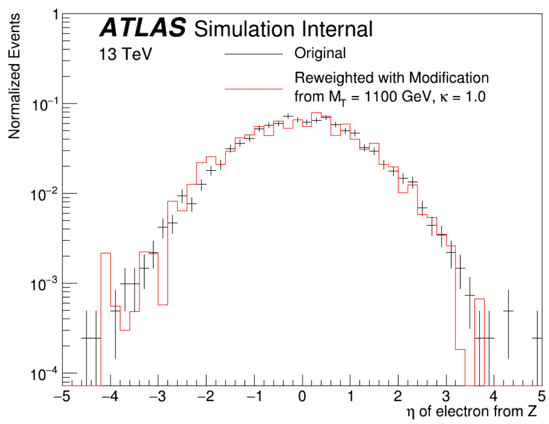

(a)

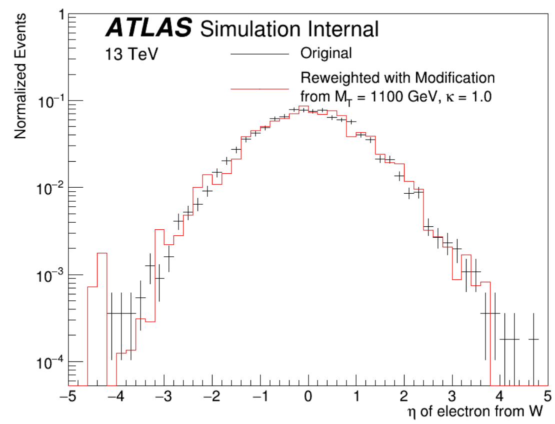

(b)

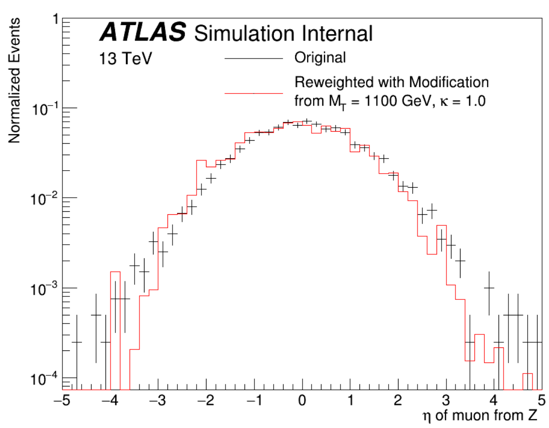

(c)

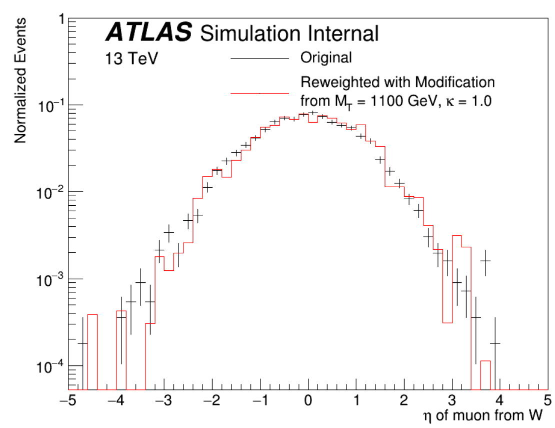

(d)

Figure 5.7: Comparison between original and modified-reweighted distributions of pseudorapidity of electrons (top) and muons (bottom), where the lepton is obtained from the decay of the Z boson (left) and W boson (right) respectively, for $M_T = 1100$ GeV at a coupling of $\kappa = 0.3$. The reweighted distributions are obtained by reweighting events generated for a Top Partner mass of $M_T = 1100$ GeV with coupling $\kappa = 1.0$.

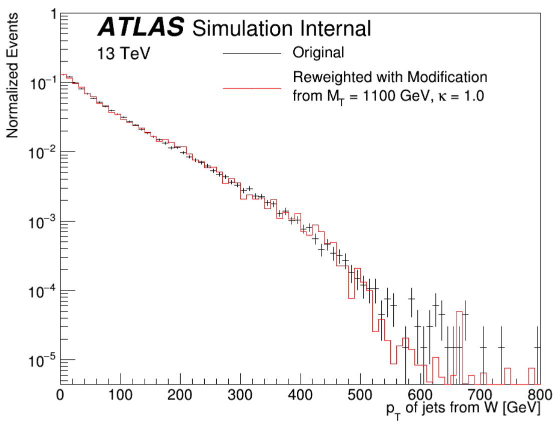

(a)

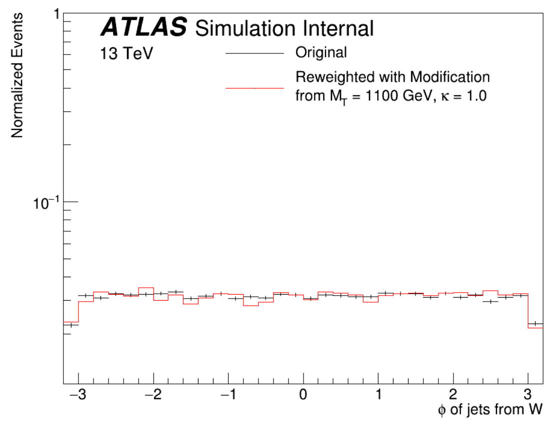

(b)

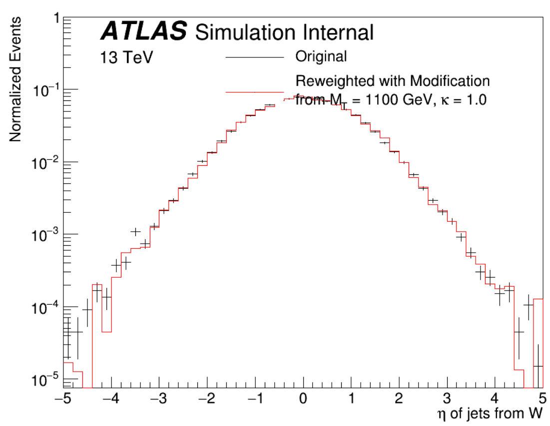

(c)

Figure 5.8: Comparison between original and modified-reweighted distributions of (a) transverve momentum, (b) azimuthal angle, and (c) pseudorapidity of jets obtained from the decay of W boson, for $M_T = 1100$ GeV at a coupling of $\kappa = 0.3$. The reweighted distributions are obtained by reweighting events generated for a Top Partner mass of $M_T = 1100$ GeV with coupling $\kappa = 1.0$.

5.2 Interfernce between Signal and SM Processes

Given the absence of flavor changing neutral current in the SM and owing to the very narrow width of the t quark, SM processes that have the same final state as the one observed in Z mediated decay of the Top Partner are expected to have a very small interfering contribution. However, it is important to quantify the interference effect for two reasons–

First, cross-section for single VLQ processes can be very much model-dependent and depend on the choice of couplings. Hence, it is important to probe the relative contribution of interference for different choices of mass and couplings.

Second, the effect of interference can be significantly different at different regions of kinematic phase space. Therefore, the interfering signal can become important at certain localities of the phase space.

Assuming that $|i\rangle$ and $|f\rangle$ respectively represent the initial and final states of the intended production and decay of single Top Partners, the matrix element squared for the transition is given by

$$\begin{aligned}\mathcal{M}^2_{i\to f} &= |\mathcal{M}_{\text{VLQ}} + \mathcal{M}_{\text{SM}}|^2 \\ &= |\mathcal{M}_{\text{VLQ}}|^2 + 2\text{Re}\left[\mathcal{M}_{\text{VLQ}}\mathcal{M}^*_{\text{SM}}\right] + |\mathcal{M}_{\text{SM}}|^2 \end{aligned} \tag{5.4}$$

The first term on the right side of Eqn. 5.4 represents the squared matrix element coming from diagrams that only include single-VLQ propagators. The third term represents the same quantity for diagrams only including SM processes with the same initial and final states. The second term, $2\text{Re}\left[\mathcal{M}_{\text{VLQ}}\mathcal{M}^*_{\text{SM}}\right]$ represents the contribution from interference between signal and SM processes. Given that differential cross-section $d\sigma \propto |\mathcal{M}|^2$, we can define the so-called *interference cross-section* from Eqn. 5.4 as,

$$d\sigma_{\text{int}} = d\sigma_{i\to f} - d\sigma_{\text{VLQ}} - d\sigma_{\text{SM}} \tag{5.5}$$

where $d\sigma_{i\to f} \propto |\mathcal{M}_{i\to f}|^2$ is the inclusive differential cross-section for the $|i\rangle \to |f\rangle$ process while $d\sigma_{\text{VLQ}} \propto |\mathcal{M}_{\text{VLQ}}|^2$ and $d\sigma_{\text{VLQ}} \propto |\mathcal{M}_{\text{VLQ}}|^2$ represent differential cross-sections for processes exclusively including VLQ propagators and SM processes respectively. It should be noted that σ_{int} does not represent a physical quantity by itself. Rather, it is a convenient metric to evaluate the relative impact of the interference term.

In order to investigate the effects of interference with standard model processes on the single production of top partner and its decay into the Z mediated channel, MadGraph was used to generate MC events for each of the contributing processes in the right hand side of Eqn. 5.4. In these process simulations, the decays of Z boson and t quark are ignored in order to allow faster event generation.

- `PROC-SIGONLY`: The *Signal-only* process explicitly requires the production of a Z boson and a t quark from the decay of a top partner and responsible for the $\mathcal{M}_{\text{VLQ}}$ part of the matrix element. The process description specifically asks for the production of a top partner by a W boson fusion and then decay it in the Z mediated channel. The corresponding process syntax is identical to the `PROC-PARTDECAY` process.

- `PROC-INCLUSIVE`: The *Inclusive* process, generating the matrix element for the $|i\rangle \to |f\rangle$, allows the final state to be produced via signal and SM background processes alike. The process description only requires a Z boson and a t quark in its final state and while process diagram does not involve VLQs other than the Top Partner.

- `PROC-BKGONLY`: The *Background-only* process allows the production of the Z boson and the t quark to be produced by SM processes only corresponding to the $\mathcal{M}_{\text{SM}}$ term. The process description explicitly excludes diagrams involving any VLQ.

To evaluate the sensitivity of interference at different corners of the parametric hyperspace, this study is performed for top partner masses of $M_T = 1100$ GeV and $M_T = 2000$ GeV for the choices of coupling being $\kappa = 0.3$ and $\kappa = 1.0$. Table 5.1 lists the cross-section values of the different processes as obtained from the MadGraph simulations for the aforementioned choices of Top Partner masses and couplings. It has been observed that the contribution of the interference term, evaluated as σ_{int}, is much smaller than the Signal-only process for all values of masses and couplings, suggesting that the impact of interference on our signal processes is rather marginal.

m_T [GeV], κ	PROC-INCLUSIVE	PROC-SIGONLY	PROC-BKGONLY	Interference
1100, 1.0	0.8849	0.2583	0.6208	0.0058
1100, 0.3	0.6485	0.0276	0.6208	0.0001
2000, 1.0	0.635	0.0137	0.6208	0.0006
2000, 0.3	0.6235	0.0026	0.6208	0.0001

Table 5.1: Cross-section values (*pb*) as obtained from MadGraph for `PROC-INCLUSIVE`, `PROC-SIGONLY`, and `PROC-BKGONLY` different processes. The contribution of the interference term is evaluated according to Eqn. 5.5

In order to further identify any phase subspace that is significantly affected by the interference with SM backgrounds, we compare the weighted sum of the distributions from background-only and signal-only processes with kinematic distributions obtained from the inclusive processes. The relative contributions of `PROC-SIGONLY` and `PROC-BKGONLY` processes in the weighted sum of their distributions are proportional to their cross-sections as reported in Table 5.1. Figures 5.9 and 5.10 compare the distributions of a number of kinematic variables for $m_T = 1100$ GeV where the coupling choices are set to $\kappa = 0.3$ and $\kappa = 1.0$ respectively. Figures 5.11 and 5.12 repeat the same exercise for $m_T = 2000$ GeV where the couplings are set to $\kappa = 0.3$ and $\kappa = 1.0$ respectively. It can be evidently seen from these comparisons that interference effects play a very insignificant role in determining the kinematic distributions of our process of interest. Hence, we can safely ignore the interference effects in our analysis.

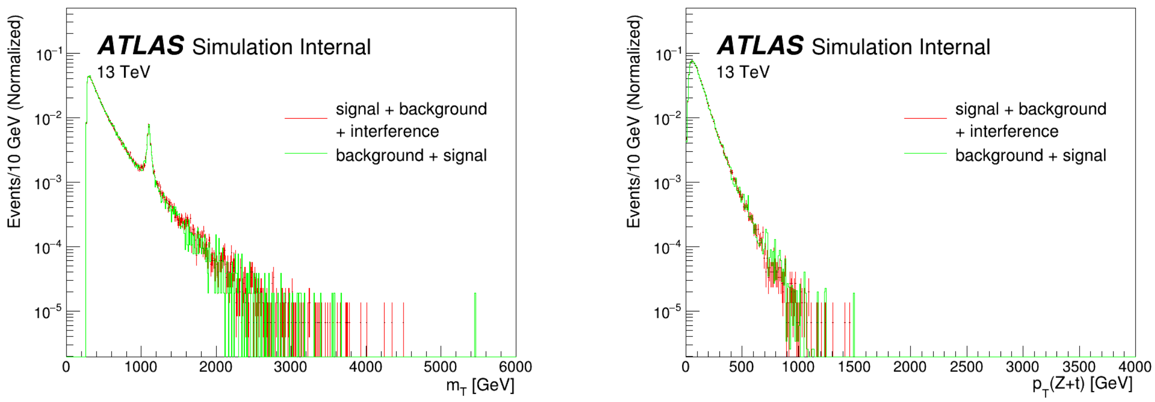

(a) (b)

Figure 5.9: Comparison of the weighted sum of `PROC-BKGONLY` and `PROC-SIGONLY` distributions for (a) the invariant mass of Top Partner and (b) transverse momentum of Top Partner with the distributions obtained from the inclusive process for $M_T = 1100$ GeV and $\kappa = 0.3$. All distributions are evaluated at truth level before parton showering is applied to the events.

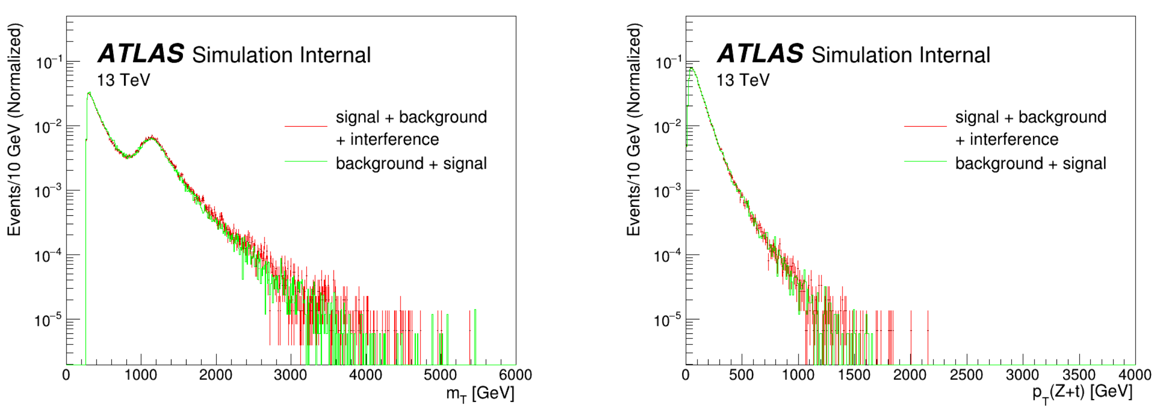

(a) (b)

Figure 5.10: Comparison of the weighted sum of `PROC-BKGONLY` and `PROC-SIGONLY` distributions for (a) the invariant mass of Top Partner and (b) transverse momentum of Top Partner with the distributions obtained from the inclusive process for $M_T = 1100$ GeV and $\kappa = 1.0$. All distributions are evaluated at truth level before parton showering is applied to the events.

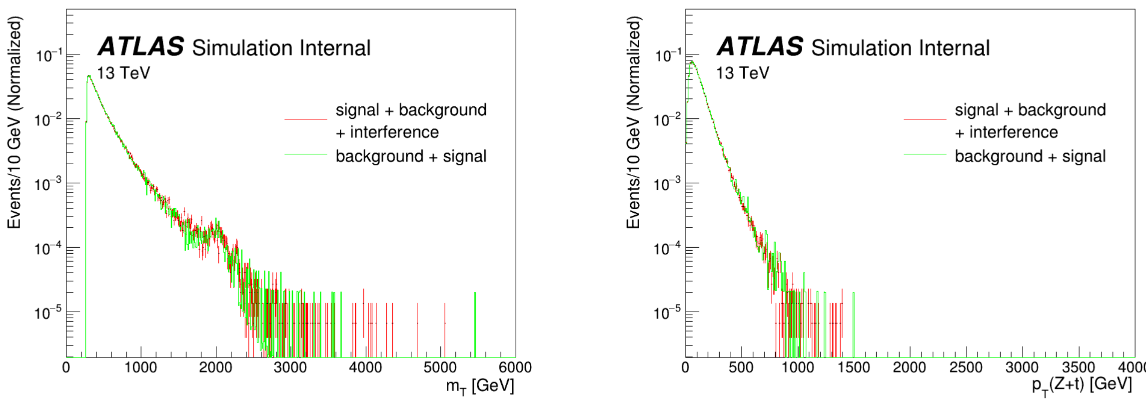

(a) (b)

Figure 5.11: Comparison of the weighted sum of PROC-BKGONLY and PROC-SIGONLY distributions for (a) the invariant mass of Top Partner and (b) transverse momentum of Top Partner with the distributions obtained from the inclusive process for $M_T = 2000$ GeV and $\kappa = 0.3$. All distributions are evaluated at truth level before parton showering is applied to the events.

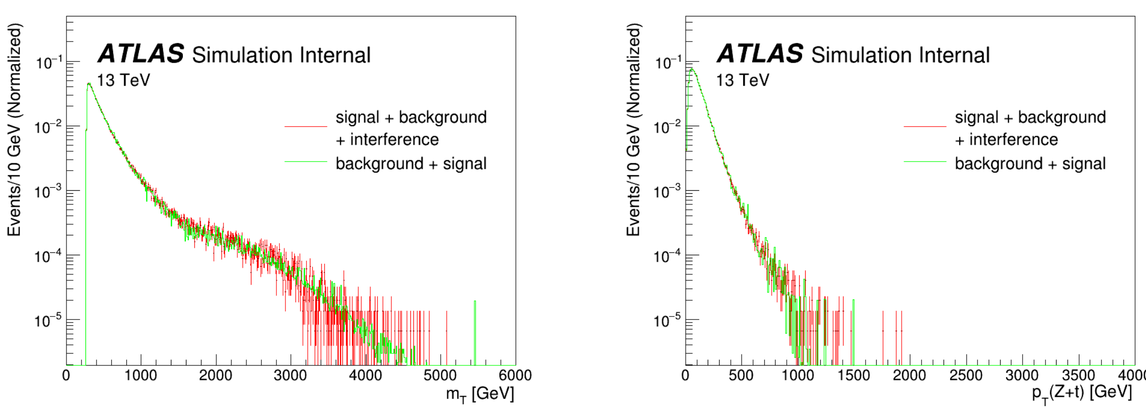

(a) (b)

Figure 5.12: Comparison of the weighted sum of PROC-BKGONLY and PROC-SIGONLY distributions for (a) the invariant mass of Top Partner and (b) transverse momentum of Top Partner with the distributions obtained from the inclusive process for $M_T = 2000$ GeV and $\kappa = 1.0$. All distributions are evaluated at truth level before parton showering is applied to the events.

5.3 Contribution of subleading Diagrams

The Feynman diagrams shown in Figure 5.2 remain the dominant contributor to the process of single production of Top Partners with a Z boson and a top quark in the final state. The squared four-momentum of the T propagator in this topology is given by the Mandelstam variable s, and hence this diagram is identified as the s-channel diagram.

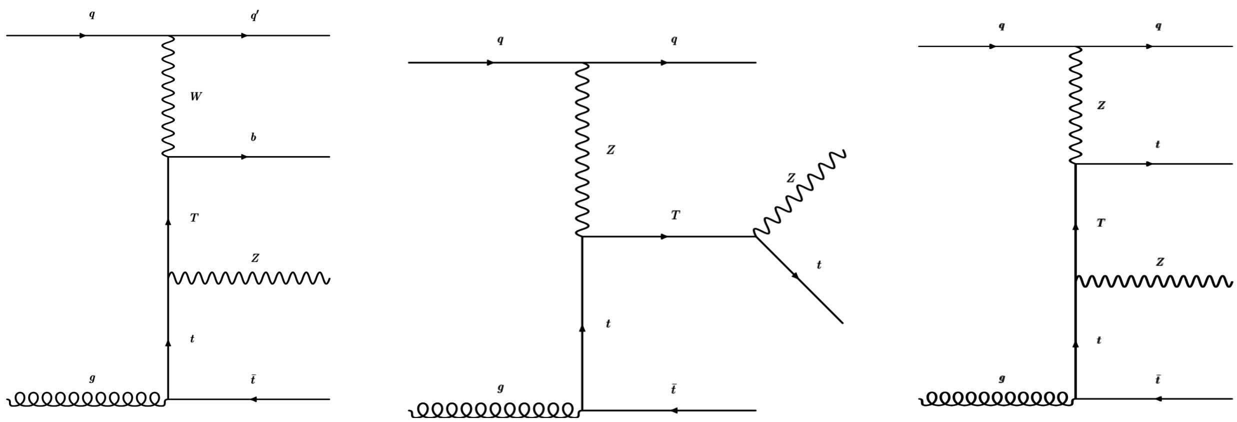

(a) (b) (c)

Figure 5.13: Feynman diagrams corresponding to (a) t-channel production of the $WTZt$ process, (b) s-channel production of the $ZTZt$ process, and (c) t-channel production of the $ZTZt$ process

However, additional diagrams can also have subleading contributions to the process of production of single Top partners. These diagrams are shown in Figure 5.13. The first diagram to consider is the t-channel $WTZt$ process (Figure 5.13a), which still has an off-shell W exchange in the process of producing a Z boson and a t quark via the exchange of a T propagator. The t-channel process requires a gluon splitting to a couple of t quarks while the s channel process has the gluon splitting to a couple of b quarks. Since $m_t \gg m_b$, the t-channel process has a significantly lower cross-section compared to the s-channel process. This can be seen from the comparison of inclusive $s + t$ channel process cross-section with s-channel only cross-section for different choices of mass of T and relative decay widths in Figure 5.14.

In Figures 5.15 and 5.16, the $m(Zt)$ distribution from $s + t$-channel diagrams with s-channel only diagrams for different choices of relative decay width are compared for $M_T =$

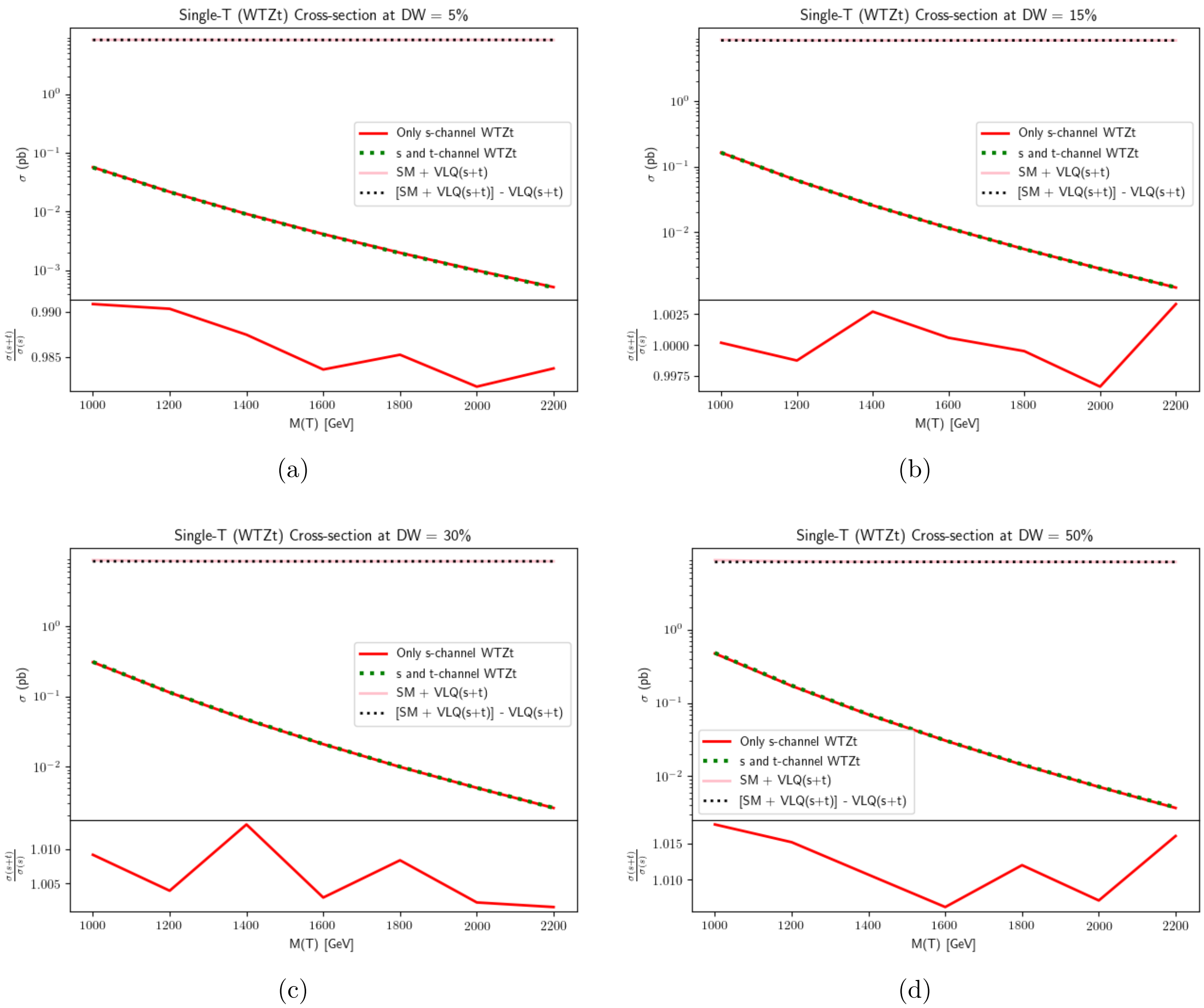

Figure 5.14: Comparison of $WTZt$ process cross-sections of s-channel only diagrams (red solid line) with the s and t-channel inclusive diagrams (green dotted line) for relative decay widths of (a) 5%, (b) 15%, (c) 30%, and (d) 50% for different choices of mass of T. The solid pink line shows process cross-section when both standard model and T-inclusive processes are allowed to generate the same $|i\rangle \to |f\rangle$ process. The dotted black line shows the quantity $\sigma_{\text{int}} + \sigma_{\text{VLQ}}$ from Eqn. 5.5. Since $\sigma_{\text{int}} + \sigma_{\text{VLQ}}$ remains flat across all masses and decay widths, the interference between T-mediated and SM processes can be neglected.

1200 GeV and $M_T = 2000$ GeV respectively. Similar to what is seen in the Figure 5.14, we find near perfect agreement between the distributions from $s + t$-channel inclusive process and the s-channel only process. These comparisons across a wide range of masses and widths for T suggest that the t-channel diagrams have a very negligible impact for $WTZt$ processes.

The second subdominant contribution for singly produced Ts with a Z and t in final

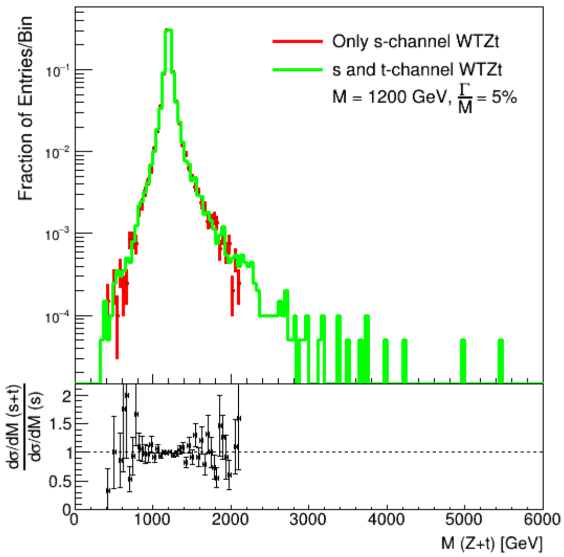

(a)

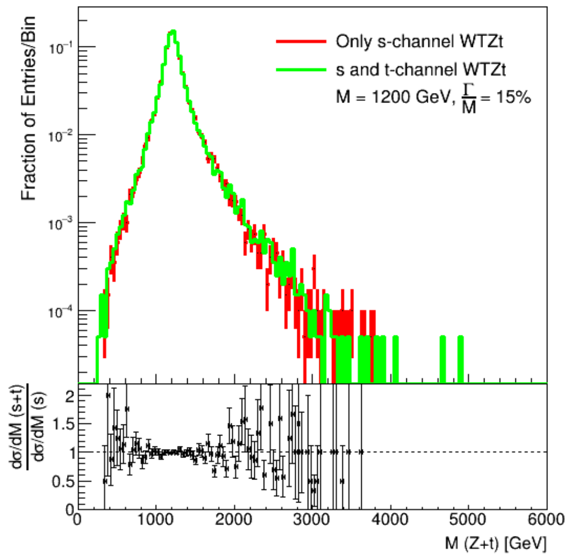

(b)

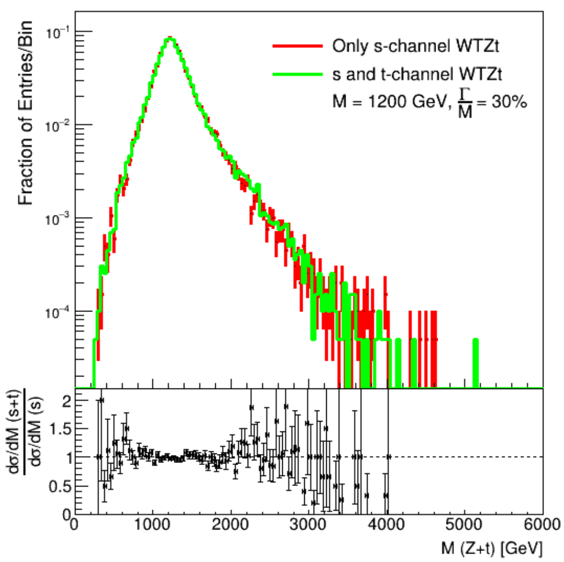

(c)

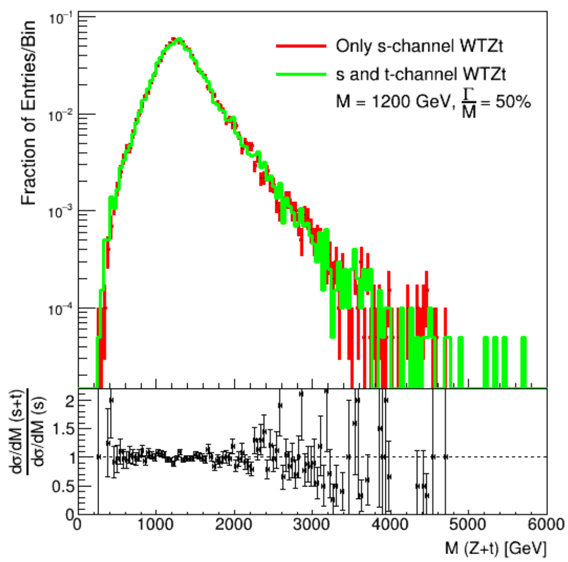

(d)

Figure 5.15: Comparison of the $m(Zt)$ distribution of $WTZt$ process for s-channel only diagrams (red) with the s and t-channel inclusive diagrams (green) for relative decay widths of (a) 5%, (b) 15%, (c) 30%, and (d) 50% for $M_T = 1200$ GeV.

state comes from the Z-mediated production mode. The s and t channel diagrams for this process are shown respectively in Figures 5.13b and 5.13c. Since the $ZTZt$ processes require a gluon splitting to a couple of top quarks, it is expected to have a relatively smaller

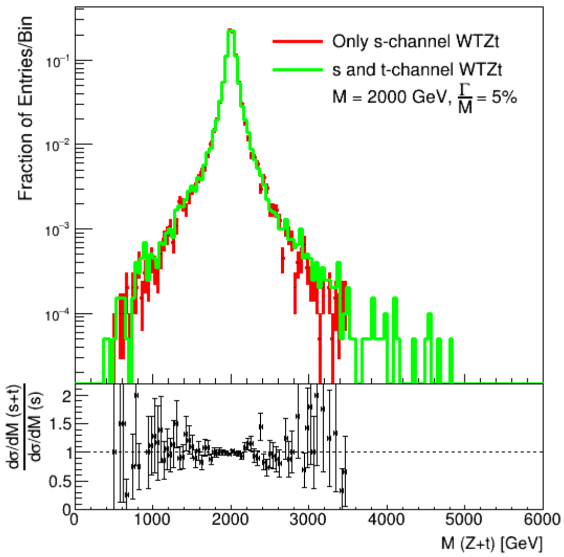

(a)

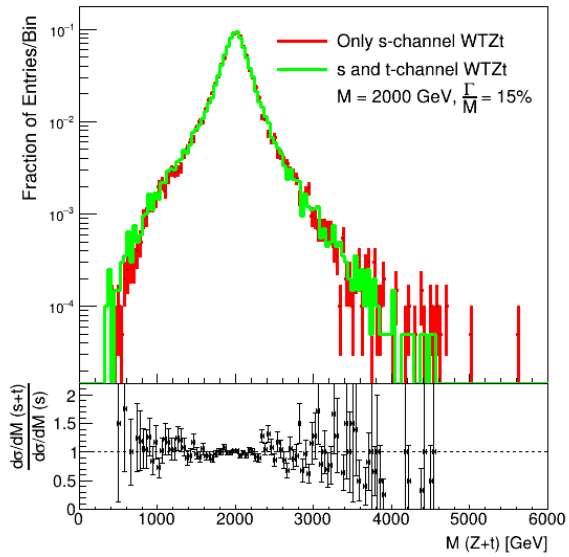

(b)

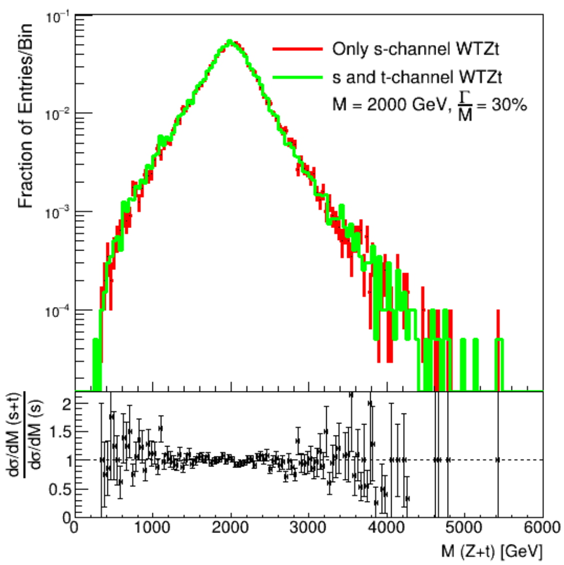

(c)

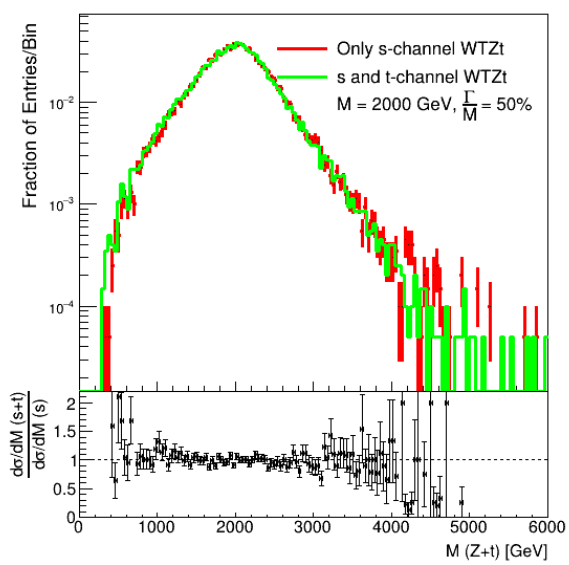

(d)

Figure 5.16: Comparison of the $m(Zt)$ distribution of $WTZt$ process for s-channel only diagrams (red) with the s and t-channel inclusive diagrams (green) for relative decay widths of (a) 5%, (b) 15%, (c) 30%, and (d) 50% for $M_T = 2000$ GeV.

contribution. However, the kinematics and the cross-section of weak force mediated single production of VLQs depend on the choice of representation and couplings. Therefore, for certain choices of couplings and branching ratios, the Z-mediated production mode can have a sizable, even dominant cross-section compared to $WTZt$ processes. One perfect example is the doublet representations where BR($T \to Wb$) ~ 0. However, in the context of a more general interpretation as outlined in Chapter 4, the sensitivity of single-VLQ searches can be significantly improved, especially with the entire Run-2 dataset from ATLAS, by the inclusion of $ZTZt$ signals. As shown in Ref. [46], $\sigma_{WT}(\tilde{c}_W = 1)$ is about an order of magnitude higher than $\sigma_{ZT}(\tilde{c}_Z = 1)$. This implies that the contribution from $ZTZt$ process in the $Z + t$ final state will be comparable to $WTZt$ processes for $\frac{\mathrm{BR}(T \to Wb)}{\mathrm{BR}(T \to Zt)} \lesssim \frac{1}{10}$. However, the contribution can be non-negligible even for less extreme choices.

It can be additionally seen in Figures 5.13b and 5.13c that both s and t channel diagrams require a gluon splitting to a $t\bar{t}$ pair. This is suggestive of a sizable contribution from t-channel, contrary to what we have seen for $WTZt$ processes. The comparison of cross-section between $s + t$-channel inclusive diagrams with s-channel only diagrams for $ZTZt$ processes are shown in Figure 5.17. Depending on the choice of mass and relative decay width, the t-channel processes tend to have a modest impact on the cross-section calculation, the deviation being of $\mathcal{O}(20\%)$ in the most extreme cases.

However, the comparison of cross-section hardly gives the complete picture. The interference between the s and t channel diagrams can have a noticeable impact on the shape of kinematic distributions. In Figures 5.18 and 5.19, the $m(Zt)$ distribution from $s + t$-channel diagrams with s-channel only diagrams for different choices of relative decay width are compared for $M_T = 1200$ GeV and $M_T = 2000$ GeV respectively. Since the final state for $ZTZt$ processes has two top quarks, the combination of $Z + t$ that has a larger invariant mass has been chosen. The shift in the distribution that emerges from interference effects between the s and t channel diagrams start becoming visible even at a relatively low mass of 1200 GeV and small relative decay width of 15%. This effect gets more pronounced as we move to higher masses and couplings.

To summarize, the studies on $WTZt$ and $ZTZt$ signal modeling presented in this chapter suggest that the LHE Refurbishing algorithm is a useful method to allow event-by-

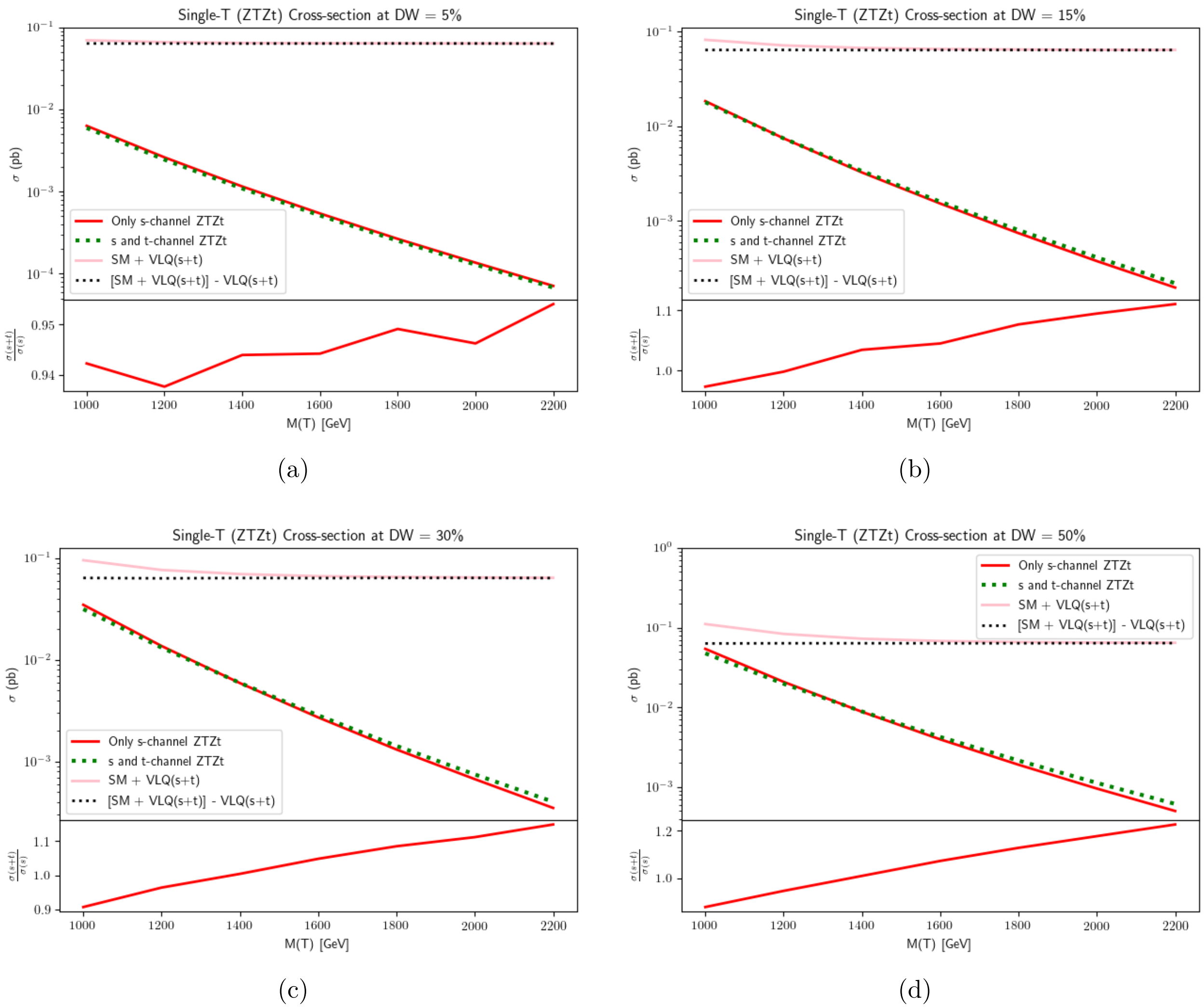

Figure 5.17: Comparison of $ZTZt$ process cross-sections of s-channel only diagrams (red solid line) with the s and t-channel inclusive diagrams (green dotted line) for relative decay widths of (a) 5%, (b) 15%, (c) 30%, and (d) 50% for different choices of mass of T. The solid pink line shows process cross-section when both standard model and T-inclusive processes are allowed to generate the same $|i\rangle \rightarrow |f\rangle$ process. The dotted black line shows the quantity $\sigma_{\text{int}} + \sigma_{\text{VLQ}}$ from Eqn. 5.5. Since $\sigma_{\text{int}} + \sigma_{\text{VLQ}}$ remains flat across all masses and decay widths, the interference between T-mediated and SM processes can be neglected.

event matrix element reweighting in order to obtain signal lineshapes for a wide range of masses and couplings. Additionally, interference effects between single-T and SM processes can be ignored. The t-channel diagrams for $WTZt$ processes have a negligible impact on the cross-section and physical kinematic distributions. However, the $ZTZt$ process can become important for certain corners of the parametric hyperspace, especially when BR($T \rightarrow Zt$)

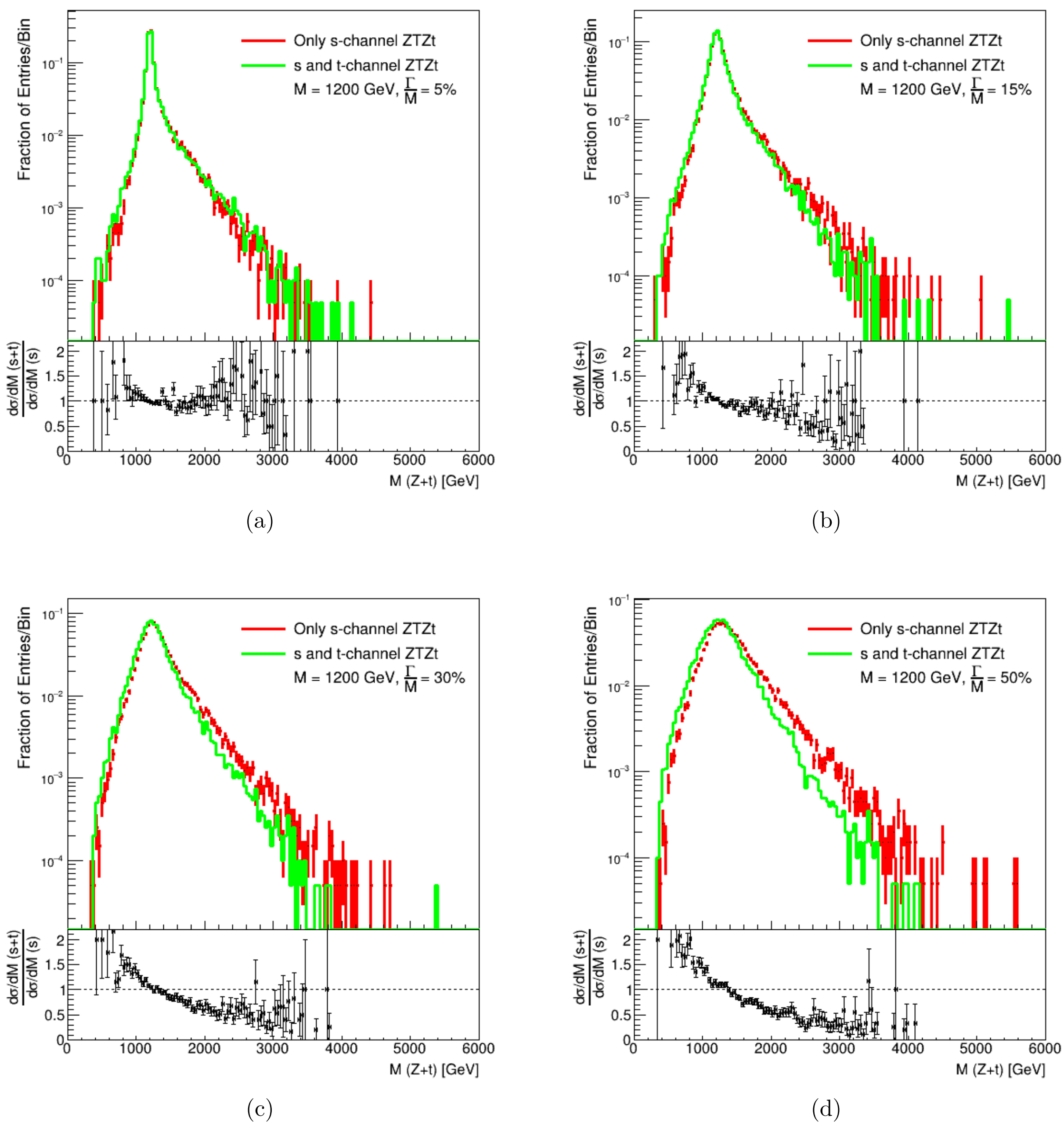

Figure 5.18: Comparison of the $m(Zt)$ distribution of $ZTZt$ process for s-channel only diagrams (red) with the s and t-channel inclusive diagrams (green) for relative decay widths of (a) 5%, (b) 15%, (c) 30%, and (d) 50% for $M_T = 1200$ GeV.

starts to become larger than $\mathrm{BR}(T \to Wb)$. The t-channel diagram for this process has a modest impact on overall cross-section, but there is a noticeable change in the kinematic distributions due to interference between the s and t channel diagrams. For the analysis

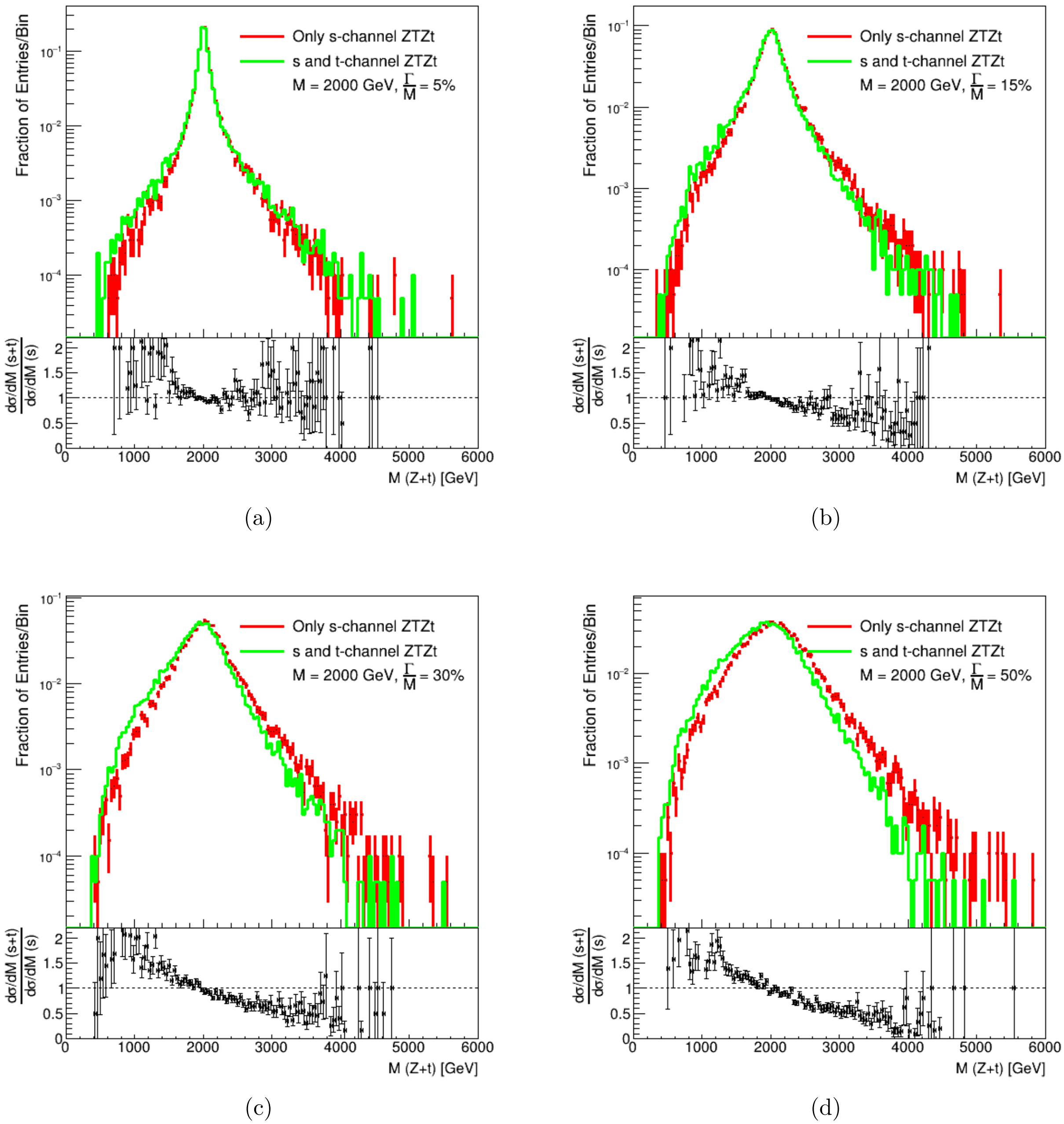

Figure 5.19: Comparison of the $m(Zt)$ distribution of $ZTZt$ process for s-channel only diagrams (red) with the s and t-channel inclusive diagrams (green) for relative decay widths of (a) 5%, (b) 15%, (c) 30%, and (d) 50% for $M_T = 2000$ GeV.

that intends to incorporate the entire Run-2 dataset, the t-channel inclusive $ZTZt$ signal needs to be included for a comprehensive interpretation.

Chapter 6

Extending the Search for Top Partners with 139 fb^{-1}data collected by the ATLAS Detector in Run 2

This chapter outlines the strategy and early results from the ongoing search for Top Partners decaying to a Z boson and a t quark in the trilepton final state. Essentially, this analysis is an extension of the one described in Chapter 3 for the entire Run 2 dataset from ATLAS, amassing a total 139 fb^{-1} of pp collision data. Moreover, the signal modeling studies presented in Chapter 5, the generalized interpretation strategy outlined in Chapter 4 along with improved event categorization and analysis strategy have enabled this analysis to be set up for a thorough scan of the parametric hyperspace to set model-independent limits and eventually contribute to the combination of ATLAS's single Top Partner searches with better sensitivity and stronger limit-setting ability.

6.1 Updated Background and Signal Modeling

In search for Top Partners with trilepton signature, where a pair of opposite sign same flavor leptons constitute the Z boson candidate and a third lepton arises from leptonic decay of the top quark, the major background processes and the corresponding MC samples are listed in Section 3.1. For the full Run 2 analysis, MC event generators, choice of corresponding PDF and shower tunes for majority of the background samples remain the same as listed in Table 3.1 with the exception of diboson and triboson samples for which the MC generators have been updated to Sherpa 2.2.2 and Sherpa 2.2.1 respectively. The signal samples are still produced by MadGraph, but the branching ratios to W, Z, and H channels are set to 0.5, 0.25, and 0.25 respectively according to what is expected for singlet representations. The signal MC are generated for masses in the range of 1100–2300 GeV in 200 GeV spacing. The choice of default coupling is set to $\kappa = 1.0$. The new set of signal MC utilizes the LHE Refurbishing algorithm described in Section 5.1 that allows us to recycle our MC events for a wide range of masses and couplings by applying leading order matrix element reweighting. Each set of signal MC is reweighted to a fine grid of coupling in the range of $0.1 \leq \kappa \leq 1.6$ for the mass point of default simulation as well as the mass point 100 GeV lower than that.

Moreover, the MC sample for each background and signal process has been separated into three *pileup campaigns* to properly mimic the varying data taking conditions across the years 2015-2018. Figure 2.3 shows the distribution of the number of proton-proton interactions, i.e. the pile-up profile, during a single bunch crossing at the ATLAS detector. The three subset of MC samples are independently reweighted to match the pile-up profile of ATLAS data from 2015-16, 2017, and 2018. Estimation of MC events is performed by normalizing each subset with the integrated luminosity of the corresponding data taking period.

The analysis has also adapted a new jet reconstruction algorithm. In the previous analysis, jets were reconstructed from topological clusters of calorimeter cells. The calorimeters' energy resolution is generally worse for low energy showers. That can be compensated by factoring in information from the trackers which provides better resolution at lower transverse momenta. The particle flow algorithm [179] cleverly combines information both from ATLAS's trackers and calorimeters to obtain reconstructed jet candidates. This algorithm significantly improves the jet energy resolution at lower momenta and therefore, provides better modeling of pile-up activity and improved vertex reconstruction. Given the superiority of the particle flow algorithm in jet resolution and pile-up stability, it has been an ATLAS-wide recommendation to use jets reconstructed by the particle flow algorithm.

Another major change has been introduced in the *b*-tagging algorithm. The previous analysis used a Boosted Decision Tree based `MV2c10` tagger, which in the current analysis has been replaced by the Deep Neural Network based `DL1r` tagger [143]. The primary motivation of this recommendation has been due to superior light and charm jet rejection by the latter that would significantly improve the quality of background modeling and the sensitivity to b-jet enriched final states like the one being analyzed in this chapter.

6.2 Optimization of Event Categorization

The *Primary Selection* of events remain identical to what has been described in Section 3.3.1, requiring (i) at least three electrons or muons with one pair of OS-SF leptons comprising the Z bososn candidate, (ii) on-shell Z candidate with an invariant mass within a 10 GeV range of the Z boson pole mass, and (iii) a minimum of two central jets. However, the cut $n(\text{jets}) \times H_T(\text{jets}) < 6$ TeV has been moved to the Signal Region (SR) alone. As studies in Appendix A show, this cut has very little impact on background selection in the Control Regions (CRs).

6.2.1 Modified Signal, Control, and Validation Region Definitions

Among the selections that were previously introduced to isolate potential signal events, the cut on Z candidate p_T has been increased to a value of 300 GeV. This is inspired from the shift of the analysis to even higher Top Partner masses, yielding significantly harder Z boson candidate as can be seen from Figure 6.1b. Given that the combination of ATLAS's pair production analyses set a limit on T mass at around 1400 GeV [67], the signal benchmark for the current analysis has been set to $WTZt$ production of singlet T of 1500 GeV at a coupling of $\kappa = 0.5$ which represents a modest $\Gamma_T = 272.5$ GeV with a relative decay width of about 18%. Figure 6.1b shows the distribution of the Z boson candidate p_T for the benchmark signal with very little contribution in the phase space of $p_T(ll) < 300$ GeV.

In order to improve the background separation in Signal Region (SR) even further, additional cuts on angular separation of the Z boson candidate and the third lepton (l_3) as well as the leading b-jet (b_{lead}) have been introduced. The distribution of $\Delta\phi(Z, l_3)$ at

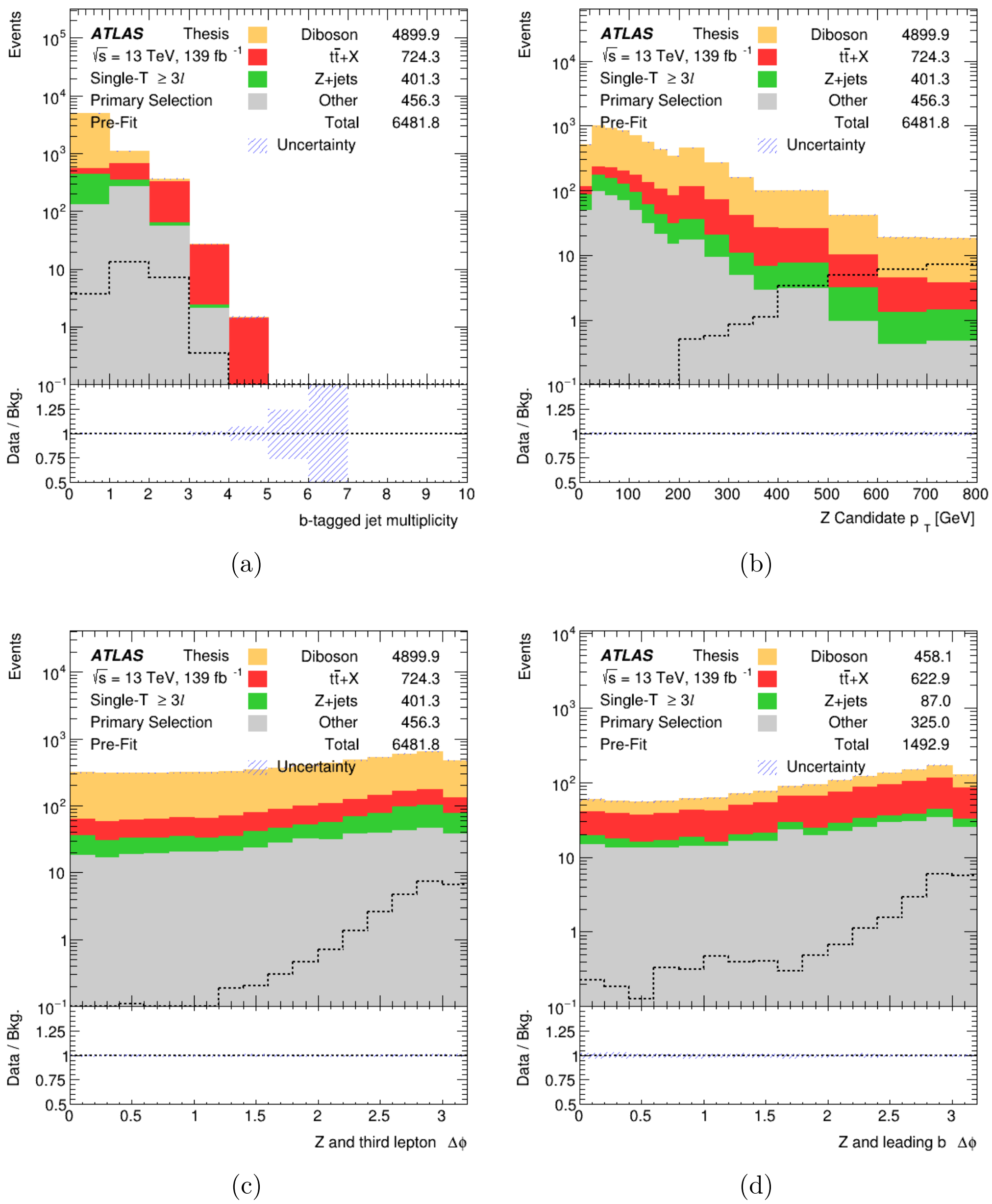

Figure 6.1: MC predicted distributions of (a) b-tagged jet multiplicity, (b) p_T of the Z boson candidate, (c) $\Delta\phi$ between the Z candidate and the third lepton, and (d) $\Delta\phi$ between the Z candidate and the leading b-tagged jet for the major background processes at primary selection. Only statistical uncertainties are considered. The overlaid black line represents the relative shape of the signal contribution for a Top partner with a mass of 1500 GeV and a coupling of $\kappa = 0.5$.

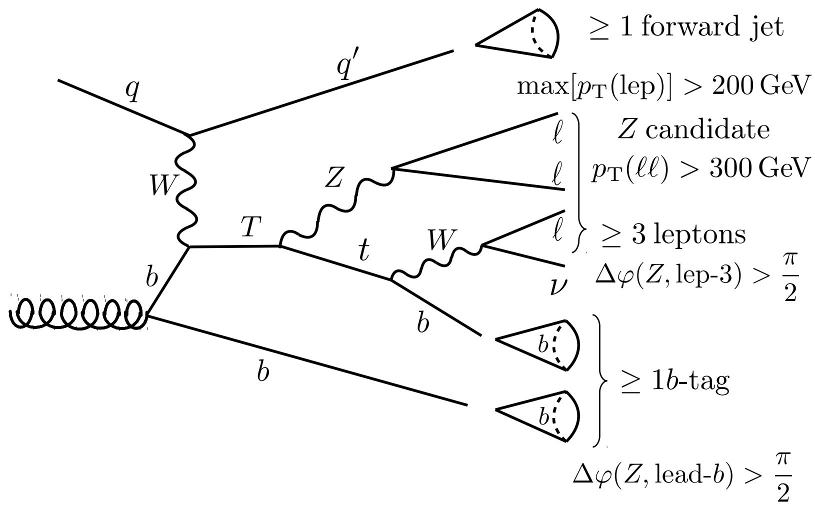

Figure 6.2: The process topology and the signal region event selection for the analysis aiming 139 fb^{-1} data collected by the ATLAS detector in Run 2.

primary selection is shown in Figure 6.1c where the signal shows a clearly distinguishable shape compared to the sum of backgrounds. The same conclusion holds for the distribution of $\Delta\phi(Z, b_{\text{lead}})$ in Figure 6.1d. Hence, along with the previously mentioned cuts, additional $\Delta\phi$ cuts are introduced in the signal region with $\Delta\phi(Z, l_3) > \frac{\pi}{2}$ and $\Delta\phi(Z, b_{\text{lead}}) > \frac{\pi}{2}$. Figure 6.2.1 summarizes the set of cuts that define the SR.

Since Diboson and $t\bar{t}+X$ processes are the major backgrounds, the control regions are designed to model these backgrounds in signal-depleted phase space. Similar to the previous analysis, the **Diboson Control Region** is defined by rejecting events with any b-tagged jets that pass the primary selection. This CR has a very high purity in diboson processes. However, the previously chosen $t\bar{t}+X$ CR had a significant contribution from diboson processes that primarily comes from events with exactly 1 b-tagged jet. With a larger dataset at hand, it is now possible to define a region with higher purity in $t\bar{t}+X$ contribution by requiring at least 2 b-tagged jets in event selection. Hence, we define two control regions in the current analysis- the **1 b-jet Control Region**, also called the **Mixed Control Region** selects events with exactly 1 b-tagged jet while the $t\bar{t}+X$ **Control Region** requires events to have at least 2 b-tagged jets. Both of these CRs reject events with forward jets and require a selection on the the angular separation between the Z boson candidate and the third lepton, $\Delta\phi(Z, l_3) < 2.6$.

In order to validate the modeling of background distributions as observed in the control regions, a third region, called the **Validation Region** is defined. This region places the same set of selections on the b-tagged jet and forward jet multiplicities as the signal region, but is orthogonalized by requiring that at least of the $\Delta\phi$ cuts is reversed, i.e. $\Delta\phi(Z, l_3) < \frac{\pi}{2}$ or $\Delta\phi(Z, b_{\text{lead}}) < \frac{\pi}{2}$

Table 6.1 summarizes the event categorization and the cuts applied to define the CRs and the SR.

Diboson CR	Mixed CR	$t\bar{t}$+X CR	Validation Region	Signal Region
≥ 3 leptons				
≥ 1 pair of OS-SF leptons with $\lvert m(l^+l^-) - m_Z \rvert < 10$ GeV				
0 b-tagged jets	1 b-tagged jet	≥ 2 b-tagged jet	≥ 1 b-tagged jet	
	0 fwd. jet		≥ 1 fwd. jet	
	$\Delta\phi(Z, l_3) < 2.6$		$\Delta\phi(Z, l_3) < \frac{\pi}{2}$ or, $\Delta\phi(Z, b_{\text{lead}}) < \frac{\pi}{2}$	$\Delta\phi(Z, l_3) > \frac{\pi}{2}$ $\Delta\phi(Z, b_{\text{lead}}) > \frac{\pi}{2}$ $\max(p_T(l)) > 200$ GeV $p_T(Z) > 300$ GeV $H_T(\text{jets}) \times n(\text{jets}) < 6$ TeV

Table 6.1: Summary of selections applied to define the CRs, the VR, and the SR for the full Run 2 analysis

6.2.2 Improving Background Modeling by Kinematic Reweighting

The MC-predicted distributions of Z boson candidate p_T for the different SM processes along with the observed data are shown in Figure 6.3. One of the observed features of the kinematic distributions is a noticeable mismatch between the background prediction and observed data in these regions. Significant improvement in background modeling can be obtained by matching the MC-predicted background prediction with the data distribution for a kinematically independent variable. In this process of kinematic reweighting, a reweighting factor is applied to each MC-simulated event to adjust the mismodeling observed in the variable that is being matched with data. In the context of the current analysis, we consider two orthogonal distributions in order to perform this by reweighting to account for mismodeling in the two major background processes. The MC-predicted central jet distributions at primary selection for events with zero and at least one b-tagged jets are shown in Figure 6.4.

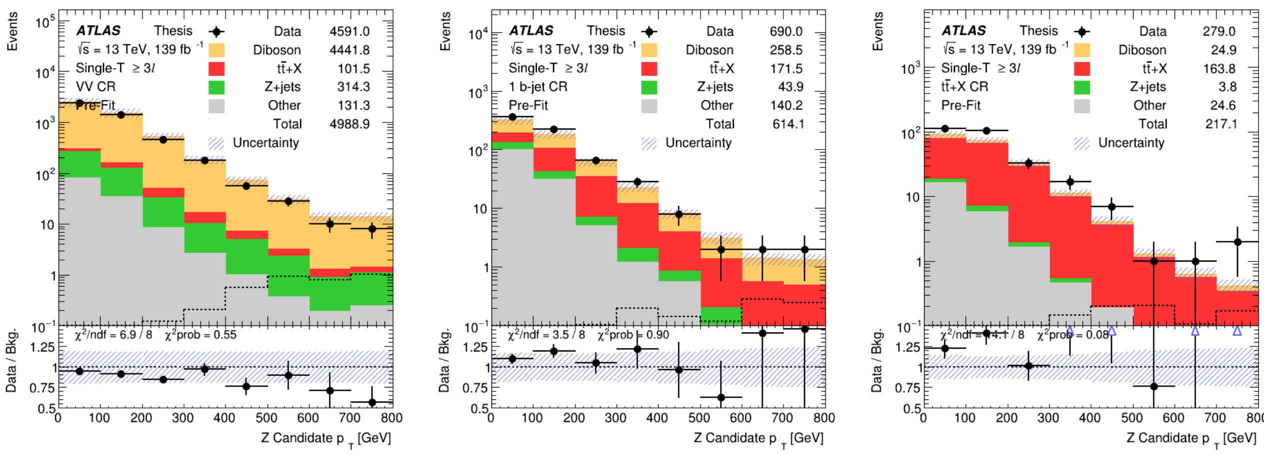

(a) (b) (c)

Figure 6.3: Comparison of MC predicted pre-fit distributions with data for the Z candidate p_T in (a) VV CR, (b) Mixed CR, and (c) $t\bar{t}+X$ CR. The overlaid black line represents the signal contribution for a Top partner with a mass of 1500 GeV and a coupling of $\kappa = 0.5$.

For each bin of the central jet multiplicity distribution, a pair of kinematic reweighting factors (v_i, t_i) are assigned for the VV and $t\bar{t}+X$ processes respectively. The observed data, and MC-predicted backgrounds are related with these kinematic factors as

$$
\begin{aligned}
d_{0,i} &= v_i[\texttt{VV}]_{0,i} + t_i[\texttt{ttX}]_{0,i} + [\texttt{MC}]_{0,i} \\
d_{1,i} &= v_i[\texttt{VV}]_{1,i} + t_i[\texttt{ttX}]_{1,i} + [\texttt{MC}]_{1,i}
\end{aligned}
\tag{6.1}
$$

where d, [VV], [ttX], and [MC] respectively represent observed data, MC-predicted VV, MC-predicted $t\bar{t}+X$, and MC-predicted contribution from minor backgrounds. The subscripts 0/1 represent the phase space of $0/\geq 1$ b-tagged jets. The (v_i, t_i) factor for each bin is solved by simultaneously solving the pair of equations in Eqn. 6.1 and are given in Figure 6.2.2. The post-reweighting closure of these distributions are shown in Figure 6.6.

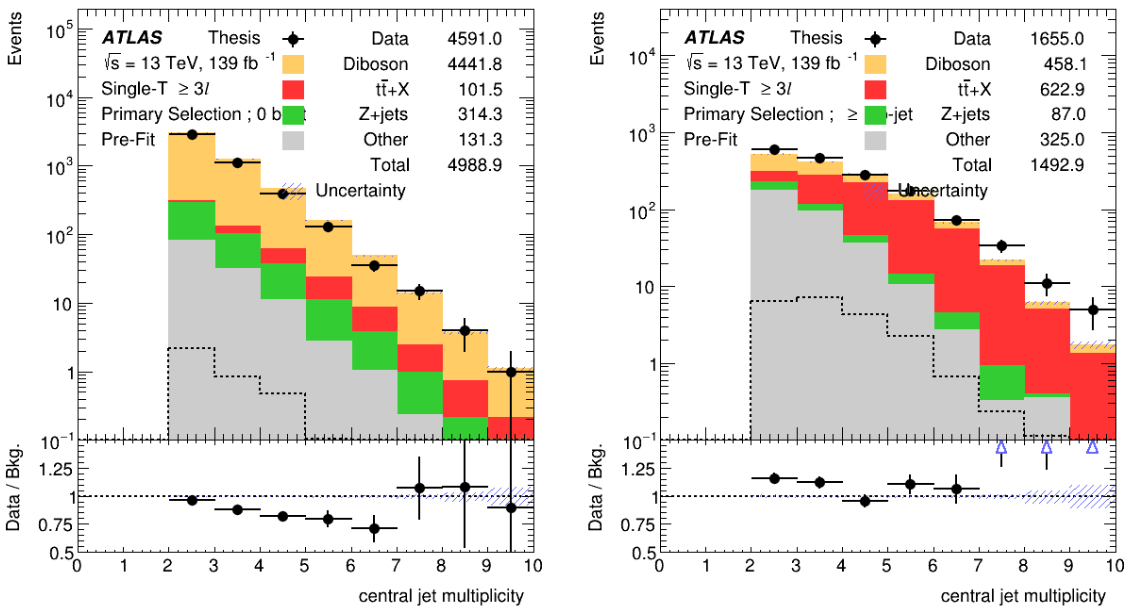

(a) (b)

Figure 6.4: Comparison of MC predicted pre-fit distributions with data for the central jet multiplicity at primary selection for events with (a) 0 b-tagged jets and (b) ≥ 1 b-tagged jets. Only statistical uncertainties are considered. The overlaid black line represents the signal contribution for a Top partner with a mass of 1500 GeV and a coupling of $\kappa = 0.5$.

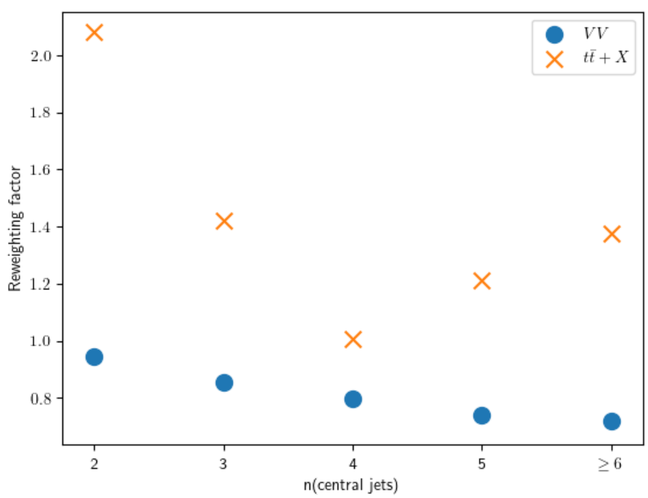

Figure 6.5: Kinematic reweighting factor for VV and $t\bar{t} + X$ processes as a function of the number of central jets.

The pre-fit and post-fit distributions after performing the kinematic reweighting for the main observables in this channel, the transverse momentum of the Z candidate ($p_T(Z)$)

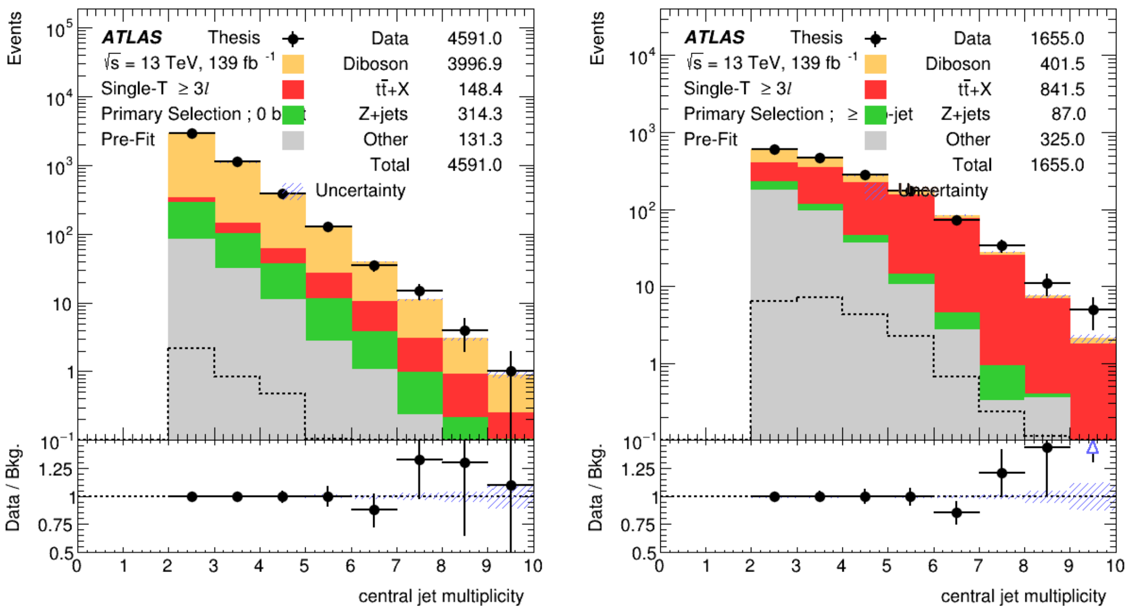

(a) (b)

Figure 6.6: Comparison between kinematically reweighted pre-fit background distributions and data for the central jet multiplicity at primary selection for events with (a) 0 b-tagged jets and (b) ≥ 1 b-tagged jets. Only statistical uncertainties are considered. The overlaid black line represents the signal contribution for a Top partner with a mass of 1500 GeV and a coupling of $\kappa = 0.5$.

and the scalar sum of transverse momenta of jets and leptons ($H_{\mathrm{T}}(\text{jets} + \text{leptons})$), are shown in Figures 6.7–6.11 for the different control and signal regions. The setup for statistical fitting remains identical to what was described in Section 3.5. Statistical fitting is performed to validate the background MC distributions against data in the control regions. However, in addition to the proposed changes in the definition of the control, validation, and signal regions, the current analysis uses the Z boson candidate p_T as the discriminating variable for the analysis. A number of kinematic variables were investigated, they have been summarized in Appendix C. It has been found that $p_T(Z)$ gives the strongest limits and hence, the highest sensitivity to potential VLQ signals. The data and MC yields for different processes in the control, validation and signal regions before and after performing the statistical fitting are given in Table 6.2 and Table 6.3 respectively.

	Diboson CR	1-bjet CR	$t\bar{t}+X$ CR	VR	SR
Single-T (1500 GeV, $\kappa=0.5$)	3.7 ± 0.4	1.12 ± 0.17	0.90 ± 0.16	1.59 ± 0.24	9.6 ± 0.7
Diboson	4000 ± 800	230 ± 70	21 ± 8	6.7 ± 2.3	2.3 ± 0.8
$t\bar{t}+X$	150 ± 80	240 ± 110	210 ± 80	13 ± 6	14 ± 5
Z+jets	310 ± 310	44 ± 34	4 ± 5	0.9 ± 0.6	0.3 ± 0.4
$t\bar{t}$	72 ± 30	91 ± 29	8 ± 9	0.6 ± 1	0.004 ± 0.011
Single top	38.1 ± 2.2	47.6 ± 1.5	16.5 ± 0.8	1.59 ± 0.14	1.95 ± 0.14
Triboson	21.7 ± 1.4	1.20 ± 0.12	0.087 ± 0.023	0.078 ± 0.030	0.023 ± 0.010
Total Bkg.	4600 ± 800	650 ± 140	260 ± 80	23 ± 7	18 ± 5
Data	4591	690	279	21	24
Data/Bkg.	1.00 ± 0.17	1.06 ± 0.23	1.07 ± 0.34	0.91 ± 0.34	1.33 ± 0.46

Table 6.2: Observed number of events in data and pre-fit expected number of signal and background events in the control, validation, and signal regions for the single-production search in the trilepton channel, i.e. before the fit to data in the control regions. For the signal, the expected number of events for the single-T benchmark process with $M_T = 1500$ GeV and $\kappa = 0.5$ is shown. Statistical uncertainties from the limited size of Monte-Carlo samples and systematic uncertainties are added in quadrature. The different nuisance parameters are considered uncorrelated.

	Diboson CR	1-bjet CR	$t\bar{t}+X$ CR	VR	SR
Diboson	3860 ± 190	230 ± 50	21 ± 5	7.1 ± 1.7	2.4 ± 0.6
$t\bar{t}+X$	166 ± 28	259 ± 30	234 ± 20	15.2 ± 2.5	16.0 ± 2.2
Z+jets	430 ± 160	55 ± 18	5.2 ± 2.6	0.8 ± 0.4	0.43 ± 0.24
$t\bar{t}$	76 ± 20	95 ± 23	4 ± 6	0.9 ± 1.2	0.006 ± 0.012
Single top	38.7 ± 2.1	47.2 ± 1.5	16.4 ± 0.8	1.62 ± 0.19	1.96 ± 0.14
Triboson	22.3 ± 1.3	1.21 ± 0.12	0.087 ± 0.023	0.078 ± 0.030	0.023 ± 0.010
Total Bkg.	4590 ± 100	689 ± 28	281 ± 17	25.7 ± 3.0	20.8 ± 2.2
Data	4591	690	279	21	24
Data/Bkg.	1.00 ± 0.03	1.00 ± 0.06	1.00 ± 0.08	0.82 ± 0.21	1.15 ± 0.28

Table 6.3: Observed number of events in data and post-fit expected number of background events in the control, validation, and signal regions for the single-production search in the trilepton channel, i.e. after the fit of background to data in the control and signal regions. Statistical uncertainties from the limited size of Monte-Carlo samples and systematic uncertainties are added in quadrature. Systematic uncertainties take the correlations among nuisance parameters into account.

6.3 Results of Statistical Fitting

The nuisance parameters that represent the different systematic uncertainties regarding detector performance and background and signal modeling have been introduced in Section 3.4. Nearly the same set of systematic uncertainties are accounted for in the current

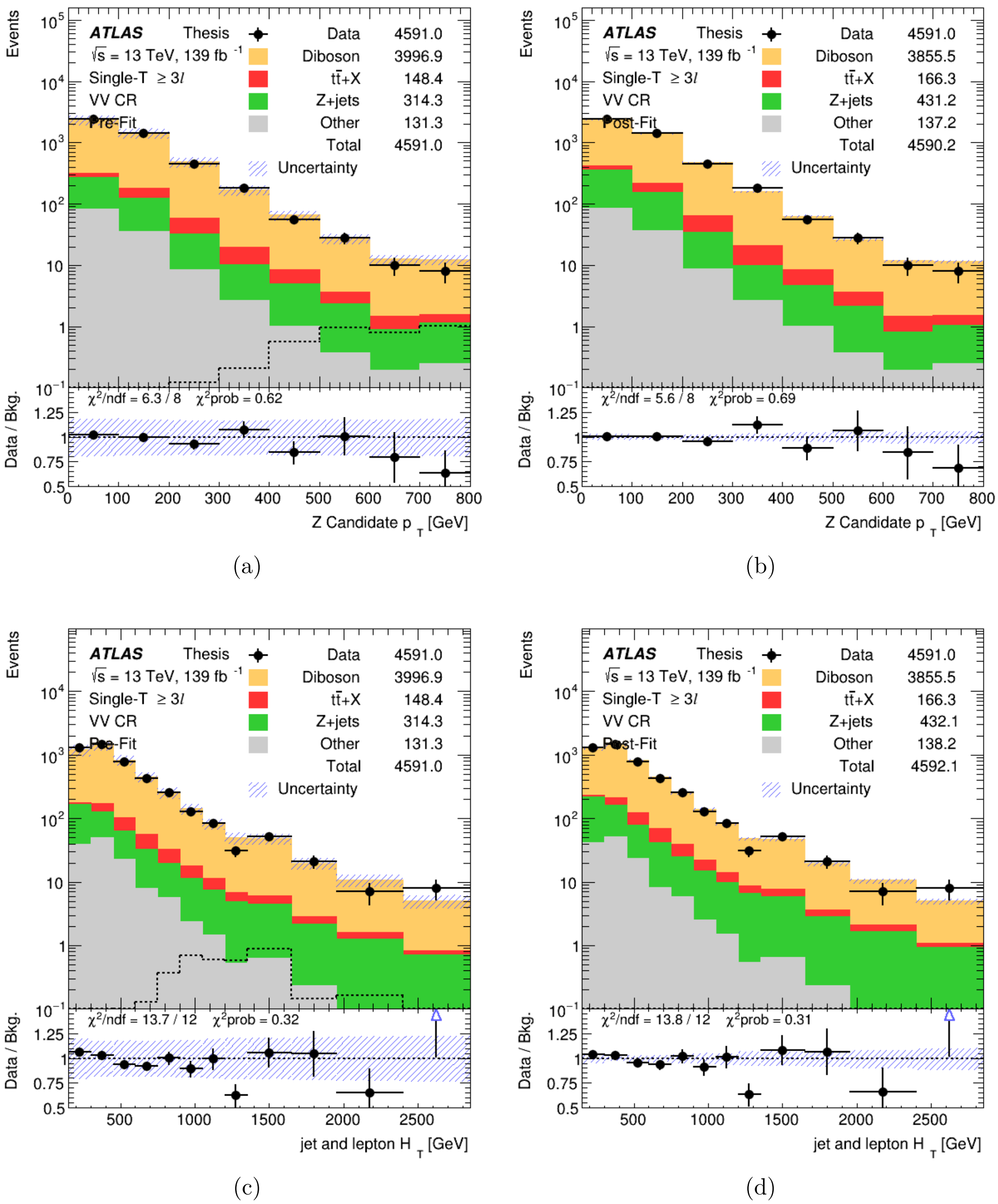

Figure 6.7: Post-fit distribution (right) compared with the pre-fit distributions (left) for the Z candidate p_T (top) and $H_T(\text{jets} + \text{leptons})$ (bottom) distributions in the VV CR. The overlaid black line represents the signal contribution for a Top Partner with a mass of 1500 GeV and a coupling of $\kappa = 0.5$.

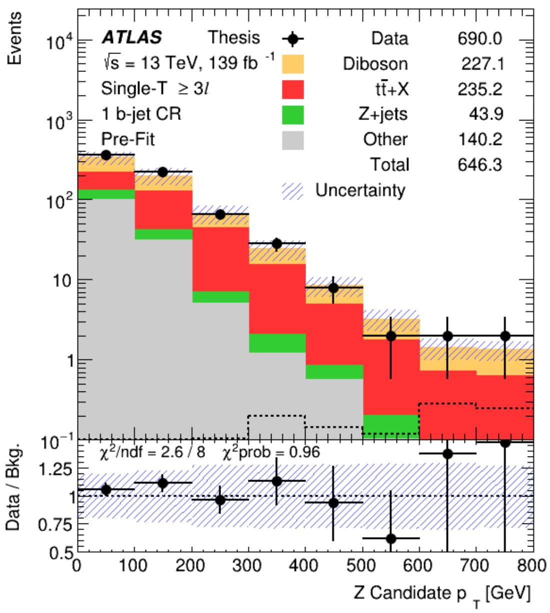

(a)

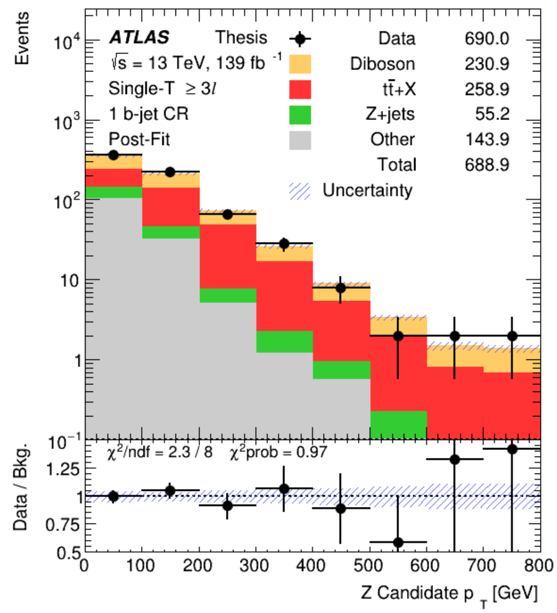

(b)

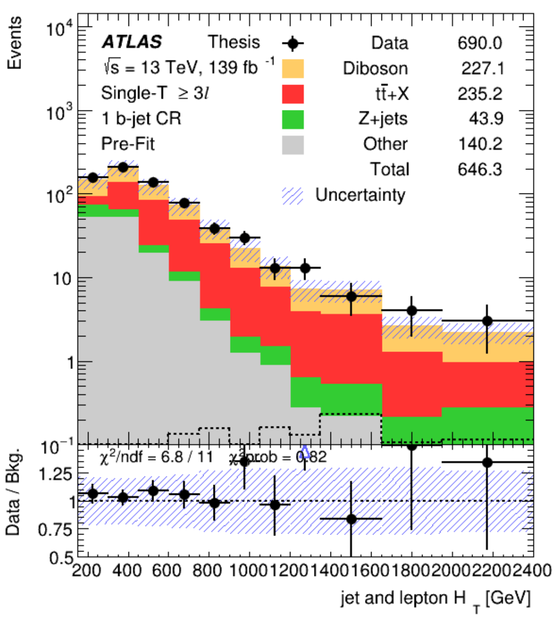

(c)

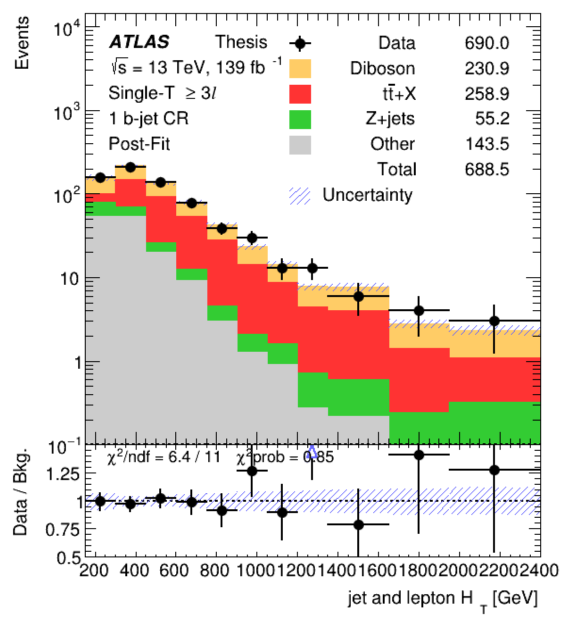

(d)

Figure 6.8: Post-fit distribution (right) compared with the pre-fit distributions (left) for the Z candidate p_T (top) and H_T(jets + leptons) (bottom) distributions in the mixed (1 b-jet) CR. The overlaid black line represents the relative shape of the signal contribution for a Top Partner with a mass of 1500 GeV and a coupling of $\kappa = 0.5$.

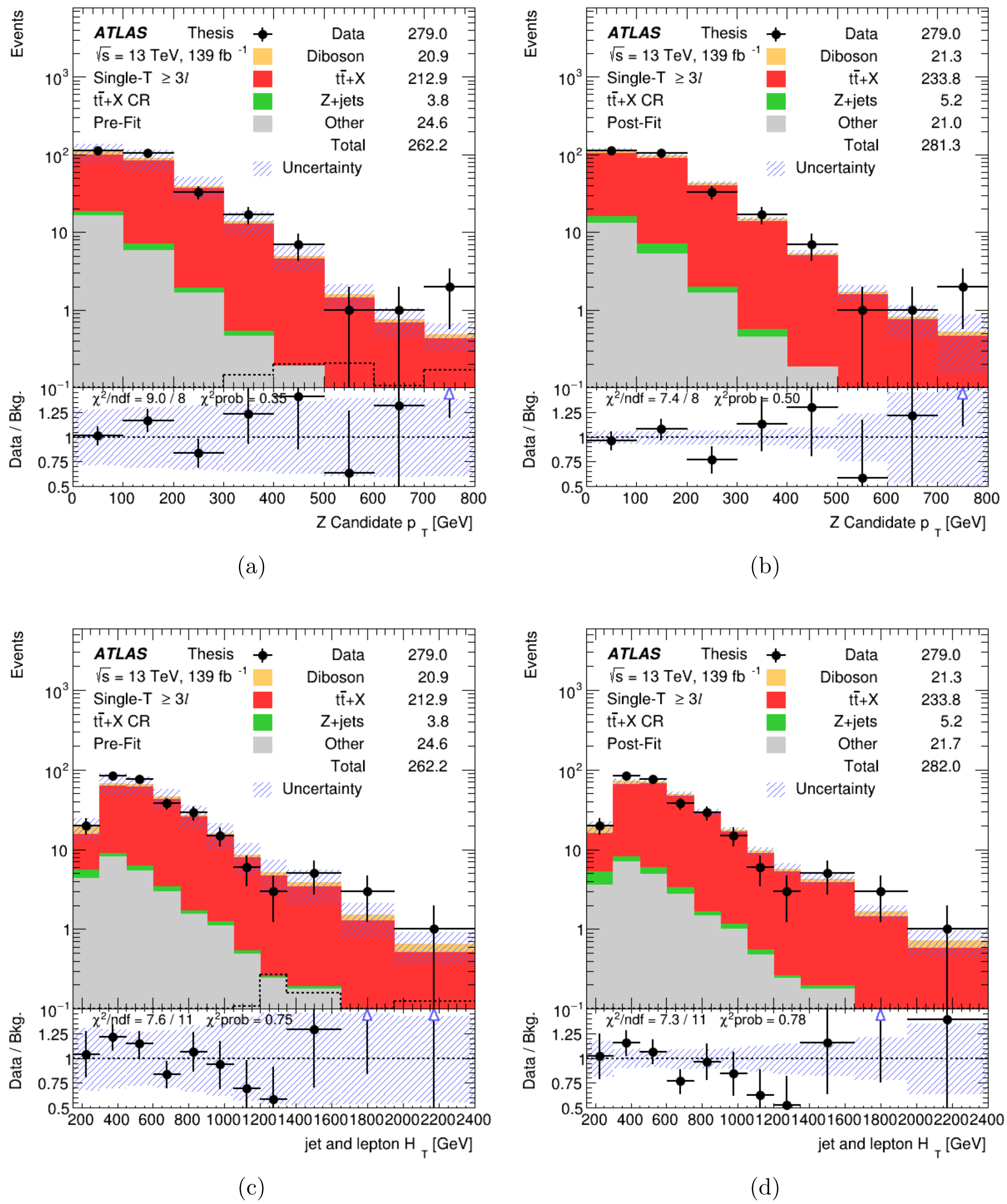

(a) (b) (c) (d)

Figure 6.9: Post-fit distribution (right) compared with the pre-fit distributions (left) for the Z candidate p_T (top) and H_T(jets + leptons) (bottom) distributions in the $t\bar{t}$+X CR. The overlaid black line represents the relative shape of the signal contribution for a Top Partner with a mass of 1500 GeV and a coupling of $\kappa = 0.5$.

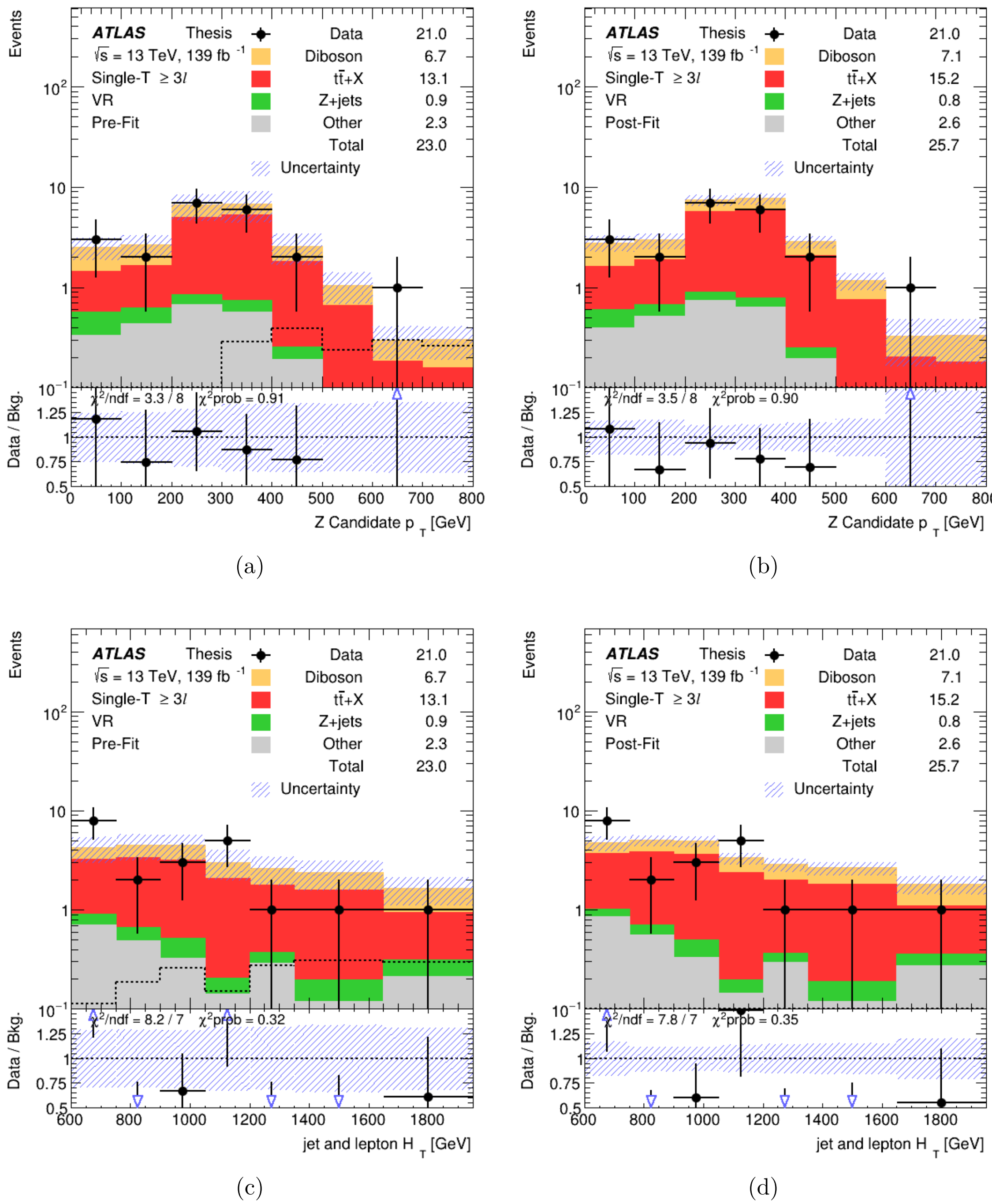

Figure 6.10: Post-fit distribution (right) compared with the pre-fit distributions (left) for the Z candidate p_T (top) and H_T(jets + leptons) (bottom) distributions in the Validation Region. The overlaid black line represents the relative shape of the signal contribution for a Top Partner with a mass of 1500 GeV and a coupling of $\kappa = 0.5$.

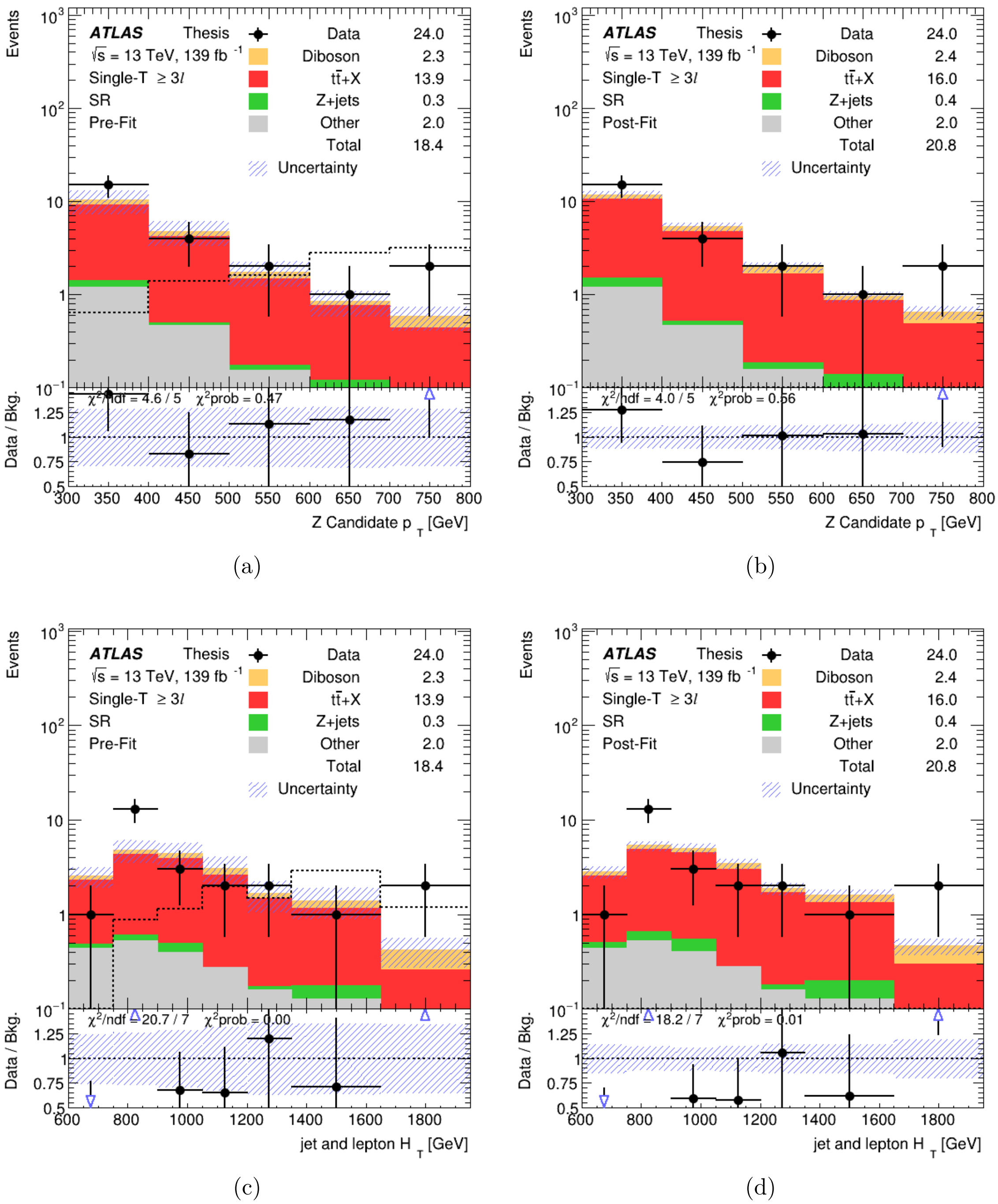

Figure 6.11: Post-fit distribution (right) compared with the pre-fit distributions (left) for the Z candidate p_T (top) and H_T(jets + leptons) (bottom) distributions in the SR. The overlaid black line represents the relative shape of the signal contribution for a Top Partner with a mass of 1500 GeV and a coupling of $\kappa = 0.5$.

analysis. The global uncertainty on the integrated luminosity of the entire Run 2 dataset is set to 1.7%. Envelopes extracted from comparing 7 point variation in renormalization and factorization scales of the $t\bar{t}+V$ samples have been assigned as $\pm 1\sigma$ variation corresponding to the scale variation uncertainty of $t\bar{t}+X$ samples (`ttbarV_PDFScale` NP). Additionally, the scale variation for VV samples have been split into shape and acceptance uncertainties and also decorrelated between regions with 0 and ≥ 1 b-tagged jets. Table 6.4 provides a summary of the different types of uncertainties that are taken into account in the current analysis and the number of NPs associated with each of them.

The normalization of the VV and the $t\bar{t}+X$ processes are fixed by the statistical fitting. The relative strengths of these normalization factors with respect to the kinematically reweighted pre-fit distributions are found to be 1.06 ± 0.36 and 0.97 ± 0.19 respectively. Additional modeling uncertainties are associated with VV and $t\bar{t}+X$ processes to account for the shape variation due to reweighting.

Type of Uncertainty	Number of Nuisance Parameters
Luminosity	1
Pile-up	1
Jet Vertex Tagger	1
Electron Trigger, Resolution, and Efficiency	6
Muon Trigger, Resolution, and Efficiency	15
Jet Reconstruction, Efficiency, and Resolution	38
b-tagging Efficiency	22
Cross-section	3
Z + Jets Modeling	3
VV Modeling	7
$t\bar{t}+X$ Modeling	5
$t\bar{t}$ Modeling	7

Table 6.4: Different types of uncertainties and number of NPs associated with them

Following the recipe of statistical fitting described in Section 3.5, the MC prediction of different background processes are fitted against the observed data in the control and signal regions. In order to assess the compatibility of the observed data distributions with the null hypothesis, i.e. the background-only hypothesis, the fit strategy is to obtain a background-only (BONLY) fit in the control and signal regions (CRSR). Hence, the signal strength parameter μ is removed from the fit.

The stability of the fitting procedure is tested using ASIMOV fit where the observed data in in each region is replaced by a representative dataset obtained from the MC prediction with $\theta = 0$. Figure 6.12 show the result from BONLY-CRSR ASIMOV fit (with no signal injected into the regions) where all the NPs have recovered the best fit values at $\theta = 0$. This plot also shows how the post-fit uncertainty associated with each NP compares with the pre-fit uncertainty predicted by the same NP. The green and yellow bands in Figure 6.12 represent pre-fit $\pm 1\sigma$ and $\pm 2\sigma$ deviations while the error bar on each marker shows how the post-fit $\pm 1\sigma$ deviation compares with the pre-fit one. This plot reveals constraints (restricted or smaller post-fit deviations compared to pre-fit deviations) on NPs associated with Z+jets samples (Zjets_Generator respectively). This constraint largely arises from relatively large variations imposed in normalizations of the corresponding background samples. The line-shapes corresponding to $\pm 1\sigma$ variation of the Zjets_Generator NP is shown in Figure6.13. The relative shape of the variations is mostly independent of the phase space. However, the difference in overall normalization is much larger than what other systematics experience, which is typically of the order of a few percent. This large deviation in normalization causes the NPs to be constrained to maintain the quality of the fit.

Figure 6.14 show the pulls experienced by the NPs when collision data is fitted against the predictions in the CRs. No major pull is experienced by any of the NPs.

While the individual NPs are treated as independent in the pre-fit setting, the correlations among the different NPs are revealed during the maximization of the likelihood function. Figure 6.15 shows the correlation among different NPs where only the pairs of NPs having at least 20% correlation in magnitude are shown. The normalization factor for VV samples (mu_VV) shows strong negative correlation with the VV heavy flavor fraction uncertainty (VV_HF) and the normalization uncertainty associated with scale variations for the VV samples (VV_PDFScale_0b_norm). This is expected since all these NPs directly impact the

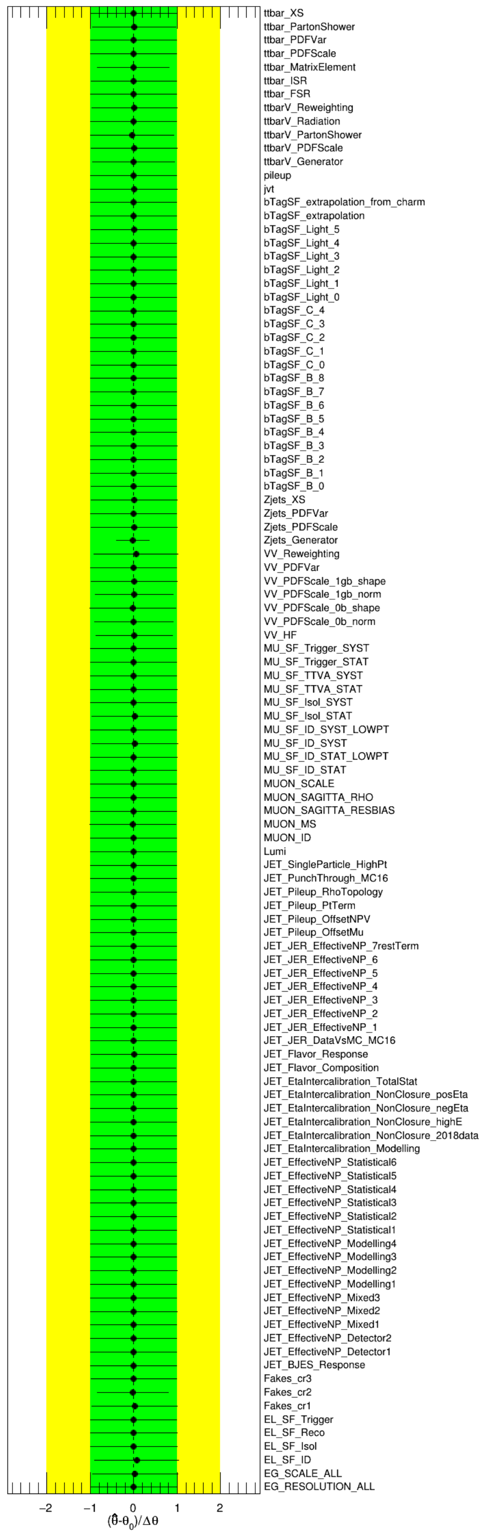

Figure 6.12: Pull plot of the post-fit nuisance parameters for a background-only fit with ASIMOV dataset in control regions.

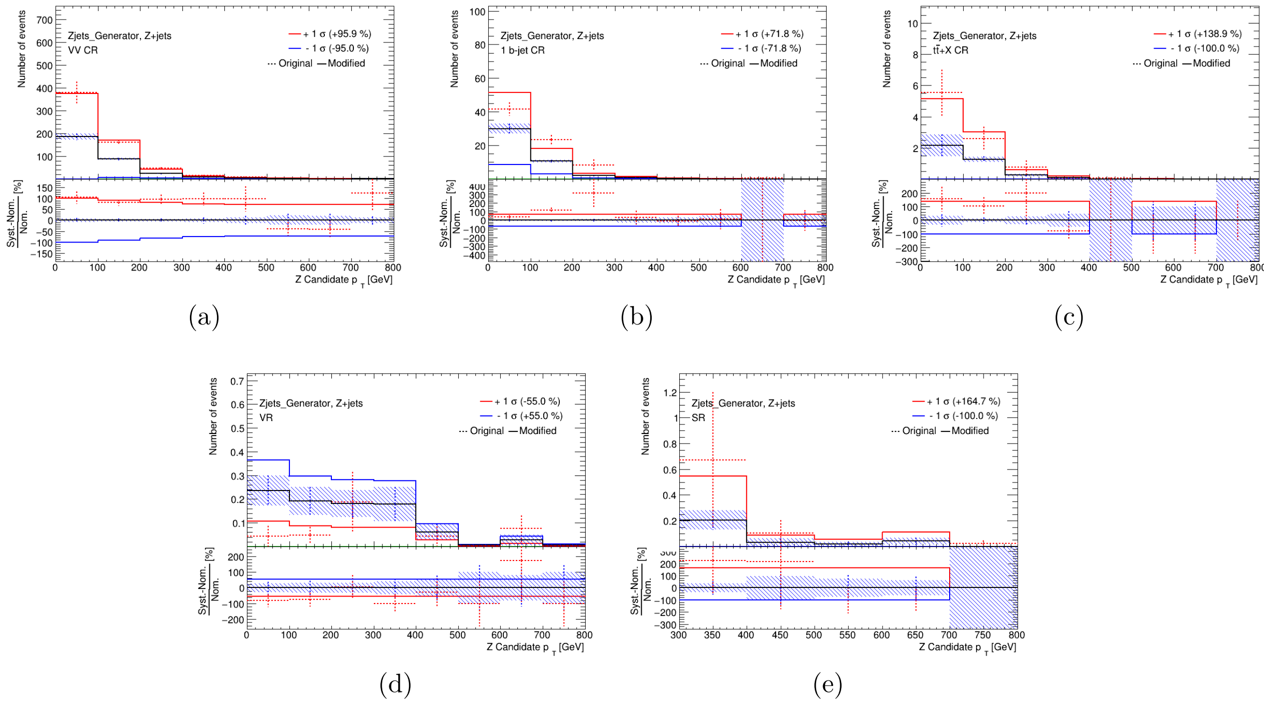

Figure 6.13: Relative variation of Z+jets background lineshape in (a) VV CR, (b) 1 b-jet CR,(c) $t\bar{t}+X$ CR, (d) VR and (e) SR due to $\pm 1\sigma$ variation of the `Zjets_Generator` NP.

overall normalization of VV samples. For similar reasons, the normalization factor for $t\bar{t}+X$ samples (`mu_ttV`) shows strong positive correlations with the $t\bar{t}+V$ generator uncertainty (`ttbarV_Generator`) and the parton shower uncertainty (`ttbarV_PartonShower`).

The ranking plot in Figure 6.16 summarizes the impact of different NPs on the POI. The ranking plot is obtained by performing a signal-plus-background in all CRs and the SR. The plot shows how the POI would vary in response to $\pm 1\sigma$ variation of each NP. Only the top 15 NPs with the largest impact on μ are shown in this plot.

6.4 Limits and Interpretation

The SR data distributions do not show any significant excess. Hence, we calculate expected and observed limits on the $WTZt$ process cross-section at 95% CL using the CL$_s$ method as a function of VLT mass. The limits on $WTZt$ process cross-sections for a benchmark coupling of $\kappa = 0.5$ is given in Figure 6.17a. Both statistical and systematic

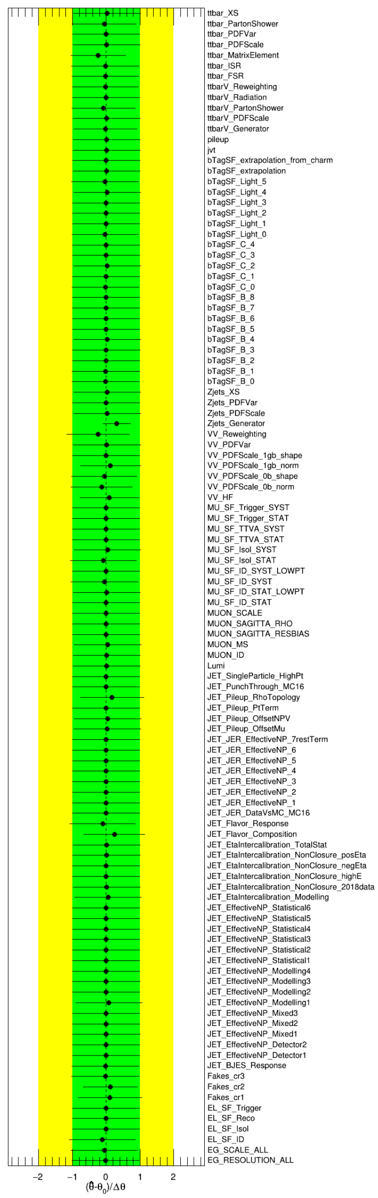

Figure 6.14: Pull plot of the post-fit nuisance parameters for background-only fit with observed data in control regions.

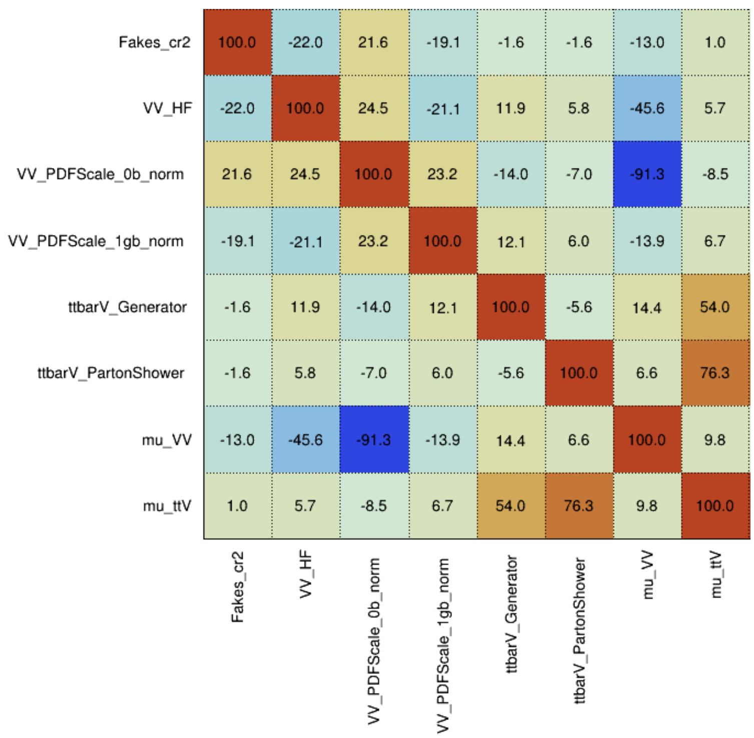

Figure 6.15: Correlation matrix of the post-fit nuisance parameters in the trilepton single-production channel for the background-only fit in control regions.

uncertainties have been accounted for while setting these limits, and a benchmark coupling of $\kappa = 0.5$ for the singlet representation has been chosen for the signal.

However, similar to what we found during limit calculation in Section 3.5.1, the statistical uncertainties remain the dominant factor in determining these cross-section limits. Figure 6.17b shows the cross-section upper limits for different Top Partner masses for a coupling of $\kappa = 0.5$ when statistical uncertainties alone are taken into account. The ratio between stat-only limits and limits accounting for both systematic and statistical uncertainties is consistently larger than 0.9 for all choices of Top Partner masses, implying that the NPs play a rather marginal role in determining the upper limits on $WTZt$ process cross-section.

Since the cross-section limits are functions of both the mass and coupling of the Top Partner, these limits are calculated for a fine grid of κ. These limits are shown in Appendix D. The limits calculated for a fine grid of Top Partner mass and couplings allow using the interpretation framework laid out in Chapter 4.

The interpretation framework described in Chapter 4 translates these cross-section limits into limits on the free parameters of the VLQ Lagrangian. Figure 6.18a shows the limits on the coupling associated with the TWb vertex, c_W, while the branching ratio in the Z channel is set to a fixed value of 0.25. Comparing with the limits that are obtained from analyzing the partial Run 2 dataset (Figure 3.18a), the current analysis sets much stronger limits on c_W for a wider range of masses. The same limits are cast in terms of mixing angle between the T and the top quark in a singlet model in Figure 6.18b. Having a finer grid of exclusion limits as a function of Top Partner mass and coupling, the current limits have a much smoother lineshape compared to what we found in Figure 3.18b. It should be noted that the limits shown in this chapter are from analyzing the data in trilepton channel alone, while the limits shown in Chapter 3 are from combination of trilepton and dilepton channels. Given the limits from the trilepton channel alone are much stronger than what was obtained from the combination of two channels in the previous analysis, the foreseen combination of the two channels is expected to produce even more competitive results.

A more generalized interpretation is provided in Figure 6.19a where the limits on expected excluded VLQ mass are calculated as a function of c_W and c_Z couplings. The Higgs vertex coupling is set by requiring equal branching ratios in the Higgs and Z channels, as expected in most VLQ representations at larger VLQ masses [51]. The interpretation as a function of BR($T \to Wb$) and relative decay width $\frac{\Gamma}{M}$ is given in Figure 6.19c.

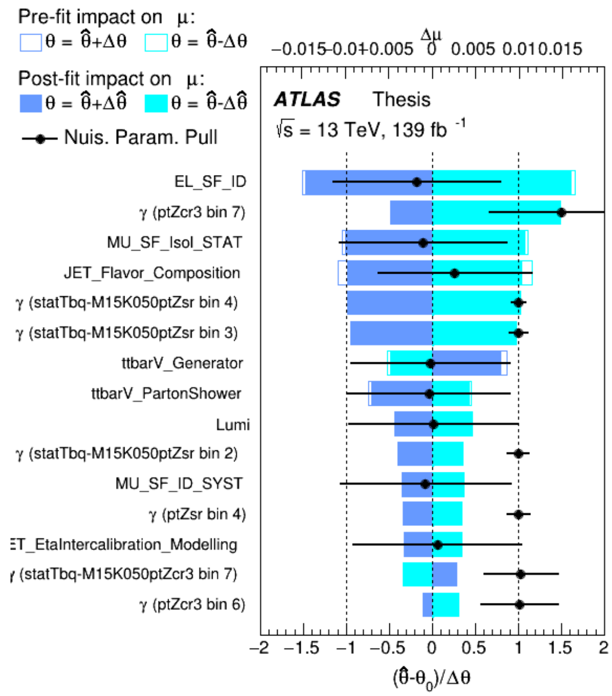

Figure 6.16: Ranking plot for the highest impact post-fit nuisance parameters in the trilepton single-production channel for the signal-plus-background fit in control and signal regions. Data is blinded in the signal region and ASIMOV dataset is used instead.

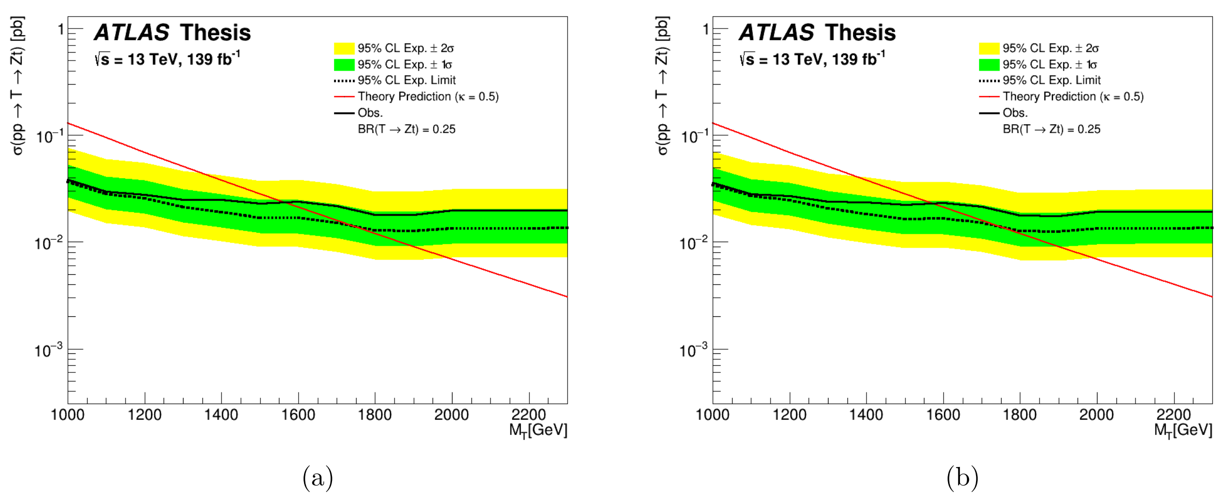

Figure 6.17: Expected and observed upper limits on the $WTZt$ process cross-section as a function of the mass of T at 95% C.L. for a benchmark coupling of $\kappa = 0.5$ and singlet representation when (a) both statistical and systematic uncertainties are considered and (b) only statistical uncertainties have been included.

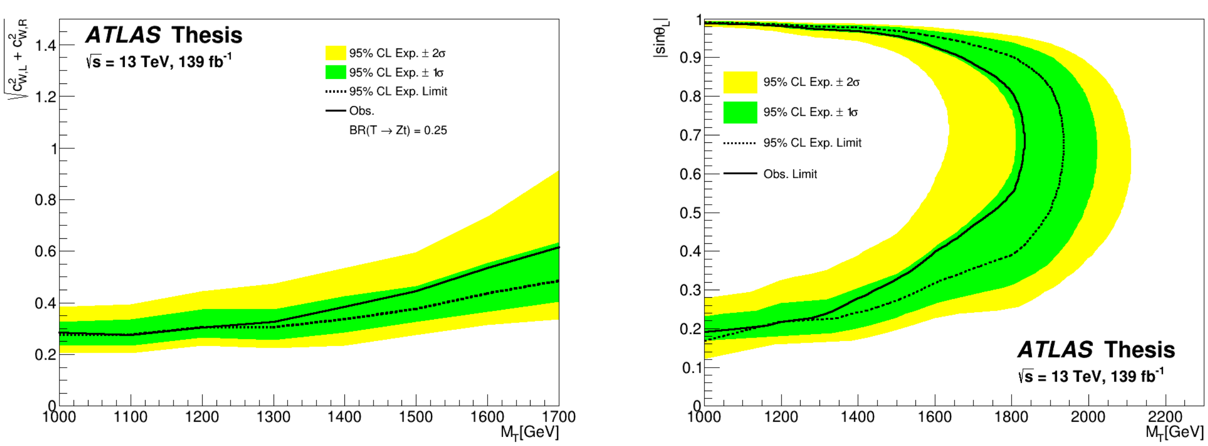

(a)

(b)

Figure 6.18: (a) Cross-section limits interpreted in terms of coupling between a T and the W boson as a function of the VLT mass while the branching ratio is set to $\mathrm{BR}(T \to Zt) \approx 0.25$ in fixed branching ratio model. (b) The same limits are recast in terms of mixing angle between the T and a top quark in a singlet model as a function of the VLT mass where the region enclosed by the two branches are excluded.

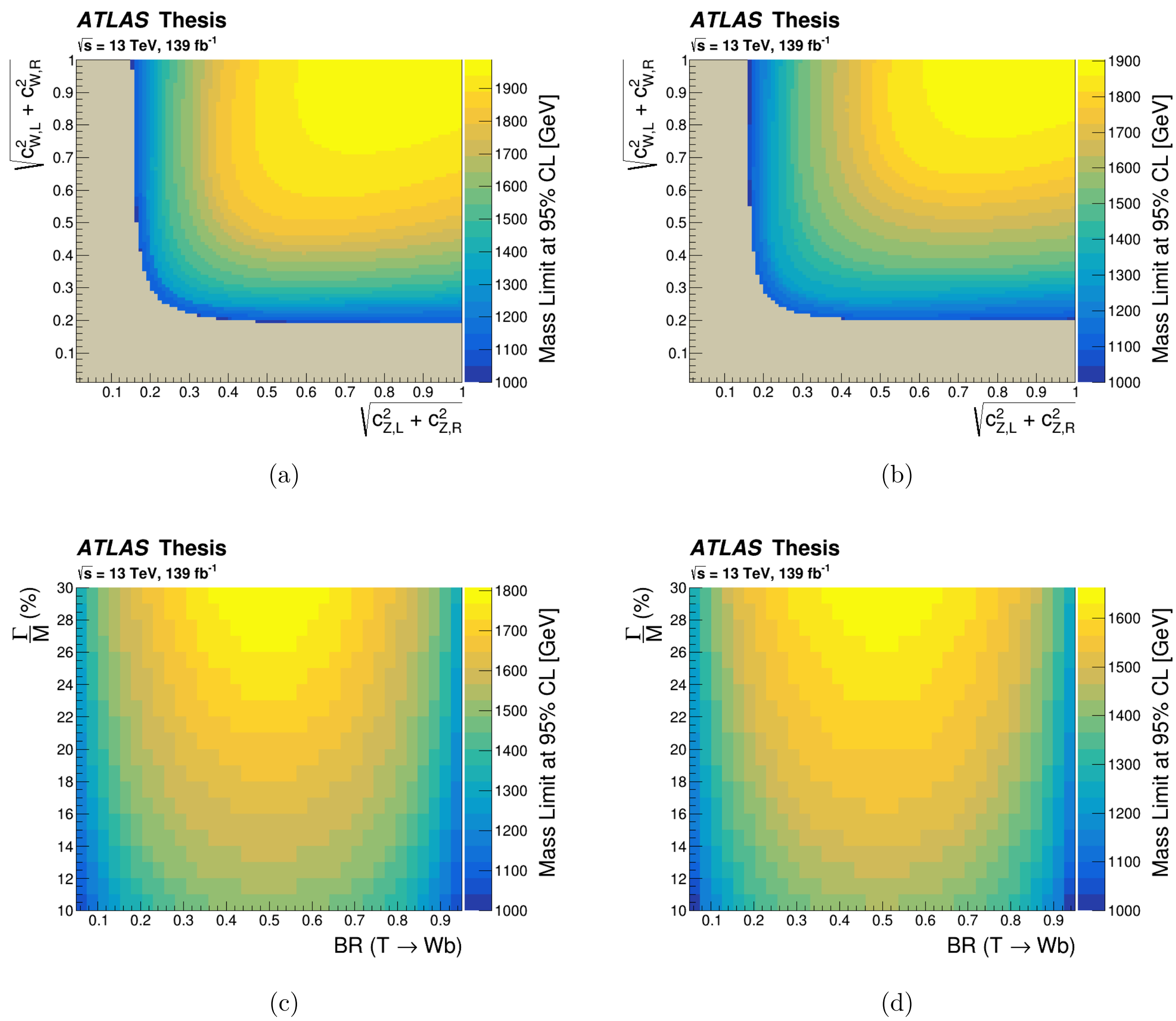

Figure 6.19: (a) Expected and (b) Observed cross-section limits interpreted in terms of upper limits on excluded T mass as a function couplings c_W and c_Z. The grey regions in the low coupling corners represent parametric subspaces beyond the sensitivity of the analysis. In (c) and (d) respectively, the same limits are recast in terms of upper limits on excluded T mass as a function couplings BR($T \to Wb$) and relative decay width $\frac{\Gamma}{M}$ (%). The coupling to the Higgs channel is set by requiring equal branching ratios in the H and Z channels.

Chapter 7

Summary of a Phase Transition

Over the course past six chapters, I have tried to summarize the work I have done as a graduate student. Many of these projects are indeed work in progress, and there is room for improvement and progress. An immediate goal of near future is to complete the ongoing analysis described in Chapter 6. The results from the accompanying dilepton channel will be combined with the final results of the trilepton channel to calculate the discovery potential and combined limits on single production of Top Partners. Right now this analysis is limited to the study of W-mediated production of Top Partners decaying to a Z boson and a t quark, the $WTZt$ signal process while we are working on generating the MC samples for the $ZTZt$ processes. Given the large number of Feynman diagrams that contribute to the production of $ZTZt$ signals when s and t channel diagrams are jointly taken into account, generating MC for this process is computationally very expensive. Once these additional signal samples become available, they will be incorporated in the ongoing analysis to provide an even broader, model-independent search of Top Partners and interpretation thereof.

Much of the work presented on interpretation of single VLQ searches in Chapter 4 and VLQ signal modeling in Chapter 5 has been adapted by all ongoing single VLQ search attempts within ATLAS. The proposed interpretation framework gives a compact and comprehensive representation of VLQ limits in terms of physical quantities that actually dictate their physics. Besides, the studies done to evaluate the relative contribution of the t channel diagrams for the single VLQ processes have been extended for other single VLQ analyses as well. Right now, there are eight different analyses within ATLAS are looking for single VLQ signatures in a multitude of final states. Studies have been done to evaluate contribution of t channel diagrams for all of these searches by directly using the code and framework used to obtain the results in Chapter 5. Nevertheless, these studies can be improved and perfected. Our current estimates rely on leading order signal simulation. Extending simulation of VLQ single production at large decay widths and next-to-leading order still remains a major challenge.

The LHE Refurbishing algorithm introduced in Chapter 5 has been successfully used to apply matrix element based event-by-event reweighting for MC simulation used by all single VLQ analyses. The novelty of this algorithm lies in its simplicity and generality. Our estimates suggest that this algorithm has given us access to a single VLQ signal grid that would otherwise have been about an order of magnitude more expensive in terms of computational and memory resources. However, this algorithm can find its use beyond the scope of VLQ searches. As it simply relies on narrow width approximation of SM particles, LHE refurbishing can make matrix element based reweighting possible for almost any beyond standard model search where the final state particles emerge from decay of SM vector bosons and/or top quark.

Together with the generalized interpretation strategy and unified, harmonized signal modeling of VLQs, ATLAS is now aiming to perform a combination of single VLQ searches. As the many single VLQ searches within ATLAS, including the one presented in this dissertation, reach a more matured stage, we will perform a simultaneous statistical analysis of all these searches that will give us a superior discovery potential or significantly stronger limits on the parameters of VLQ Lagrangian. The combination of single VLQ searches using the Run 2 dataset will remain a major research effort for the ATLAS collaboration in the next year. As Run 3 for the LHC is planned to start in 2022, the result of this combination will set an important benchmark for single VLQ searches for future.

Reweighting in general is a very powerful tool to meet the ever growing challenges MC simulation for large collider experiments. Reweighting is widely used for estimating variations of choice of renormalization and factorization scales, variation of parton density functions, and effects related to detector performance and data taking environments. However, a large part of the demand for MC comes from simulation of physics beyond the standard model– VLQs, heavy vector bosons, and dark matter candidates to name a few. Most of these models probe a grid of hyperparameters of the corresponding novel Lagrangian. Reweighting MC datasets for alternate choices of model parameters can be very useful and economical. Exploring non-conventional means of such reweighting can be very useful to recycle existing MC datasets for extending existing analyses, defining new analyses or phenomenological reinterpretation of published analyses. I am working on developing a neural network based reweighting method that can extract the reweighting factors from partial information about the hard scattering process. This work is still in its early stages, but studies performed on reweighting single VLQ signals are promising.

The LHC has already delivered its greatest promise, the Higgs boson. However, it is no secret that the absence of evidence in favor of any new physics across a wide range of popular and strong beyond SM theories is at least creating tensions. People, including expert physicists [180], are questioning the wisdom of our theoretical and experimental approaches to find new physics. But my journey as a graduate student has made me realized that finding the correct solution often requires exhaustive search. A discovery is always welcome, but it requires the collective effort of generations of physicists, many of whom will never make newspaper headlines. Work done by every physicist is just another small avenue traversed on the way, and I sincerely hope that the work I have presented in this thesis qualifies as the first right step along that road.

Appendices

Appendix A

Studies on Reduction of Pair Produced VLQ Signal

Search for single production of VLQs requires reduction of pair production contamination, not only to decouple different modes of VLQ production but also to meaningfully interpret the single production VLQ limits. Since pair production events are likely to be enriched in jets, it is expected that the jet multiplicity and H_{T}(jets) should provide some degree of separation between single production and pair production events. The following figures show the distributions for these variables in the unconstrained signal region (signal region without requiring any pair production contamination mitigation) for mass points of 0.9, 1.2 and 1.4 TeV. The single production events in these plots have been normalized to cross sections calculated by MadGraph for a benchmark coupling of $\kappa_T = 0.5$.

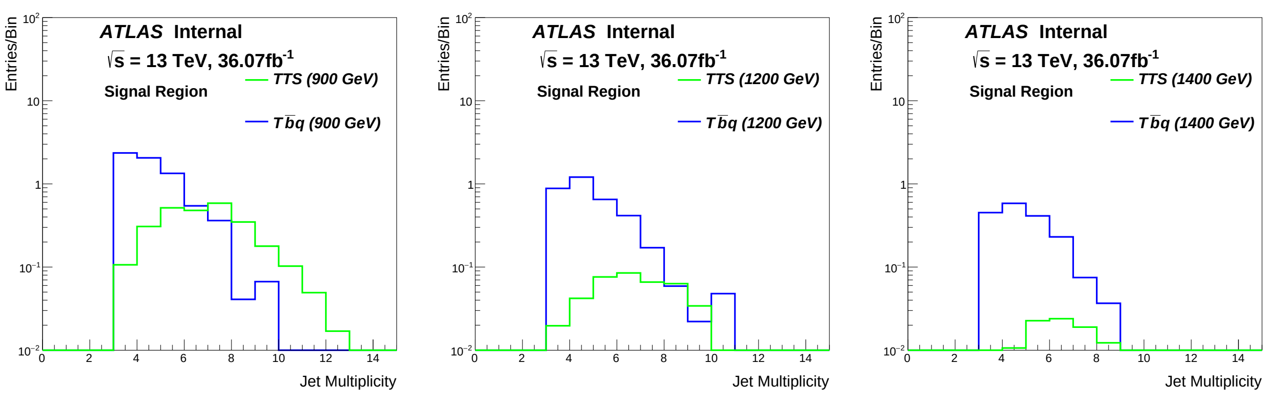

(a) (b) (c)

Figure A.1: Jet Multiplicity distribution of single and pair production events in unconstrained signal region for 900 GeV (a), 1200 GeV (b), and 1400 GeV (c) mass points.

As shown in Figure A.1, the jet multiplicity distribution shows reasonable discriminating power for lower mass points but performs poorly at higher mass points. On the other hand, Figure A.2, H_{T}(jets) distribution has better discriminating characteristics for higher

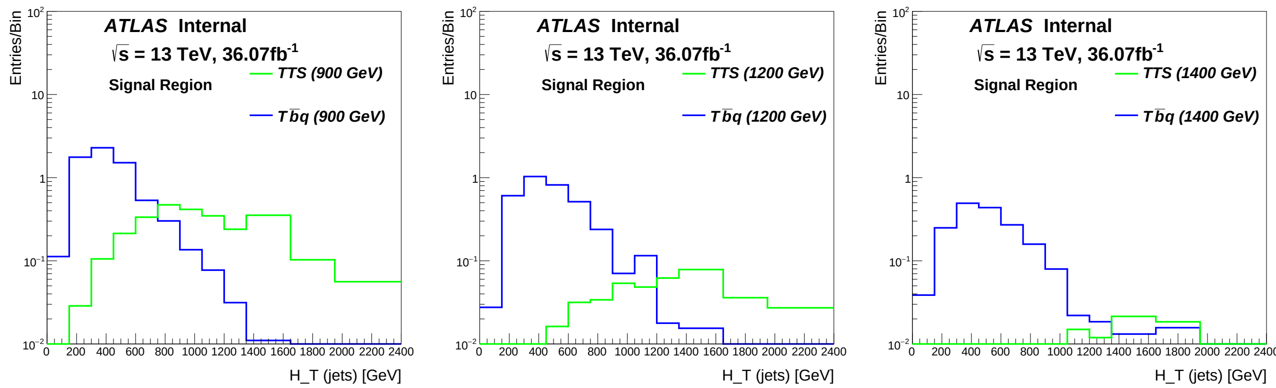

(a) (b) (c)

Figure A.2: H_{T}(jets) distribution of single and pair production events in unconstrained signal region for 900 GeV (a), 1200 GeV (b), and 1400 GeV (c) mass points.

mass points. This motivates using the distribution of $n(\text{jets}) \times H_{\mathrm{T}}(\text{jets})$ (Figure A.3) which combines together the discriminating features of these two variables.

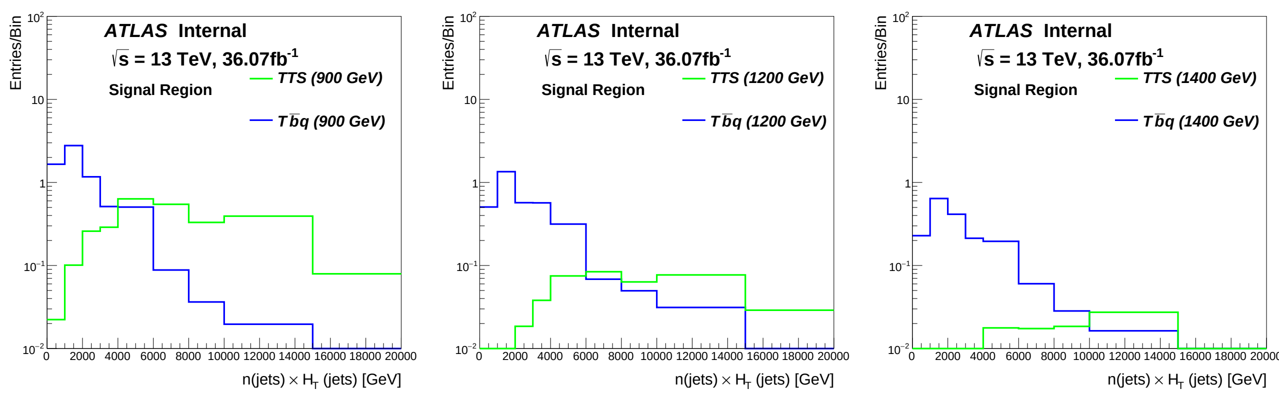

(a) (b) (c)

Figure A.3: $n(\text{jets}) \times H_{\mathrm{T}}(\text{jets})$ distribution of single and pair production events in unconstrained signal region for 900 GeV (a), 1200 GeV (b) and 1400 GeV (c) mass points.

Figure A.4 compares the performance of cuts on jet multiplicity, H_{T}(jets) and $n(\text{jets}) \times H_{\mathrm{T}}(\text{jets})$ with different benchmark cuts. The efficiency is measured as the fraction of events from unconstrained signal region that satisfies the designated cut. It can be seen that $n(\text{jets}) \times H_{\mathrm{T}}(\text{jets}) < 6$ TeV serves best in retaining most of the single production events from the unconstrained signal region while substantially reducing pair production contamination for all mass points.

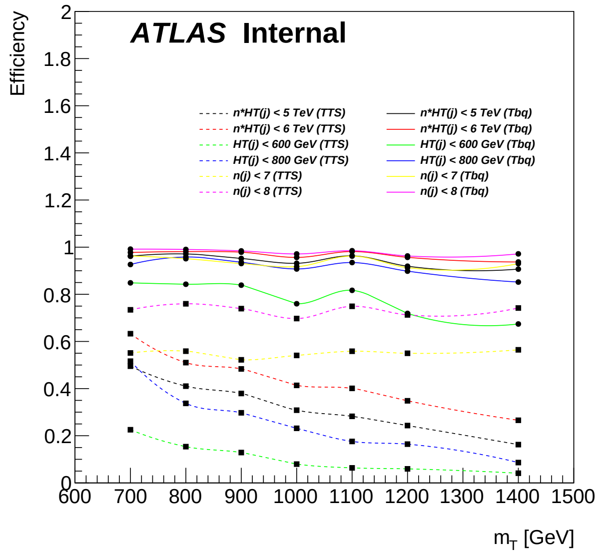

Figure A.4: Efficiency, as a function of VLT mass, of the n(jets),H_{T}(jets) and n(jets) $\times$ H_{T}(jets) cuts in selecting the single production events (solid lines) and in selecting the pair production events (dashed lines)

The final discriminant used in the trilepton channel is $H_T(\text{jets} + \text{leptons})$, it is important to investigate the impact of the cut on the distribution of the discriminant. As showed in Figure A.5, the shape of the distribution of the final discriminant is similar before and after applying the cut.

The yields from pair and signal production events in the signal region before and after applying the cut are summarized in Table A.1.

Kinematic signatures of the control regions, the $t\bar{t} + V$ control region in particular, are very similar to that of pair production events. Hence, the cut on $n(\text{jets}) \times H_{\mathrm{T}}(\text{jets})$ have been incorporated at preselection and its impact on the control region has been studied as well. Table A.2 shows that placing a cut for $n(\text{jets}) \times H_{\mathrm{T}}(\text{jets}) < 6$ TeV, we lose a minimal fraction of background events in both control regions where we still manage to substantially reduce contamination from pair production events.

A final study was done to study the effect of this cut on exclusion limits. Statistics

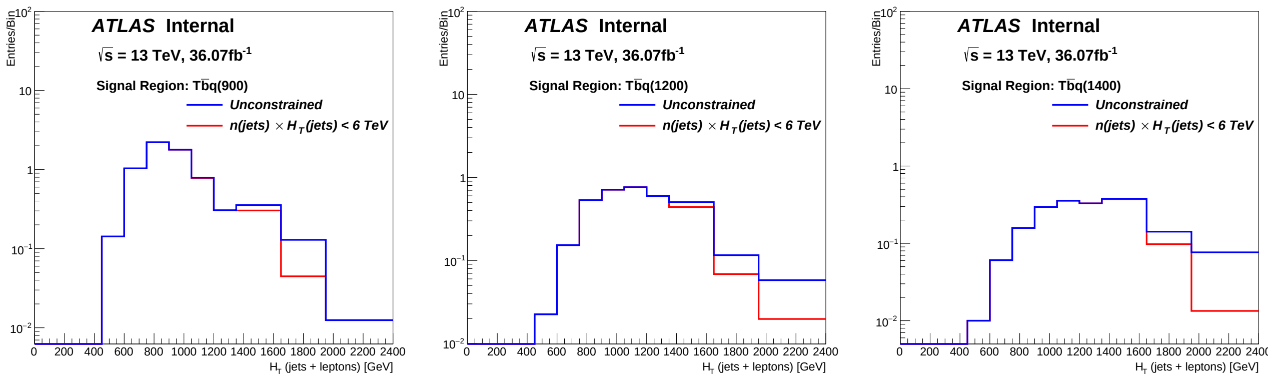

(a) (b) (c)

Figure A.5: $H_{\mathrm{T}}(\text{jets}+\text{leptons})$ distribution in signal region before and after applying the $n(\text{jets})\times H_{\mathrm{T}}(\text{jets}) < 6$ TeV cut for 900 GeV (a), 1200 GeV (b), and 1400 GeV (c) mass points.

	Pair Production Yields		Single Production Yields	
Mass Point	Before	After	Before	After
700	9.43	5.97	6.13	5.99
800	5.15	2.63	7.07	6.94
900	2.67	1.29	6.69	6.55
1000	1.45	0.60	5.61	5.37
1100	0.77	0.31	4.51	4.43
1200	0.40	0.14	3.42	3.27
1400	0.106	0.0281	1.79	1.68

Table A.1: Pair and signal production yields in signal region before and after applying the $n(jets) \times H_T(jets) < 6$ TeV cut

	VV Control Region		$t\bar{t}+V$ Control Region	
Mass Point	Before	After	Before	After
700	6.99	5.48	54.19	38.82
800	3.19	2.25	26.17	17.67
900	1.65	1.07	12.44	7.96
1000	0.912	0.536	6.44	3.61
1100	0.541	0.329	3.43	1.78
1200	0.321	0.186	1.89	0.903
1400	0.112	0.0482	0.530	0.216
900 (Doublet)	2.338	1.337	24.821	13.719
All Backgrounds	1026.18	1018.37	259.98	257.3

Table A.2: Yields from pair production events and standard model backgrounds in control regions before and after applying the $n(\text{jets}) \times H_{\mathrm{T}}(\text{jets}) < 6$ TeV cut only limits were obtained using TRexFitter and no significant change was observed.

Mass Point	Before	After
700	0.455	0.457
800	0.308	0.308
900	0.248	0.248
1000	0.210	0.211
1100	0.186	0.183
1200	0.173	0.173
1400	0.170	0.166
1600	0.131	0.131
1800	0.137	0.134

Table A.3: Exclusion limits on $\sigma(pp \rightarrow T\bar{b}q) \times BR(T \rightarrow Zt)$ [pb] at 95% confidence level before and after the pair production contamination suppression

Appendix B

MadGraph Process Syntax for Different Processes

The following block of code describes the common configuration used for different signal modeling studies presented in Chapter 5

```
import model VLQ_v4_4FNS_UFO
define p = g u c d s u~ c~ d~ s~
define j = g u c d s u~ c~ d~ s~
define bb = b b~
define WW = w+ w-
define tt = t t~
define ferm = ve vm vt u c d s b e- mu- ta- e+ mu+ ta+ ve~ vm~ vt~ u~ c~ d~ s~ b~
define VLQ = tp tp~
```

The aforementioned code block primarily identifies the necessary particles and creates multi-particle denominations to be used in the exact `generate` sequence. The following enlists the processes previously explored and the corresponding MadGraph syntax for event generation.

- `PROC-FULLDECAY`: $WTZt$ process where the decay chain of Z boson and t quark are included

  ```
  generate p p > j VLQ bb / tp tp~ p t t~ y y~ bp bp~ x x~ z h a,
  (VLQ > z tt, z > ferm ferm, tt > ferm ferm bb)
  ```

- `PROC-PARTDECAY`: $WTZt$ process where the decay chain of Z boson and t quark are not included, identical to the `PROC-SIGONLY` process used to generate signal-only events for interference studies

  ```
  generate p p > j VLQ bb / tp tp~ p t t~ y y~ bp bp~ x x~ z h a,
  (VLQ > z tt)
  ```

- `PROC-INCLUSIVE`: Process with the same initial and final sates as for the $WTZt$ process, but allows both VLQ and SM propagators

```
generate p p > j z tt bb / y y~ bp bp~ x x~ z h a
```

- `PROC-BKGONLY`: Process with the same initial and final sates as for the $WTZt$ process, but allows only SM propagators

```
generate p p > j z tt bb / y y~ bp bp~ x x~ z h a tp tp~
```

- t-channel inclusive $WTZt$ Process (VLQ Propagators only): $WTZt$ process inclusive of both s and t-channel diagrams, but allows only VLQ propagators

```
add process p p > j t z b~ /p y y~ bp bp~ x x~ z h a~ VLQ==2 QED=1
add process p p > j b z t~ /p y y~ bp bp~ x x~ z h a~ VLQ==2 QED=1
```

  The coupling orders specified in the process syntax ensures that diagrams that include exactly two VLQ electroweak couplings and at most one SM QED coupling in the matrix-element are included.

- t-channel inclusive $WTZt$ Process (VLQ and SM Propagators): $WTZt$ process inclusive of both s and t-channel diagrams along with SM propagators

```
add process p p > j t z b~ /p y y~ bp bp~ x x~ z h a~ VLQ=0
add process p p > j b z t~ /p y y~ bp bp~ x x~ z h a~ VLQ=0
add process p p > j t z b~ /p y y~ bp bp~ x x~ z h a~ VLQ==2 QED=1
add process p p > j b z t~ /p y y~ bp bp~ x x~ z h a~ VLQ==2 QED=1
```

- t-channel inclusive $ZTZt$ Process (VLQ Propagators only): $ZTZt$ process inclusive of both s and t-channel diagrams, but allows only VLQ propagators

```
add process p p > j t z t~ /p y y~ bp bp~ x x~ WW h a~ VLQ==2 QED=1
```

- t-channel inclusive $ZTZt$ Process (VLQ and SM Propagators only): $ZTZt$ process inclusive of both s and t-channel diagrams along with VLQ propagators

```
add process p p > j t z t~ /p y y~ bp bp~ x x~ WW h a~ VLQ==2 QED=1
add process p p > j t z t~ /p y y~ bp bp~ x x~ WW h a~ VLQ=0
```

- s-channel only $ZTZt$ Process: $ZTZt$ process for s-channel diagrams

```
generate p p > j VLQ tt / tp tp~ p t t~ y y~ bp bp~ x x~ WW h a,
(VLQ > z tt)
```

Appendix C

Expected Limits on $WTZt$ Process Cross-section for Different Choices of Discriminating Variables Full Run 2 data

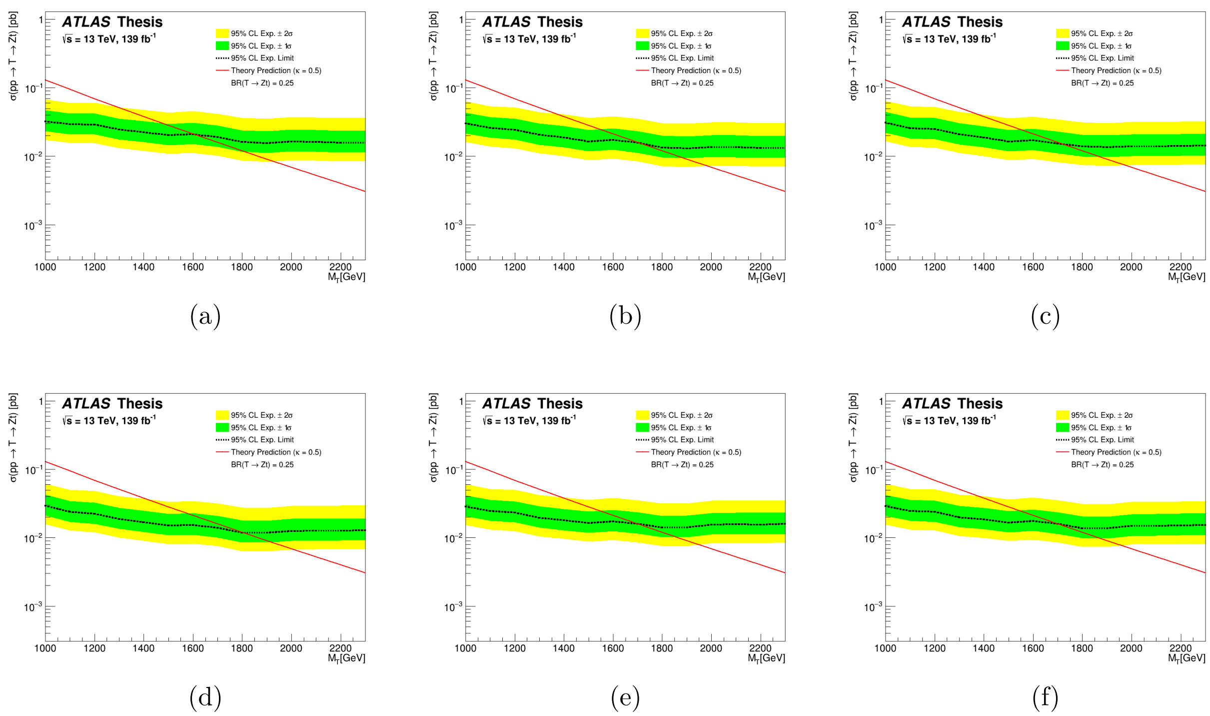

Figure C.1: Excluded cross-section limit at 95% CL for $\kappa = 0.5$ when the discriminating variable is chosen as (a) scalar sum of jet and lepton p_T, $H_T(\text{jets} + \text{leptons})$, (b) scalar sum of lepton p_T, $H_T(\text{leptons})$, (c) invariant mass of the three leptons, $m_T(l_1 l_2 l_3)$, (d) p_T of Z boson candidate, $p_T(Z)$, (e) invariant mass of the Z boson candidate and the leading b-jet, $m_T(Z b_{\text{lead}})$, and (f) invariant mass of the three leptons and the leading b-jet, $m_T(l_1 l_2 l_3 b_{\text{lead}})$. Only statistical uncertainties are considered. The Z-boson candidate gives the strongest limit and has the strongest sensitivity for this analysis

Appendix D

Expected and Observed Limits on $WTZt$ Process Cross-section for Different Choices of κ from the Full Run 2 data

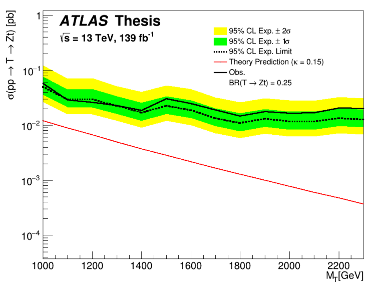

(a)

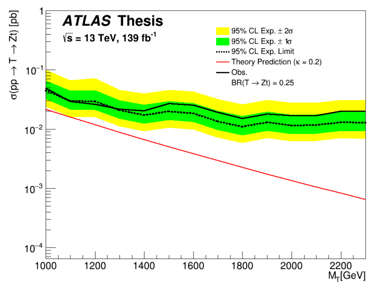

(b)

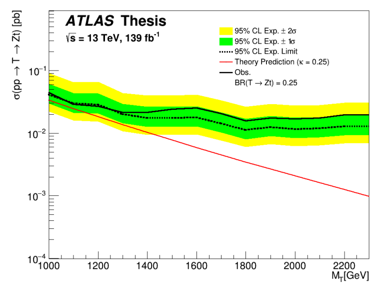

(c)

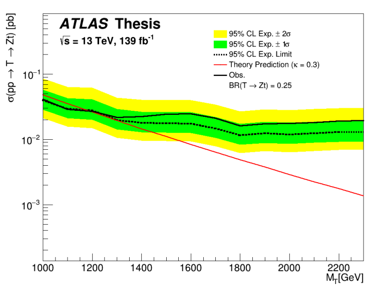

(d)

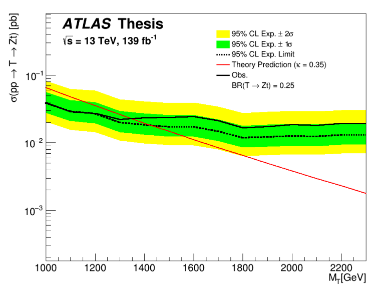

(e)

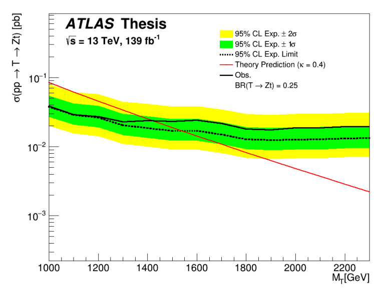

(f)

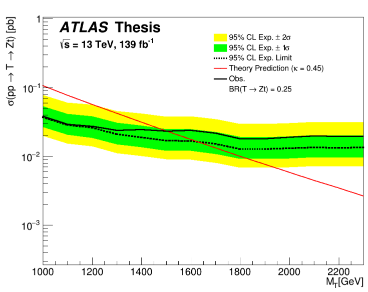

(g)

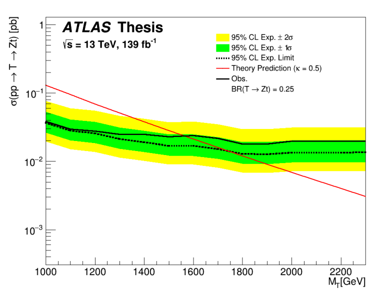

(h)

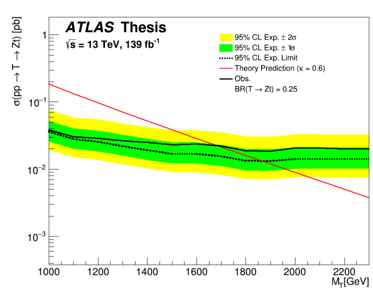

(i)

Figure D.1: Excluded cross-section limit at 95% CL for κ values of 0.15, 0.2, 0.25 (top row, left to right), 0.3, 0.35, 0.4 (middle row, left to right) and 0.45, 0.5, 0.6 (bottom row, left to right) respectively

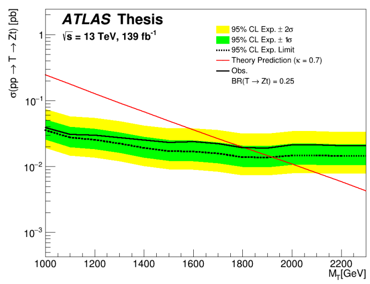

(a)

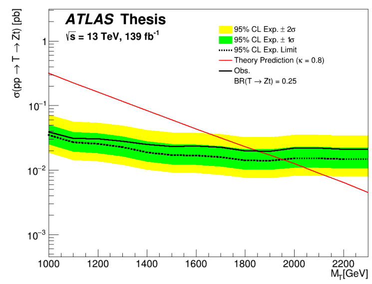

(b)

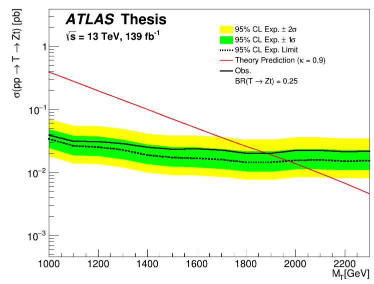

(c)

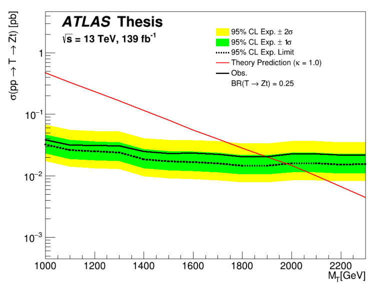

(d)

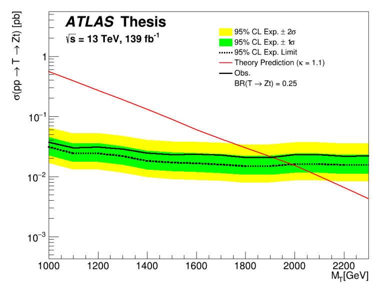

(e)

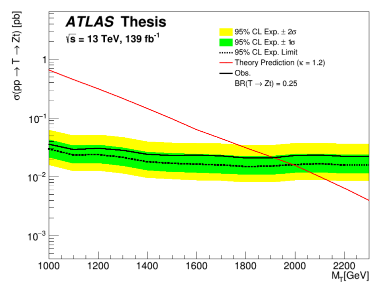

(f)

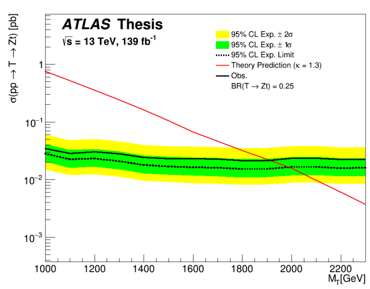

(g)

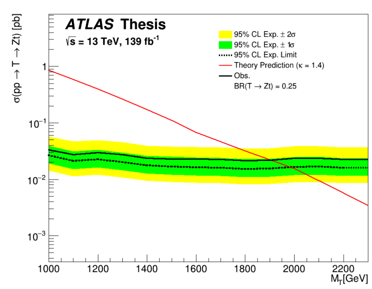

(h)

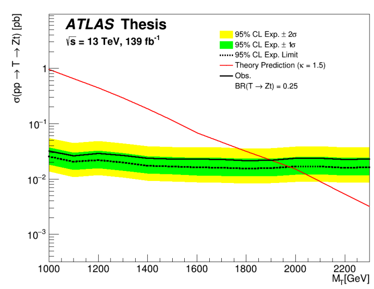

(i)

Figure D.2: Excluded cross-section limit at 95% CL for κ values of 0.7, 0.8, 0.9 (top row, left to right), 1.0, 1.1, 1.2 (middle row, left to right) and 1.3, 1.4, 1.5 (bottom row, left to right) respectively

Bibliography

[1] M. Tanabashi et al. Review of Particle Physics. Phys. Rev., D98(3):030001, 2018.

[2] Tom WB Kibble. The standard model of particle physics. European Review, 23(1):36–44, 2015.

[3] Sheldon L Glashow. Partial symmetries of weak interactions. Nuclear Physics, 22(4):579–588, 1961.

[4] A Salam and JC Ward. Electromagnetic and weak interactions. Physics Letters, 13(2):168–171, 1964.

[5] Steven Weinberg. A model of leptons. Physical Review Letters, 19(21):1264, 1967.

[6] Harald Fritzsch, Murray Gell-Mann, and Heinrich Leutwyler. Advantages of the color octet gluon picture. Physics Letters B, 47(4):365–368, 1973.

[7] Peter W Higgs. Broken symmetries and the masses of gauge bosons. Physical Review Letters, 13(16):508, 1964.

[8] Valerio Faraoni. Three new roads to the Planck scale. American Journal of Physics, 85(11):865–869, 2017.

[9] T Daniel Brennan, Federico Carta, and Cumrun Vafa. The string landscape, the swampland, and the missing corner. arXiv preprint arXiv:1711.00864, 2017.

[10] Abhay Ashtekar and Eugenio Bianchi. A short review of loop quantum gravity. Reports on Progress in Physics, 2021.

[11] Antonio Riotto and Mark Trodden. Recent progress in baryogenesis. Annual Review of Nuclear and Particle Science, 49(1):35–75, 1999.

[12] Michael Dine and Alexander Kusenko. Origin of the matter-antimatter asymmetry. Reviews of Modern Physics, 76(1):1, 2003.

[13] Sebastian Bruggisser, Benedict Von Harling, Oleksii Matsedonskyi, and Géraldine Servant. Baryon asymmetry from a composite Higgs boson. Physical Review Letters, 121(13):131801, 2018.

[14] Vedran Brdar, Alexander J Helmboldt, Sho Iwamoto, and Kai Schmitz. Type I seesaw mechanism as the common origin of neutrino mass, baryon asymmetry, and the electroweak scale. Physical Review D, 100(7):075029, 2019.

[15] Michael S Turner. Dark matter and dark energy in the universe. In Particle Physics And The Universe, pages 210–220. World Scientific, 2001.

[16] Stefano Giagu. WIMP dark matter searches with the ATLAS detector at the LHC. Frontiers in Physics, 7:75, 2019.

[17] Felix Kahlhoefer. Review of LHC dark matter searches. International Journal of Modern Physics A, 32(13):1730006, 2017.

[18] Anson Hook. TASI lectures on the strong CP problem and axions. arXiv preprint arXiv:1812.02669, 2018.

[19] Roberto D Peccei and Helen R Quinn. Constraints imposed by CP conservation in the presence of pseudoparticles. Physical Review D, 16(6):1791, 1977.

[20] DV Forero, M Tortola, and JWF Valle. Global status of neutrino oscillation parameters after Neutrino-2012. Physical Review D, 86(7):073012, 2012.

[21] Yasaman Farzan and Mariam Tórtola. Neutrino oscillations and non-standard interactions. Frontiers in Physics, 6:10, 2018.

[22] Stephen F King. Models of neutrino mass, mixing and CP violation. Journal of Physics G: Nuclear and Particle Physics, 42(12):123001, 2015.

[23] Yusuke Shimizu, Kenta Takagi, and Morimitsu Tanimoto. Neutrino CP violation and sign of baryon asymmetry in the minimal seesaw model. Physics Letters B, 778:6–16, 2018.

[24] The CMS Collaboration. Observation of a new boson at a mass of 125 GeV with the CMS experiment at the LHC. Physics Letters B, 716(1):30–61, 2012.

[25] The ATLAS Collaboration. Observation of a new particle in the search for the Standard Model Higgs boson with the ATLAS detector at the LHC. Physics Letters B, 716(1):1–29, 2012.

[26] CMS Collaboration and ATLAS Collaboration. Combined Measurement of the Higgs Boson Mass in pp Collisions at $\sqrt{s} = 7$ and 8 TeV with the ATLAS and CMS Experiments. Physical Review Letters, 114(19):191803, 2015.

[27] Gian Francesco Giudice. The dawn of the post-naturalness era. arXiv preprint arXiv:1710.07663, 2017.

[28] Gian Francesco Giudice. Naturally Speaking: The Naturalness Criterion and Physics at the LHC. Perspectives on LHC Physics, page 155, 2008.

[29] M Schmaltz. Little Higgs goes to TASI. In Physics In D $\geq$ 4 Tasi 2004: TASI 2004, pages 463–492. World Scientific, 2006.

[30] Laura Reina. TASI 2011: Lectures on Higgs-boson physics. arXiv preprint arXiv:1208.5504, 2012.

[31] Pierre Fayet. Supersymmetry and weak, electromagnetic and strong interactions. Physics Letters B, 64(2):159–162, 1976.

[32] Steven Weinberg. The quantum theory of fields: volume 3, supersymmetry. Cambridge university press, 2005.

[33] Oliver Witzel. Review on composite Higgs models. PoS-Proceedings of Science, 334, 2019.

[34] F Del Aguila and Mark J Bowick. The possibility of new fermions with ΔI= 0 mass. Nuclear Physics B, 224(1):107–136, 1983.

[35] David B Kaplan, Howard Georgi, and Savas Dimopoulos. Composite Higgs scalars. Physics Letters B, 136(3):187–190, 1984.

[36] Kaustubh Agashe, Roberto Contino, and Alex Pomarol. The minimal composite Higgs model. Nuclear Physics B, 719(1-2):165–187, 2005.

[37] Roberto Contino, Leandro Da Rold, and Alex Pomarol. Light custodians in natural composite Higgs models. Physical Review D, 75(5):055014, 2007.

[38] Nima Arkani-Hamed, Andrew G Cohen, Emanuel Katz, and Ann E Nelson. The littlest higgs. Journal of High Energy Physics, 2002(07):034, 2002.

[39] Yutaka Hosotani, Shusaku Noda, and Kazunori Takenaga. Dynamical gauge-Higgs unification in the electroweak theory. Physics Letters B, 607(3-4):276–285, 2005.

[40] Ignatios Antoniadis, Karim Benakli, and Mariano Quirós. Finite Higgs mass without supersymmetry. New Journal of Physics, 3(1):20, 2001.

[41] Thomas Appelquist, Hsin-Chia Cheng, and Bogdan A Dobrescu. Bounds on universal extra dimensions. Physical Review D, 64(3):035002, 2001.

[42] F Del Aguila, Ll Ametller, Gordon L Kane, and Jorge Vidal. Vector-like fermion and standard Higgs production at hadron colliders. Nuclear Physics B, 334(1):1–23, 1990.

[43] Juan Antonio Aguilar-Saavedra. Identifying top partners at lhc. Journal of High Energy Physics, 2009(11):030, 2009.

[44] Otto Eberhardt, Geoffrey Herbert, Heiko Lacker, Alexander Lenz, Andreas Menzel, Ulrich Nierste, and Martin Wiebusch. Impact of a Higgs boson at a mass of 126 GeV on the standard model with three and four fermion generations. Physical Review Letters, 109(24):241802, 2012.

[45] Eric Kuflik, Yosef Nir, and Tomer Volansky. Implications of Higgs searches on the four-generation standard model. Physical Review Letters, 110(9):091801, 2013.

[46] Oleksii Matsedonskyi, Giuliano Panico, and Andrea Wulzer. On the interpretation of top partners searches. Journal of High Energy Physics, 2014(12):97, 2014.

[47] Mathieu Buchkremer, Giacomo Cacciapaglia, Aldo Deandrea, and Luca Panizzi. Model-independent framework for searches of top partners. Nuclear Physics B, 876(2):376–417, 2013.

[48] Benjamin Fuks and Hua-Sheng Shao. QCD next-to-leading-order predictions matched to parton showers for Vector-like Quark models. European Physical Journal C, 77(2):135, 2017.

[49] Anupama Atre, Georges Azuelos, Marcela Carena, Tao Han, Erkcan Ozcan, José Santiago, and Gokhan Unel. Model-independent searches for new quarks at the LHC. Journal of High Energy Physics, 2011(8):80, 2011.

[50] Giacomo Cacciapaglia, Aldo Deandrea, Daisuke Harada, and Yasuhiro Okada. Bounds and decays of new heavy vector-like top partners. Journal of High Energy Physics, 2010(11):159, 2010.

[51] Juan Antonio Aguilar-Saavedra, Rachid Benbrik, Sven Heinemeyer, and Manuel Pérez-Victoria. Handbook of vectorlike quarks: Mixing and single production. Physical Review D, 88(9):094010, 2013.

[52] The ATLAS Collaboration. Search for pair and single production of new heavy quarks that decay to a Z boson and a third-generation quark in pp collisions at $\sqrt{s} = 8$ TeV with the ATLAS detector. Journal of High Energy Physics, 2014(11):a104, 2014.

[53] Mikael Chala, José Juknevich, Gilad Perez, and José Santiago. The elusive gluon. Journal of High Energy Physics, 2015(1):92, 2015.

[54] Cesare Bini, Roberto Contino, and Natascia Vignaroli. Heavy-light decay topologies as a new strategy to discover a heavy gluon. Journal of High Energy Physics, 2012(1):157, 2012.

[55] Juan Pedro Araque, Nuno Filipe Castro, and José Santiago. Interpretation of vector-like quark searches: heavy gluons in composite Higgs models. Journal of High Energy Physics, 2015(11):120, 2015.

[56] The ATLAS Collaboration. Search for production of vector-like quark pairs and of four top quarks in the lepton-plus-jets final state in pp collisions at $\sqrt{s} = 8$ TeV with the ATLAS detector. Journal of High Energy Physics, 2015(8):105, 2015.

[57] The ATLAS Collaboration. Search for vectorlike b quarks in events with one isolated lepton, missing transverse momentum, and jets at $\sqrt{s} = 8$ TeV with the ATLAS detector. Physical Review D, 91(11):112011, 2015.

[58] The CMS Collaboration. Search for vectorlike charge 2/3 T quarks in proton-proton collisions at $\sqrt{s}$= 8 TeV. Physical Review D, 93(1):012003, 2016.

[59] The CMS Collaboration. Search for pair-produced vectorlike B quarks in proton-proton collisions at $\sqrt{s}$= 8 TeV. Physical Review D, 93(11):112009, 2016.

[60] The CMS Collaboration. Search for top-quark partners with charge 5/3 in the same-sign dilepton final state. Physical Review Letters, 112(17):171801, 2014.

[61] The ATLAS Collaboration. Search for single production of vector-like quarks decaying into Wb in pp collisions at $\sqrt{s} = 8$ TeV with the ATLAS detector. European Physical Journal C, 76(8):442, 2016.

[62] The ATLAS Collaboration. Search for pair production of up-type vector-like quarks and for four-top-quark events in final states with multiple b-jets with the ATLAS detector. Journal of High Energy Physics, 2018(7):89, 2018.

[63] The ATLAS Collaboration. Search for pair production of heavy vector-like quarks decaying to high-pt W bosons and b quarks in the lepton-plus-jets final state in pp collisions at $\sqrt{s} = 13$ TeV with the ATLAS detector. Journal of High Energy Physics, 2017(10):141, 2017.

[64] The ATLAS Collaboration. Search for pair production of vector-like top quarks in events with one lepton, jets, and missing transverse momentum in $\sqrt{s} = 13$ TeV pp collisions with the ATLAS detector. Journal of High Energy Physics, 2017(8):52, 2017.

[65] The ATLAS Collaboration. Search for new phenomena in events with same-charge leptons and b-jets in pp collisions at $\sqrt{s} = 13$ TeV with the ATLAS detector. Journal of High Energy Physics, 2018(12):39, 2018.

[66] The ATLAS Collaboration. Search for pair production of heavy vectorlike quarks decaying into hadronic final states in p p collisions at s= 13 TeV with the ATLAS detector. Physical Review D, 98(9):092005, 2018.

[67] The ATLAS Collaboration. Combination of the searches for pair-produced vectorlike partners of the third generation quarks at $\sqrt{s} = 13$ TeV with the ATLAS detector. Physical Review Letters, 121(21):211801, 2018.

[68] The CMS Collaboration. Search for pair production of vector-like T and B quarks in single-lepton final states using boosted jet substructure in proton-proton collisions at $\sqrt{s} = 13$ TeV. Journal of High Energy Physics, 2017(11):085, 2017.

[69] The CMS Collaboration. Search for pair production of vector-like quarks in the $bw\bar{b}w$ channel from proton–proton collisions at $\sqrt{s} = 13$ TeV. Physics Letters B, 779:82–106, 2018.

[70] The CMS Collaboration. Search for vector-like T and B quark pairs in final states with leptons at $\sqrt{s} = 13$ TeV. Journal of High Energy Physics, 2018(8):177, 2018.

[71] The ATLAS Collaboration. Search for pair and single production of vectorlike quarks in final states with at least one Z boson decaying into a pair of electrons or muons in pp collision data collected with the ATLAS detector at $\sqrt{s}$= 13 TeV. Physical Review D, 98(11):112010, 2018.

[72] The ATLAS Collaboration. Search for single production of vector-like quarks decaying into Wb in pp collisions at $\sqrt{s} = 13$ TeV with the ATLAS detector. Journal of High Energy Physics, 2019(5):164, 2019.

[73] The ATLAS Collaboration. Search for large missing transverse momentum in association with one top-quark in proton-proton collisions at $\sqrt{s} = 13$ TeV with the ATLAS detector. Journal of High Energy Physics, 2019(5):41, 2019.

[74] The CMS Collaboration. Search for single production of a vector-like T quark decaying to a Z boson and a top quark in proton–proton collisions at $\sqrt{s} = 13$ TeV. Physics Letters B, 781:574–600, 2018.

[75] The CMS Collaboration. Search for single production of vector-like quarks decaying to a top quark and a W boson in proton-proton collisions at $\sqrt{s} = 13$ TeV. European Physical Journal C, 79(2):90, 2019.

[76] The CMS Collaboration. Search for single production of vector-like quarks decaying to a b quark and a Higgs boson. Journal of High Energy Physics, 2018(6):31, 2018.

[77] The CMS Collaboration. Search for electroweak production of a vector-like T quark using fully hadronic final states. Journal of High Energy Physics, 2020(1):36, 2020.

[78] Oliver Sim Brüning, Paul Collier, P Lebrun, Stephen Myers, Ranko Ostojic, John Poole, and Paul Proudlock. LHC Design Report. CERN Yellow Reports: Monographs. CERN, Geneva, 2004.

[79] The ATLAS Collaboration. The ATLAS Experiment at the CERN Large Hadron Collider. Journal of Instrumentation, 3:S08003. 437 p, 2008. Also published by CERN Geneva in 2010.

[80] The CMS Collaboration. CMS Physics: Technical Design Report Volume 1: Detector Performance and Software. 2006.

[81] The ALICE Collaboration. The ALICE experiment at the CERN LHC. A Large Ion Collider Experiment. Journal of Instrumentation, 3:S08002. 259 p, 2008.

[82] The LHCb Collaboration. The LHCb Detector at the LHC. Journal of Instrumentation, 3:S08005, 2008. Also published by CERN Geneva in 2010.

[83] E Boltezar, H Haseroth, Werner Pirkl, Günther Plass, T R Sherwood, U Tallgren, P Têtu, D Warner, and M Weiss. Performance of the new CERN 50 MeV linac. IEEE Transactions on Nuclear Science, 26:3674–3676, 1979.

[84] Simone Gilardoni, Django Manglunki, Jean-Paul Burnet, Christian Carli, Michel Chanel, Roland Garoby, Massimo Giovannozzi, Steven Hancock, Helmut Haseroth, Kurt Hübner, et al. Fifty years of the CERN Proton Synchrotron: Volume 2. CERN Yellow Reports: Monographs. Sep 2013. Comments: 58 pages, published as CERN Yellow Report https://cds.cern.ch/record/1597087.

[85] Lyndon R Evans. The proton-antiproton collider. John Adams' memorial lecture. CERN, Geneva, 1988. Delivered at CERN, 25 Nov 1987.

[86] Luigi Di Lella and Carlo Rubbia. The Discovery of the W and Z Particles. Advanced Series on Directions in High Energy Physics, 23:137–163, 2015.

[87] Christiane Lefèvre. The CERN accelerator complex. Complexe des accélérateurs du CERN. Dec 2008.

[88] Werner Herr and B Muratori. Concept of luminosity. 2006.

[89] The ATLAS Collaboration. ATLAS data quality operations and performance for 2015-2018 data-taking. Journal of Instrumentation, 15:P04003. 43 p, Nov 2019.

[90] S Haywood, L Rossi, R Nickerson, and A Romaniouk. ATLAS Inner Detector: Technical Design Report, 2. Technical design report. ATLAS. CERN, Geneva, 1997.

[91] Norbert Wermes and G Hallewel. ATLAS pixel detector: Technical Design Report. Technical design report. ATLAS. CERN, Geneva, 1998.

[92] M Capeans, G Darbo, K Einsweiller, M Elsing, T Flick, M Garcia-Sciveres, C Gemme, H Pernegger, O Rohne, and R Vuillermet. ATLAS Insertable B-Layer Technical Design Report. Technical report, Sep 2010.

[93] The ATLAS Collaboration. Track Reconstruction Performance of the ATLAS Inner Detector at $\sqrt{s} = 13$ TeV. Technical report, CERN, Geneva, Jul 2015.

[94] Karolos Potamianos. The upgraded Pixel detector and the commissioning of the Inner Detector tracking of the ATLAS experiment for Run-2 at the Large Hadron Collider. Technical report, CERN, Geneva, Aug 2016. 15 pages, EPS-HEP 2015 Proceedings.

[95] J N Jackson. The ATLAS semiconductor tracker (SCT). Nuclear Instrumentation Methods Phys. Res., A, 541:89–95, 2005.

[96] ATLAS TRT Collaboration. The ATLAS TRT Barrel Detector. Journal of Instrumentation, 3:P02014, 2008.

[97] ATLAS TRT Collaboration. The ATLAS TRT end-cap detectors. Journal of Instrumentation, 3:P10003, 2008.

[98] The ATLAS Collaboration. ATLAS liquid-argon calorimeter: Technical Design Report. Technical design report. ATLAS. CERN, Geneva, 1996.

[99] The ATLAS Collaboration. ATLAS tile calorimeter: Technical Design Report. Technical design report. ATLAS. CERN, Geneva, 1996.

[100] The ATLAS Collaboration. ATLAS muon spectrometer: Technical Design Report. Technical design report. ATLAS. CERN, Geneva, 1997.

[101] The ATLAS Collaboration. Operation of the ATLAS trigger system in Run 2. Journal of Instrumentation, 15:P10004. 60 p, Jul 2020.

[102] T. Gleisberg, Stefan. Hoche, F. Krauss, M. Schonherr, S. Schumann, et al. Event generation with SHERPA 1.1. Journal of High Energy Physics, 02:007, 2009.

[103] Stefan Höche, Frank Krauss, Steffen Schumann, and Frank Siegert. QCD matrix elements and truncated showers. Journal of High Energy Physics, 05:053, 2009.

[104] Tanju Gleisberg and Stefan Höche. Comix, a new matrix element generator. Journal of High Energy Physics, 12:039, 2008.

[105] Steffen Schumann and Frank Krauss. A Parton shower algorithm based on Catani-Seymour dipole factorisation. Journal of High Energy Physics, 03:038, 2008.

[106] Richard D. Ball et al. Parton distributions for the LHC Run II. Journal of High Energy Physics, 04:040, 2015.

[107] Giovanni Ossola, Costas G Papadopoulos, and Roberto Pittau. Reducing full one-loop amplitudes to scalar integrals at the integrand level. Nuclear Physics B, 763(1-2):147–169, 2007.

[108] Johan Alwall, R Frederix, S Frixione, V Hirschi, Fabio Maltoni, Olivier Mattelaer, H-S Shao, T Stelzer, P Torrielli, and M Zaro. The automated computation of tree-level and

next-to-leading order differential cross sections, and their matching to parton shower simulations. Journal of High Energy Physics, 2014(7):79, 2014.

[109] Johan Alwall, Michel Herquet, Fabio Maltoni, Olivier Mattelaer, and Tim Stelzer. Madgraph 5: going beyond. Journal of High Energy Physics, 2011(6):128, 2011.

[110] Torbjorn Sjöstrand, Stephen Mrenna, and Peter Z. Skands. A Brief Introduction to PYTHIA 8.1. Computer Physics Communications, 178:852, 2008.

[111] Richard D Ball, Valerio Bertone, Stefano Carrazza, Christopher S Deans, Luigi Del Debbio, Stefano Forte, Alberto Guffanti, Nathan P Hartland, José I Latorre, Juan Rojo, et al. Parton distributions with LHC data. Nuclear Physics B, 867(2):244–289, 2013.

[112] The ATLAS Collaboration. ATLAS Pythia 8 tunes to 7 TeV data. Technical report, CERN, Geneva, Nov 2014.

[113] Wolfgang Lukas. Fast simulation for ATLAS: Atlfast-II and ISF. In Journal of Physics: Conference Series, volume 396, page 022031. IOP Publishing, 2012.

[114] Paolo Nason. A New method for combining NLO QCD with shower Monte Carlo algorithms. Journal of High Energy Physics, 11:040, 2004.

[115] Stefano Frixione, Paolo Nason, and Carlo Oleari. Matching NLO QCD computations with Parton Shower simulations: the POWHEG method. Journal of High Energy Physics, 11:070, 2007.

[116] Simone Alioli, Paolo Nason, Carlo Oleari, and Emanuele Re. A general framework for implementing NLO calculations in shower Monte Carlo programs: the POWHEG BOX. Journal of High Energy Physics, 06:043, 2010.

[117] Michal Czakon and Alexander Mitov. Top++: a program for the calculation of the top-pair cross-section at hadron colliders. Computer Physics Communications, 185:2930, Dec 2011.

[118] M Beneke, P Falgari, Sebastian Klein, and C Schwinn. Hadronic top-quark pair production with nnll threshold resummation. Nuclear Physics B, 855(3):695–741, 2012.

[119] Matteo Cacciari, Michał Czakon, Michelangelo Mangano, Alexander Mitov, and Paolo Nason. Top-pair production at hadron colliders with next-to-next-to-leading logarithmic soft-gluon resummation. Physics Letters B, 710(4-5):612–622, 2012.

[120] Manuel Bähr, Stefan Gieseke, Martyn A Gigg, David Grellscheid, Keith Hamilton, Oluseyi Latunde-Dada, Simon Plätzer, Peter Richardson, Michael H Seymour, Alexander Sherstnev, et al. Herwig++ physics and manual. European Physical Journal C, 58(4):639–707, 2008.

[121] Johannes Bellm et al. Herwig 7.0/Herwig++ 3.0 release note. European Physical Journal C, 76(4):196, 2016.

[122] Lucian A Harland-Lang, AD Martin, P Motylinski, and RS Thorne. Parton distributions in the LHC era: MMHT 2014 PDFs. European Physical Journal C, 75(5):1–53, 2015.

[123] Peter Zeiler Skands. Tuning Monte Carlo Generators: The Perugia Tunes. Physical Review D, 82:074018, 2010.

[124] Nikolaos Kidonakis. Next-to-next-to-leading-order collinear and soft gluon corrections for t-channel single top quark production. Physical Review D, 83(9):091503, 2011.

[125] Nikolaos Kidonakis. Next-to-next-to-leading logarithm resummation for s-channel single top quark production. Physical Review D, 81(5):054028, 2010.

[126] Nikolaos Kidonakis. Two-loop soft anomalous dimensions for single top quark associated production with a W^- or H^-. Physical Review D, 82(5):054018, 2010.

[127] Jun Gao, Marco Guzzi, Joey Huston, Hung-Liang Lai, Zhao Li, Pavel Nadolsky, Jon Pumplin, Daniel Stump, and C-P Yuan. CT10 next-to-next-to-leading order global analysis of QCD. Physical Review D, 89(3):033009, 2014.

[128] Celine Degrande, Claude Duhr, Benjamin Fuks, David Grellscheid, Olivier Mattelaer, and Thomas Reiter. UFO–the Universal FeynRules Output. Computer Physics Communications, 183(6):1201–1214, 2012.

[129] Sea Agostinelli, John Allison, K al Amako, John Apostolakis, H Araujo, Pedro Arce, Makoto Asai, D Axen, Swagato Banerjee, GJNI Barrand, et al. GEANT4—a simulation toolkit. Nuclear instruments and methods in physics research section A: Accelerators, Spectrometers, Detectors and Associated Equipment, 506(3):250–303, 2003.

[130] The ATLAS Collaboration. The ATLAS simulation infrastructure. European Physical Journal C, 70(3):823–874, 2010.

[131] ATLAS Collaboration. Electron reconstruction and identification efficiency measurements with the ATLAS detector using the 2011 LHC proton–proton collision data. European Physical Journal C, 74:2941, 2014.

[132] The ATLAS Collaboration. Electron efficiency measurements with the ATLAS detector using 2012 LHC proton–proton collision data. European Physical Journal C, 77(3):1–45, 2017.

[133] ATLAS Collaboration. Electron and photon energy calibration with the ATLAS detector using LHC Run 1 data. European Physical Journal C, 74:3071, 2014.

[134] Keith Rehermann and Brock Tweedie. Efficient identification of boosted semileptonic top quarks at the lhc. Journal of High Energy Physics, 2011(3):1–27, 2011.

[135] ATLAS Collaboration. Muon reconstruction performance of the ATLAS detector in proton–proton collision data at $\sqrt{s} = 13\,\text{TeV}$. European Physical Journal C, 76:292, 2016.

[136] Matteo Cacciari, Gavin P. Salam, and Gregory Soyez. The anti-k_t jet clustering algorithm. Journal of High Energy Physics, 04:063, 2008.

[137] Matteo Cacciari, Gavin P Salam, and Gregory Soyez. Fastjet user manual. European Physical Journal C, 72(3):1–54, 2012.

[138] ATLAS Collaboration. Topological cell clustering in the ATLAS calorimeters and its performance in LHC Run 1. European Physical Journal C, 77:490, 2017.

[139] ATLAS Collaboration. Properties of Jets and Inputs to Jet Reconstruction and Calibration with the ATLAS Detector Using Proton-Proton Collisions at $\sqrt{s} = 13$ TeV. Technical report, CERN, Geneva, Aug 2015. All figures including auxiliary figures are available at https://atlas.web.cern.ch/Atlas/GROUPS/PHYSICS/PUBNOTES/ATL-PHYS-PUB-2015-036.

[140] ATLAS Collaboration. Jet energy measurement and its systematic uncertainty in proton–proton collisions at $\sqrt{s} = 7$ TeV with the ATLAS detector. European Physical Journal C, 75:17, 2015.

[141] ATLAS Collaboration. Jet Calibration and Systematic Uncertainties for Jets Reconstructed in the ATLAS Detector at $\sqrt{s} = 13$ TeV. Technical report, CERN, Geneva, Jul 2015.

[142] ATLAS Collaboration. Performance of pile-up mitigation techniques for jets in pp collisions at $\sqrt{s} = 8\,\text{TeV}$ using the ATLAS detector. European Physical Journal C, 76:581, 2016.

[143] ATLAS Collaboration. Machine learning algorithms for b-jet tagging at the atlas experiment. In Journal of Physics: Conference Series, volume 1085, page 042031. IOP Publishing, 2018.

[144] The ATLAS Collaboration. Optimisation of the ATLAS b-tagging performance for the 2016 LHC Run. Technical report, CERN, Geneva, Jun 2016.

[145] The ATLAS Collaboration. Luminosity determination in pp collisions at $\sqrt{s} = 8$ TeV using the ATLAS detector at the LHC. European Physical Journal C, C76(12):653, 2016.

[146] The ATLAS Collaboration. Electron efficiency measurements with the ATLAS detector using the 2015 LHC proton-proton collision data. Technical report, CERN, Geneva, Jun 2016.

[147] The ATLAS Collaboration. Electron and photon energy calibration with the ATLAS detector using data collected in 2015 at $\sqrt{s} = 13$ TeV. Technical report, CERN, Geneva, Aug 2016. All figures including auxiliary figures are available at https://atlas.web.cern.ch/Atlas/GROUPS/PHYSICS/PUBNOTES/ATL-PHYS-PUB-2016-015.

[148] ATLAS Collaboration. Muon reconstruction performance of the ATLAS detector in proton–proton collision data at $\sqrt{s} = 13$ tev. European Physical Journal C, 76(5):1–30, 2016.

[149] ATLAS Collaboration. Jet energy scale measurements and their systematic uncertainties in proton-proton collisions at s= 13 TeV with the ATLAS detector. Physical Review D, 96(7):072002, 2017.

[150] The ATLAS Collaboration. Multi-Boson Simulation for 13 TeV ATLAS Analyses. Technical report, CERN, Geneva, Jan 2016. All figures including auxiliary figures are

available at https://atlas.web.cern.ch/Atlas/GROUPS/PHYSICS/PUBNOTES/ATL-PHYS-PUB-2016-002.

[151] The ATLAS Collaboration. Modelling of the $t\bar{t}H$ and $t\bar{t}V$ $(V = W, Z)$ processes for $\sqrt{s} = 13$ TeV ATLAS analyses. Technical report, CERN, Geneva, Jan 2016.

[152] The ATLAS Collaboration. Simulation of top quark production for the ATLAS experiment at $\sqrt{s} = 13$ TeV. Technical report, CERN, Geneva, Jan 2016.

[153] Sayipjamal Dulat, Tie-Jiun Hou, Jun Gao, Marco Guzzi, Joey Huston, Pavel Nadolsky, Jon Pumplin, Carl Schmidt, Daniel Stump, and C-P Yuan. New parton distribution functions from a global analysis of quantum chromodynamics. Physical Review D, 93(3):033006, 2016.

[154] Wouter Verkerke and David Kirkby. The RooFit toolkit for data modeling. In Statistical Problems in Particle Physics, Astrophysics and Cosmology, pages 186–189. World Scientific, 2006.

[155] TRExFitter Package: https://gitlab.cern.ch/TRExStats/TRExFitter.

[156] Lorenzo Moneta, Kevin Belasco, Kyle Cranmer, Sven Kreiss, Alfio Lazzaro, Danilo Piparo, Gregory Schott, Wouter Verkerke, and Matthias Wolf. The RooStats project. arXiv preprint arXiv:1009.1003, 2010.

[157] Glen Cowan, Kyle Cranmer, Eilam Gross, and Ofer Vitells. Asymptotic formulae for likelihood-based tests of new physics. European Physical Journal C, 71:1554, 2011. [Erratum: European Physical JournalC73,2501(2013)].

[158] Kyle Cowan, Glenand Cranmer, Eilam Gross, and Ofer Vitells. Erratum to: Asymptotic formulae for likelihood-based tests of new physics. European Physical Journal, C73(7):2501, 2013.

[159] Thomas Junk. Confidence level computation for combining searches with small statistics. Nuclear Instrumentation Methods, A434:435–443, 1999.

[160] A L Read. Presentation of search results: the CL_s technique. Journal of Physics G, 28(10):2693, 2002.

[161] Avik Roy, Nikiforos Nikiforou, Nuno Castro, and Timothy Andeen. Novel interpretation strategy for searches of singly produced vectorlike quarks at the LHC. Physical Review D, 101(11):115027, 2020.

[162] Natascia Vignaroli. New W' signals at the LHC. Physical Review D, 89(9):095027, 2014.

[163] Davide Greco and Da Liu. Hunting composite vector resonances at the LHC: Naturalness facing data. Journal of High Energy Physics, 2014(12):126, 2014.

[164] Giacomo Cacciapaglia, Thomas Flacke, Myeonghun Park, and Mengchao Zhang. Exotic Decays of Top Partners: Mind the Search Gap. Physics Letters B, 798:135015, 2019.

[165] Bogdan A Dobrescu and Felix Yu. Exotic signals of vectorlike quarks. Journal of Physics G: Nuclear and Particle Physics, 45(8):08LT01, 2018.

[166] Rachid Benbrik, E Bergeaas Kuutmann, D Buarque Franzosi, Venugopal Ellajosyula, Rikard Enberg, Gabriele Ferretti, Max Isacson, Y-B Liu, Tanumoy Mandal, Thomas Mathisen, et al. Signatures of vector-like top partners decaying into new neutral scalar or pseudoscalar bosons. Journal of High Energy Physics, 2020(5):1–48, 2020.

[167] Matthew J Dolan, JL Hewett, M Krämer, and TG Rizzo. Simplified models for Higgs physics: Singlet scalar and vector-like quark phenomenology. Journal of High Energy Physics, 2016(7):39, 2016.

[168] Mikael Chala. Direct bounds on heavy toplike quarks with standard and exotic decays. Physical Review D, 96(1):015028, 2017.

[169] Juan Antonio Aguilar-Saavedra, Daniel E López-Fogliani, and C Muñoz. Novel signatures for vector-like quarks. Journal of High Energy Physics, 2017(6):95, 2017.

[170] N Kauer. Narrow-width approximation limitations. Physics Letters B, 649(5-6):413–416, 2007.

[171] D Berdine, N Kauer, and D Rainwater. Breakdown of the narrow width approximation for new physics. Physical Review Letters, 99(11):111601, 2007.

[172] Eamonn Maguire, Lukas Heinrich, and Graeme Watt. HEPData: a repository for high energy physics data.

[173] The ATLAS Collaboration. HEPData Entry for ATLAS Analysis [71], 2018.

[174] Michael S. Chanowitz and Mary K. Gaillard. The TeV physics of strongly interacting W's and Z's. Nuclear Physics B, 261:379–431, 1985.

[175] Giuliano Panico and Andrea Wulzer. The Composite Nambu-Goldstone Higgs. Springer, 2016.

[176] Alexandra Carvalho, Stefano Moretti, Dermot O'Brien, Luca Panizzi, and Hugo Prager. Single production of vectorlike quarks with large width at the large hadron collider. Physical Review D, 98(1):015029, 2018.

[177] Olivier Mattelaer. On the maximal use of Monte Carlo samples: re-weighting events at NLO accuracy. European Physical Journal C, 76(12):1–10, 2016.

[178] Johan Alwall, Alessandro Ballestrero, Paolo Bartalini, Sergey Belov, E Boos, Andy Buckley, Jonathan M Butterworth, L Dudko, Stefano Frixione, L Garren, et al. A standard format for les houches event files. Computer Physics Communications, 176(4):300–304, 2007.

[179] ATLAS Collaboration. Jet reconstruction and performance using particle flow with the ATLAS detector. European Physical Journal C, 77(7):1–47, 2017.

[180] Sabine Hossenfelder. Lost in math: How beauty leads physics astray. Hachette UK, 2018.